

Development and Assessment
of *In Vitro* Models of
Osteogenic Microstructures



University of
Sheffield

A thesis submitted in partial fulfilment of the requirements
for the degree of Doctor of Philosophy

Alice J. Hann

**Department of Materials Science and
Engineering**

The University of Sheffield

March 2023

Abstract

In vitro models of bone aim to use materials that encourage the fast deposition of significant amounts of mineral and collagen. Although this would be beneficial in tissue engineering applications, using this for *in vitro* modelling oversimplifies the organised structure that is observed in mature bone. Furthermore, cortical and trabecular bone have notably different architectures. Within this thesis, two differential scaffolds were developed and tested, for use in lamellar and trabecular bone models, to mimic structural features of the two bone-type organisations that are commonly overlooked in *in vitro* models.

For a model of lamellar bone, aligned and non-aligned polycaprolactone fibres were explored, to test whether human cells at an early stage of osteogenic differentiation would deposit collagen exhibiting a twisted plywood deposition behaviour and provide a model system of laboratory-grown lamellae. On aligned fibres, there was an observable spacial change in collagen direction comparable to that seen within physiological human lamellae, which shows a gradual change in fibril direction between 10-60° from the initial orientation of the fibrils closest to the osteon's centre. A method to produce a more cortical bone-like structure may be valuable for a variety of applications, including the development of more accurate models of lamellar osteogenesis, or for use in high-throughput drug testing.

To produce a trabecular-like material, a novel method for producing a porous emulsion was explored. By the combination of mechanical properties of methacrylated polycaprolactone-triol (3PCL-MA) and the biocompatibility of gelMA, this work aimed to develop a tuneable and mechanically robust porous bioink for the 3D printing of trabecular bone, using a curable two-phase emulsion system. 3PCL-MA/GelMA emulsions provide a viable route for the fabrication of stiff, printable inks. The mechanical properties of the inks are significantly higher than that of pure gelMA, which may make them a more promising option for the culture of bone cells.

Dedication

To Dad,

You gave me your love of learning, and your stubbornness to not give up.

I wish you could have read this.

Acknowledgements

I would like to thank my supervisor, Professor. Gwendolen Reilly, for the continued support and encouragement throughout, even from my undergraduate degree, and for giving me the opportunity of this PhD. I would also like to thank Dr Nicola Green and Professor Fred Claeysens, equally for your support and guidance throughout. Thank you to the University of Sheffield for my studentship and to the EPSRC for funding this.

I would also like to acknowledge Professor Shrike Zhang, and the Royal Society, for the amazing opportunity to work at the Brigham and Woman's Hospital in Boston. It was an honour to work alongside the team there and to meet so many wonderful people. Also to Nanosurf, for funding my electrospinning work in Pisa, and to Linari Nanotech for hosting me. I am sorry for managing to break the Nespresso machine on my first day... I would also like to thank Professor Serena Danti for generously letting me use her equipment at The University of Pisa, and her students for so kindly accommodating me.

My PhD would not have been the same without all the great friends I got to meet throughout. My lab colleagues, Denata, Jose, Ballard, Tugba, Areli and Caitlin, and to everyone who passed through along the way, you made the days in the lab so much brighter. Also, to Will, thank you for the coffee breaks, the continuous reassurance, and being a friendly face in the audience during scary presentations. Thank you to Julie, for keeping C+09 running and for always being there for tea and a chat (and a bit of gossip!). Thank you to everyone in Kroto (and more often, The Red Deer) for the laughs, chaos, increasingly strange conversations, and endless support both in and out of the lab. Also, to my friends outside the lab, but most of all to Sophie and Rose, for always being there to pick me up after a long day. You are all genuinely what got me through the days, and I am eternally grateful.

Joe, thank you for being so encouraging throughout, and especially for flying out to Boston during a pandemic to spend Christmas with me. I'm so glad I had you by my side.

And finally, a special thanks to my family, and especially to my Mum, for being my inspiration into a career into science and biology. Thank you for always supporting me 100% through all my life choices.

List of Figures

Figure 1-1: Hierarchical structure of cortical bone. Image obtained from Zimmermann et al with permissions pending [324]	11
Figure 1-2: Fibrillar orientation relative to the haversian canal. The orientation of the fibrils changes with a periodicity of 5 – 7 μ m. Fibrils of the outermost lamella show a different chirality to that of the inner lamellae. Reprinted with permission from Wagermaier [31] et al Copyright 2023 American Vacuum Society	13
Figure 1-3: RANKL is produced by osteoblasts and binds to RANK receptors on the surface of osteoclast pre-cursors. This stimulates the osteoblast pre-cursor to differentiate into an osteoclast. Further binding activates the osteoclast, allowing it to bind to the bones surface and secrete bone-resorbing factors. Created using BioRender.	17
Figure 1-4: Two photons interact within a non-centrosymmetric molecule (e.g collagen) and are combined to form a new photon with twice the energy (2ω) and half the wavelength of the initial photons. Image produced in BioRender.	24
Figure 1-5: RhoA/ROCK mediated pathway in response to cell morphology on fibrous matrices. Reprinted with permission from Chang et al [273] Copyright 2023 American Chemical Society	29
Figure 1-6: Functionalisation of a 3-arm PCL (a) with methyl anhydride, forming 3-arm PCL methacrylate. The resulting product can either be fully methacrylated (bi) or partially methacrylated (bii, biii). Image taken from Field et al[156] under the terms of the Creative Commons Attribution License (CC BY).	36
Figure 1-7: Cells encapsulated in pure GelMA hydrogels can be seen to adopt a rounded conformation. With the addition of a soluble, low MW PEO, a porous hydrogel may be created. PEO may be washed out, leaving pores that may allow for the spreading of cells. Created using BioRender	38
Figure 1-8: An osteogenesis-on-a-chip model, using negative replica moulding and polyHIPEs to produce a microfluidic chip with both micro- and macro-porosity, mimicking the multiscale porosity observed in trabecular bone. A, B, C) Fluid channels can be observed, with hexagonal struts. D, E) Interconnected micropores with a 5-30 μ m diameter F) Distribution of the pores. Image from Bahmaee et al under the terms of the Creative Commons Attribution License (CC BY).....	42
Figure 1-9: Schematic of the electrospinning process. A syringe pump is used to slowly extrude polymer from a blunt tip needle, connected to a positive high voltage generator (P-HVG). This is then drawn towards a grounded collection drum, with a controllable rotary speed between 200-2000 rotations per minute.	46
Figure 3-1: Collagen deposited on top of the polymer scaffolds was assessed using second harmonic generation. The polymer scaffold was taken as the point of 0 μ M.....	65
Figure 3-2: Workflow for the analysis of nuclear size and morphology using the image processing software, ImageJ. Thresholded images of DAPI-stained nucleus on either	

aligned or non-aligned PCL fibres are processed using the “Analyse Particles” tool. At least 400 measurements are taken across 6 separate images for each condition. 65

Figure 3-3: CellCrown™ transwell inserts are used to hold PCL fibres. 68

Figure 3-4: General workflow for the production of emulsions and subsequent encapsulation of MG63 cells. Figure created using BioRender.com..... 77

Figure 4-1: SEM images of aligned and non-aligned electrospun PCL fibres. **A)** 10kV, 2000RPM **B)**10kV, 200RPM **C)** 11.5kV, 2000RPM **D)** 11.5kV, 200RPM **E)** 13kV, 2000RPM **F)** 13kV, 200RPM **G)** 15kV, 2000RPM **F)** 15kV, 200RPM. Scale bar = 200µM..... 81

Figure 4-2: Histograms showing the relative frequency distribution of fibre alignment of fibres spun at 10, 11.5, 13 or 15kV, and 2000 or 200RPM, as measured using the Directionality plug in from Fiji. 2000RPM spinning resulted in a more aligned fibre construct, as noted by the distinct peak on the histogram, whilst 200RPM produced non-aligned constructs, with a wide distribution of fibres. 82

Figure 4-3 Histograms representing the distribution of fibre diameters of electrospun PCL fibres, as measured using ImageJ. Histogram represents the measurements of 100 randomly chosen fibres across 3 separate images for each condition. 82

Figure 4-4: SEM image of visible nanopores formed on the surface of a fibre produced at 2000RPM and 11.5kV. Scale bar represents 20µm. 83

Figure 4-5: Digital images of contact angle testing of aligned and non-aligned fibres before and after treating with air plasma at 0.8mBar, 50V for 60 seconds. It can be seen that for both aligned and non-aligned fibres that hydrophobicity is greatly reduced, allowing the fibres to become fully wettable 84

Figure 4-6: Young’s modulus (A) and ultimate tensile strength (UTS) (B) measured for aligned and non-aligned fibres. Aligned fibres were tested in both the transverse and longitudinal orientations. Results are shown as mean ± SD. Tested using one-way ANOVA with Tukey’s *post-hoc* for multiple comparisons. n=4. Significant p values are reported as a=<0.0001 b=<0.0001 c=<0.0001 d=0.0001..... 85

Figure 4-7: 7 day metabolic activity, inferred from metabolic activity of h-TERT Y201 cells seeded on TCP and cultured in either DMEM, StemMACs XFM or CD2, and either coated with gelatin or seeded directly onto the TCP. CD1 shows the highest metabolic activity of the cells in both gelatin coated or TCP conditions. Tested using two-way ANOVA Tukey’s *post-hoc* test for multiple comparisons with Results are shown as mean ± SD. n=6 * = <0.0001 86

Figure 4-8: Resazurin reduction for assessment of metabolic activity of Y201 cells at day 21 of culture in varying concentrations of AA2P and in presence or absence of dexamethasone. Results shown as mean ± SD (n=6). Tested using Kruskal-Wallis test with Dunn’s multiple comparisons. Results shown as mean±SD. 87

Figure 4-9: Sirius Red Staining for collagen deposition of Y201 cells at day 21 of culture in varying concentrations of AA2P and in presence or absence of dexamethasone. Results shown as mean ± SD (n=6). Tested using a two-way ANOVA with Tukey’s *post-hoc* test for multiple comparisons. Significant p number shown as a=0.0329 88

Figure 4-10: Alizarin red staining for mineral deposition of Y201 cells at day 21 of culture in varying concentrations of AA2P and in presence or absence of dexamethasone. Results shown as mean ± SD (n=6). Tested using Kruskal-Wallis test

with Dunn's multiple comparisons. Results shown as mean \pm SD. Significant p values shown as a=0.0105 and b=0.008.....	88
Figure 4-11: Resazurin reduction of Y201 cells cultured at a density of either 0.5×10^4 , 1×10^4 or 2×10^4 cells per scaffold. A) Fibronectin coated aligned fibres, B) Fibronectin coated non-aligned fibres C) Fibronectin coated coverslips D) Plasma coated aligned fibres E) Plasma coated non-aligned fibres F) Plasma coated coverslips G) Plasma + fibronectin coated aligned fibres H) Plasma + fibronectin coated non-aligned fibres and I) Plasma + fibronectin coated coverslips. Measured at days 1, 7 and 14. Results shown as mean \pm SD. n=4.....	90
Figure 4-12: Resazurin reduction of h-TERT Y201 cells cultured at a density of 1×10^4 cells on either PCL-aligned, non-aligned scaffolds or spin-coated coverslips scaffolds after 7 days of culture. Scaffolds were treated with either fibronectin, air plasma or plasma + fibronectin. Results are shown as mean \pm SD. n=4. Statistically tested using a two-way ANOVA with Dunn's post-hoc test for multiple comparisons. Statistically significant p values are represented as a=0.0018 b=0.0066 c=0.0338 d=0.0025 e=0.0251	91
Figure 4-13: Sirius red staining (Top) and SHG imaging (bottom) of collagen after 14 days culture on aligned scaffolds. A) Plasma treatment only, B) Plasma + FN C) FN only. Scale bar = 50 μ M	92
Figure 5-1: Timeline of assays carried out at each time point. Samples are either treated with expansion media (EM), formed of xenofree media supplemented with ascorbic-2-phosphate (AA2P), or osteogenic media (OM), formed of xenofree media supplemented with dexamethasone, AA2P and β -glycerolphosphate (β -GP) Quantitative Polymerase Chain Reaction (PCR), second harmonic generation (SHG), Sirius red stain (SRS), Alizarin Red stain (ARS) and alkaline phosphatase enzyme activity (ALP) were all carried out were indicated along the timeline.	105
Figure 5-2 Quantification of collagen deposition using Sirius Red Stain and cell attachment of Y201 cells seeded on aligned and non-aligned fibres treated with either plasma only or plasma + fibronectin coated. Statistical analysis carried out using a two-way ANOVA and Tukey's post-hoc test for multiple comparisons. Results shown as mean \pm SD (n=9).....	106
Figure 5-3: Quantification of mineral deposition using Alizarin Red Stain (ARS). Statistical analysis carried out using Kruskal-Wallis test with Dunn's multiple comparisons. Results shown as mean \pm SD. n=6. p values are reported as a=0.0173 b=0.0374	107
Figure 5-4: Quantification of double sided DNA content using Quant-IT dsDNA quantification. Tested using Kruskal-Wallis test with Dunn's multiple comparisons. Results shown as mean \pm SD. n=9	108
Figure 5-5: Quantification of SHG intensity using mean grey value. Results shown as mean \pm SD of 18 separate images across a sample size of n=9. Statistical analysis performed using two-way ANOVA with Tukey's post-hoc test for multiple comparisons. Significant p values shown as a=<0.0001 b=0.0001 c=0.0002 d=<0.0001 e=0.0044 f	109
Figure 5-6: Alkaline phosphatase activity taken at days 7, 14, 21 and 28. Enzyme activity was calculated as nmol pNPP converted per minute and normalised to total DNA within	

the sample. Tested with two-way ANOVA and Tukey's post-hoc test for multiple comparisons. Results show mean \pm SD (n=9) a=0.0321 b=0.0013 c=0.0146 110

Figure 5-7: A-D: Representative SHG images of collagen deposited by Y201 cells cultured on aligned and non-aligned fibres at day 14 of culture with OM. Each image represents 5 μ m slices, with the average (mean) orientation of the fibres from the original PCL fibre axis written beneath. Measurement in top left describes distance from PCL scaffold. Scale bar represents 100 μ m. 111

Figure 5-8: A-D: SHG images of collagen cultured on aligned and non-aligned fibres at day 21 of culture with OM. Each image represents 5 μ m slices, with the average orientation of the fibres from the original PCL fibre axis written beneath. Scale bar represents 100 μ m. **E-H:** 3D histograms highlighting changes in directionality of collagen fibres in relation to depth for each 5 μ m stack of SHG slices. Y-axis: Ratio of fibres in each analysed image at a particular angle from 0 to 180. Each histogram is of a single Z-stack image that is deemed representative of the general trend for each condition. 113

Figure 5-9: Difference in the orientation of collagen fibre alignment from the slice closest to the scaffold, compared to the top-most slice. Y201 cells were seeded on either plasma-coated or fibronectin-coated aligned fibres and measurements taken at days 14, 21, and 28. Measurements were taken across 16-20 separate images per condition, across a sample size of n=9. Results show mean \pm SD * p \leq 0.05 **Error!**

Bookmark not defined.

Figure 5-10: A-D SHG images of collagen cultured on aligned and non-aligned fibres taken on day 28 of culture with OM. Each image represents 5 μ m slices, with the average orientation of the fibres from the original PCL fibre axis written beneath. Scale bar represents 50 μ m. **E-H** 3D histograms highlighting changes in the directionality of collagen fibres in relation to depth for each 5 μ m stack of SHG slices. Y-axis: Ratio of fibres in each analysed image at a particular angle from 0 to 180. Each histogram is of a single Z-stack image that is deemed representative of the general trend for each condition..... 115

Figure 5-11: Difference in the orientation of collagen fibre alignment from the slice closest to the scaffold, compared to the top-most slice. Y201 cells were seeded on either plasma-coated or fibronectin-coated aligned fibres and measurements taken at days 14, 21, and 28. Measurements were taken across 10-16 separate images per condition, across a sample size of n=9. Results show mean \pm SD Tested with a two-way ANOVA with Sidak's post-hoc test for multiple comparisons. Significant p number is shown as a=0.0382 116

Figure 5-12: Change in orientation of fibre alignment from the PCL fibres on plasma coated or fibronectin coated aligned fibres at day 28 in either EM or OM. Measurements were taken across 16-20 separate images per condition, across a sample size of n=9 (OM) and n=6 (EM). Results show mean \pm SD. Tested with a two-way ANOVA with Sidak's post-hoc test for multiple comparisons. Significant p numbers indicated as *= $<$ 0.001 117

Figure 5-13: A-B SHG images of aligned fibres taken at day 28 of culture with EM. Each image represents 5 μ m slices, with the average orientation of the fibres from the original PCL fibre axis written beneath. Scale bar represents 50 μ m. **E-H** 3D histograms

highlighting changes in directionality of collagen fibres in relation to depth for each 5µm stack of SHG slices. Y-axis: Ratio of fibres in each analysed image at a particular angle from 0 to 180. Each histogram is of a single Z-stack image that is deemed representative of the general trend for each condition..... 117

Figure 5-14: Confocal images of the cell nucleus (DAPI in blue) and cytoskeleton (phalloidin-TRITC in red) of h-TERT Y201 cells seeded on non-aligned (A) and aligned (B) scaffolds at day 7. Cells on aligned PCL fibres show a cytoskeleton that is aligned along the axis of the fibres, whilst non-aligned PCL fibres appear to have no notable organisation. Scale bar at 200 µM 118

Figure 5-15: Circularity and nuclear area of h-TERT Y201 cells at days 7, 14, 21 and 28 of culture on aligned or non-aligned scaffolds in either expansion media (EM), or osteogenic media (OM). Results are shown as mean ± SD of 500 measurements taken over 9-12 separate images per condition. Analysed using Kruskal-Wallice test with Dunn's post-hoc for multiple comparisons. Significant p values represented by a=0.055 b=0.0325 c=0.0419 d=0.0213 and *= p<0.0001 119

Figure 5-16: Toughness (**A-C**), ultimate tensile strength (UTS) (**D-F**) and Young's modulus (**G-I**) measured on aligned and non-aligned PCL fibres, cultured with h-TERT Y201 cells for 28 days in either EM or OM. Blank condition represents an acellular scaffold placed in OM for 28 days at 37°C All PCL fibres were plasma + fibronectin coated. Aligned fibres were tested in both the transverse and longitudinal orientations. Results are shown as mean ± SD. n=4 Analysed using a one-way ANOVA with Tukey's post-hoc test for multiple comparisons. Significant p values are shown as a=0.041 b=0.0113 c=0.0003 d=0.0084 e=0.0002 f=<0.0001 g=<0.0001 h=0.0021..... 120

Figure 5-17: Osteogenic gene expression of Y201 cells at days 3 and 21, shown as log₂ of fold-change, compared to OM-treated 2D controls. Results shown mean±SD (n=3 (SPP1) n=3-5 (ALP) or n=5-6 (RUNX2))..... 122

Figure 5-18: RUNX2 expression from h-TERT Y201 cells at day 21, cultured in either EM or OM. Results are shown as log₂ of fold-change, compared to EM-treated 2D controls. Results shown mean±SD (n=5-6) Statistical analysis performed using two-way ANOVA with Tukey's post-hoc test for multiple comparisons. Significant p values shown as a=0.0211 123

Figure 5-20: Mechanotransduction-related gene expression of Y201 cells at day 3. Shown as log₂ of fold-change, compared to OM treated 2D controls. Results shown mean±SD (n=5-6). Statistical analysis performed using two-way ANOVA with Tukey's post-hoc test for multiple comparisons. Significant p values shown as a=0.0028. 124

Figure 5-19: RhoA expression of h-TERT Y201 cells at days 3 and 21. Shown as log₂ of fold-change, compared to OM treated 2D controls. Results shown mean±SD (n=3 (Day 3) or n=6 (Day 21)). Statistical analysis performed using two-way ANOVA with Tukey's post-hoc test for multiple comparisons..... 124

Figure 5-21: SHG images of collagen produced by MG63 cells after 21 days in culture with osteogenic supplementation. Each image represents 5 1µm slices, with the average orientation of the collagen fibres from the original PCL fibre axis written beneath. Scale bar represents 50µm 125

Figure 6-1: Emulsions after 1hr of incubation at 37°C with varying wt/wt% of alginate and PEO in standard 1.5 mL Eppendorf tubes . Rhodamine B was added to assist with

visualisation of separation of the aqueous and oil phase. Labels correspond to samples outlined in Table 1.	142
Figure 6-2: Fluorescent microscope images of 60% emulsions imaged with varying percentages of alginate and PEO. Samples labelled with Rhodamine B and imaged at $\lambda_{ex}550/\lambda_{em}573$ nm. Scale bar at 200 μ M.	143
Figure 6-3: Analysis of pore size of 3PCLMA emulsions at varying degrees of the aqueous phase. Graph shows the mean \pm SD of 100 pores measured using imageJ. Statistical analysis performed using Krushkal-Wallis with Dunn's post-hoc test for multiple comparisons. Significant p values shown as a=0.008 b=<0.0001 c=<0.0001 ...	144
Figure 6-4: Fluorescent microscope images of P5A3 emulsions imaged with varying percentages of aqueous percentages. Samples labelled with Rhodamine B and imaged at $\lambda_{ex}550/\lambda_{em}573$ nm. Scale bar at 200 μ M.	145
Figure 6-5: Confocal images of 60% emulsions stained with Rhodamine B (PCLMA, red) either immediately after curing (Left), and after 48 hours in expansion media (EM) (right), to allow for elution of polyethylene oxide (PEO) Scale bar at 200 μ M.	146
Figure 6-6: Young's modulus (A) and ultimate tensile strength (B) of pure 3PCLMA after autoclaving at 121°C for 30 minutes. Results show as mean \pm SD (n=5) Statistical analysis performed using an upaired t-test. Significant p values shown as a=0.0033 and ns=0.1549.	148
Figure 6-7: Representative tensile stress/strain curves of 60% aqueous phase 3PCLMA emulsions with varying degrees of HAp dispersed within the oil phase.	149
Figure 6-8: A) Young's modulus and B) ultimate tensile strength of 60% aqueous phase 3PCLMA emulsions with varying degrees of HAp. Results show as mean \pm SD (n=5). Statistical analysis performed using one-way ANOVA with Tukey's post-hoc test for multiple comparisons. Significant p values shown as a=0.047 b=<0.0001 c=<0.0001 d=<0.0001 e=0.0003 f=0.0002 g=0.0004 h=<0.0001 i=<0.0001.	149
Figure 6-9: Light microscopy images of MG63 cells after 14 days of culture, with varying degrees of exposure to UV. Scale bar at 500 μ M.	150
Figure 6-10: Assessment of the metabolic activity and matrix-producing potential of MG63 cells exposed to UV for varying durations. It was seen that there were no significant effects of exposure duration on either metabolic activity or matrix production. Results shown as mean \pm SD (n=9) Statistical analysis performed using one-way ANOVA with Tukey's post-hoc test for multiple comparisons.	151
Figure 6-11: Resazurin assay for metabolic activity of cells encapsulated in GelMA/alginate, or a 3PCLMA emulsion at 70% aqueous phase 24 hours after encapsulation. Results shown as mean \pm SD (n=9). Statistical analysis performed using one-way ANOVA with Tukey's post-hoc test for multiple comparisons. Significant p values represented as a=0.0170 b=<0.0001 c=<0.0001.	152
Figure 6-12: Fluorescent microscopy of 3T3 cells encapsulated in either pure GelMA/Alginate (Top) or a 3PCLMA emulsion containing 70% aqueous phase (Bottom) labelled with Calcein AM (Live cells) or ethidium homodimer-1 (dead cells). It is seen that the emulsions give off a high degree of autofluorescence, preventing the observation of live and dead cells. Scale bar at 200 μ M.	153
Figure 6-13: Metabolic activity of MG63 cells seeded on TCP with the addition of cured 60% emulsions directly on top. D0 represents the metabolic activity of the MG63	

directly before the addition of scaffolds. Results shown as mean \pm SD (n=3). Statistical analysis performed using one-way ANOVA with Tukey's post-hoc test for multiple comparisons. Significant p values shown as a=0.0048 b=0.0194 c=<0.0001..... 154

Figure 6-14: Metabolic activities of cells seeded post-fabrication on scaffolds containing a 60% aqueous phase in comparison to TCP, taken days 1, 3 and 7. Results shown as mean \pm SD (n=6)..... 155

Figure 6-15: Schematic of the final system. Green represents the dispersed aqueous phase formed of GelMA and alginate, whilst the blue continuous phase is formed of 3PCLMA. PEO dispersed within the oil phase acts as a soluble porogen to form interconnects between the 3PCLMA. 156

Figure 7-1: m-SiO₂ made via method 1. Shows profound differences between the two yields..... 170

Figure 7-2: Simple test for hydrophobicity of resulting m-SiO₂ particles. Particles are combined with water and shaken for 10 seconds. **A)** m-SiO₂ made via method 1. **B)** m-SiO₂ made by method 2 **C)** Unmodified fumed SiO₂..... 171

Figure 7-3: SEM images of emulsions formed with varying solvents and % Wt of m-SiO₂. Scale bar = 100 μ M. **A)** Toluene with 3% m-SiO₂ **B)** toluene with 5% m-SiO₂ **C)** Chloroform with 3% m-SiO₂. **D)** Chloroform with 5% m-SiO₂ **E)** Toluene and chloroform with 3% m-SiO₂ 174

Figure 7-4: SEM images of emulsions formed with chloroform and varying % wt. of m-SiO₂ and Span 80. **A)** 3% m-SiO₂. Scale bar at 300 μ M **B)** 5%SiO₂. Scale bar at 300 μ M. **C)** High magnification SEM images of 3 %wt and 5 %wt m-SiO₂ emulsions with 0.3g Span 80. Scale bar at 50 μ M..... 176

Figure 0-1: Light microscope images of Y201 cells..... 190

Figure 0-2 Day 10 metabolic activity of h-TERT Y201 cells seeded on TCP. Results are shown as mean \pm SD. n=6 * = p \leq 0.05 191

Figure 0-3: Day 21 collagen (SRS) and mineral (ARS) deposition of h-TERT Y201 cells cultured on TCP. Results are shown as mean \pm SD. n=6 * = p \leq 0.05 191

List of Tables

Table 1: Structural features and scales found in bone.....	9
Table 2: A non-exhaustive list of non-collagenous bone proteins and their functions... 10	
Table 3: Brief summary of mechanical properties of human bone from various locations and sample sizes. NM = Not Measured	26
Table 4: Descriptions of various common model cells for in vitro bone models and their pro's and con's.....	50
Table 6: Summary of all components required for qPCR. The reaction is carried out in a MicroAmp™ Fast Optical 96-Well Reaction Plate with a final reaction volume of 20µL	71
Table 7: Thermal protocol for StepOnePlus™ thermocycler. Protocol specified by PCR Biosystems for amplification under fast-cycling systems.	72
Table 8: Primer assay IDs of all qPCR primers used. Primers purchased from Thermofisher consist of a pair of unlabeled forward and reverse PCR primers, a TaqMan probe with a dye label on the 5' end and a minor groove binder (MGB) and non-fluorescent quencher (NFQ) on the 3' end. All primers have been validated within the literature.	72
Table 9: Respective UVA doses received by MG63 cells with increasing time exposure	75
Table 10: Average diameters of electrospun PCL fibres. Measured from the average of 100 fibres across 3 images for each electrospinning condition. Showing mean ± SD	83
Table 11: Compositions tested with varied wt/wt% of PEO and alginate. Stability was assessed after 1hr after incubation at 37°. Emulsions were considered to be stable if no visible separation was observed.	141
Table 12: Formulation of emulsions, formed with varying solvents and % Wt of m-SiO ₂ . Maximum aqueous phase is the maximum amount of water that can be emulsified into the system before phase separation occurs. %silica is calculated relative to the solvent volume. An emulsion is considered formed once it turns an opaque white with a viscous, mayonnaise-like consistency.	172
Table 13: Attempted emulsion set ups using Span 80 surfactant. Solvent is chloroform and used to form a 10% PCL solution (Oil phase). Maximum aqueous phase is the maximum amount of water that can be emulsified into the system before phase separation occurs. %silica is calculated relative to the solvent volume. An emulsion is considered formed once it turns an opaque white with a viscous, mayonnaise-like consistency.	175
Table 14: Summary of freezing solutions examined	190

Abbreviations

AA2P	Ascorbic acid 2-phosphate
ALP	Alkaline Phosphatase
ANOVA	Analysis of variance
ARS	Alizarin red stain
ATP	Adenosine triphosphate
BM	Basal media
BMP-2	Bone morphogenetic protein-2
BMP-7	Bone morphogenetic protein-7
BMSC	Bone marrow-derived mesenchymal stromal cells
BSP	Bone sialoprotein
CAB	Cell assay buffer
CaP	Calcium phosphates
CD	Chemically derived media
CDB	Cell digestion buffer
CO₂	Carbon dioxide
CT	Calcitonin
DAPI	4', 6-diamidino-2- phenylindole dihydrochloride
DCM	Dichloromethane
Dex	Dexamethasone
DMSO	Dimethyl sulfoxide
DMEM	Dulbecco's modified eagle's medium
dsDNA	Double stranded deoxyribonucleic acid
ECM	Extracellular matrix
EDTA	Ethylenediaminetetraacetic acid

FBS	Foetal bovine serum
FN	Fibronectin
FSS	Fluid shear stress
GelMA	Gelatin methacrylate
HAp	Hydroxyapatite
HBSS	Hank's balanced salt solution
h-TERT	Human telomerase reverse transcriptase
IGF	Insulin-like growth factors
IL-6	Interleukin-6
MBG	Mesoporous bio glasses
MC3T3-E1	Mouse calvaria 3T3 clone-E1
MGB	Mean grey value
MLO-A5	Murine long bone osteocyte A5
MLO-Y4	Murine long bone osteocyte Y4
MMP	Matrix metalloproteinase
mRNA	Messenger ribonucleic acid
MSC	Mesenchymal stem cells
NA	Numerical aperture
OA	Osteoarthritis
OM	Osteogenic media
OPG	Osteoprotegrin
PBS	Dulbeco's phosphate buffered saline
PCR	Polymer chain reaction
PCL	Polycaprolactone
PEG	Polyethylene glycol
PLA	Polylactic acid

PolyHIPE	Polymerised high-internal-phase-emulsion
PTH	Parathyroid Hormone
PU	Polyurethane
RANK	Receptor activator of nuclear factor-kappa-B
RGD	Arginine-glycine-aspartic acid
RhoA	Ras homolog family member A
ROCK	Rho-associated protein kinase
RT-PCR	Reverse transcriptase polymer chain reaction
q-PCR	Quantitative polymer chain reaction
SEM	Scanning electron microscope
SHG	Second harmonic generation
SRS	Sirius red stain
TAZ	Transcriptional coactivator with PDZ-binding motif
TEOS	Tetraethyl orthosilicate
TGF-β	Transforming growth factor beta
UTS	Ultimate tensile strength
XFM	Xeno-free media
YAP	Yes-associated protein

Publications

[1] Delaine-Smith, Robin M., Alice Jane Hann, Nicola H. Green, and Gwendolen Clair Reilly. 2021. “Electrospun Fiber Alignment Guides Osteogenesis and Matrix Organization Differentially in Two Different Osteogenic Cell Types.” *Frontiers in Bioengineering and Biotechnology* 9 (October): 564. <https://doi.org/10.3389/FBIOE.2021.672959/BIBTEX>.

[2] Maksoud, Fouad Junior, María Fernanda Velázquez de la Paz, Alice J. Hann, Jeerawan Thanarak, Gwendolen C. Reilly, Frederik Claeyssens, Nicola H. Green, and Yu Shrike Zhang. 2022. “Porous Biomaterials for Tissue Engineering: A Review.” *Journal of Materials Chemistry B* 10 (40): 8111–65. <https://doi.org/10.1039/D1TB02628C>.

Conferences

Podium Presentations

[1] A J Hann, G Tetteh, N H Green, G C Reilly, “The use of aligned nano-fibres encourages lamellae-like organization of collagen” presented at the BiTEG., The University of Sheffield., December 2021

[2] A J Hann, G Tetteh, N H Green, F Claeyssens, G C Reilly, “Lamellae-Like Organisation of Collagen is Deposited by Human Osteogenic MSCs on Aligned Nano-Fibres”, Orthopaedic Research Society., Tampa, FL., January 2022

[3] A J Hann, N H Green, F Claeyssens, Y S Zhang, G C Reilly, “Methacrylated polycaprolactone-triol and gelatin methacrylate emulsions enable the production of stiff and porous bioinks for use in 3d cell printing”, presented at BioSheffield., The University of Sheffield, June 2022

[4] A J Hann, G Tetteh, N H Green, F Claeyssens, G C Reilly, “Aligned Electrospun Fibres Guide Collagen Deposition To Support A Lamella-Like Twisted Orientation by MSCs” presented at the 27th Congress of the European Society of Biomechanics., Porto., June 2022

Poster Presentations

[1] A J Hann, G Tetteh, N H Green, F Claeysens, G C Reilly, “MSCs Support a Lamella-Like Twisting Orientation of Collagen When Cultured on Aligned Electrospun Polycaprolactone Fibres”, presented at the TERMIS European Chapter., Krakow., June 2022

[2] [1] A J Hann, G Tetteh, N H Green, G C Reilly, “MSCs Support A Lamella-Like Twisting of Collagen When Cultured on Aligned Electrospun Polycaprolactone Fibres”, BiTEG. University of York, December 2022 - *Prize for best poster presentation*

Thesis Summary

There is an increasing movement presently towards the use of *in vitro* models for a wide range of applications, including studying diseases, drug interactions, cell-cell interactions and cell dynamics. The use of models that more accurately represent the 3D *in vivo* tissues may more accurately mimic cellular behaviour, speeding up scientific understanding and minimising the requirement for animal models. This thesis aims to produce two different materials that may fill gaps in the existing technologies in *in vitro* bone modelling.

Although the complexity behind the distinctions between the definitions of cortical, lamellar and osteonal bone is known, from this point forward, “lamellar bone” is used to describe bone with a twisted plywood, osteonal structure commonly observed in cortical bone, and “trabecular bone” is used to describe bone formed of interconnected trabeculae.

This first aim was to produce a model that more closely resembles the lamellar microstructure, as cortical bone is widely overlooked in many *in vitro* bone models.

To achieve this, polycaprolactone aligned and non-aligned micro fibrous scaffolds were electrospun. Alignment was controlled by altering the rotating speed of the collecting drum, as well as altering the voltage. The resulting scaffolds then underwent plasma surface treatment, which was shown to decrease surface hydrophobicity and increase cell attachment. Finally, the scaffolds were either further coated with fibronectin, or left uncoated, to assess its effects on both cellular attachment and the resulting collagen and extracellular matrix produced.

An immortalised tri-lineage human, mesenchymal stem cell line, h-TERT Y201 was used in this work, and xeno-free media was predominantly used. The culture and osteogenic differentiation of h-TERT Y201 in xeno-free media was investigated.

Electrospun scaffolds were seeded with h-TERT Y201, and cultured over 28 days and their ability to support osteogenic differentiation, characterised by collagen and mineral deposition, and ALP activity, was assessed. The addition of fibronectin on its capacity to improve collagen production was examined, as well as whether this had any effect on the collagen organisation.

Collagen orientation was assessed on the fibres using the 2-photon laser imaging technique, second harmonic generation. The special organisation of collagen was examined periodically over 28 days. SHG was chosen due to its capacity to give both quantitative and qualitative information on the deposited collagen. Collagen organisation was examined under osteogenic conditions, fibroblastic conditions and for a osteosarcoma-derived cell line, MG-63.

Differential gene expression was assessed using qPCR for Y201 cells cultured on aligned and non-aligned fibres under osteogenic or fibroblastic culture conditions. Markers of osteogenic differentiation, as well as mechanotransduction-related genes were examined.

The second part of this thesis explored methods of producing interconnected, porous emulsions that can be used to produce multi-scale porosity models of trabecular bone. Many models of trabecular bone focus on a single scale of porosity, which over simplifies the complexity of the structure. Within single-scale porosity models, cells would be sitting along the outside of the trabecular “struts”, rather than within, which is what is observed *in vivo*. A secondary aim of the work was to

produce these emulsions with minimal cytotoxic components, intending to minimise the current requirements for extensive post-processing of traditionally produced polymer high internal phase emulsions.

Freeze-dried, polycaprolactone Pickering HIPEs were first explored, to remove the need for photo initiators and surfactants. However, it was observed that the process often resulted in collapsing of the porous structure, and a non-interconnected porous network. The second method explored producing an emulsion that used the popular 3D printable hydrogel, gelatin methacrylate (GelMA), as an aqueous phase.

GelMA was emulsified with a 3-arm methacrylated polycaprolactone, to produce a material that was 3D printable, but with better mechanical properties than gelMA alone. To stabilise the emulsion, the viscosity of the aqueous phase was increased with the addition of alginate, whilst interconnectivity of the polycaprolactone was created by the addition of soluble molecule, polyethylene oxide, which may be eluted off post-curing.

Mechanical properties of the emulsions at various aqueous phase percentages were examined, as well as the effects of hydroxyapatite. Finally, the potential of the ink to be used for direct cell encapsulation was explored, as well as it's potential to be used within direct cell seeding.

Contents

Acknowledgements	v
Publications	xviii
Conferences	xviii
Podium Presentations	xviii
Poster Presentations	xix
Thesis Summary	xx
1 Literature Review	6
1.1 Bone structure and function	8
1.1.1 Cell types of bone	9
1.1.2 Cortical bone	11
1.1.3 Trabecular Bone	14
1.1.4 Woven Bone	15
1.2 Stages of bone remodelling:	16
1.2.1 Activation	16
1.2.2 Resorption	17
1.2.3 Reversal	18
1.2.4 Formation	18
1.3 Collagen structure and organisation	18
1.3.1 Collagen arrangement in bone	19
1.3.2 Lamellae Formation	20
1.3.3 Fibronectin and its role in collagen production	22
1.3.4 Second Harmonic Generation as an imaging technique	23
1.4 Mechanical properties of bone	25
1.4.1 Effects of mechanical loading	26
	29
1.5 Bone diseases	29
1.5.1 Osteogenesis Imperfecta	30
1.5.2 Osteoarthritis	31
1.6 Modelling bone – Materials	33
1.6.1 Calcium Phosphates	34
1.6.2 Polymers	34

1.6.3	GelMA	36
1.6.4	Alginate	38
1.7	<i>In Vitro</i> Modelling of Bone- Methods	39
1.7.1	PolyHIPEs	41
1.7.2	Pickering Emulsions	43
1.7.3	Electrospinning	46
1.8	3D Printing	47
1.9	Culture conditions	48
1.9.1	Cell Choice	48
1.9.2	Flow systems	51
1.9.3	Chemically defined media	53
2	Aims and objectives	56
2.1	Summary of review	56
2.2	Aims	57
2.3	Objectives	58
3	Materials and Methods	59
3.1	General Cell Culture	59
3.1.1	Culture media preparation	59
3.1.2	Passaging and counting	59
3.1.3	Freezing	60
3.1.4	Cell Digestion	60
3.1.5	Resazurin Reduction Assay	61
3.1.6	DNA quantification	61
3.1.7	Cell Fixing	62
3.1.8	Scanning electron microscopy	62
3.1.9	Fluorescent microscopy	62
3.2	Electrospun scaffold cell culture assessment	63
3.2.1	Sirius Red Staining	63
3.2.2	Direct Red 80	63
3.2.3	Second Harmonic Generation Imaging	63
3.2.4	Collagen orientation analysis	64
3.2.5	Nuclear analysis	65
3.3	PolyHIPE optimisation	66
3.3.1	Nano silica production method one	66

3.3.2	Nano silica production method two	66
3.3.3	Picking emulsion production	66
3.3.4	Picking emulsion with surfactant production	67
3.4	Electrospinning Optimisation	67
3.4.1	Electrospinning PCL	67
3.4.2	Scaffold surface coating optimisation	68
3.4.3	Mechanical Testing	69
3.5	Media Optimisation	69
3.5.1	Y201 hTERT-MSCs media investigations	69
3.6	Gene expression of h-TERT Y201 cells on electrospun fibres	70
3.6.1	RNA extraction	70
3.6.2	cDNA synthesis	70
3.7	GelMA/3PCLMA Emulsions	73
3.7.1	Cell culture	73
3.7.2	Gelatin methacrylate Synthesis	73
3.7.3	Emulsion Development	73
3.7.4	Mechanical Testing	74
3.1.5	Cell toxicity	75
3.7.5	UV Irradiation	75
3.7.6	Toxicity Testing	76
3.7.7	Encapsulation	76
3.8	Statistical Analysis	77
4	Development of Aligned and Non-Aligned Fibres for Use in Xeno-Free Osteogenic Culture of MSCs	78
4.1	Introduction	78
4.2	Aims and Objectives	79
4.3	Experimental Design	80
4.4	Results	81
4.4.1	Electrospinning voltage effects	81
4.4.2	Plasma Coating	84
4.4.3	Mechanical testing	84
4.4.4	Basal media testing	85
4.4.5	Osteogenic media supplementation	87
4.4.6	Scaffold seeding optimisation.	89

4.4.7	Surface functionalisation and coating	92
4.5	Discussion	93
4.5.1	Fibre fabrication	93
4.5.2	Media composition	95
4.5.3	Cell seeding optimisation.	99
4.6	Summary and conclusions	101
5	Investigation of Microfibres Effect on Spatial Collagen Organisation of Osteogenically Differentiated MSCs	103
5.1	Introduction	103
5.3	Aims and Objectives	104
5.4	Experimental Design	105
5.5	Results	106
5.5.1	Mineral and Collagen Deposition	106
5.5.2	Alkaline phosphatase activity	109
5.5.3	Collagen Organisation	110
5.5.4	Cell alignment	117
5.5.5	Construct mechanical properties	119
5.5.6	Gene expression on aligned and non aligned PCL fibres	121
5.6	Collagen deposition of MG-63 cells	125
5.7	Discussion	126
5.7.1	Matrix deposition and organisation	126
5.8	Summary	134
6	Methacrylated Polycaprolactone-triol and Gelatin Methacrylate Emulsions for the Production of Stiff and Porous Bioinks for Use in 3D Cell Printing.	136
6.1	Introduction	136
6.2	Aims and objectives.	138
6.3	Experimental Design	139
6.4	Results	139
6.4.1	Stability	139
6.4.2	Fluorescent imaging	142
6.4.3	Mechanical testing	146
6.4.4	Addition of hydroxyapatite.	148
6.4.5	Effects of UV Exposure on cells	149
6.4.6	Cell toxicity- Encapsulation	151

3.1.1	Indirect toxicity testing	153
6.4.7	Cellular adhesion to scaffolds	154
6.5	Discussion	155
4.4	Summary and conclusions	166
7	Development of a 3D porous ink with Minimal Cytotoxic Components – Alternative Attempts	167
7.1	Introduction	167
7.2	Aims and Objectives	169
7.3	Results	169
7.3.1	Production of hydrophobic nano-silica	169
7.3.2	Pickering emulsion solvent optimisation	171
7.3.3	Effects of surfactant on morphology	174
7.4	Discussion	177
8	Future Work	181
8.1	Development of a lamellar-like organisation for modelling of lamellar bone	181
8.2	Methacrylated polycaprolactone-triol and gelatin methacrylate emulsions for the production of stiff and porous bio-inks for use in 3D cell printing	184
	Appendix	189
	Serum-free mediums for replacement of FBS	189
	Methods	189
	Results and discussion	190

1 Literature Review

Introduction

Current 2D *in vitro* models used for pre-clinical testing in the field of bone research often face significant challenges when transitioning to *in vivo* studies. These difficulties arise from a multitude of factors, with one prominent issue being the absence of a truly representative 3D environment [1]. This problem underscores the need for a shift in our approach to pre-clinical testing, particularly in the context of reducing our reliance on animal experiments, a concept pioneered by the 1959 publication "The Principles of Humane Experimental Technique," which introduced the ethical framework of the 3 R's (Reduce, Refine, Replace) for animal experimentation [2]. To genuinely reduce our dependence on animal models, we must first improve our *in vitro* testing methodologies.

When it comes to developing materials for implantation and subsequent bone regeneration, the choice of material must be one that can facilitate several critical functions, including promoting effective infiltration, osteoinduction, and osteointegration, achieved through the rapid deposition of the extracellular matrix (ECM). It may be argued that precisely mimicking the physiological organization of the ECM may be of secondary importance, as bone possesses an inherent capacity to gradually remodel a disorganized matrix, a process similar to natural fracture healing. However, in the context of *in vitro* models, replicating the highly organized structure of collagen and mineral within bone, along with the intricate cellular interactions within this matrix, could prove

beneficial. This is due to the organization of ECM having been shown to significantly impact the mechanical properties of resultant tissues, which, in turn, play a pivotal role in regulating and influencing cellular behaviour [3]–[11].

Furthermore, it is essential to acknowledge that cortical and trabecular bone, two fundamental types of bone tissue, exhibit profoundly different architectural organizations. Consequently, they also differ in the organization of their ECM. However, many *in vitro* models tend to treat bone as a single-phase tissue, a simplification that more closely resembles osteoid tissue. Nevertheless, numerous studies have highlighted differing effects of drugs and diseases on cortical and trabecular bone [12]–[14]. These distinctions can be attributed to a variety of factors, including variations in bone density, the availability of cell surface area, intercellular connectivity, and the activation of distinct mechanotransductive pathways.

In summary, the challenges faced by current 2D *in vitro* models when transitioning to *in vivo* studies underscore the pressing need for improvements in pre-clinical testing methodologies. This shift is vital not only to enhance the efficiency and ethical considerations of research but also to provide more accurate representations of the complex interactions within bone tissue. By incorporating a more nuanced understanding of ECM organization and recognizing the unique characteristics of cortical and trabecular bone, we can move closer to developing *in vitro* models that better mimic the intricacies of bone physiology and pathology.

1.1 Bone structure and function

Bone is a dynamic tissue that serves various roles. These include protecting internal organs and marrow, giving structural support to the body, providing anchorage to muscles, allowing for movement, and as a store of minerals such as calcium and phosphorus, as part of mineral homeostasis. Bone is a composite material that comprises an organic phase, and an inorganic phase. The organic phase accounts for around 30% of bone's dry weight, and is around 90% type I collagen, as well as small amounts of type III and type V present. The remaining content is formed of various non-collagenous proteins such as glycoproteins and proteoglycans. The inorganic component of bone, the remaining 70% of the bone's dry weight, is formed of minerals. This mineral is a form of hydroxyapatite (HAp), or biological apatite, containing calcium and phosphorus, as well as smaller trace amounts of carbonate, magnesium, sodium, and potassium. HAp is seen to be deposited along the axis of the collagen [15]. The high proportion of collagen is what gives the bone its elasticity, and contributes to the tensile strength provided by the HAp component. A summary of the different structures and their length-scales found within bone is given below in **Table 1**.

Table 1: Structural features and scales found in bone.

Feature	Scale	Size
Whole bone	Macroscale	Variable
Cortical and trabecular bone	Mesoscale	N/A
Singular osteons and trabeculae	Microscale	1-500 μ M
Single lamellae	Micro to nanoscale	5-7 μ M
Collagen fibrils and mineral	Nanoscale	<1 μ M

Bone is covered by a periosteum, which is a fibrous, highly vascularised, and innervated sheath that surrounds the outermost surface of the bone. It acts as a significant contributor of blood to the bone and surrounding muscle [16]. Periosteum is a major contributor of cells during fracture, as part of the bone healing process [17].

1.1.1 Cell types of bone

Bone is highly dynamic, and is continuously undergoing a process of remodelling, which will be described in more detail in **section 1.4**. This process is vital for bone health and maintenance, as well as for mineral homeostasis. Bone remodelling is largely controlled by bone cells, of which bone contains three main cell types: osteoblasts, osteocytes, and osteoclasts.

Osteoblasts are mono-nucleated cells derived from osteoprogenitor cells and are involved in the deposition of extracellular matrix (ECM) components and regulation of calcium deposition and mineralisation through the production of several bone-regulating non-collagenous proteins such as osteopontin and osteocalcin, summarised in greater detail in **table 2** [16]. They have an elongated, flat shape, which is thought to assist with the deposition of collagen, which

occurs parallel to its long-axis orientation [18]. Osteoblasts eventually become embedded within their matrix within a lacuna, becoming terminally differentiated osteocytes.

Osteocytes are smaller, stellate cells with many processes protruding out through channels known as canaliculi. These processes then allow for connections between the processes of other surrounding osteocytes or osteoblasts. They serve several important functions, including acting as mechanosensors, which in turn allows for regulation of bone remodeling and maintenance of mineral balance.

Osteoclasts are large, multinucleated cells that can break down and resorb the bone tissue and play a vital role in the maintenance, remodelling and repair of bone. Bone homeostasis is maintained by a careful balance of the activities of osteoclasts and osteoblasts, disruption of bone homeostasis can lead to a variety of diseases, such as osteoporosis, Paget’s disease and osteopetrosis [19].

Table 2: A non-exhaustive list of non-collagenous bone proteins and their functions

Protein	Function	Gene Name	Citation
Osteocalcin	Expressed solely by osteoblasts, plays a minor role in ECM mineralisation and many other metabolic pathways	BGLAP	[20]
Osteopontin	A sialoprotein produced by osteoblasts and MSCs. Anchors osteoclasts to the mineral matrix of bones. Binds to calcium atoms at available crystal surfaces as a mineralisation inhibitor	OPN	[21]
Bone sialoprotein (BSP)	A phosphorylated glycoprotein that is synthesized by osteoblasts. Mediates cell-cell interactions via an integrin-binding site. Plays a role in the nucleation of HAp	SPP1	[22]
Osteonectin	Glycoprotein secreted by osteoblasts. Found in bone and other locations. Binds to calcium during bone	SPARC	[23]

	formation, initiating mineralization and promoting mineral crystal formation. Also plays a role in collagen binding.		
Alkaline Phosphatase (ALP)	Membrane-bound metalloenzyme found in various locations of the body. Synthesised by osteoblasts and involved in bone matrix calcification and an early osteogenesis indicator.	ALPL	[22]
Bone morphogenetic protein-2 (BMP-2)	Osteogenic growth factor that can induce bone formation. FDA approved for clinical use. Key role in osteoblast differentiation. Involved in TGF-beta signalling and hedgehog pathway	BMP2	[24]
Bone morphogenetic protein-7 (BMP-7)	Necessary for the differentiation of pre-osteoblasts into mature osteoblasts	BMP7	[25]

1.1.2 Cortical bone

Cortical bone, also known as compact bone, is the dense, outer layer of bone. It has a porosity of only 10-15% and makes up around 80% of the overall skeletal mass. It has an anisotropic strength, generally being stronger in the longitudinal direction than the circumferential.

Cortical bone in humans is mainly comprised of osteons. There are two forms of osteons. The first are primary osteons which form during appositional growth of bone. Secondary osteons are produced through the remodelling of bone, formed of units consisting of concentric lamellae (formed of type I collagen), surrounding a central canal, which houses the blood vessels and nerve fibres

(Figure 1-1).

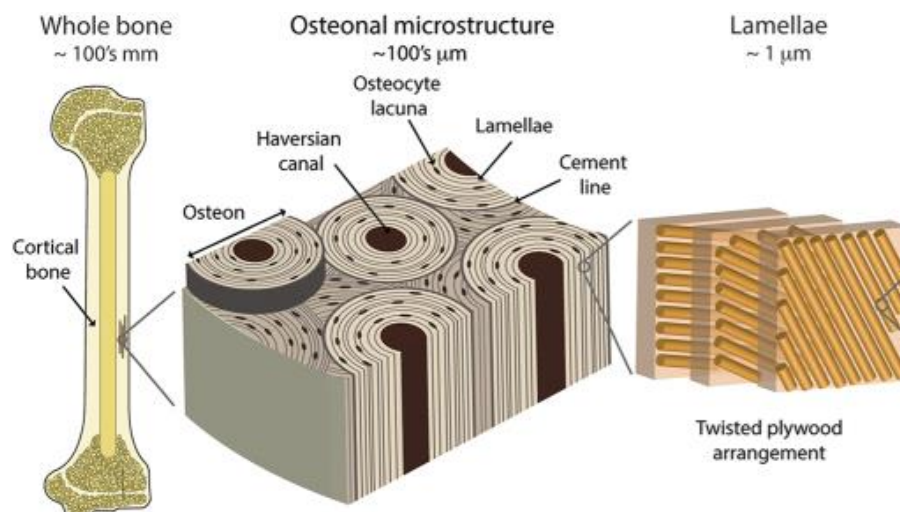


Figure 1-1: Hierarchical structure of cortical bone. Image obtained from Zimmermann *et al* with permissions pending [325]

There is still much debate on the organisation of the bone lamellae, with a few different proposed models of the structural motifs of bone. These include the twisted plywood structure and alternating lamellae. The alternating lamellae, or orthogonal lamellae, the organisation is described to have collagen that is highly aligned in a single layer, with an abrupt change between each layer so that the collagen is laying transversely across the previous layer[26]. This model arose since when imaged under polarised light, there are visible alternating light and dark bands due to the birefringent properties of collagen, and it was thought that this was caused by the collagen being either parallel or transverse to the plane of imaging. However- the darkness of the band is not related purely to orientation and may be affected by the quality, quantity, presence of minerals and orientation of the sectioning-thus making its interpretation difficult [27], [28].

The now more widely accepted model of collagen arrangement is the twisted plywood structure, proposed by Giraud-Guille *et al.* in 1988. Using transmission electron microscopy of a transversely sectioned osteon, an arcing pattern of collagen was observed [29]. From this, it was proposed that bone lamellae are arranged concentrically around a central canal, sometimes referred to as a Haversian canal. Each lamella is formed of 5 collagen sheets, with each one slightly offset to the previous by an angle of 5-25° (**Figure 1-2**) [30], [31]. Wagermaier *et al* used scanning small angle x-ray scattering to try and resolve the individual 1µm layers of lamellae across an osteon, to distinguish the relative orientations of the layers[31]. They showed that the orientation of the individual layers gradually changed across 0-90°, with a periodicity of 5-7µm- roughly the width of a single lamella. The outermost lamellae are also shown to have a different chirality to the rest of the inner lamellae, as highlighted in **Figure 1-2**.

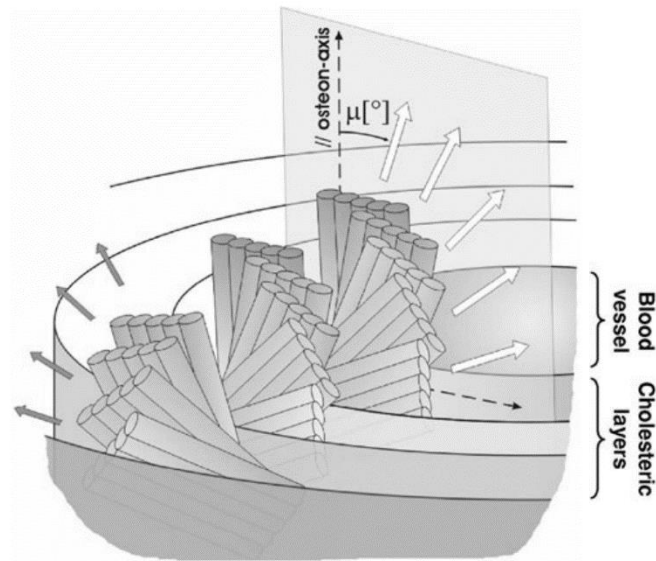


Figure 1-2: Fibrillar orientation relative to the haversian canal. The orientation of the fibrils changes with a periodicity of 5 – 7 μ m. Fibrils of the outermost lamella show a different chirality to that of the inner lamellae. Reprinted with permission from Wagermaier [31] *et al* Copyright 2023 American Vacuum Society

Conversely, work by Marotti *et al* concluded a slightly different model of bone, which is formed of alternating collagen-rich, and collagen-poor layers, described as dense and loose lamellae, respectively. In this model, the osteocytes are confined to the loose lamellae only, with the dense lamellae being considered acellular[28].

More recently Reznikov *et al* showed that within lamellar bone there may exist a composite of both highly ordered and disordered bone. In a small study of human cortical bone, it was shown that in between compartments of organised and “twisting” lamellae, there also exists a continuous network of disorganised lamellae [32], [33]. It is also seen that there is an added complexity, where collagen predominant orientation may change depending on the location within the body, particularly within areas of high loading [34], [35].

1.1.3 Trabecular Bone

Trabecular bone is highly porous, formed of “struts” of bone known as trabeculae. The ECM composition of the trabecular bone is the same as that seen in the cortical bone discussed previously. The type I collagen fibrils are organised within sheets of lamellae, however, these are orientated along the axis of the trabeculae in flat sheets, as opposed to the osteonal organisation seen within the cortical bone [36].

In particular, the subchondral trabeculae, the bone beneath the cartilage within an articular joint, shows high metabolic activity and is a dynamic structure with high bone turnover. It possesses the ability to adapt to the changing mechanical stresses placed on the joints through the remodelling of the trabeculae, to create an organisation with high levels of mechanical anisotropy and preferential orientation of trabecular struts, to equally distribute stresses along the articular cartilage surface [37].

Collagen within the trabecular bone also has a lamellar structure but is slightly different to that of the cortical lamellae. Trabecular lamellae are organised into $6\mu\text{m}$ “lamellar packets” where one packet is all aligned and was produced within a single deposition event, and are separated from the neighbouring lamellae by a cement line [38]. The lamellae of different packets have different orientations, resulting in a patch-work like arrangement of differently ordered lamellae [39]. There is some evidence, in a study by Ruben *et al*, that there may also be a twisted-plywood arrangement of lamellae in some cases within trabecular bone also[40].

1.1.4 Woven Bone

Woven bone is generally the bone produced transiently during the healing of a fracture, in cases of fast growth such as foetal development in humans or diseases where fast bone turnover is observed, such as Paget's disease and hyperparathyroidism [18], [41]. It is characterised by a disorganised matrix of collagen, and a lower mineral content, resulting in inferior mechanical properties to that of the mature trabecular and cortical bone [18]. Collagen within woven bone also has no specific organisation around the blood vessel, compared to what is seen in Haversian systems in cortical bone [42]. Within woven bone, the osteoblasts adopt a more cuboidal shape surrounding themselves circumferentially in loosely deposited collagen [18].

Woven bone can be produced rapidly, to quickly stabilise a fracture or general bone damage, which then provides a matrix for the slower and more controlled deposition of the organised matrix observed within cortical and trabecular bone [15].

1.2 Stages of bone remodelling:

Bone first develops through one of two processes, intramembranous ossification, where bone develops directly from sheets of mesenchymal connective tissue, or endochondral ossification, where cartilage is first formed, before going through a process of cellular differentiation, and mineralised matrix deposition. The process of endochondral ossification occurs during foetal growth and continues up to early adolescence.

Bone then continues to remodel throughout life, in response to various physiological queues, mechanical forces and hormones, allowing it to gradually adapt in a process known as Wolff's Law [43]. Furthermore, remodelling allows bone to respond to and repair microcracks and breaks that may occur to the bone. Bone remodelling is carried out through a careful balance of resorption and deposition by the bone's osteoclasts and osteoblasts respectively. Calcitonin (CT), parathyroid hormone (PTH) and vitamin D3 are the major hormone regulators of osteoclastic bone regulation [44], [45].

1.2.1 Activation

Activation is the first stage of bone remodelling, occurring in response to a remodelling signal such as shear stress, microdamage, or hormone release. This then results in the recruitment and activation of mononuclear monocyte-macrophage osteoclast precursors from circulation, which fuse to form multinucleated preosteoclasts in a process known as osteoclastogenesis [46]. These then can then tightly bind to the vitronectin, osteopontin and bone sialoprotein proteins within the bone matrix via integrin receptors such as $\alpha v \beta 3$, and Arginylglycylaspartic acid (RGD)-containing peptides, creating resorbing

compartments and protecting the surrounding, non-targeted bone from the osteoclast actions [47], [48].

The process of resorption is controlled by the receptor activator of nuclear factor kappa-B ligand (RANKL) pathway (**Figure 1-3**). RANKL is released by osteoblasts, which then binds to receptor activator of nuclear factor-kappa-B (RANK) receptors on osteoclast pre-cursors, subsequently activating the osteoclast into active resorption [49], [50].

1.2.2 Resorption

Activated osteoclasts can then begin resorption. This occurs by decreasing the pH of the resorbing compartment, through the secretion of hydrogen ions via H⁺-Adenosine triphosphate(ATP)-ase proton pumps and chloride channels in their cell membranes. In an acidic environment, the bone mineral begins to dissolve. RANKL also stimulates the osteoclasts to secrete cathepsin K, matrix metalloproteinase (MMPs), and gelatinase from cytoplasmic lysosomes, causing the degradation of the remaining matrix and resulting in the formation of

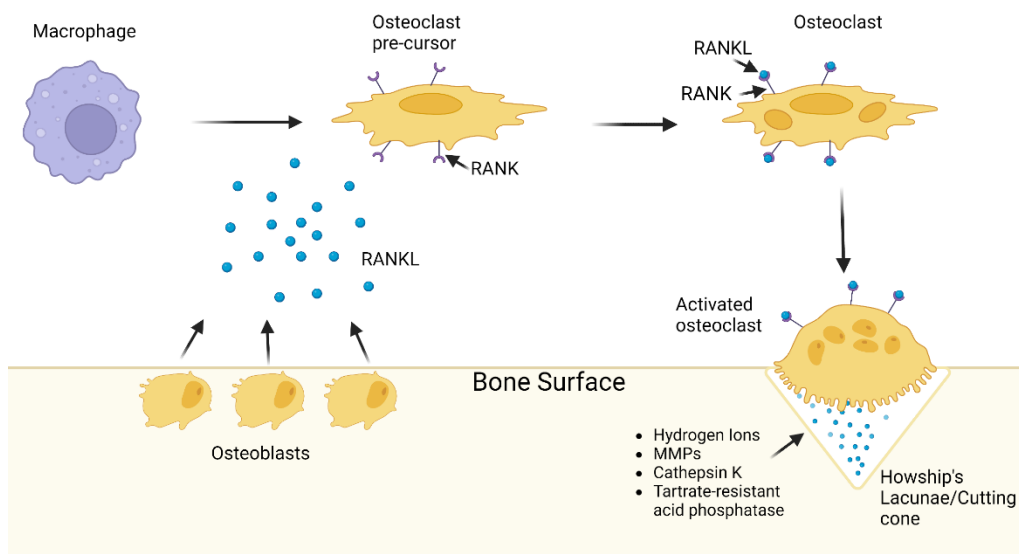


Figure 1-3: RANKL is produced by osteoblasts and binds to RANK receptors on the surface of osteoclast pre-cursors. This stimulates the osteoblast pre-cursor to differentiate into an osteoclast. Further binding activates the osteoclast, allowing it to bind to the bones surface and secrete bone-resorbing factors. Created using BioRender.

Howship's lacunae in trabecular bone and a cutting cone in cortical bone [49], [50].

1.2.3 Reversal

Reversal is the transitional phase before bone formation begins. Although this stage is still not fully understood, it is thought that a population of circulating monocytes can prepare the bone surface for the addition of new bone, and cytokines such as transforming growth factor beta (TGF- β), bone morphogenic proteins (BMPs) and insulin-like growth factors (IGFs) begin to stimulate the recruitment of pre-osteoblasts and osteogenic progenitor cells. Osteoclasts can also be inhibited by osteoprotegerin (OPG) which can antagonise RANKL and prevent the binding to RANK [51].

1.2.4 Formation

Finally, the formation of new bone occurs through the action of osteoblasts. Osteoblasts first secrete collagen, forming the organic matrix, before mineralising the new fibrils. As described previously, they eventually become embedded within their matrix, and then either undergo apoptosis or become terminally differentiated osteocytes.

1.3 Collagen structure and organisation

Type I collagen forms a major part of the organic component of bone. Type I collagen is formed of two $\alpha 1$ chains and one $\alpha 2$ chain, which coil into a right-handed triple helix, with a short, non-helical end of 15-25 amino acid subunits [52].

The synthesis of type I collagen begins with the transcription of the COL1A1 and COL1A2 genes, which are then translated into pro-alpha chains in the rough endoplasmic reticulum. The pro-alpha chains undergo several post-translational modifications, including hydroxylation of specific proline and lysine residues, as well as glycosylation of some hydroxylysine residues, forming glycosylated hydroxylysine. The triple helical pro-collagen molecule is then formed via the pro-alpha chains joining together in the endoplasmic reticulum.

Outside the cell, procollagen molecules undergo enzymatic cleavage to remove amino- and carboxyl-terminal propeptides attached to the alpha chains, via procollagen peptidases such as bone morphogenetic protein 1. These cleaved helical molecules are known as tropocollagen, and can then assemble hierarchically to form the more complex strands that form the fibrils which may range anywhere from 50nm to 500nm in diameter [53]. At the end of the tropocollagen molecules, there are free ends known as N- and C-terminal telopeptides. Telopeptides consist of 1- to 26-residue non-triple-helical domains, which assist in initiating fibrillogenesis of the collagen molecules, as well as stabilising collagen through the formation of covalent cross-links of neighbouring tropocollagen molecules, facilitated via action of enzymes such as lysyl oxidase.[54], [55].

1.3.1 Collagen arrangement in bone

The collagen organisation in bone varies depending on location, bone type, and age. As discussed in **section 1.1**, highly organised and aligned collagen is seen within the lamellar and trabecular bone, whilst a more disorganised matrix is seen within the woven.

Furthermore, HAp, the inorganic calcium phosphate component within bone has also been shown to play a vital role in the strength of mature bone, with the *c*-axis of the crystals aligned with the collagen fibre direction [56]. It has been shown that the degree of alignment of HAp is also strongly correlated with the mechanical strength of the bone [57]–[59]. Despite the evidence of the importance of alignment of the mineralised collagen fibres on bone mechanical properties, reproducing this structural anisotropy still proves difficult, and therefore is rarely attempted for laboratory grown bone-like matrices.

1.3.2 Lamellae Formation

Collagen deposition is believed to be a dynamic process. The processes of collagen subunit synthesis and assembly are well known, whereas there is much less knowledge on the processes of collagen assembly and remodelling extracellularly into its functional structures, such as that of the osteonal lamellae. Although it is widely observed that the collagen produced by osteoblasts is produced in the direction of the cell orientation, it is unknown whether it is the cell that deposits its collagen along the axis of its orientation, or whether the pre-deposited matrix assists in the aligning of the cell [60]. It is observed that when seeded on aligned fibres or substrates, osteoblasts will align themselves along the axis of the fibres, and in-turn begin to produce their collagen in the direction of the fibrous substrate [61]–[63]. Alternatively, when seeded on 2D plates without guidance, cells have no preferential alignment and produce their collagen randomly, which may suggest that cells do require guidance by the ECM to arrange into highly organised lamellae [59], [64], [65]. This raises the question of whether the ECM and collagen organisation is regulated actively by cells, or is a process of self-assembly. Collagen is known to

be able to self-assemble into D-banded fibrils as part of an entropy-driven process and this can be achieved acellularly, with the use of purified collagen molecules in an acidic solution. With the manipulation of collagen concentration, temperature and pH, it is possible for the molecules to bind and assemble into fibrils [52], [66], [67]. However, *in vivo*, or *in vitro* collagen assembly is much more complex, with many interacting factors. Furthermore, the conditions that are required for acellular fibrinogenesis are not representative of the *in vivo* environment, with temperatures above 35°C resulting in poorly banded and disorganised fibrils, suggesting that collagen assembly *in vivo* may occur through a different mechanism [52],[67].

Some theories suggest that there may also be physical manipulation of collagen organisation through cellular actions. Using MLOA-5 osteoblast-like murine cells modified to produce fluorescently-tagged collagen, Lu *et al* suggested that reorganisation of the collagen matrix is a highly dynamic process, with continuous movement of osteoblasts throughout the deposition, and that the osteocytes may “push” collagen, forming holes within the network [68]. Shiflett *et al.* also confirmed this “pushing” mechanism within mouse primary calvarial cells [69]. These studies, however, use systems with non-aligned collagen, so again this may be a more comparable structure to that of woven bone. It may also be mentioned that cells in culture do not spontaneously align collagen without external stimuli such as shear stresses or physical guidance via aligned substrates [70]–[74].

The lamellar organisation of collagen is not unique to bone, with a similar phenomenon also being observed in the cornea and the intervertebral disc. Whereas in other tissues such as tendons, collagen can be seen to be highly

aligned, but with the absence of relative twisting of the collagen fibrils. It has been seen previously that corneal fibroblasts when cultured on aligned collagen substrates, are able to produce an initial cell layer that follows the guidance of the fibres, before translating this into a physical cue that induces the second cell layer to shift in orientation [72], [75].

1.3.3 Fibronectin and its role in collagen production

Production of the ECM is a dynamic process that relies on the interaction between various matrix components. As discussed in **section 1.3.2**, the assembly of collagen is believed to be an entropy-driven process *in vitro*, however, *in vivo*, it appears to be cell-mediated. It is also seen to be heavily influenced by the presence of fibronectin [52], [68], [76], [77]. Fibronectin is a strain-sensitive, high molecular-weight glycoprotein that plays many roles within the ECM. It is known to have specific domains to promote cell-to-cell adhesion and cell-to-basement-membrane attachment, as well as many other roles including embryogenesis and wound healing [78], [79]. Fibronectin is also known to bind to enzymatic cleavage sites along the $\alpha 1$ chain of collagen (I), protecting collagen from degradation[80]. Several recent studies have also outlined a pivotal role played by fibronectin in the early stages of collagen production and organisation, with the co-dependency of the two having been observed in early matrix formation, where the two appear to closely template one another [68], [77]. In a study by Lu *et al* using the late osteoblast-like cell line, MLO-A5, in the absence of fibronectin few collagen fibrils were assembled, but with exogenous fibronectin, collagen deposition was significantly increased [68]. Additionally, an acellular study investigating the molecular interactions between collagen and fibronectin also demonstrated that FN appears to stabilize collagen nucleation and

accelerate the growth of collagen fibrils [81]. These findings appear to suggest that fibronectin is necessary for early-stage synthesis and templating of collagen.

1.3.4 Second Harmonic Generation as an imaging technique

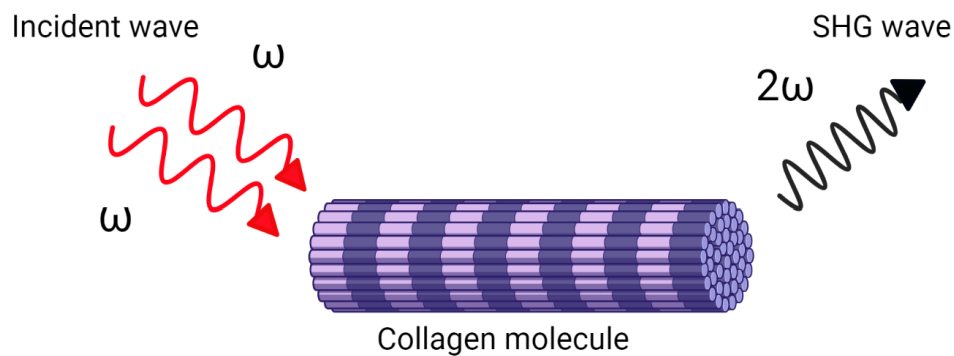
To properly understand collagen organisation and deposition behaviour, it is important to be able to properly image the fibrillar structure. Common methods for the characterisation of collagen, such as antibody staining and Sirius Red stains (SRS) require processing steps such as fixing, staining, and washing the samples. It may be debated that these additional processing steps may affect the overall structure and organisation of the collagen.

Second harmonic generation (SHG) is a form of two-photon microscopy that allows for visualization of a sample's ability to form second harmonic signal. It

has been shown to be a powerful imaging tool for fibrillar collagen, with promising uses within disease diagnosis and prognosis due to its high level of detail in the structure and organisation of *in vivo* collagen [82]–[84]. Furthermore, SHG allows for deep tissue imaging whilst being non-invasive, and non-destructive and can be done with no (or minimal) processing of the samples that usually occurs with other common methods of collagen visualisation, such as immunostaining.

For a signal to be produced, the molecule in question must be non-centrosymmetric, that is, having no inversion symmetry. The laser light required for SHG has greater directionality and can be focused on a diffraction-limited spot less than a micron in diameter. This in turn excites the molecule with two near-infrared incident photons of equal wavelength and low energy which scatter

non-linearly, and produce an SHG wave with twice the energy but half the wavelength of that of which it was excited by (**Figure 1-4**). In SHG, the resultant emission is then stronger in the transmitted light direction compared to the epi-direction. The measurement of the SHG intensity collected in the transmitted light direction can be compared with that collected in the epi-direction and used to estimate the size of the fibrillar structures that generate the SHG.



Created in [BioRender.com](https://www.biorender.com) 

Figure 1-4: Two photons interact within a non-centrosymmetric molecule (e.g collagen) and are combined to form a new photon with twice the energy (2ω) and half the wavelength of the initial photons. Image produced in BioRender.

Collagen type I and II are both known to produce strong SHG signals due to the chirality of the triple helices, making them non-centrosymmetric. In contrast, type IV and III are not fibrillar *in vivo* so are unable to produce signals [85], [86]. SHG does, however, show variations of signal intensity depending on the angle of the plane of polarisation, with maximum signal intensity occurring when the fibre axis is parallel to the plane of polarization. With the use of SHG, it is possible to gain useful information on the alignment of the fibrils and the quantity of overall collagen.

1.4 Mechanical properties of bone

It is difficult to give a precise number to the mechanical properties of bone. Furthermore, the value which provides the most relevance when trying to recreate these mechanical properties is still a topic of much debate and will differ vastly depending on the question being asked. Mechanical properties of bone will differ significantly, depending on how it is measured, and what volume it is measured in [87]. For example, a whole bone measurement will differ significantly from that of a small biopsy of pure trabecular or pure cortical bone, or of that of a single trabecula. Furthermore, whether there is marrow present also adds further complexity. As bone is an anisotropic material, the mechanical properties also vary dramatically depending on the direction of the applied force. This is especially true of bone that undergoes loading in predominantly a single direction, such as the femoral neck.

There are many different mechanical properties looked at when assessing bone strength, which is generally assessed through a typical stress-strain curve. These include but are not limited to Young's modulus, shear modulus, ultimate tensile stress and ultimate compressive stress [88]. It is also possible to assess the properties at the nanoscale, through technical such as hardness testing via microscale and nanoscale indentation [89]–[91]

Bone will generally exhibit an elastic region, in which deformation is linear. Within this region, any strain exerted onto the bone will not cause any damage, with the bone returning back to its previous state. However, above the yield strength of bone, permanent damage will occur, which usually forms microcracks within the bone [92], [93]. Bone's elasticity or stiffness can therefore be quantified through the use of Young's modulus, which can be obtained by

measuring the gradient of the elastic region on the stress-strain curve. In the case of metabolically active bone within living organisms, this curve, including the elastic region, may alter over repeated tests due to the adaptive nature of bone and the cellular responses to mechanical forces such as strain or shear [94].

Ultimate tensile strength is the highest force that the bone can receive before the commencement of fracture, which is signified by a sharp drop off on the stress-strain curve. After this point total bone fracture would occur. This can occur in tension, compression, or bending, which imparts a combination of tension and compression, or torsion.

Table 3: Brief summary of mechanical properties of human bone from various locations and sample sizes. NM = Not Measured

Sample type	Structural Scale	Young's, Ultimate tensile strength	Reference
Subchondral bone plate of femoral head	Macroscale	19.8GPa, NM	[95]
		3.5±1.2GPa, 30±7.5MPa	[96]
Trabecular bone of mandible with marrow	Mesoscale	56MPa±29.6, 3.9MPa ± 3.9	[97]
Micro specimen of cortical bone from tibia	Microscale	18.6GPa±3.5, NM	[98]
Single trabecular from tibia	Microscale	10.4±3.5GPa, NM	[98]

1.4.1 Effects of mechanical loading

Mechanical loading is essential for normal bone health, playing a key role in maintaining the skeletal architecture through a balance of deposition and resorption. An increase in mechanical loading should increase bone density,

whilst an absence of loading, for example in cases of paralysis or long-term bed rest, causes a notable reduction in bone density [99].

During loading, compression of the lacunae and canalicular network results in changes in pressure, causing interstitial fluid flow and subsequent fluid shear stresses applied to the surfaces of the surrounding cells. It is generally predicted that the fluid shear stress that is experienced by cells within lacunae varies between 0.8-3Pa [100]. It was once believed that osteocytes were completely inactive cells, however, it is now known that they play a significant role in the mechanosensing of bone. Osteocytes are known to be sensitive to mechanical shear stress and can convert these mechanical signals into biochemical responses in a process called mechanotransduction. This process involves several mechanisms, including the activation of stretch-activated ion channels, which can detect changes in fluid flow within the canalicular system of bone. One specific calcium ion channel, known as Piezo1, is seen to be highly expressed in osteocytes [101]. When Piezo1 is active, it leads to increased expression of a signalling molecule called Wnt1, which, in turn, activates the Wnt/ β -catenin signalling pathway, where the Wnt signalling molecule is shown to act on osteoblast precursors and promote differentiation of osteoblast pre-cursors into mature osteoblasts [94], [102]–[104].

Mechanical compression or stretching may also be directly transmitted to the nuclear envelope, through tugging on integrin adhesion receptors, and results in altered transport of transcription factors, as well as causing remodelling of the nucleoskeleton [105]–[108]. Dupont *et al* demonstrated that HIPPO pathway effectors, Yes-associated protein (YAP) and Transcriptional coactivator with PDZ-binding motif (TAZ), act as mechanotransducers that can relay cytoskeletal

tensions to the nucleus and result in alteration of cellular behaviour [106]. This pathway may be activated by external cues such as altering the stiffness of the substrate, or by confining cells to a specific area and subsequently altering morphology [5], [106], [109], [110]. Some investigators believe that osteocytes are the primary mechanosensors in bone, however, this is also disputed, with others arguing that osteoblasts may also be able to respond to mechanical stimuli in a similar manner [70].

As discussed previously, differently differentiated cells are seen to have different shape conformations. It is believed that this shape change in fact plays a key role in the commitment process of a cell's differentiation and behaviour [9], [111]–[113]. In a study by McBeath *et al*, it was shown that part of the cells commitment proces was mediated by Ras homolog family member A (RhoA) and its interactions with Rho-associated protein kinase (ROCK)-mediated cytoskeletal tensions [114]. RhoA is shown to play a role in stress-fibre organisation, as well as the maintenance of spindle assembly, and is seen to be expressed more greatly in spread cells compared to rounded cells (**Figure 1-5**) [8], [107], [115]. It has also been shown that through direct infection with a viral form of RhoA, there is observable osteogenesis occurring even in absence of induction media, suggesting that the cytoskeletal organisation plays a large role in triggering differentiation, as opposed to differentiation causing cytoskeletal changes [114].

1.5 Bone diseases

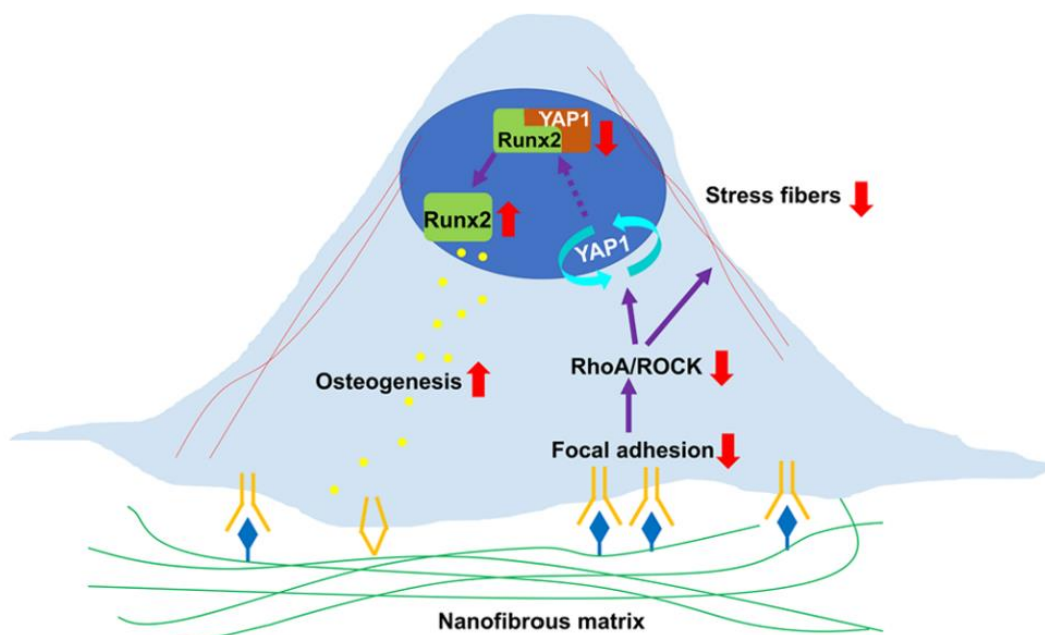


Figure 1-5: RhoA/ROCK mediated pathway in response to cell morphology on fibrous matrices. Reprinted with permission from Chang et al [274] Copyright 2023 American Chemical Society

Currently, bone diseases such as osteoarthritis, are most commonly studied within animal models, which are used to reproduce the symptoms, expression and progression of the disease seen within humans [116]–[120]. The ideal animal model would progress with similar mechanisms and severity as humans, but in a shorter time frame, to allow for the more efficient testing of therapies and identification of key stages and disease mechanisms. There are a large number of limitations with the use of animal models, however, mostly due to differences in anatomy, biomechanics and repair processes between animal and human joints [121]. The critical differences between human and animal models are considered to be one of the key reasons for the clinical trial failure of new compounds for clinical use, with approximately 89% of novel drugs failing human clinical trials, and with roughly half of those failures due to unanticipated human toxicity [122]

All musculoskeletal diseases would benefit from bone models, however, some diseases would have different requirements in order to be a useful model.

For example, some musculoskeletal diseases exhibit elevated bone turnover, which involves a delicate balance between bone formation and resorption. Paget's disease, for instance, is characterized by excessive bone remodeling, leading to bone deformities and fragility. In such cases, creating an effective bone model necessitates the presence of both osteoclasts and osteoblasts. An accurate model for Paget's disease must capture the intricate interplay between these cell types. Alternatively, osteonecrosis arises from inadequate blood supply to bone tissue, resulting in bone cell death. For diseases like osteonecrosis, vascularization within the bone model becomes paramount.

Certain musculoskeletal diseases, such as Osteogenesis Imperfecta and Osteoarthritis, are characterized by dysregulation in the production and organization of the extracellular matrix (ECM), specifically collagen. To create suitable models for these conditions, researchers must focus on replicating the disordered collagen organization and mineralization, as well as changes in ECM composition and structure. Such models offer a unique opportunity to investigate the genetic, molecular, and cellular mechanisms underpinning these disorders.

1.5.1 Osteogenesis Imperfecta

Osteogenesis imperfecta (OI), or “brittle bone disease” is a genetic disorder, characterised by a dramatic increase in bone fragility and resulting in fracture even without a significant degree of force, as well as skeletal deformities of variable severity. OI is caused by a genetic mutation, most commonly of the

COL1A1 and *COL1A2*, genes which code for type 1 collagen, effecting its structure and functions[123][123]. Although *COL1A1* and *COL1A2* mutations account for around 85% of overall OI phenotypes, other variations include but are not limited to, genes encoding proteins that play crucial roles within collagen synthesis (*BMP1*), collagen post-translational modifications (*CRTAP*, *P3H1*), collagen crosslinking (FKBP6), bone mineralisation (SERPINF1) and osteoblast functionality (*SP7*, *TMEM38B*) [124]–[128]. Investigation into these genes may provide a deeper understanding of how healthy osteogenesis is regulated.

Asharani *et al* showed that a knockout of *BMP1* in zebrafish results in an inability to create mature collagen fibrils, whilst the addition of a mutated variation results in a loss of collagen order and structure [129]. Although *BMP1*'s exact function is unclear, it is known to be involved with the proteolytic removal of the C-pro-peptides from procollagen precursors of type I collagen [130]. They also noted that the osteoblasts adopted a more cuboidal shape, as opposed to the elongated shape seen in healthy osteoblasts in regular lamellar bone. These results suggest that *BMP1* may play a role in the control of healthy type I collagen deposition and arrangement.

1.5.2 Osteoarthritis

Osteoarthritis (OA) is a disease of the osteochondral interface that presents with symptoms of pain, swelling and stiffness within the joints. The pathophysiology is complex but fundamentally results in the progressive destruction of the articular cartilage and thickening of the underlying subchondral bone within the articular joint. As cartilage lacks a significant regenerative capability, it results in irreversible damage to the joint, alongside changes to the pathology of the surrounding soft tissues, nerves and blood vessels which in turn results in the

pain and swelling commonly presented by patients [131]. There is debate on the origin of osteoarthritis, on whether the disease originates within the articular or calcified cartilage, the subchondral bone that lies beneath, or elsewhere within the joint [116], [120], [132], [133]. In OA patients, the bone is seen to be of poorer quality and abnormally low degree of mineralisation, with an increased turnover and it was previously thought that any changes to the bone within osteoarthritis were secondary to the cartilage damage, however, more recently there is evidence that changes to the subchondral bone may occur before measurable changes to the articular cartilage [95], [134]. In a longitudinal study of changes within OA-affected joints, radiographical images were able to show an apparent thickening of the cortical bone plate in both hand and knee OA joints as the disease progresses, which in turn could suggest that the subchondral bone may play an important role in the development of OA[135]. Evidence also suggests that bone sclerosis- the thickening and forming of hard nodules- is linked to early-stage thickening of the cortical bone. It was shown that in cynomolgus macaques the severity of articular cartilage lesions increased with increasing subchondral bone plate thickness, whilst below a threshold of subchondral plate thickness there was a complete absence of the formation of cartilage lesions [136].

Currently, without a proper understanding of the mechanisms behind the origins of osteoarthritis, it makes it difficult to study and find suitable drugs for treating osteoarthritis without surgical intervention. Despite the obvious effects on the subchondral cortical bone, it is a commonly neglected component of osteochondral models, which generally focus on creating a biphasic bone/cartilage model where an unorganised, sponge-like structure (and consequently woven bone-like) is used to represent both the subchondral

cortical and trabecular bone [137], [138]. The development of an *in vitro* model of organised cortical bone would also lend itself well to the development of an osteochondral interface model and a better understanding of the mechanism behind the origins and progression of osteoarthritis.

1.6 Modelling bone – Materials

An ideal material for use in *in vitro* bone modelling would have similar requirements to that of materials created for bone regeneration. It would need to first be biocompatible, allowing for attachment, growth and spreading of cells without any adverse effects on their viability. It would also need to be osteoconductive, allowing for the deposition of a bone-like ECM. It would preferentially be osteoinductive as well, inducing differentiation of MSCs or immature osteoblasts into mature osteoblasts and osteocytes without the addition of extra osteogenic differentiation factors such as dexamethasone. However, this would not be an essential requirement.

When designing scaffolds for the use of bone regeneration or formation, the porosity and material topography plays an imperative role in helping modulate osteogenesis and vascularisation of the scaffolds. Although high porosity is ideal for nutrient diffusion during culture, as well as the development of the matrix and mineralisation, there is generally a decrease in mechanical strength of the bulk structure of scaffolds as porosity increases, which proves a challenge for when the scaffolds must be implanted in areas of high loading. Furthermore, due to the apparent effects of the material's mechanical properties on cell behavior, it would be reasonable to argue that in the absence of mechanical loading, as in

the case for *in vitro* models, it may still be important to recreate mechanical properties that are close to that of the *in vivo* bone.

1.6.1 Calcium Phosphates

Calcium phosphates (CaPs), although hold great promise within their biocompatibility and osteoconductivity, are limited heavily by their toughness. Numerous studies have demonstrated the enhanced toughness of CaPs with the addition of type I collagen [139]–[143]. Inzana *et al* recently produced macroporous 2wt% collagen CaP scaffolds using a low-temperature inkjet 3D printing methodology and 8.75 wt% phosphoric acid as a binder [142]. Their results showed that the fabricated scaffolds were improved in both mechanical strength and their bone regenerative capabilities within a critically sized murine femoral defect.

1.6.2 Polymers

Synthetic biocompatible and biodegradable polymers such as polylactic acid (PLA), polyethylene glycol (PEG), and polycaprolactone (PCL) are also popular choices within bone scaffold development due to their customisable chemical, physical and mechanical properties. Composite scaffolds have also been shown to help improve osteoconductive properties, for example, the addition of PEG into porous PLA scaffolds showing to support the growth of mineralising osteoblasts [144].

PCL is also commonly used as a material for bone tissue engineering, being used both alone or as a composite to further improve its properties [61], [145]–[150]. PCL is a semi-crystalline polyester, that is widely biocompatible, cheap and easy to work with. It can biodegrade naturally through hydrolysis under physiological

conditions over a longer period of 2-3 years, making it an excellent option for bone tissue engineering as it would provide a solid base to stabilise the defect, whilst slowly integrating and degrading as the bone naturally reintegrates and remodels into mature bone.

PCL is, however, very hydrophobic, causing poor cellular attachment on pure, untreated PCL. Various studies have used composites of PCL with more bioactive materials such as chitosan, gelatin and polylactic acid to promote cell attachment and osteogenic activity, whilst still maintaining the desirable mechanical properties of PCL [148], [150], [151].

Furthermore, PCL is modifiable with acrylates and methacrylate, to produce photocurable polymers, giving potential for their uses in 3D printing. Elomaa *et al* showed them to be non-cytotoxic, and they have since been used in various 3D printing applications, including bone-tissue engineering, peripheral nerve conduits and small intestine villi [147], [152]–[155]. With the use of star-shaped PCLs such as PCL-triol, it is possible to carefully control the degree of methacrylation by altering the reaction time with methyl anhydride (**Figure 1-6**) [156]. With longer reaction times, the PCL would be either fully methacrylated, with all arms functionalised with a methacrylate group, or partially methacrylated, with only one or 2 arms containing a methacrylate group [156]. By controlling the methacrylation, further control of mechanical and degradation properties can be achieved, with increased methacrylation corresponding to an increased cross-linking density achievable, making them a desirable material with a wide range of applications.

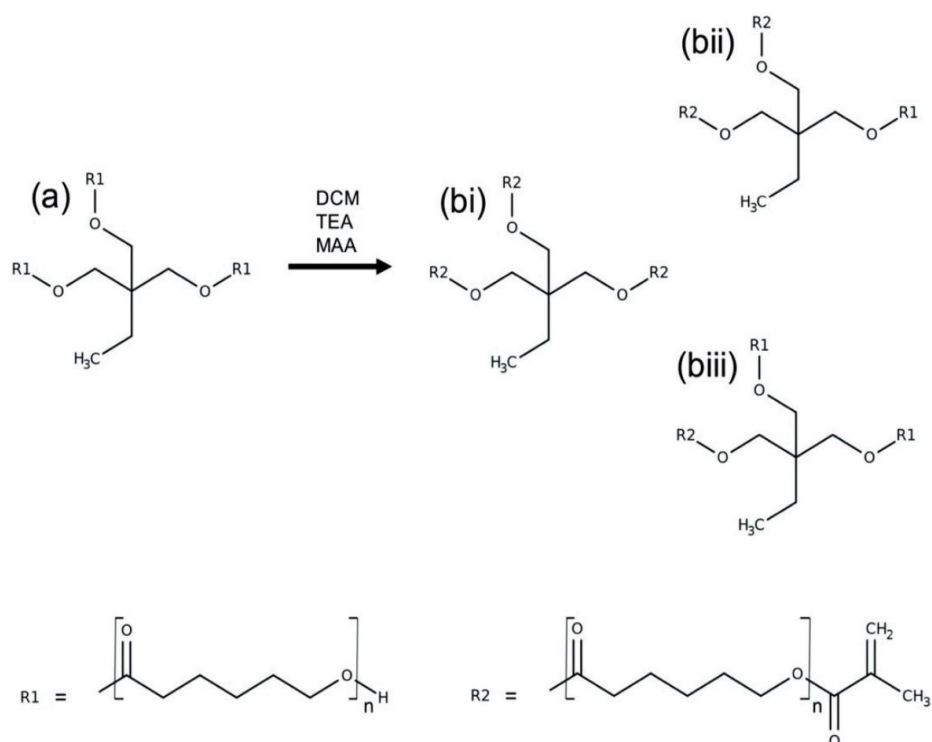


Figure 1-6: Functionalisation of a 3-arm PCL (a) with methyl anhydride, forming 3-arm PCL methacrylate. The resulting product can either be fully methacrylated (bi) or partially methacrylated (bii, biii). Image taken from Field *et al*[157] under the terms of the Creative Commons Attribution License (CC BY).

1.6.3 GelMA

Gelatin methacrylate (GelMA) is a commonly used photocurable hydrogel, popular due to its biocompatibility, cost, and ease of synthesis. GelMA is derived from gelatin, providing it with the arginine-glycine-aspartic acid (RGD) binding motifs which subsequently accommodate cell attachment, and has been used within many applications within the biomedical field, including tendon, blood vessels and injectable drug delivery [158]–[162].

GelMA is produced by the reaction of gelatin with methacrylic anhydride. This results in the amino groups presenting on the side chains of gelatin being replaced by methacrylate groups, forming gelMA. With the addition of a water-soluble photoinitiator, commonly lithium phenyl-2,4,6-

trimethylbenzoylphosphinate (LAP), it can then be cured under UV light, allowing the formation of cross-links.

GelMA, however, is extremely mechanically weak. Although the compressive strength varies depending on multiple aspects, such as %Wt, degree of methacrylation and source of gelatin precursor, it is generally seen to be below 100kPa [163], [164]. This is remarkably weaker when compared to the mechanical properties of trabecular bone, which again varies tremendously depending on a multitude of factors, but generally has a compressive strength that sits in the range of megapascals [97], [165].

Within GelMA, cells will generally adopt a circular confirmation, as opposed to spreading, and subsequently affects cell interconnection, cross-talk and cellular behaviours. It is therefore desirable to produce a hydrogel that also contains an interconnected porosity that allows space for cell interconnection (**Figure 1-7**). One way of producing this was shown by Ying *et al*, whereby aqueous solutions of poly(ethylene glycol) and gelMA, two hydrophilic biomaterials, are mixed, resulting in an aqueous two-phase suspension that can be photocured into a porous scaffold [166]. These scaffolds showed to be favourable over traditional non-porous gelMA, with increased cell viability, spreading and forming an interconnected network.

Pure GelMA, despite its excellent biocompatibility, low mechanical strength, short degradation time, and high swelling rate, significantly restrict its applications within bone tissue engineering. However, it has been used in conjunction with other materials as a composite. For example, GelMA/PEGDA hydrogels were used by Wang *et al* and were shown to allow for high viability and proliferation of the pre-osteoblast cell line MC3T3-E1, whilst also having

increased mechanical properties, with a compressive strength of 70.6kPa, 6-times that of pure 10%wt GelMA [167].

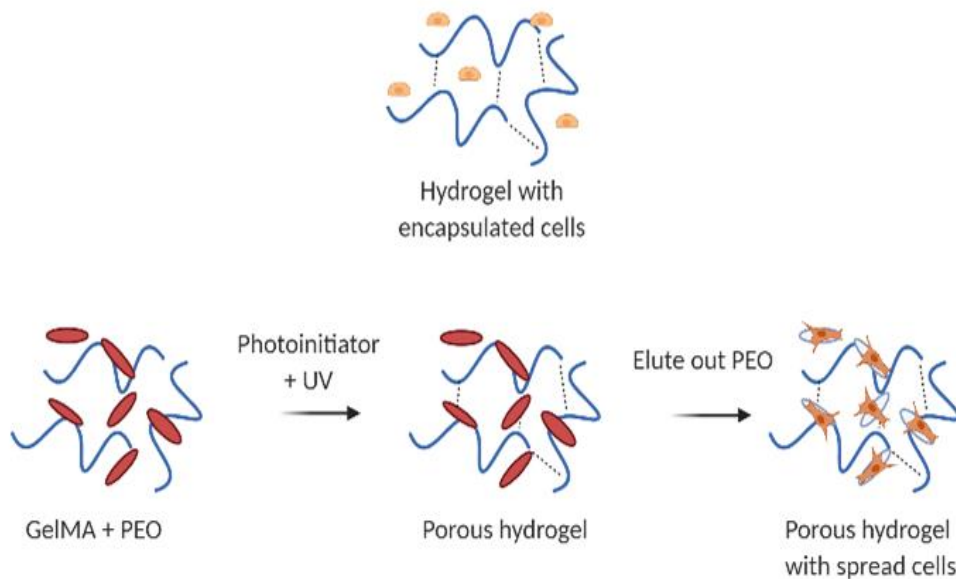


Figure 1-7: Cells encapsulated in pure GelMA hydrogels can be seen to adopt a rounded conformation. With the addition of a soluble, low MW PEO, a porous hydrogel may be created. PEO may be washed out, leaving pores that may allow for the spreading of cells. Created using BioRender

Other composite materials used include gold nanoparticles, seen to promote the differentiation and production of ALP in human adipose-derived stem cells, and nano-silicates, which are also seen to increase the mechanical properties 4-fold, as well as also promoting ALP production and mineralisation in MCT3TC-E1 cells [168], [169].

1.6.4 Alginate

Alginate is another commonly used material for the development of hydrogels. It is a biodegradable and biocompatible polysaccharide and can be naturally derived from seaweed. However, unlike gelatin, alginate lacks cellular adhesion sites, limiting its uses for cell culture. It is, however, still very popular in 3D printing applications. It is easily crosslinked ionically by calcium ions, as well as

strontium and barium, bypassing the need for functionalisation or the use of toxic chemical cross-linking components such as photo-initiators.

You *et al.* produced alginate scaffolds with various levels of porosity varying the contact angle between strands whilst using sequential strand deposition [170]. This methodology usually uses automatic dispensing systems and sometimes tends towards pneumatic dispensing mechanisms (also known as bio plotters) that deposit strand-like materials on a surface and are useful for 2D and 3D scaffolds, in a process similar to fused filament fabrication. Researchers found that a 2 %w/v sodium alginate-based hydrogel with a polyethyleneimine crosslinker was optimal for maintaining the structure. Optimisation of the calcium ion concentration (used as the crosslinker) produced a mechanically stable, porous scaffold with controlled degradation rates.

To overcome the issues of poor cellular adhesion, alginate has been introduced into gelMA hydrogels to provide a more suitable environment for the attachment and growth of cells. With the combination of alginate and gelMA, it is possible to increase and tune the mechanical properties of the material when the hydrogel is crosslinked both chemically and ionically [171]–[173]. Furthermore, with the addition of alginate to gelMA, it is able to dramatically increase the viscosity and therefore increase its printability compared to that of pure gelMA.

1.7 *In Vitro* Modelling of Bone- Methods

When developing an *in vitro* model with applications of drug testing, modelling the mature bone may have additional benefits to simply healing woven bone. Although a model of woven bone would also be highly beneficial for the examination of potential drugs and their effects on bone healing, it is also

important to examine the effects on organised and healthy bone. Furthermore, drug diffusion profiles may occur differently through the mature bone, with more organised collagen and mineral than that of disorganised bone[14]. Certain drugs may also be seen to interact with the addition of mechanical loading, for example, recombinant parathyroid hormone treatment and loading have been seen to have synergistic effects on increasing density within the cortical bone, but with little effect on the trabecular bone [13].

Not only do cortical, trabecular and woven bone have significant structural differences, but there have also been observed different gene expressions between cortical and woven bone. McKenzie *et al* applied 1hr of loading on woven and cortical bone and were able to identify 395 genes that were differentially expressed, and after 3 days this increased to 5974 genes [174]. A large portion of these genes were those related to inflammation and wound healing pathways.

Although woven bone models should theoretically begin to reorganise themselves into structures resembling mature bone, this would be a lengthy process that would likely take several months to mature [18]. *In vitro* cell culture of this length would not only be difficult but would also be expensive and time-consuming, making an inappropriate method for the development of an *in vitro* model of organised bone. Therefore, it is of interest to create a scaffold that may assist with the production of a more organised bone and bypasses the woven bone stage.

This section discusses the current materials and methods used for the development of bone scaffolds and models.

1.7.1 PolyHIPEs

Production of high internal phase emulsion polymers (PolyHIPEs) is an increasingly popular method of producing highly porous scaffolds. Formed via emulsion templating, polyHIPEs are produced by the mixing of two immiscible liquids (an “oil phase” and a “water phase”) to form an “oil-in-water” solution. The oil phase, which is also known as the continuous phase, is then polymerised and emulsion drops are removed to form a highly porous material. If this porosity is over 74% then it is considered a HIPE. PolyHIPEs are formed of pores and windows, with windows being the connecting channels between the pores, allowing for interconnectivity of the material.

Emulsions are thermodynamically unstable systems and will tend towards separation. The stability of the system can be tuned, however, through control of the specific components. With an increase in the viscosity of the continuous phase, there is a general increase in stability. However, a viscosity too high would prevent efficient mixing of the two phases, resulting in poor dispersion. Increased stability may also occur with the addition of a surfactant, an amphiphilic molecule that can sit at the interface between the aqueous and oil phase.

PolyHIPEs may be finely tuned to gain specific levels of porosity, pore sizes, and interconnectivity, and have been explored for their uses as a potential bone construct [145], [175]. These, however, still possess only a single-scale porosity as discussed in the previous report, and would not possess larger pore sizes that would be necessary for blood vessel infiltration, which requires a porosity of at least around 300µm [176]. Subsequently, the use of 3D printing methods has been used to produce HIPEs with a multiscale porosity [147], [176], [177]. For example,

Dikici *et al.* proposed a method of 3D printing PCL polyHIPES and were able to form a scaffold with a multiscale porosity architecture that allowed for the successful infiltration of the bone cell line MLO-A5, and subsequent successful matrix production and induction of angiogenic activity [147].

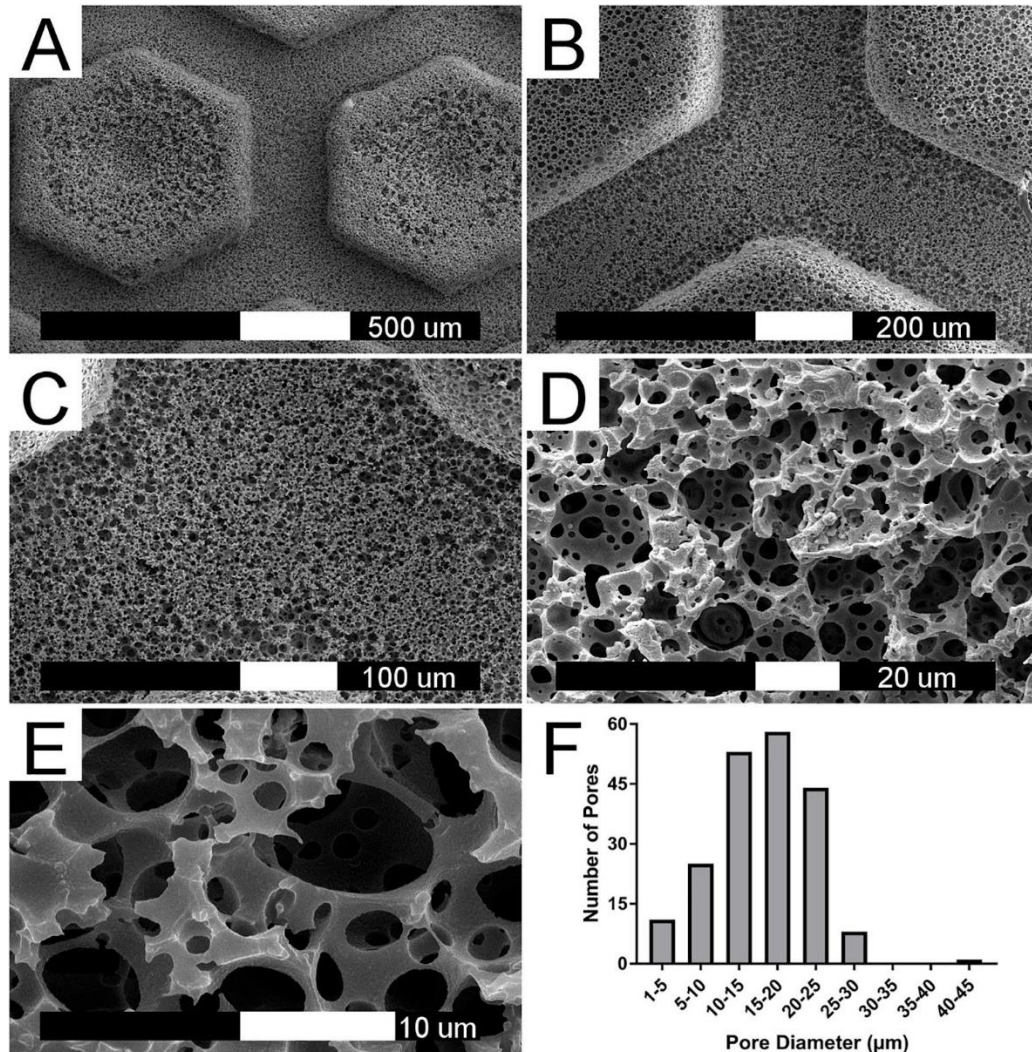


Figure 1-8: An osteogenesis-on-a-chip model, using negative replica moulding and polyHIPES to produce a microfluidic chip with both micro- and macro-porosity, mimicking the multiscale porosity observed in trabecular bone. A, B, C) Fluid channels can be observed, with hexagonal struts. D, E) Interconnected micropores with a 5-30μm diameter F) Distribution of the pores. Image from Bahmaee *et al* under the terms of the Creative Commons Attribution License (CC BY).

Bahmaee *et al* used a polyHIPES approach to create an “Osteogenesis-on-a-chip” device and used negative replica modelling to produce a construct that showed microporosity within the HIPE of 5-30μM, and larger channels for fluid flow of

around 310-430 μ M (**Figure 8**) [177]. It has also been shown that there is the possibility for cells to spread with long processes similar to osteocytes, when cultured within interconnected polyHIPEs [178].

Producing polyHIPEs does, however, require the use of photocurable materials, and subsequently the use of initiators, monomers or cross-linkers used to solidify the emulsions. This consequently may result in a reduction in cell viability or the need for additional steps to remove the toxic components. An alternate method that bypasses the use of photocuring is to create Pickering emulsions.

1.7.2 Pickering Emulsions

Pickering emulsions are colloidal suspensions that are formed through the use of solid particles in place of surfactants. These particles sit at the water-oil interface, allowing for protection against coalescence and effectively stabilising the emulsion. The stabilising particle may also be chosen with beneficial properties for its use- for example, the use of HAp has been used within Pickering emulsions, which are known to help with osteoinduction within the use of bone scaffolds [179]. Different particles have also been proved to stabilise Pickering emulsions such as starch, and micro- and nano-silica [179]–[182]. The stability of Pickering emulsion is predominantly influenced by the surface wettability of the particles, however, particle size, shape and concentration also contribute to the emulsion behaviours. The use of hydrophobic particles will have a greater affinity to the oil phase, and consequently are better for the stabilising of W/O emulsions, whilst hydrophilic will generally stabilise O/W. Pickering emulsions have a wide range of uses within many industries, including food, cosmetics, drug delivery and the development of porous materials.

SiO₂ is a popular stabilising particle for Pickering HIPEs, due to its biocompatibility and ability to be modified, and therefore is extremely useful within drug delivery. The Stöber process is a widely used chemical process that is used to prepare silica (SiO₂) particles [183]. The method uses a sol-gel process, whereby a molecular precursor such as tetraethyl orthosilicate (TEOS) is first reacted with water in an alcoholic solution. The resulting molecules then join together to build larger structures, producing silica particles with diameters ranging from 50 to 2000 nm. The Stöber method produces a hydrophilic SiO₂, so the further reaction is then required to modify the particles. Surface modification with silanes is a popular method, which occurs via a hydrolysis and condensation reaction, which act as the nucleation and growth mechanisms throughout the reaction [183]–[185]

A method was developed by Hu *et al.*, in which a multiscale porous scaffold was able to be printed, using PCL, hydrophobically modified HAp and hydrophobically modified SiO₂ (m-SiO₂) [179]. The method used a highly viscous emulsion to allow for its printing, before being left for 24 hours in order for the solvent to begin to evaporate. Another study used m-SiO₂ and PCL to create emulsions for electrospinning and found that they were able to enhance the tensile strength of the resulting scaffolds compared to pure PCL [180]. These scaffolds, however, lack interconnects between the micropores. The lack of interconnectivity may be due to the absence of surfactant within the emulsions. The surfactant's main role within photocurable polyHIPEs is to reduce the interfacial tension of the emulsion and plays a part in the interconnectivity of a HIPE. By increasing the surfactant within a photocurable polyHIPE, it is generally seen that smaller pores with a larger number of interconnects are formed [185].

Emulsions are commonly produced with the use of solvents and surfactants. The surfactant is required to reduce the surface tension of an emulsion and allows for the subsequent stabilization of the system and prevents the separation of the phases into two distinct layers. Furthermore, when a highly viscous, or solid oil phase is required, solvents are often used to allow for efficient mixing of the two phases. However, solvents and surfactants are largely cytotoxic. In order to use the scaffolds, post-processing steps such as lengthy washing and Soxhlet extraction are required to remove these toxic components. This not only may reduce cell viability post-seeding if improper washing is carried out but also would be incompatible with direct cell printing. When seeded post-production, scaffolds are limited by the cell's ability to infiltrate deep into the centre of the scaffolds. Methods such as perfusion, rocking and conditioning may increase the depth in which cells penetrate, however, cell infiltration is largely dictated by the bulk size of the scaffold, and often results in a non-homogeneous distribution throughout the construct.

To make an emulsion that is viable for direct cell printing, both surfactant and solvent need to be eliminated.

Solvents are also not essential for the formation of an emulsion, and in fact, the use of a more viscous pre-polymer solution may assist in the stability of the emulsion. Despite this, the viscosity must still be controlled to allow for the efficient mixing of the two phases. One method for this is to also increase the viscosity of the water phase.

1.7.3 Electrospinning

Electrospinning is an extrusion-based method for the fabrication of nanofibers from polymers. It is a method widely used within tissue engineering for the development of scaffolds. The technique is achieved by extruding a polymeric solution out of a needle at high voltage to form a charged jet of the polymer that solidifies as the solvent evaporates off. This is then collected on a grounded, rotating collector drum.

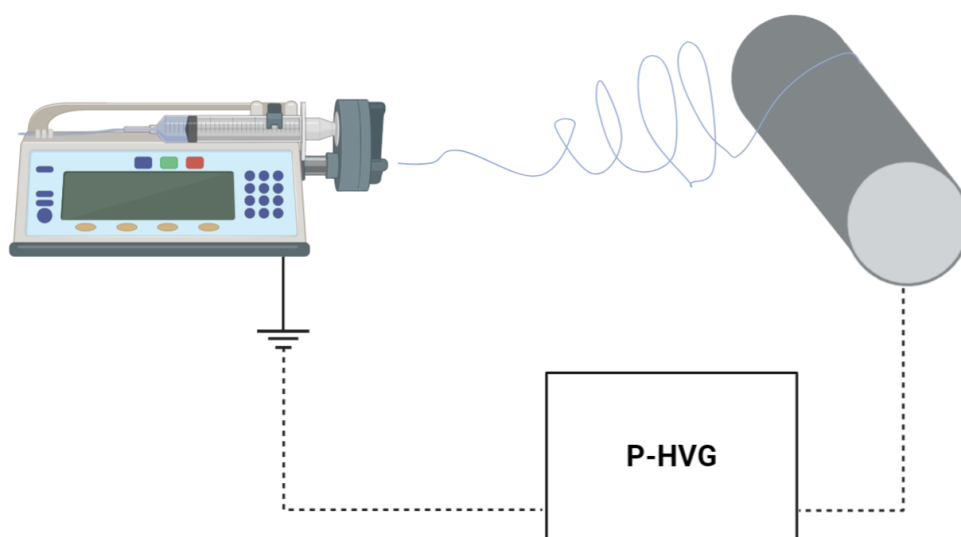


Figure 1-9: Schematic of the electrospinning process. A syringe pump is used to slowly extrude polymer from a blunt tip needle, connected to a positive high voltage generator (P-HVG). This is then drawn towards a grounded collection drum, with a controllable rotary speed between 200-2000 rotations per minute.

Electrospinning has gained attention in recent years, due to the ability to fine-tune the process to produce fibres with a tuneable diameter and degree of alignment. Furthermore, these fibres possess a large surface area, supporting cell

attachment and growth, as well as directing cell preferential alignment along the axis of the fibre.

The use of electrospun fibres have been shown to be effective as a scaffold for the formation of bone, as well as facilitating the differentiation of stem cells into an osteogenic lineage [37], [148], [150], [151], [186], [187]. Commonly used for bone scaffold fabrication is PCL, due to it being biocompatible, biodegradable and having both tailorable structural and mechanical properties [188]. Furthermore, it has favourable rheological and viscoelastic properties, which allow for ease of spinning.

Most studies of electrospun fibres use randomly orientated fibrous mats, however, a few studies have begun to investigate the effects of highly aligned fibres on the regeneration of bone [59], [187], [189]. For example, the use of parallel composite nanofibers formed of a composite of HAp and tussah silk to imitate collagen fibrils in natural bone was able to elicit cell adhesion, proliferation, and bone formation more effectively than pure silk or coverslip [187].

1.8 3D Printing

3D printing, often known also as additive manufacturing, solid-freeform technology, or rapid prototyping, is a technology widespread across many industrial and engineering fields. Within the last 10 years, there has been a huge increase in interest in its uses within bioengineering and regenerative medicine. Of particular interest to this review is its capabilities of printing with “bio-inks”, where viable cells are encapsulated within printing materials which may allow for the printing of more complex and accurate architectures than other 3D

fabrication methods commonly used in the field, such as foaming and salt leaching [190]. Bio-inks are not without their issues, however, due to a large number of parameters such as temperature, extrusion time and velocity, and nozzle shear stresses being seen to affect the viabilities of the encapsulated cells [191]–[194]. Furthermore, the inclusion of cells within materials already optimised for printing has been seen to have effects on the rheological behaviours of the inks and hence altering optimal printing parameters [195]. Billiet *et al* demonstrated the possibility of printing cell-laden gelatin methacrylamide hydrogels whilst still maintaining a mechanically stable scaffold. An increased concentration of polymer allowed for faster physical gelation and more circular geometry of strands, resulting in a mechanically stable structure without the collapsing of pores[193]. Furthermore, >97% of cell viability could be achieved through the careful control of machine operating parameters such as temperature and needle tip alterations, without the need for viscosity-increasing additives.

1.9 Culture conditions

1.9.1 Cell Choice

Another important consideration within the development of an *in vitro* model is the choice of cell source. For bone models, there are a few different cell choices to consider, and many different sources have been used throughout the literature discussed above, and various common cell types have been summarised below in **table 4**.

There are various cell lines commonly used. MG63, SOAS-A2 and M3T3C-E1 are all considered osteoblast cell types at varying degrees of maturity [196]. There are

fewer osteocyte cell lines but MLO-Y4 is commonly used, while MLO-A5 is considered a pre-osteocyte in the early stages of differentiation [197]. The use of cell lines benefits from generally faster proliferation, longer life span in culture and stability across a wide variation of passages. Furthermore, they are generally considered reproducible and are widely used in the literature [61], [68], [148], [198]–[201]. However, many of these are seen to have dysregulated functions when compared directly to that of osteoblasts, such as differently expressing genes. Although these cell lines are beneficial for various applications, such as assessing adhesion, toxicity or bio functionality of new materials, they would be unlikely to mimic the functional behaviours of the *in vivo* tissues, and would not be beneficial in *in vitro* models for use of drug testing.

Primary osteoblasts from donors may be an option, however, these bring issues with their limited *in vitro* proliferation capacity, as well as dedifferentiation within prolonged culture, ultimately losing their phenotype.

Alternatively to the use of differentiated primary cells are MSCs. Bone marrow-derived mesenchymal stromal cells (BMSCs) are a source of MSCs and are a common choice of cell within osteochondral engineering, due to their potential for differentiation along both osteogenic and chondrogenic pathways. However, being formed of heterogeneous populations, there is a lot of variability within the population in potency, with tri-lineage (Adipogenic, chondrogenic and osteogenic), restricted lineage and precursor cells within a single sample, resulting in significant variation in differentiation capacity and behaviour *in vitro*[202]. Furthermore, it is seen with increasing passage comes a sequential loss of differentiation capacity, or a loss in the inherent “stem-ness” of the cell, as well as high donor-donor variability.

To address some of these issues, there is a potential to immortalise a population with human telomerase reverse transcriptase (hTERT), which overcomes lifespan limitations caused by normal senescence of the telomere. James *et al.* used this alongside clonal selection to create homogenous cell subpopulations showing a series of different differentiation traits [203]. The specific cell line hTERT Y201 was found to be tri-Lineage, with the capacity for differentiation into adipogenic, osteogenic and chondrogenic lines, without undergoing replication senescence [203]. This, in turn, allows for a single cell source with a reliant ability to form both lineages necessary for osteochondral repair.

Table 4: Descriptions of various common model cells for *in vitro* bone models and their pro's and con's.

Cell Name	Primary/ Cell Line	Species	Pro's	Con's
MG63	Cell line	Human	Easy and fast growing Human-derived Reproducible over a wide range of passages Beneficial in adhesion studies	Derived from an osteosarcoma, potentially giving it dysregulated functions compared to that of healthy osteoblasts Shows minimal markers of osteoblastic activity
MLO-A5	Cell line	Murine	High expansion capacity Express late-osteoblast markers Reproducible outcomes Produces high amounts of collagen Spontaneously mineralises in culture	Non-human Mineral is secreted in sheets, as opposed to discreet nodules seen in primary osteoblasts
MLO-Y4	Cell line	Murine	Osteocyte cell line Produces large amounts of osteocalcin and low levels of ALP Widely used in mechanotransduction studies Proliferates in culture	Does not express various genes commonly expressed in healthy osteocytes Non-human
Primary osteoblasts	Primary	Various	Can be further differentiated into osteocytes	Lengthy process of isolation

			Will closely resemble the behaviours of <i>in vivo</i> bone cells compared to cell lines	<p>Slow doubling times</p> <p>Low number of usable passages</p> <p>Donor-donor differences</p> <p>Need for bone biopsies</p>
Primary osteocytes	Primary	Various		<p>The process for isolating osteocytes has an added difficulty due to their location within the lacunae</p> <p>Terminally differentiated so will not proliferate in culture</p>
Bone Marrow Derived MSC's	Primary	Various	Can be differentiated into osteoblasts and osteocytes	<p>Low number of usable passages</p> <p>Painful collection from bone marrow with risk of donor site morbidity</p>
MC3T3-E1	Cell line	Murine	<p>Expresses pre-osteoblast markers- can be differentiated into osteoblasts.</p> <p>Deposits collagen and mineral in nodules</p>	Non-human
SAOS-2			Positive for many osteoblastic markers[196]	Osteosarcoma cell line

1.9.2 Flow systems

As the size and complexity of a scaffold's architecture increase, so does the need for more efficient nutrients and waste transport. Without sufficient circulation of media throughout the scaffold there is generally poor differentiation and

matrix formation within the centre of the scaffold, as well as a risk of the formation of a necrotic core.

Furthermore, matrix deposition of bone is highly dependent on mechanosensing stimulation as discussed in **section 1.4**, and an imbalance in these mechanical properties is seen to have pathological consequences [94]. It is known that the application of flow in both 2D and 3D culture can increase differentiation into an osteogenic lineage, as well as enhanced deposition of an extracellular matrix, and a greater level of organisation, with collagen fibres generally seen to be deposited along the axis of flow[72], [177], [204]–[206].

The use of a perfusion system that can circulate media throughout a scaffold could hold great benefit over static culture, with the potential to benefit both nutrient and waste transport, as well as an increase in overall differentiation and matrix production. There are several different perfusion reactors available on the market, such as the Quasi Vivo® *in vitro* bioreactor that allows dynamic media flow through 3 separate chambers.

With a perfusion system, oscillatory flow can be applied or continuous perfusion. The use of oscillatory flow may be seen to be more physiologically relevant, due to the oscillatory nature of interstitial fluid flow within bone. Alternatively, continuous fluid flow in various *in vitro* studies has been shown to be a more potent stimulator of bone-matrix deposition.

Rocker plates are often chosen due to their simplicity, whilst allowing for oscillatory fluid flow. Rockers can be used with standard cell culture dishes and depending on size can be used to apply FSS to many plates simultaneously, making them an excellent choice for high-throughput work. Furthermore, as

they only need small amounts of media, it makes them more cost-effective compared to other flow devices that require large reservoirs of media. However, when using a rocker, there is generally a much lower FSS experienced by cells when compared to other methods of shear stress application. It is possible to calculate these shear stresses, but it is also noted that the shear experienced across the surface of the scaffolds is not evenly distributed, with higher shear occurring at the edges of the wells compared to that in the centre[207].

Despite this, low-magnitude FSS has still been shown to be beneficial for certain applications and has been shown to promote differentiation into an osteogenic-like cell type, as well as also guiding collagen orientation [71], [208]–[211].

1.9.3 Chemically defined media

A final important consideration within the design and implementation of *in vitro* models is the choice of culture media. The use of foetal bovine serum (FBS) is common practice within cell culture. Introduced in the 1950s, it is extracted from the blood from a bovine foetus and used to supplement culture medium at a concentration of generally 5-15%, so to stimulate the growth of cells and tissues. FBS is a natural cocktail containing most of the factors required for cell attachment, growth, and proliferation, such as hormones, vitamins, transport proteins and trace elements [212]. Despite its prevalence still in modern-day cell culture, its use entails a number of scientific, ethical and practical issues.

FBS, as a by-product of the beef industry, is subject to a large batch-to-batch variation and unpredictability in supply, as well as having an unknown exact composition [212]. This variability then translates to uncertainty and lack of repeatability when it comes to experimental cell culture. Furthermore,

collection of FBS occurs through a cardiac puncture of the unborn foetus, without any form of anaesthesia, bringing about ethical concerns of foetal distress, pain and suffering that may occur as a result [213].

In light of the issues faced with the use of FBS, there are several alternatives to its use, such as serum-free medium, protein-free medium, xeno-free medium and chemically defined medium. There are currently no universally accepted definitions which add to some confusion, with different manufacturers using a variety of terms.

Xeno-free or serum-free media are generally defined as media that are not supplemented with animal-derived plasma. They may, however, still contain purified human proteins, sometimes referred to as semi-defined medium. Whilst it removes a large potential cause of variability, there is still a potential for minor batch-to-batch variability [214].

Chemically defined medium consists of mixtures of characterized and quantitated ingredients and is completely free of any animal-derived or unknown components, using recombinant proteins and synthetic peptides alternatively. The well-characterised nature of chemically defined media allows for reproducibility and reliability of performance in cell culture, as well as the elimination of factors found in serum that may interfere with hormones or growth factors when studying their interaction with cells [215]. A key hurdle to many serum-free and chemically defined media is that their highly specific formulas often mean they are not effective across many different cell lines and protocols, meaning significant optimisation is often required with their use [214]. Furthermore, the specifics of their formulas and data often are not published by the companies who develop them.

2 Aims and objectives

2.1 Summary of review

Bone is a dynamic and intricate tissue, with a highly specialised structure that is essential for its function. Although there has been extensive work in replicating the porous structure of trabecular bone, there are very few attempts to replicate the highly organised collagen observed in cortical bone. Furthermore, there is a limited understanding of how the lamellar organisation is controlled. A comprehensive understanding of these regulatory pathways could potentially unveil novel avenues for therapeutic interventions targeting conditions characterized by dysregulated matrix production, such as Osteogenesis Imperfecta (OI) and Osteoarthritis (OA) such as OI and OA.

Reducing the complexity of bone tissue to a single-scale, porous material within in vitro models can be considered an oversimplified approach. This oversimplification tends to mimic the behaviour of immature or healing woven bone rather than the nuanced and intricate responses exhibited by mature bone tissue. Notably, woven bone, in contrast to its mature counterpart, displays distinct characteristics, including a heightened expression of genes associated with inflammation and angiogenesis. Consequently, it is reasonable to expect that in vitro models employing these simplified single-scale porous materials may yield responses that deviate from those observed in the context of mature bone.

Furthermore, the collagen deposition behaviour of bone is highly dependent on its mechanoregulatory properties, which are seen to be affected by cellular morphology through various mechanosensitive pathways. As cells are seen to adopt different conformations depending on the materials on which they are cultured on, it may be assumed that to mimic mature bone, the scaffold in question should allow the cells to achieve a conformation of mature osteoblasts, that is, aligned and elongated.

The development of an *in vitro* model that more precisely replicates the properties of mature bone offers a multitude of advantages. Such a model would not only serve as a valuable tool for investigating the effects of various pharmaceutical agents on bone health and function but also enhance our understanding of the fundamental processes underlying healthy bone development. The potential implications of such a model extend beyond drug testing, encompassing a broader spectrum of research in the field of bone biology and pathology.

2.2 Aims

This thesis aims to develop two separate scaffolds that can be used for the culture of cortical and trabecular bone-like micro-tissues, for future application in *in vitro* models.

The first aim was to try and create a material that induces the production of an organised ECM and gene expression that more closely resembles that of a mature, cortical bone, over a material that rapidly produces a disorganised matrix, which is commonly chosen for bone scaffolds for clinical applications. It is hypothesised that materials that allow for cellular conformation that more

closely resembles that of cells in mature bone, should result in a better-organised bone matrix.

The second aim of this thesis was to investigate materials for the development of multiscale porous scaffolds for trabecular bone models, which would allow greater infiltration into pores, and resemble more closely the cellular distribution seen in trabecular bone tissue. It aimed to use the method of emulsion templating, but to simplify the protocol, to require less downstream processing in order for it to be non-cytotoxic.

2.3 Objectives

To achieve the above aims, the project was divided into the following objectives:

1. Development of a highly aligned, fibrous scaffold for mimicking aligned collagen in mature bone
2. Assess the subsequent matrix and specifically the organisation of the deposited collagen.
3. Development of a porous and multi-scaled scaffold for mimicking trabecular bone

3 Materials and Methods

All materials and reagents were purchased from Sigma-Aldrich (UK) unless otherwise stated.

3.1 General Cell Culture

3.1.1 Culture media preparation

The xeno-free media (XFM), StemMACS™ MSC Expansion Media Kit XF (Miltenyi Biotech, UK) was used in all experiments. Media was supplemented with StemMACS™ MSC Expansion Supplement (Miltenyi Biotech, UK), 100 µg/mL penicillin and 100 µg/mL streptomycin. XFM was used throughout unless stated otherwise.

The differentiation media is XFM supplemented with additives to promote differentiation down an osteogenic lineage. These additives are 0.5M β-glycerol phosphate (β-GP), 5mg/ml ascorbic acid 2-phosphate solution (AA2P) and 10µM dexamethasone solution (Dex). Media containing these additives will be referred to as osteogenic media (OM)

3.1.2 Passaging and counting

Media was removed and cells were washed twice with PBS. 1.5ml of Trypsin-EDTA was added and then incubated for 5 minutes before being deactivated with 5ml of XFM. Cells were transferred to a microcentrifuge and spun at 3000 RCF for 5 minutes. The supernatant was discarded, and cells were resuspended in a known volume of XFM. For cell counting, 20µl of cell suspension and 20 µl of Trypan

blue were combined into an Eppendorf tube before adding 10 μ l to a haemocytometer.

3.1.3 Freezing

Alternative xeno-free freezing mediums were assessed (Appendix 1), however, showed to be sub-optimal compared to FBS. Therefore, future work will involve assessing further alternatives, to fully remove the reliance on FBS.

Cells were first allowed to reach 80% confluency and the protocol for passaging was followed to the point of counting. Cells were then centrifuged at 3000RCF for 5 minutes. The supernatant was discarded and cells were resuspended at a density of 1×10^5 cells/mL in a solution of foetal bovine serum (FBS) and dimethyl sulphoxide (DMSO) at a ratio of 1:10 respectively. Cells were transferred to a Mr Frosty™ Freezing Container and placed at -80°C for 24 hours, before being transferred to -196°C for long-term storage.

3.1.4 Cell Digestion

To produce lysates for ALP activity and DNA assays, cells were digested. For 2D samples, media was removed and the cells were washed twice in PBS. 300 μ l of cell digestion buffer (CDB) (10 vol% CAB (1.5 M Tris-HCL, 1 mM ZnCl₂, 1 mM MgCl₂ in diH₂O) in diH₂O with 1 vol% Triton-X100) was added to the well and incubated for 30 minutes. Wells were then scraped, and the lysates were transferred to 1.5 mL tubes. Lysates were vortexed briefly and refrigerated overnight.

For scaffolds, media was removed, and the scaffolds were washed twice with PBS. 400 μ l of CDB was added to each well and incubated for 30 minutes. Scaffolds and

CDB were then transferred to a 1.5 mL tube and refrigerated overnight. After refrigeration, lysates were stored at -80°C until their use.

For use in assays, lysates underwent a freeze-thaw cycle (-80°C 10 mins, 37°C 15 mins) three times with vortexing for 15 seconds at the end of each cycle. Samples were then centrifuged at 10,000 rpm for 5 minutes.

3.1.5 Resazurin Reduction Assay

As a marker of cell metabolic activity, resazurin assays were carried out. Resazurin assays are based on the reduction of the oxidized blue dye to a pink fluorescent resorufin product within the mitochondria of living cells. The medium was removed, and cells were washed twice using PBS. 1ml of the resazurin solution (90% Hanks Balanced Salt Solution (HBSS), 10% resazurin reagent) was placed in each well incubated away from light at 37°C for 1 hour. 100 µl of each sample was added in triplicate to a 92-well plate before being read at λ_{ex} 540 nm, λ_{em} 590 nm on a Tecan infinite 200-pro fluorescent microplate reader.

3.1.6 DNA quantification

Total DNA was measured using a fluorescent Quant-iT dsDNA high-sensitivity assay kit (Invitrogen, UK). The Quant-iT DNA Assay reagent was diluted 1:200 in the Quant-iT DNA Assay Buffer. 90µl of the working solution was added to a black 96-well plate and 10µl cell lysate was then also added. The 96-well plate was then added to a fluorescent microplate reader (Tecan infinite 200-pro) and was gently shaken for 10 seconds to fully mix lysate and reagent. It was then left for 10 minutes to allow the dsDNA and assay reagent to fully conjugate. After a

further 10 seconds of shaking, the plate was read at $\lambda_{ex}485$ nm and λ_{em} 520. Total DNA was converted to ng DNA/ sample from a standard curve.

3.1.7 Cell Fixing

Cells were fixed in a 3.7 % formaldehyde solution (FA). Cells were washed twice with PBS before being submerged in 300 μ l of FA for 20 minutes in 2D and 30 minutes in 3D. FA was then removed and cells were washed once more with PBS. Cells were then stored in PBS at 4 °C for up to 1 month.

3.1.8 Scanning electron microscopy

Electrospun samples were mounted onto a stub and placed directly into the chamber of a Hitachi TM3030 Plus tabletop scanning electron microscope (SEM). Samples were imaged with a 15kV acceleration.

3.1.9 Fluorescent microscopy

To image cellular orientation and morphology, staining with 4', 6-diamidino-2-phenylindole dihydrochloride (DAPI) and Alexa Fluor™ 488 Phalloidin (Phalloidin) was performed to stain the nucleus and actin respectively. PBS was removed from previously fixed samples and samples were submerged in 0.1 vol/vol% Triton X-100 for 10 min to permeabilise the cells. The samples were washed twice with PBS. DAPI (1 μ g/mL in PBS) was applied for 15 min at room temperature before being removed and washed twice with PBS. Finally, phalloidin (10 μ g/mL in PBS) was added for 30 minutes at room temperature. Once stained samples were imaged using either an Olympus IX73 Inverted fluorescent microscope (Olympus, Japan) or a Zeiss LSM510 Meta confocal microscope (Carl Zeiss AG, Germany).

3.2 Electrospun scaffold cell culture assessment

3.2.1 Sirius Red Staining

Cells were washed twice and then fixed with 3.2 % formaldehyde for 1 h. They were then stained with 1 %(w/v) solution of Sirius Red to saturated picric acid solution for 30 min at room temperature. After removing the Sirius Red solution by aspiration, the cells were rinsed with dH₂O and were then de-stained for 15 minutes with 0.2M NaOH: Methanol at RT on an orbital rocker. The resulting solutions were then placed in triplicate in a 96-well plate and measured for absorbance (Tecan infinite 200-pro) at a wavelength of 405nm.

3.2.2 Direct Red 80

Cells were washed twice and then fixed with formaldehyde for 1 h. They were then stained with 40 mM Alizarin Red S in deionized water (pH = 4.1) for 30 min at room temperature. After removing the Alizarin Red S solution by aspiration, the cells were rinsed with deionised H₂O and subsequently de-stained with 5 % (w/v) in perchloric acid for 15 minutes at RT on an orbital rocker. The resulting solutions were then transferred to a 96-well plate for analysis on a plate reader (Tecan infinite 200-pro) at an absorbance wavelength of 405 nm.

3.2.3 Second Harmonic Generation Imaging

Samples were fixed as described in 3.1.7. Deposited collagen fibres from fixed cultured cells were visualised from second harmonic generation (SHG) images obtained using a Zeiss Axioskop 2 FS MOT upright laser-scanning confocal microscope equipped with a tuneable (700- 1060 nm) Chameleon Ti: sapphire multiphoton laser. SHG emission was collected in the backwards scattering

direction filtered through a primary dichroic (HFT KP650) before entering a descanned LSM 510 Meta detector capable of collecting emissions in narrow 10 nm bandpass filters. All experiments were performed using an excitation wavelength of 940 nm for the imaging of collagen, and 800nm for the imaging of PCL fibres. SHG emissions should be present in the collection window at half the wavelength of the excitation source, so the 10 nm bandpass filter was centred around λ_{em} 474nm and λ_{em} 400 nm for λ_{ex} 940 nm and λ_{ex} 800 nm respectively. The wavelength used for this work was taken from a previously optimised protocol [85]. For all imaging, a 40x 1.3 NA (numerical aperture) oil immersion objective was used. The pinhole was set to maximum at all times and for each set of experiments, conditions were optimised and kept constant in terms of excitation power, detector gain, and scan speeds. Five images per sample were taken on areas chosen at random. Conditions were kept constant for each experimental time point.

3.2.4 Collagen orientation analysis

Images obtained using SHG were subsequently analysed using the open-access imaging software, Fiji[216]. Before analysis, z-stacks were segmented into 5 μm sub-stacks, each made up of 5 separate 1 μm images. These images were converted into a single image using Z-projection, and each 5 μm sub stack was then analysed using the ImageJ plug-in “Directionality”, using Local Gradient Orientation. Each z-stack was also transformed into a single collapsed image for analysis of total signal intensity, using Fiji’s Z-projections function. Signal intensity was measured using Fiji’s Mean Gray Value (MGV) measuring function, using 5 images per sample.

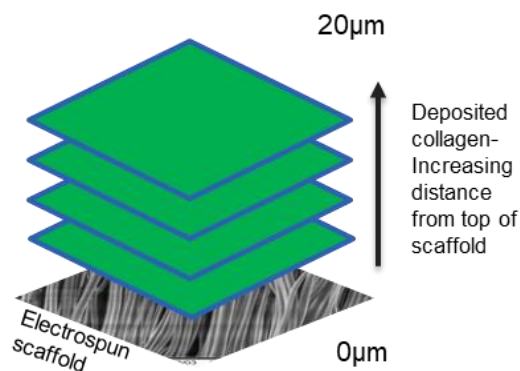


Figure 3-1: Collagen deposited on top of the polymer scaffolds was assessed using second harmonic generation. The polymer scaffold was taken as the point of 0µM

3.2.5 Nuclear analysis

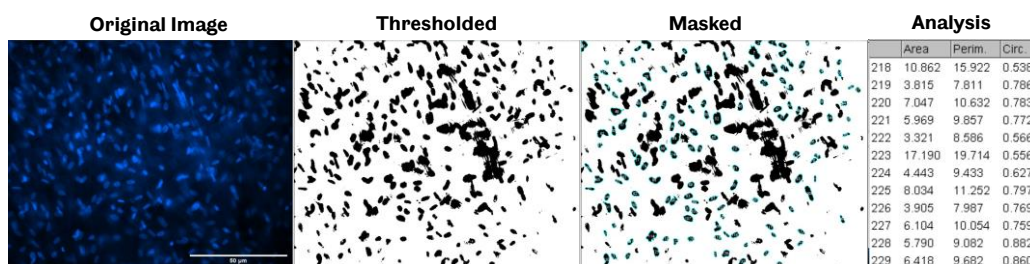


Figure 3-2: Workflow for the analysis of nuclear size and morphology using the image processing software, ImageJ. Thresholded images of DAPI-stained nucleus on either aligned or non-aligned PCL fibres are processed using the “Analyse Particles” tool. At least 400 measurements are taken across 6 separate images for each condition.

Cells were stained with DAPI as described in 2.1.11 and imaged on an inverted fluorescent microscope (Olympus IX73, Japan). Using the Fiji software, images were thresholded to form masks of the nuclei (**Figure 3-2**). Using the tool “Analyse Particles”, measurements of the nuclear area, perimeter and circularity could be obtained. The tool was set to only count in the region of 5-25 µm, to exclude merged nuclei or remaining background noise. A minimum of 400 measurements were taken across 6 images for each condition. The resulting data was then transferred to an Excel document for further analysis.

3.3 PolyHIPE optimisation

3.3.1 Nano silica production method one

The first solution was prepared by mixing distilled 2.8 ml of water, 1.5 ml ammonium hydroxide and 20 ml of ethanol and stirring for 15 min using a magnetic stirrer. The second solution is also prepared by mixing 1.7 ml of TEOS and 5 ml of ethanol in a separate glass. The two solutions were mixed when their temperatures both became 40 degrees and kept at this temperature for 30 min. In the fifth minute of the reaction, 0.6ml of DDS was added to the solution. Finally, silica particles were collected by centrifugation at 4000 rpm for 1 h and then washed with water and ethanol two times. Then the final products were dried at 100 °C for 1 h.

3.3.2 Nano silica production method two

100 ml of ethanol, with 14 ml of distilled water and 6.4 ml of ammonia, were stirred for 15 min before adding 9.4 ml of TEOS. After 90 min from the start of the synthesis, 4.4 ml of DDS was suddenly added into the solution to modify the particles' surface, and the reaction was continued for 2 h. At the end of the reaction, the solution was poured into the test tubes and was centrifuged and washed with ethanol in four consecutive 20 min cycles. Finally, nanoparticles were dried in the oven for 24 h.

3.3.3 Picking emulsion production

PCL was dissolved in either toluene, chloroform or dichloromethane at a concentration of 10% (w/v). m-SiO₂ nanoparticles (HDK H30, Wacker Chemie) were uniformly dispersed into it with ultrasound for 2 min to obtain the oil

phase. m-SiO₂ particles were added at either 3, 5, 8 or 10 %(w/v) with respect to the solvent. Water was added dropwise into the oil phase under agitation. Successful emulsions were placed in a -20 freezer for 24 hours, before being freeze-dried overnight.

3.3.4 Picking emulsion with surfactant production

PCL was dissolved in chloroform at a concentration of 10 %(w/v). m-SiO₂ nanoparticles were uniformly dispersed into it with ultrasound for 2 min to obtain the oil phase. m-SiO₂ particles were added at either 3 or 5 %(w/v) with respect to toluene. Surfactant (Span 80) was then added at either 3, 6 or 9 %(w/v) with respect to the oil phase. Water was added dropwise into the oil phase under agitation, up to a maximum of 2mL. Successful emulsions were placed in a -20 freezer for 24 hours, before being freeze-dried overnight.

3.4 Electrospinning Optimisation

3.4.1 Electrospinning PCL

The polymer solution was created by the dissolution of polycaprolactone (PCL) at M_w of 80 kDa (Sigma Aldrich) in dichloromethane (DCM) at 20 %(w/v). The polymer solution was placed in a 1 ml syringe and mounted into a syringe pump which was set to dispense at 4 ml/hr. A blunt needle was connected to the end of the syringe, with a needle-to-collector distance of 20 cm. To produce the aligned fibres a voltage of 11.5 kV was used, and the speed of the rotating collector was kept at 2000 rpm. For the non-aligned condition, a voltage of 11.5 kV was used and the speed of the rotating collector was 200 rpm. 3ml of the polymer solution was spun and a flat piece of tinfoil was used to collect PCL fibres. Scaffolds were

then placed under a vacuum for 24 hours to allow any remaining solvent to evaporate.

3.4.2 Scaffold surface coating optimisation

Aligned, non-aligned or spin-coated PCL scaffolds were cut to size and fitted into 48-well plate Cell Crown™ trans well inserts (Scaffdex, Finland). The scaffolds in the CellCrown™ inserts were then submerged in 70% ethanol solution for 2 hours. After ethanol treatment, they were washed 3 times with PBS over 24 hours to remove the residual ethanol within the scaffolds (**Figure 3-3**). Scaffolds were allowed to air dry in sterile conditions before surface treatments.



Figure 3-3: CellCrown™ transwell inserts are used to hold PCL fibres.

To investigate the conditions for optimum attachment of h-TERT Y201 cells on electrospun fibres, fibres were treated with either fibronectin (Yo proteins, Sweden) only, plasma treatment only, or fibronectin + plasma treatment. Plasma-treated condition scaffolds were treated with air plasma on both surfaces of the PCL fibres with a power of 50 W and a pressure of 0.8 mbar for 60 seconds. Fibronectin-coated scaffolds were submerged in 200µl of 5µg/mL human fibronectin solution for 1hr before any excess FN was gently aspirated.

Scaffolds were soaked in 100µl of XFM for 1hr before seeding. H-TERT Y201 cells were seeded at a density of 10,000 cells per well, using 100µl of cell suspension

per well. Cells were left to attach for one hour, before the addition of 300 μ l of XFM, to make up a final volume of 500 μ l.

3.4.3 Mechanical Testing

Rectangular-shaped (1cm x 5cm) tensile test samples were cut. Sample thickness was assessed using scanning electron microscopy (Hitachi TM3030 Plus) as described in **section 3.1.8**. Aligned fibres were cut either transversely (fibres normal to the long axis) or longitudinally (fibres parallel to the long axis). Samples were tested when wet to represent cell culture conditions. Samples were tested using MultiTest-dV motorised force tester, Mecmesin, UK, equipped with 10 N load cell for tensile. Both the force and elongation data were recorded. The ultimate tensile strength (UTS) was determined from the maximum force applied divided by the cross-sectional area of the sample. Young's modulus was obtained using the linear-elastic region of each sample's force-displacement curve. Ultimate elongation is the elongation at the failure point.

3.5 Media Optimisation

3.5.1 Y201 hTERT-MSCs media investigations

Two different brands of chemically-defined media, StemMACS MSC expansion kit XF, human (CD1) (Miltenyi Biotech, UK) and Mesenchymal Stem Cell Growth Medium DXF (Promocell, Germany) (CD2), were compared against DMEM for the culture and proliferation of the h-TERT Y201 cell line.

h-TERT Y201 MSCs (Passage 78-80) were resuspended in either CD1, CD2 or DMEM and seeded at 20,000 cells per well in a 24-well plate either coated for 30

minutes with gelatin or left uncoated. Resazurin was carried out on days 1, 3 and 7.

3.6 Gene expression of h-TERT Y201 cells on electrospun fibres

3.6.1 RNA extraction

RNA extraction was attempted using two kits- RNeasy Mini Kit(Qiagen, Germany) and Dynabeads™ mRNA DIRECT™ Purification Kit (Invitrogen, USA) to assess the best method of RNA extraction directly from fibres. RNA extracted using RNeasy also underwent on-column DNase digestion using the RNase-free DNase Set (Qiagen, Germany). All kits were used according to the manufacturer's instructions. RNA content for RNeasy kits was measured using NanoDrop2000, using 1µl of RNA per sample. RNA was stored in aliquots at -80°C for up to 3 months.

3.6.2 cDNA synthesis

cDNA conversion was carried out on the previously extracted RNA using the Omniscript® Reverse Transcription Kit (Qiagen, Germany) as per manufacturers' instructions. Oligo(dT)₁₂₋₁₈ Primer (Invitrogen, USA) and RNase Inhibitor (Applied Biosystems, USA) were not supplied and purchased separately. Reverse transcription components were added to a 0.1mL Eppendorf as stated in Error! Reference source not found., and then incubated at 37°C in an Applied Biosystems™ Veriti™ Thermal Cycler, 96-Well for 1 hour. The resulting cDNA was then stored at -20°C. All primers had FAM-MGB as the reporter dye. Probes were chosen to span an exon junction to minimise the detection of genomic DNA. Primer IDs are listed in **Table 7**.

Experiments were automatically thresholded by the StepOnePlus™ Real-Time PCR System software, and results were deemed acceptable if the Ct values were within 0.5 cycles within their triplicates. Relative-fold changes were analysed using the $2^{-\Delta\Delta Ct}$ method where data is log transformed.

Table 5: Summary of all components required for qPCR. The reaction is carried out in a MicroAmp™ Fast Optical 96-Well Reaction Plate with a final reaction volume of 20µL

Component	Volume per reaction (µL)
qPCRBIO Probe Mix Lo-ROX (2X) (PCR Biosystems, UK) (<i>Master Mix</i>)	10
TaqMan™ Gene Expression Assay (20X)	1
Nuclease-free water	8
Template cDNA	1
Total reaction volume	20

Table 6: Thermal protocol for StepOnePlus™ thermocycler. Protocol specified by PCR Biosystems for amplification under fast-cycling systems.

Step	Temperature (°C)	Time (s)	Cycles
Enzyme Activation	95	120	1
Denature	95	5	40
Anneal/Extend	60	20	

Table 7: Primer assay IDs of all qPCR primers used. Primers purchased from ThermoFisher consist of a pair of unlabeled forward and reverse PCR primers, a TaqMan probe with a dye label on the 5' end and a minor groove binder (MGB) and non-fluorescent quencher (NFQ) on the 3' end. All primers have been validated within the literature.

Primers		
Gene symbol	Gene Name	Assay ID
GAPDH	GAPDH	Hs02758991_g1[217]
YAP1	YAP	Hs00371735_m1[218]
RhoA	RhoA	Hs00357608_m1[219]
RUNX2	RUNX2	Hs01047973_m1[220]
SPP1	Osteopontin	Hs00959010_m1[220]
BGLAP	Osteocalcin	Hs01587814_g1[221]

3.7 GelMA/3PCLMA Emulsions

3.7.1 Cell culture

The human osteosarcoma cell line MG63 (European Collection of Authenticated Cell Cultures, United Kingdom) was used to assess the toxicity of cells within the gelMA/3PCLMA emulsions. MG63 cells were cultured in Dulbecco's Modified Eagle Medium (DMEM) with GlutaMAX™, and supplemented in 10% foetal bovine serum, 100 µg/mL penicillin, and 100 µg/mL streptomycin. Media was changed every 2-3 days and passaging was carried out at 80% confluency. Passage and cryopreservation were carried out as described previously.

3.7.2 Gelatin methacrylate Synthesis

Fish gelatin was mixed at 10% (w/v) into sterile PBS at 50°C and stirred at 240 RPM until fully dissolved. 5% (v/v) methacrylic anhydride was added dropwise and then left to stir for a further 2hrs at 50°C. The addition of 1X the total reaction volume of fresh PBS was then added and allowed to mix for a further 10 minutes to stop the reaction. The mixture was dialyzed against distilled water using 12-14 kDa cut-off dialysis tubing for 1 week at 50°C to remove salts and methacrylic acid. dH2O was then added and the solution was heated for a further 15 minutes at 40°C. Finally, the solution was filtered using a 0.22µM filter and the solution was lyophilized for 1 week to generate a white porous foam and stored at -80°C until further use

3.7.3 Emulsion Development

To form the polymer phase, polyethylene oxide (PEO) was added to 3PCLMA at a (w/w)% of either 3, 4, 5, 6%. Hydroxyapatite (HAp) was also added 3PCLMA at 0,

1, 5 and 10(w/w)% and dispersed evenly using a UP100H Ultrasonic processor (Hielscher Ultrasonics, Germany).

To form the aqueous phase, GelMA and alginate were dissolved in PBS to a 5(w/w)% and 3(w/w)% respectively at 37°C under continuous agitation. Diphenyl(2,4,6-trimethylbenzoyl)phosphine oxide (TPO) and Lithium phenyl (2,4,6-trimethylbenzoyl) phosphinate (LAP) were added to the polymer phase and aqueous phase respectively at 0.05(w/w)%.

The aqueous phase was slowly added dropwise to the polymer phase under continuous shear until the solution had turned from clear to a white, viscous emulsion. Emulsions with aqueous phases of 40, 50, 60, 70 and 80 %(v/v) with respect to the polymer phase were made.

3.7.4 Mechanical Testing

Rectangular 1cm x 5cm shaped tensile test samples were fabricated and cured for 20 seconds on each side. Sample thickness was assessed per sample using callipers. Samples were tested when wet to represent cell culture conditions. Samples were tested using Instron 5943 mechanical testing machine (Norwood, USA) equipped with a 100N load cell for tensile and 100kN for compression. Both the force and elongation data were recorded. The ultimate tensile strength (UTS) was determined from the maximum force applied divided by the cross-sectional area of the sample. Using the linear-elastic region of each sample's force-displacement curve. Ultimate elongation is the elongation at the failure point.

3.1.5 Cell toxicity

MG63 cells were seeded on top of scaffolds post-fabrication, to assess whether the poor survival was occurring through the encapsulation process itself, or the elution of toxic components in the scaffold into the media. MG63 cells were seeded and allowed to grow to 60% confluency. 70% GelMA/PCLMA cured inks were added on top and scaffolds were then either subjected to 5, 2 or no extra PBS washes before fresh DMEM was added and cells were returned to culture. Resazurin was carried out on days 1, 3 and 7 to assess the effects of the scaffolds on the growth rate, inferred from metabolic activity, of the MG63 cells

3.7.5 UV Irradiation

MG63 cells were resuspended in 1mL of media, and exposed to 2.7 mW/cm² of UVA for either 15, 30, 45, 60 or 120 seconds using an OmniCure Series 1000 curing system (100 W, Lumen Dynamics, Canada). UVA was applied to cells in a 6-well plate, with the lid on. The resulting doses (mJ/cm²) the cells received are summarised in table X, where (mJ/cm²) = exposure time (s) × irradiance (mW/cm²). UVA was measured using a UV Power Puck II (Eit Inc. Sterling, VA, USA)

Table 8: Respective UVA doses received by MG63 cells with increasing time exposure

Time (s)	Dose (mJ/cm ²)
15	41.55
30	83.22
45	124.83
60	166.44
120	332.88

3.7.6 Toxicity Testing

MG63 cells were seeded at a density of 1×10^4 in a 48-well plate and allowed to reach confluency. Once confluent, pre-made discs ($r=1\text{cm}$) of either 5% gelMA/ 3% alginate, pure 3PCLMA, or a 60% aqueous phase emulsion were placed on top. Cell metabolic activity was assessed on days 1, 3 and 7 using a resazurin reduction assay.

3.7.7 Encapsulation

Emulsions were formed as described in 2.7.2. MG63 cells were resuspended in pure FBS at a concentration of 1×10^6 cells per $50\mu\text{L}$. Cells were then gently mixed into the emulsions or pure gelMA at a density of 1×10^6 /mL of gelMA. Emulsions or pure gelMA were added into polydimethylsiloxane (PDMS)moulds ($r=1\text{cm}$) and placed in a glass petri-dish and cured under UV light for 30 seconds (OmniCure Series 1000 curing system (100 W, Lumen Dynamics, Canada)), before being transferred to a 48-well plate with DMEM with GlutaMAX + 10% FBS + 1% PS (**Figure 3-4**). Emulsions were maintained for 3 days, and resazurin was carried out at 1hr, day 1 and day 3.

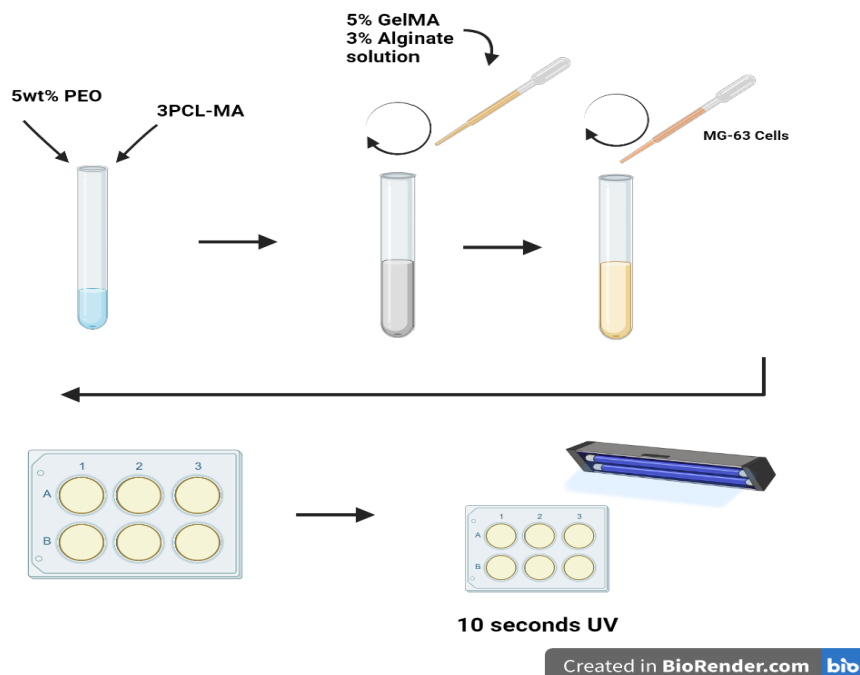


Figure 3-4: General workflow for the production of emulsions and subsequent encapsulation of MG63 cells. Figure created using BioRender.com

3.8 Statistical Analysis

Statistical analysis was carried out using either a students' T-test, one-way and two-way analysis of variance (ANOVA) where appropriate, using the statistical analysis software, GraphPad Prism, Version 7.04 for Windows (CA, USA). All data was considered unpaired. To ensure all data were normally distributed, a Shapiro-Wilk normality test was performed prior to testing. In cases where data was non-normally distributed, a non-parametric alternative was used and is described in figure caption. n values for each experiment are given in figure captions and refer to the number of biological replicates. Significance is taken at $p < 0.05$ in all cases with exact significant p values given in figure captions. Error bars indicate standard deviations in the graphs.

4 Development of Aligned and Non-Aligned Fibres for Use in Xeno-Free Osteogenic Culture of MSCs

4.1 Introduction

For this project, the material of choice as a substrate for modelling cortical bone was PCL electrospun fibres. PCL was selected, due to it being already widely characterised and used within our research group and by many others in the field of bone tissue engineering. As discussed within the literature review, it has previously been shown to support the culture of many cell types, and osteogenic differentiation, as well as being cost-effective and widely commercially available.

Electrospinning is a notoriously delicate process, that can be significantly affected by many parameters both controllable by the user (Voltage, needle gauge, material viscosity etc), and those more difficult to control in a typical academic setting (Room temperature, airflow, humidity). Although these “uncontrollable” parameters may be possible to control with commercially available electrospinning environmental chambers, these are generally extremely costly, with other limitations, such as an inability to quickly unclog a blocked needle, and restrictions in the available space for the configuration of the apparatus. Therefore, it is important to optimise electrospinning conditions for each specific set-up.

As PCL is a highly hydrophobic material, it may be necessary to carry out surface modifications, to try and increase the hydrophilicity of the material. With a

hydrophobic material, cell attachment, spreading and proliferation is inhibited, due to an inability to form strong attachment ligands to the material's surface [222]. Furthermore, the interaction of cells with the material surface plays a crucial role in the modulation of cellular behaviour, particularly in the case of differentiation of MSCs[9], [149], [223]–[227]. The use of plasma coating is a popular method for surface modification of biomaterials.

This project also intended to be carried out in the absence of FBS, so xenofree media was examined as an alternative. With the removal of FBS from *in vitro* models, the causation of any observable phenomena or effects of testing drugs can be more accurately obtained, due to the minimisation of unknown interacting factors that may be present in the FBS, as well as batch-to-batch variability. Finally, moving away from the use of FBS is of ethical concern, due to the source from which FBS is obtained, and discussed in more detail within the literature review. Optimisation of ascorbate supplementation was also examined within the xenofree media, to ensure that our cell line of choice, hTERT Y201, was able to produce sufficient amounts of collagen, for later analysis in Chapter 4.

4.2 Aims and Objectives

This chapter aims to optimise a method for the production of aligned and non-aligned electrospun PCL fibres of similar fibre diameters.

In this study, PCL dissolved in dichloromethane at 15 (w/v) % was examined and spun at various voltages to alter the fibre alignment and fibre widths. The wettability and mechanical properties were also investigated, to produce a

material that may act as a substrate for the culture of MSCs and facilitate their differentiation to osteoblasts.

Chapter-specific objectives:

- Determine the best parameters for electrospinning of both aligned and non-aligned PCL fibres.
- Characterise the material properties of the produced fibre mats.
- Optimise media composition to support collagen deposition.
- Determine the metabolic activity of cells on scaffolds and optimise cell seeding protocol

4.3 Experimental Design

15 % (W/W) solutions of PCL fibres were spun at a variety of voltages. The other main electrospinning parameters (tip-to-collector distance and solution flow rate) were maintained constant throughout as these have previously been characterised by past members of the Reilly group [61], [64].

Resulting aligned and non-aligned electrospun scaffolds were then secured into “CellCrown™” trans-well inserts in order for cell culture of the hTERT-Y201 cell line to be carried out. Scaffolds were assessed for their ability to support attachment and proliferation of cells with the use of resazurin reduction metabolic activity assays, under different media types and compositions. This was carried out, in order to ensure the best conditions for growth and matrix deposition for the later studies on collagen orientation in Chapter 5.

4.4 Results

4.4.1 Electrospinning voltage effects

Under all conditions reported, it was possible for fibre formation with distinctive, bead-free fibres. Below 10 kV it was not possible to form a continuous jet, and above 15 kV the jet became unstable and tended towards spraying.

Spinning at 2000 RPM, at all voltages examined, resulted in a much higher degree of alignment compared to when spun at 200 RPM (**Figure 4-1**).

The distribution of fibre alignment was assessed using the Fiji Plug-In “Directionality”, to quantitatively assess fibre alignment. In **Figure 4-2**, spinning at 2000 RPM resulted in a more aligned fibre construct, noted by the distinct

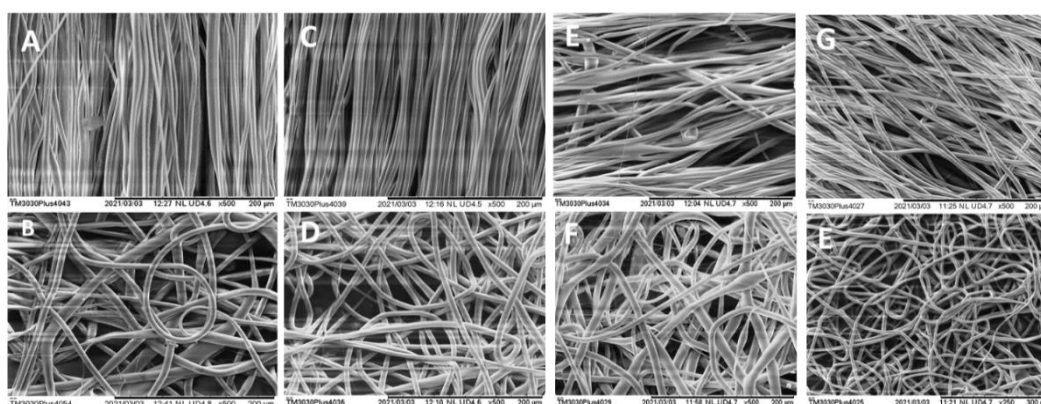


Figure 4-1: SEM images of aligned and non-aligned electrospun PCL fibres. **A)** 10kV, 2000RPM **B)** 10kV, 200RPM **C)** 11.5kV, 2000RPM **D)** 11.5kV, 200RPM **E)** 13kV, 2000RPM **F)** 13kV, 200RPM **G)** 15kV, 2000RPM **H)** 15kV, 200RPM. Scale bar = 200 μ m

peak on the histogram. By increasing voltage above 11.5 kV, a wider peak is observed, showing a decrease in alignment. In fibre mats produced by using a collecting drum speed of 200 RPM, there are no single distinguishable peaks, due to a much wider distribution of fibre direction.

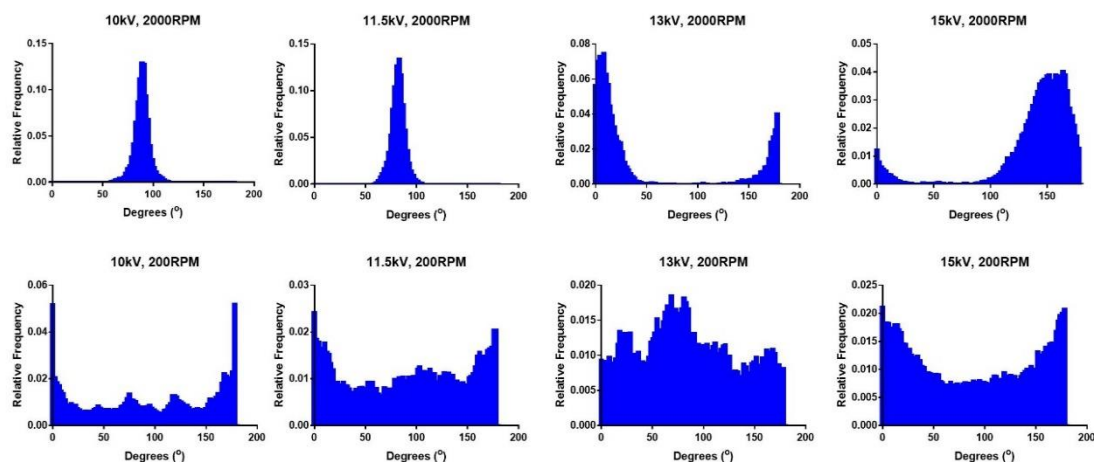


Figure 4-2: Histograms showing the relative frequency distribution of fibre alignment of fibres spun at 10, 11.5, 13 or 15kV, and 2000 or 200RPM, as measured using the Directionality plug in from Fiji. 2000RPM spinning resulted in a more aligned fibre construct, as noted by the distinct peak on the histogram, whilst 200RPM produced non-aligned constructs, with a wide distribution of fibres.

There did not appear to be any clear voltage-dependent trends in fibre width or fibre width distribution, in both aligned and non-aligned conditions (**Figure 4-3**). It was seen, however, that the largest fibre widths and width distribution were seen for 13 kV, in both conditions (**Table 9**). In all voltage conditions, it was seen that aligned fibres did have a smaller average diameter than the non-aligned fibres that were spun at the same voltage.

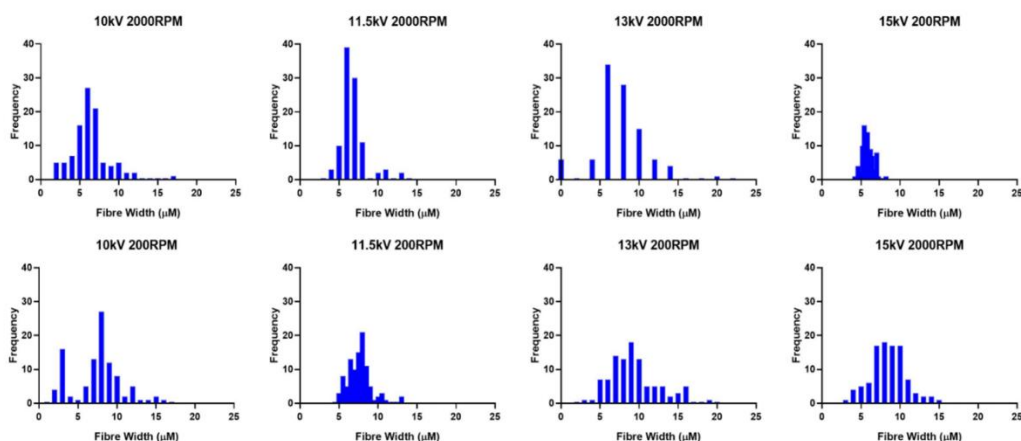


Figure 4-3 Histograms representing the distribution of fibre diameters of electrospun PCL fibres, as measured using ImageJ. Histogram represents the measurements of 100 randomly chosen fibres across 3 separate images for each condition.

Table 9: Average diameters of electrospun PCL fibres. Measured from the average of 100 fibres across 3 images for each electrospinning condition. Showing mean \pm SD

Voltage (kV)	Non-aligned mean width (μm)	Aligned mean width (μm)
10	7.61 ± 3.17	6.29 ± 2.29
11.5	7.5 ± 1.48	6.73 ± 1.57
13	9.24 ± 3.17	7.37 ± 3.18
15	8.5 ± 2.25	5.79 ± 0.85

All fibres showed what appeared to be micro/nanopores across the surfaces of the fibres (**Figure 4-4**) Due to the good parallel alignment of the 11.5 kV condition, this was the voltage used for all future experiments.

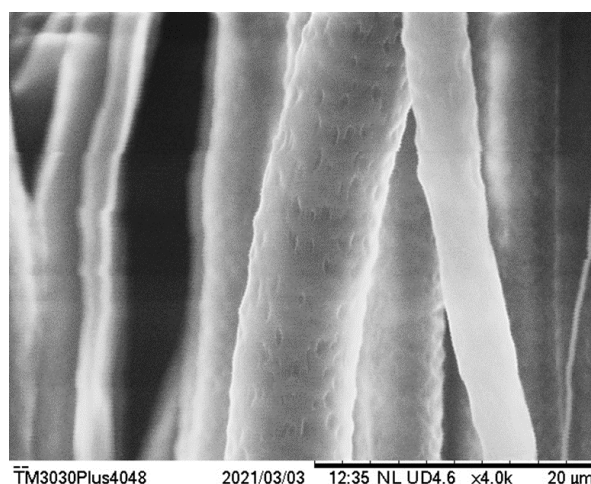


Figure 4-4: SEM image of visible nanopores formed on the surface of a fibre produced at 2000RPM and 11.5kV. Scale bar represents 20 μm .

4.4.2 Plasma Coating

With air plasma coating, the scaffolds' surface wettability was successfully increased. The contact angle pre-treatment was $123.20^{\circ} \pm 9.48$ and $120.29^{\circ} \pm 9.34$ for non-aligned and aligned respectively. After a 60-second treatment with atmospheric plasma, the surface was fully wettable (**Figure 4-5**).

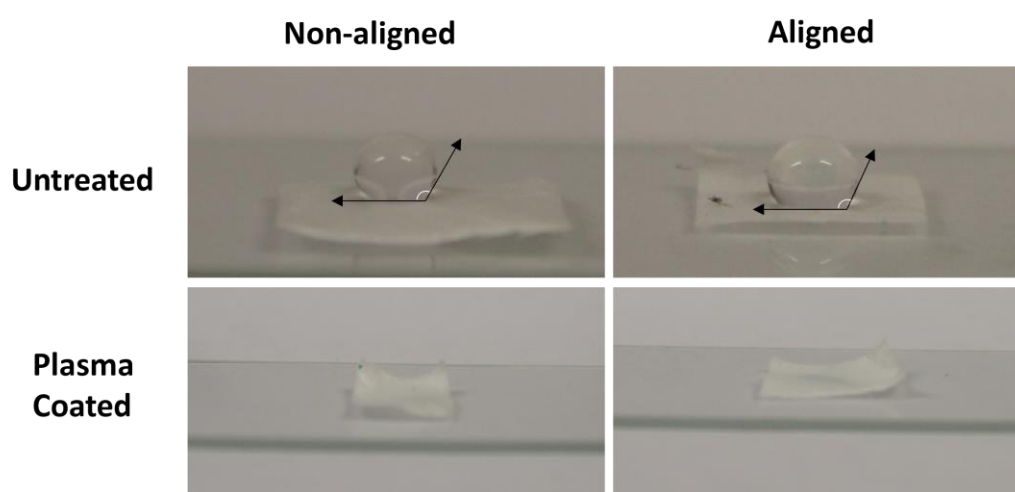


Figure 4-5: Digital images of contact angle testing of aligned and non-aligned fibres before and after treating with air plasma at 0.8mBar, 50V for 60 seconds. It can be seen that for both aligned and non-aligned fibres that hydrophobicity is greatly reduced, allowing the fibres to become fully wettable

4.4.3 Mechanical testing

Mechanical tensile testing was carried out on aligned and non-aligned samples spun at 11.5 kV. For the aligned samples, the force was applied in either the longitudinal or transverse direction of the aligned scaffolds.

Aligned scaffolds, strained in the longitudinal direction showed to be ~5-fold stiffer than non-aligned, but non-aligned showing to be significantly stiffer when compared to aligned fibres strained in the transverse direction, with Young's modulus' of 1.67 ± 0.1 MPa and 0.176 ± 0.17 MPa respectively (**Figure 4-6 A**). UTS showed a similar pattern, but with only a 2.5-fold higher UTS in the longitudinal direction compared to that of the non-aligned fibres, and <2-fold higher UTS on

the non-aligned fibres compared to the transversely strained aligned fibres. (Figure 4-6 B).

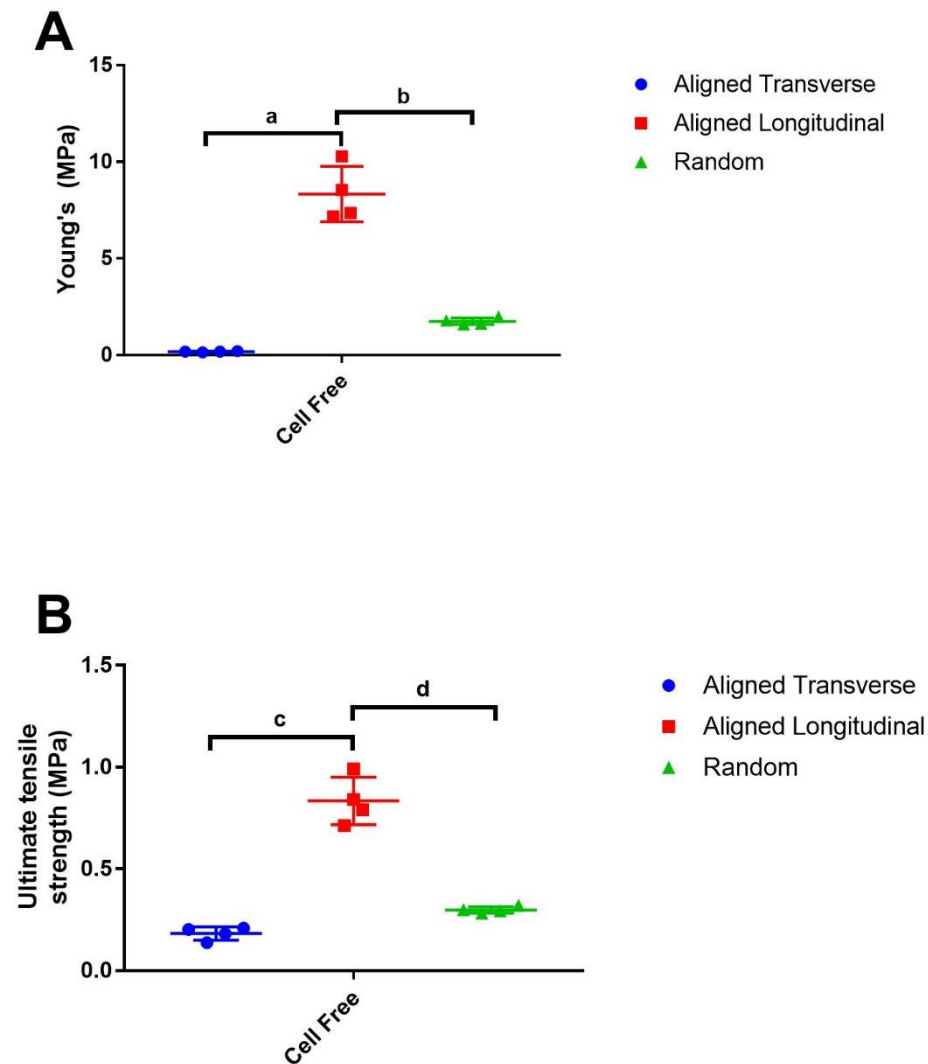


Figure 4-6: Young's modulus (A) and ultimate tensile strength (UTS) (B) measured for aligned and non-aligned fibres. Aligned fibres were tested in both the transverse and longitudinal orientations. Results are shown as mean \pm SD. Tested using one-way ANOVA with Tukey's *post-hoc* for multiple comparisons. $n=4$. Significant p values are reported as $a<0.0001$ $b<0.0001$ $c<0.0001$ $d=0.0001$

4.4.4 Basal media testing

Various cell culture media were investigated, to confirm the metabolic activity of the h-TERT Y201 cell line in the absence of FBS. Two types of commercially available chemically defined medium were investigated and compared to the

standard culture medium of this cell line, DMEM supplemented with 10% FBS. The addition of gelatin coating of T-Flasks compared to direct seeding onto the tissue culture plastic (TCP) was also assessed.

Culture medium experiments showed a significant increase in cell metabolic activity, with the use of CD1 medium (StemMACS™ MSC Expansion Media Kit XF) (**Figure 4-7**). There were no significant differences in the metabolic activity of the cells in culture when coated with gelatin or seeded directly onto the TCP of the well plate. Conversely, cells cultured in the CD2 medium (Mesenchymal Stem Cell Growth Medium DXF) showed a significant decrease in their metabolic activity when compared to the DMEM supplemented with 10 % FBS.

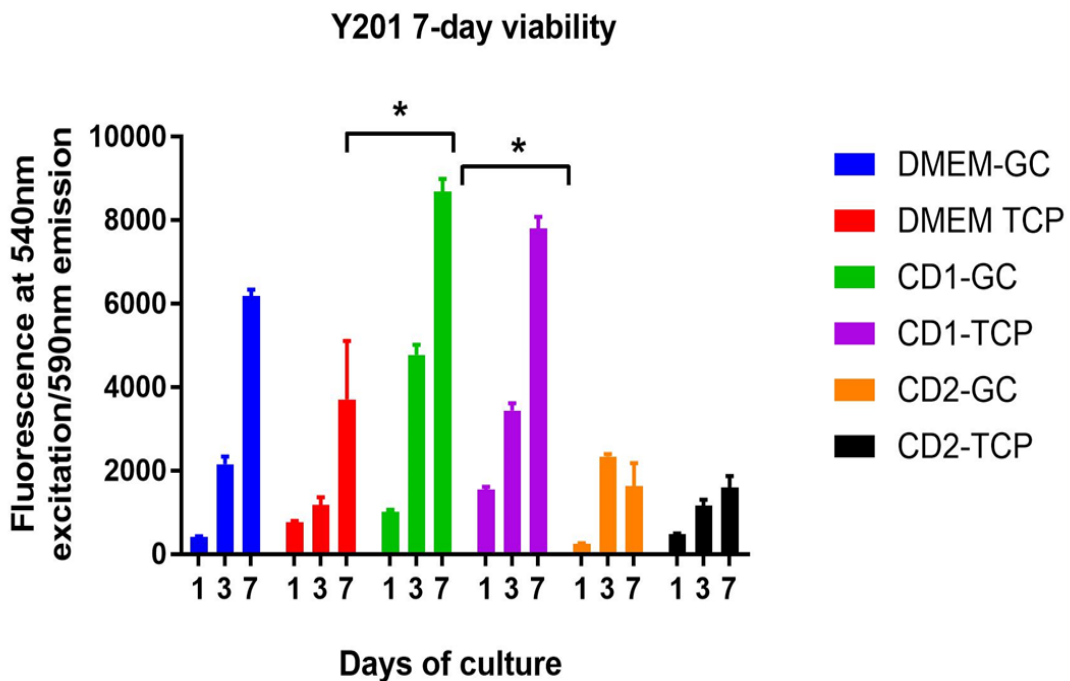


Figure 4-7: 7 day metabolic activity, inferred from metabolic activity of h-TERT Y201 cells seeded on TCP and cultured in either DMEM, StemMACs XFM or CD2, and either coated with gelatin or seeded directly onto the TCP. CD1 shows the highest metabolic activity of the cells in both gelatin coated or TCP conditions. Tested using two-way ANOVA Tukey's *post-hoc* test for multiple comparisons with Results are shown as mean \pm SD. n=6 * = <0.0001

4.4.5 Osteogenic media supplementation

The effects of AA2P, Dexamethasone and fibronectin coating on the collagen production of 2D h-TERT y201 cells were investigated to optimise the composition of supplements within the osteogenic medium. This optimisation aimed to maximise collagen deposition.

Neither dexamethasone nor any concentration of AA2P were shown to have a significant effect on the metabolic activity of the h-TERT Y201 cells, with day 21 resazurin absorbance showing no differences between any condition (**Error! Reference source not found.**).

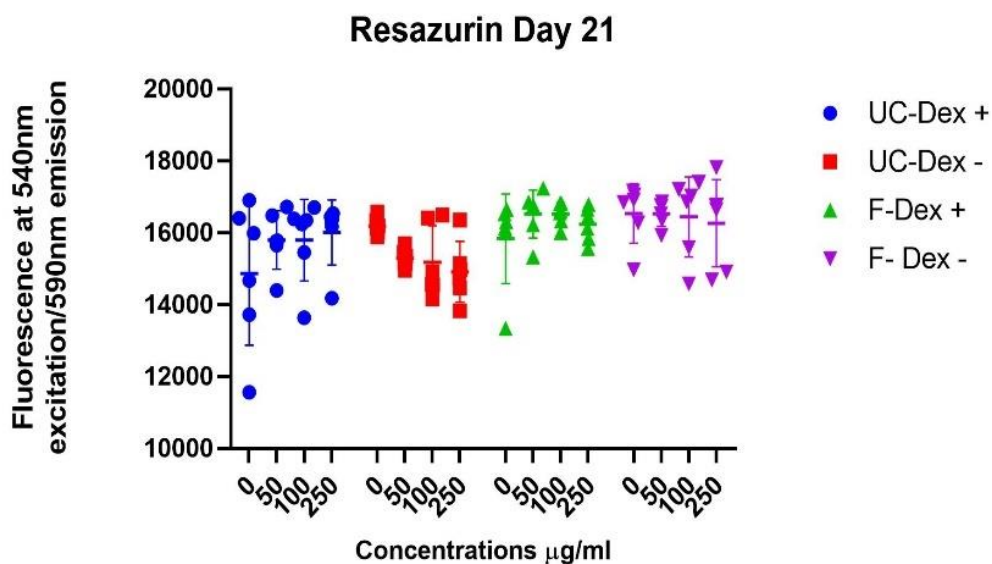


Figure 4-8: Resazurin reduction for assessment of metabolic activity of Y201 cells at day 21 of culture in varying concentrations of AA2P and in presence or absence of dexamethasone. Results shown as mean \pm SD (n=6). Tested using Kruskal-Wallis test with Dunn's multiple comparisons. Results shown as mean \pm SD.

Sirius Red Staining did show that fibronectin was able to significantly increase collagen production compared to no surface coating, in both + and - Dex conditions ($p < 0.0001$ for both conditions). The use of dexamethasone also significantly affected collagen production for both fibronectin and uncoated conditions ($p = 0.0235$ and $p = 0.0414$ respectively), with lower SRS staining observed in the presence of dexamethasone. Increasing the concentration of

AA2P does not have a significant effect on the amount of collagen, up until 250 $\mu\text{g}/\text{mL}$, where a significant reduction in collagen production was observed in the fibronectin Dex- condition ($p=0.0329$) (**Figure 4-9**). For mineral production, ARS showed that 250 $\mu\text{g}/\text{mL}$ supported lower mineral production in uncoated samples but no significant difference in mineral deposition observed with supplementation with dexamethasone. (**Figure 4-10**).

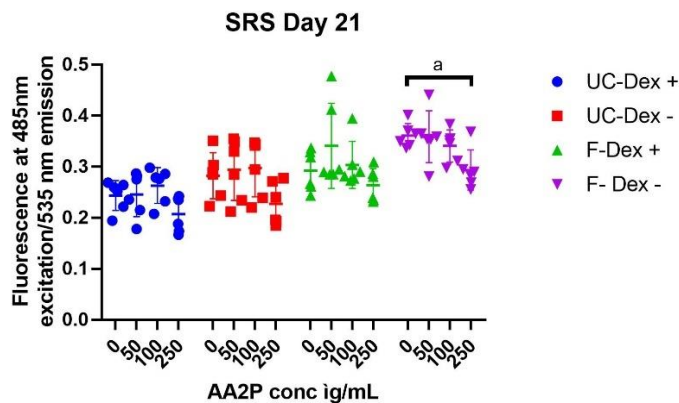


Figure 4-9: Sirius Red Staining for collagen deposition of Y201 cells at day 21 of culture in varying concentrations of AA2P and in presence or absence of dexamethasone. Results shown as mean \pm SD ($n=6$). Tested using a two-way ANOVA with Tukey's *post-hoc* test for multiple comparisons. Significant p number shown as $a=0.0329$

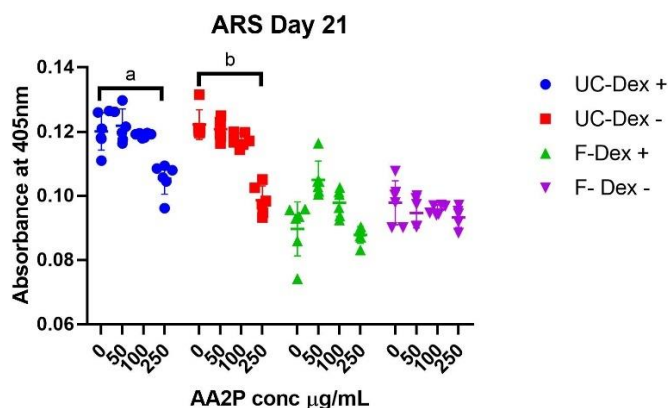


Figure 4-10: Alizarin red staining for mineral deposition of Y201 cells at day 21 of culture in varying concentrations of AA2P and in presence or absence of dexamethasone. Results shown as mean \pm SD ($n=6$). Tested using Kruskal-Wallis test with Dunn's multiple comparisons. Results shown as mean \pm SD. Significant p values shown as $a=0.0105$ and $b=0.008$.

4.4.6 Scaffold seeding optimisation.

Scaffolds were seeded with 0.5×10^4 , 1×10^4 or 2×10^4 cells per scaffold ($\sim 0.86 \times 10^4$ cells/cm², 1.7×10^4 cells/cm² and 3.4×10^4 cells/cm² respectively). The surface treatments fibronectin only, plasma + fibronectin and plasma only were compared to determine the effects of various coatings on metabolic activity. Due to the high hydrophobicity of PCL, cells are known to have very little attachment directly to the fibres without any form of surface treatment. Due to a limited number of CellCrown™ inserts available for each condition, the “No surface treatment” condition was excluded in all future experiments.

For all conditions, there appeared to be no significant difference after day 1 in cell metabolic activity regardless of cell number (**Figure 4-11**). In a few cases, there was a decrease in metabolic activity after day 14, which may suggest that cells are detaching over time, which can occur when cells over-proliferate. However, there is also a large variability in the results, making thorough analysis difficult. It was suspected that this variability may be due to the mild toxicity of resazurin, and PBS washing being insufficient to fully remove the excess salts from the scaffolds. Although resazurin is considered a non-toxic assay, there is some evidence that repeated assays over longer culture periods may have some cytotoxic effects, with different cell lines having different tolerances for the assay [222]. Alternatively, if the h-TERT Y201 cells do not have a very strong attachment to the fibres, they may simply be detaching from the repeated washing and aspiration steps. For future experiments resazurin reduction assays were only carried out on the final day of culture, to minimise interference during culture.

Media changes were also only carried out every 7 days, rather than every 3 days as this has been shown by other members within the Reilly research group to be optimum for the h-TERT Y201 cells. Due to the large variability seen in this experiment, it was not possible to conclude the best method for surface modifications from these results alone.

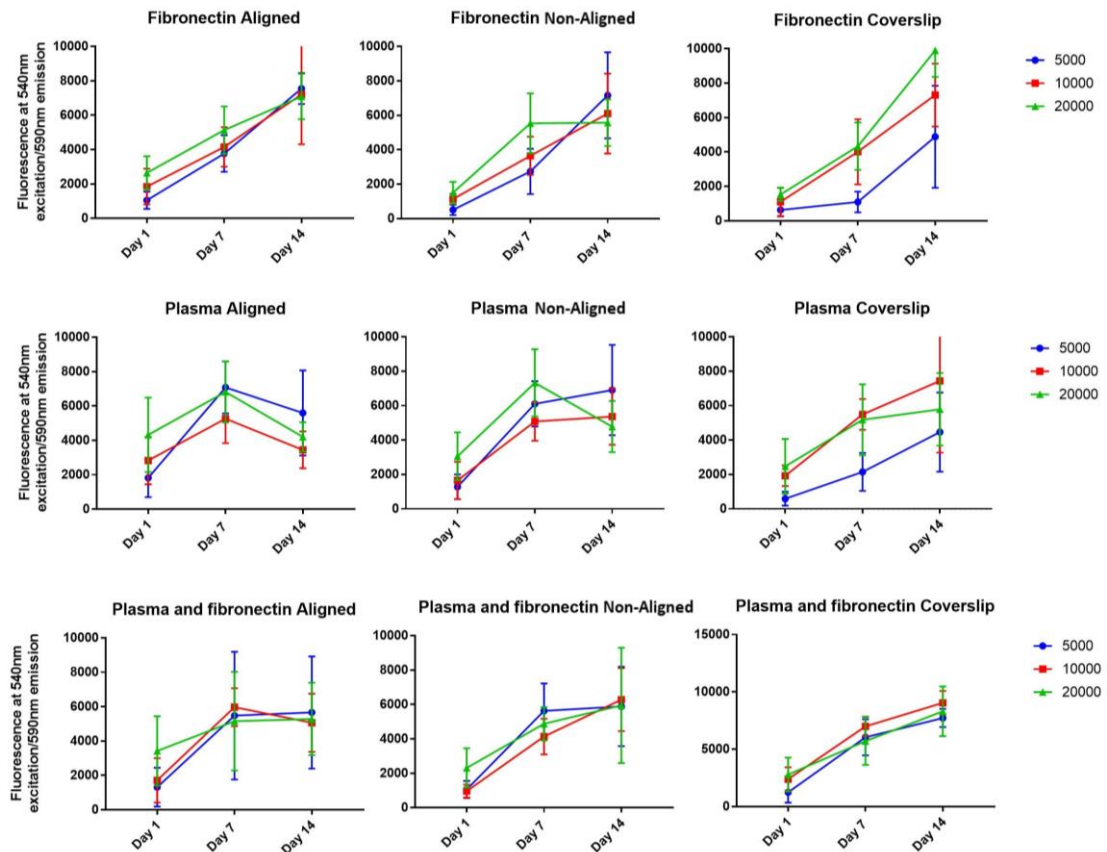


Figure 4-11: Resazurin reduction of Y201 cells cultured at a density of either 0.5×10^4 , 1×10^4 or 2×10^4 cells per scaffold. **A)** Fibronectin coated aligned fibres, **B)** Fibronectin coated non-aligned fibres **C)** Fibronectin coated coverslips **D)** Plasma coated aligned fibres **E)** Plasma coated non-aligned fibres **F)** Plasma coated coverslips **G)** Plasma + fibronectin coated aligned fibres **H)** Plasma + fibronectin coated non-aligned fibres and **I)** Plasma + fibronectin coated coverslips. Measured at days 1, 7 and 14. Results shown as mean \pm SD. n=4

Instead, resazurin was alternatively carried out on day 7 only, to investigate the cell metabolic activity without repeated resazurin reduction assays. From this study, there was a significantly higher attachment to the aligned fibres with compared to the non-aligned and coverslips ($p < 0.0001$ and $p = 0.0041$ respectively). Metabolic activity was also seen to be significantly higher in

plasma + fibronectin-coated conditions compared to fibronectin only (**Figure 4-12**).

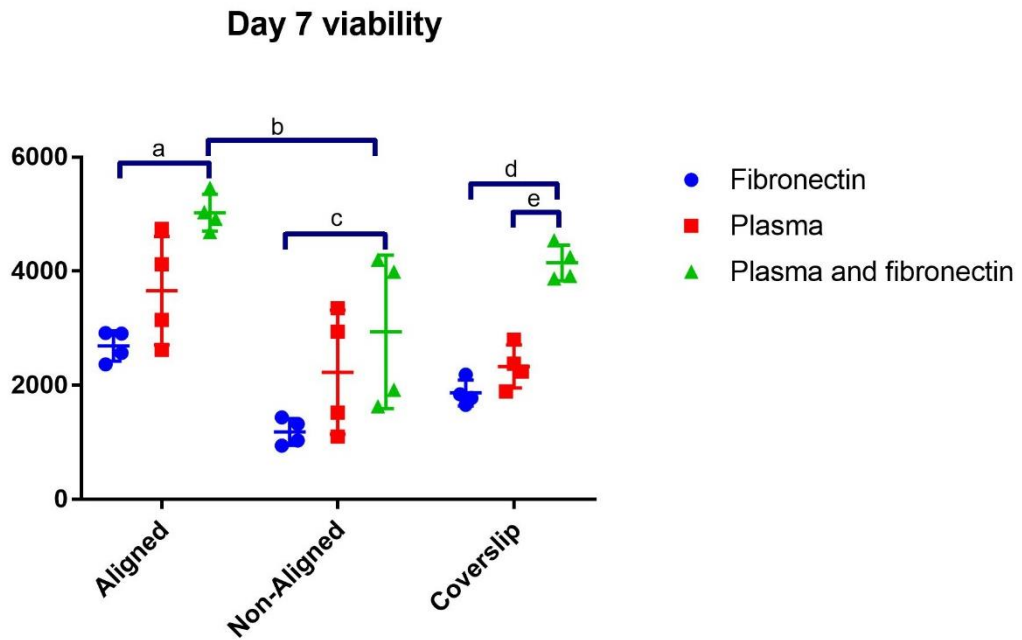


Figure 4-12: Resazurin reduction of h-TERT Y201 cells cultured at a density of 1×10^4 cells on either PCL-aligned, non-aligned scaffolds or spin-coated coverslips scaffolds after 7 days of culture. Scaffolds were treated with either fibronectin, air plasma or plasma + fibronectin. Results are shown as mean \pm SD. $n=4$. Statistically tested using a two-way ANOVA with Dunn's *post-hoc* test for multiple comparisons. Statistically significant p values are represented as a=0.0018 b=0.0066 c=0.0338 d=0.0025 e=0.0251

4.4.7 Surface functionalisation and coating

Scaffolds were then cultured for 14 days, with the addition of 50 $\mu\text{g}/\text{mL}$ AA2P. After 14 days cells were stained with SRS for collagen and imaged using SHG intensity (**Figure 4-13**). In both plasma only and fibronectin and plasma, collagen deposition was even across the surface of the PCL fibres (**Figure 4-13 A-B**). On the aligned scaffolds, SHG intensity showed the collagen fibres were aligned along the axis of the PCL fibres. Alternatively, for fibronectin-only scaffolds, the collagen grew in circular nodules on both aligned and random scaffolds (**Figure 4-13 C**). Similarly, in SHG images, the signal from the collagen appeared to be from rounded nodules.

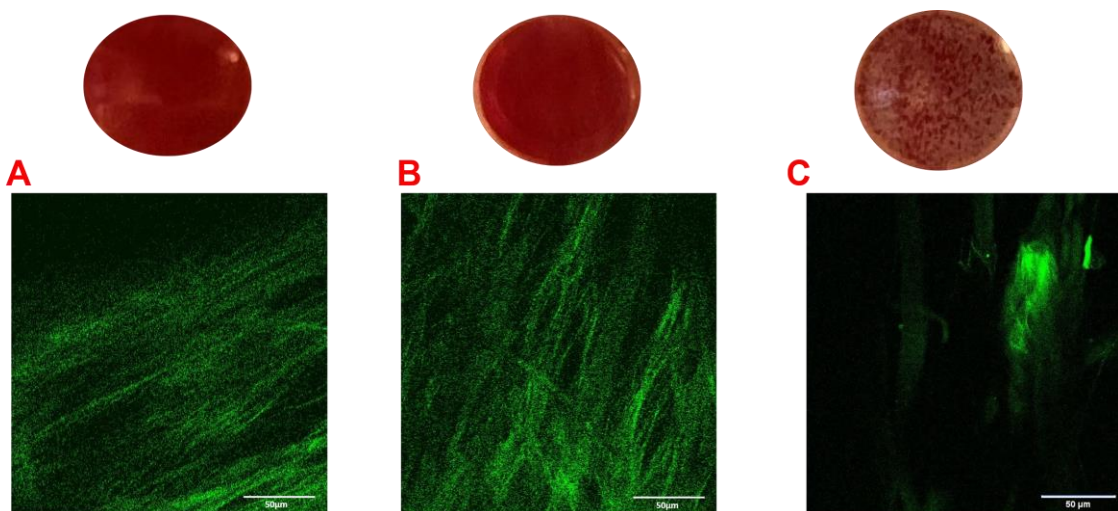


Figure 4-13: Sirius red staining (Top) and SHG imaging (bottom) of collagen after 14 days culture on aligned scaffolds. A) Plasma treatment only, B) Plasma + FN C) FN only. Scale bar = 50 μM

4.5 Discussion

4.5.1 Fibre fabrication

Electrospinning is an effective method for the development of nano- and micro-fibres with tuneable properties. However, the process is highly variable with many parameters that even with small variations can result in dramatically different results. By simply varying the voltage by small amounts, significant differences in fibre diameter, morphology and alignment is notable, further highlighting the sensitivity of this method.

Paskiabi *et al* spun aligned PCL/PGA nanofibrous scaffolds and found that interactions between high drum speeds and high voltages may interfere with one another, by where the high drum speeds stretch nanofibers uniaxially, the high levels of voltage divert nanofibers from their main axis and reduce their alignment [222]. However, the results of electrospinning are widely influenced by many other parameters, including solution viscosity, solvent properties, drum speed, temperature, tip-to-collector distance, ambient humidity, extrusion rate and many more. Therefore, it is difficult to explain the exact mechanisms behind each result as it is highly variable from laboratory to laboratory.

No fibres showed perfect alignment, despite the high RPM of the collecting drum. This lack of perfect alignment may be explained by residual charge within the individual fibres, causing a slight repulsion of the fibres being deposited on top. This also limits the overall possible thickness of the mats, as there is a gradual decrease in overall alignment with an increase in mat thickness. A non-perfect alignment may, however, be beneficial, as the overlapping fibres may contribute

towards the overall structural integrity of the scaffolds, reinforcing them in the transverse direction and preventing delamination of fibres.

All fibres showed what appeared to be nano-pores across the surfaces of the fibres. Nano-pores have been observed frequently within electrospinning [61], [228]–[230] It is theorised that the presence of nano pores are likely due to high solvent volatility. As DCM is extremely volatile, it begins to evaporate rapidly, causing local phase separation and resultant pore formation [231]. These pores may prove incidentally beneficial for cell attachment, due to the increased surface area and texture providing a better surface for adhesion[232]. Furthermore, it has been shown previously that small pores may increase differentiative capacity into an osteogenic lineage, with nano-pores of 10-200 nm being shown to be beneficial in the differentiation of BMSCs [232], [233].

The fibres spun at 11.5 kV, which were taken forward for all future work, were seen to have an average diameter of $7.5 \mu\text{M} \pm 1.48$ for aligned and $6.73 \mu\text{M} \pm 1.57$ for non-aligned. At this scale, the fibres would be considered microfibres, as opposed to nanofibers which are more commonly discussed within the literature for osteogenic differentiation [151], [187], [201], [234], [235]. There have, however, been a few examples within the literature, where larger fibre sizes have been successfully used to induce osteogenic differentiation [61], [198]. A larger fibre size also creates a larger pore size, due to the entrapment of air between fibres. This larger pore size should allow for a better diffusion of nutrients and metabolites through the construct in a more effective manner than that of the densely packed nanofibers. Furthermore, larger pores would allow for a deeper infiltration of cells throughout the scaffold, allowing them to spread throughout the scaffold, as opposed to when cultured on nano fibre sheets- where it may be

better described more closely as patterning, as opposed to a 3D construct. With infiltration into the fibres, the cells should then experience a more truly “3D” environment.

The mechanical properties of the fibres were as expected, with the fibres having a significantly weaker tensile strength in the transverse direction of the aligned fibres compared to that of aligned fibres in the longitudinal direction and the random fibres. Fibrous alignment within a single orientation is often seen *in vivo*, commonly in scenarios where the tissue must be strong in tension. For example, collagen within the tendon is seen to be highly aligned and has shown to have a linear modulus (The modulus of the region of stretch once collagen fibrils are fully un-crimped) of $34.0 \pm 15.5 \text{MPa}$ in the longitudinal orientation, and $0.157 \pm 0.154 \text{MPa}$ in the transverse [236].

4.5.2 Media composition

Although the chemically defined media chosen for investigation were designed to be used with MSCs, the manufacturers stated they had only been tested on primary MSCs [237], [238]. As the cells used within this work were a cell line, it was important to test whether the media was compatible and to find the media which supported the best proliferation. Furthermore, within the literature to date, the hTERT-Y201 cells have been cultured exclusively in FBS-containing media [203], [239]–[241].

The results showed that CD1 better supported the cell metabolic activity, inferred from cell metabolic activity, significantly more than that of DMEM with 10 % FBS. Gelatin coating was also investigated, as it is generally seen to aid with the attachment and proliferative capacities of cells when used as a base

substrate. Although it is a denatured form of collagen, gelatin still contains RGD-residues, subsequently assisting with healthy attachment and spreading of cells [242]–[244]. In this work, however, the addition of gelatin coating did not appear to have a significant effect on the cellular attachment or proliferation in any of the media types. It similarly did not appear to affect cell morphology, with cells maintaining their elongated fusiform shape. Gelatin is also generally commonly bovine-derived, and therefore not xeno-free. As this project attempts to minimise the reliance on any animal-derived products, and the addition of gelatin coating has no apparent effects within this specific cell line and media combination. Therefore, for the subsequent work, all cell culture was carried out in CD1 without the addition of gelatin coating.

As this project was specifically interested in the collagenous component of the bone matrix, it was important to maximise the deposition of collagen. Ascorbic acid, or vitamin C, is a key cofactor for lysyl hydroxylase and prolyl hydroxylase enzymes [200], [245]. These are essential in collagen synthesis, and without media supplementation with ascorbic acid, very little collagen deposition will likely occur. However, ascorbic acid is unstable under typical cell culture conditions of 37 °C and neutral pH [200]. Alternatively, a stable form of ascorbic acid, AA2P, may be used instead, and it is seen to still be an effective cofactor [200], [245], [246]. Within this work, it was seen that with increased addition of AA2P, there did not seem to be a dose-dependent effect on the deposition of collagen up to the amount of 100 µg/mL. Furthermore, even though little collagen should be produced in the absence of ascorbic acid, there were high amounts of collagen produced in all conditions, even without AA2P supplementation. It may be assumed that the manufacturers have pre-supplemented their media already with a stable form of ascorbic acid. This was

later confirmed by Miltenyi Biotech, although the supplier was unable to disclose at what concentration.

Despite no apparent decrease in metabolic activity of the h-TERT Y201 cells at high concentrations of AA2P, it was observed that there was a decrease in collagen deposition, and subsequently mineral deposition at 250 µg/mL. This suggests that while high AA2P concentrations may not induce cellular toxicity, they do seem to exert an inhibitory influence on collagen production. One plausible explanation for this phenomenon could be the impact of AA2P on the pH of the culture medium. AA2P is inherently acidic, with a solution pH of approximately 3, whereas the extracellular environment typically maintains a slightly alkaline pH range of 7.3-7.4. Even minor deviations from this optimal pH range can lead to altered cellular functionalities. Previous research by We *et al.* has demonstrated that a decrease in pH to around 6.6 significantly reduces collagen production in chondrocytes[247]. While the culture medium does contain a buffering system, at high AA2P concentrations and extended culture durations, the buffering capacity may be overwhelmed.

Furthermore, ascorbic acid plays a fundamental role as an antioxidant or reducing agent, actively mitigating the effects of circulating oxidative species. However, it has been observed that under high concentrations within the extracellular fluid, ascorbic acid has the ability to reduce copper and iron, leading to the generation of ascorbate radicals and hydrogen peroxide, which subsequently give rise to the production of reactive oxygen species (ROS)[200], [248]. Increase in ROS within culture media may result in oxidative stress and thereby giving rise to subsequent cellular dysfunction, DNA damage, or even cellular apoptosis.

The effect of fibronectin coating was also assessed as it is seen to be required for normal collagen deposition and organisation. Fibronectin is found as an exogenous component in FBS, as well as being produced endogenously by cells. It has been shown that exogenously sourced fibronectin can be incorporated into the fibronectin fibrillar network produced by the cells [249]. Furthermore, collagen and fibronectin have been shown to be linked in a co-assembly process [68], [81], [250]. It has also been shown that in MLO-A5 cells cultured in fibronectin-stripped FBS, the resulting collagen matrix was greatly reduced [68]. It was confirmed by Militenyi Biotech that the media used for this study had no additional supplementation of fibronectin. It was then hypothesised that without extra supplementation with an alternative source of fibronectin, collagen deposition and organisation may be reduced. The results showed that there was a significant increase in the production of collagen when h-TERT Y201 cells were seeded onto fibronectin-coated well-plates, despite not having any increase in cell number. However, without being able to fluorescently tag the endo- and exogenous fibronectin, it cannot be stated whether the coated fibronectin incorporated into the fibrillar structures, or whether the fibronectin coating simply promoted an increase in the endogenous production of collagen.

Dexamethasone supplementation was also investigated. Dex is a synthetic glucocorticoid, that can induce the differentiation of stem cells down an osteogenic lineage, by inducing WNT/ β -catenin signalling-dependent Runx2 expression [251]. It has been reported in some cases, however, that supplementation with Dex may result in an inhibition of the production of fibrillar collagens I and III [252]. In this study, it was confirmed that the addition of Dex did not affect the amount of collagen produced, however.

Mineral production at all concentrations was seen to be relatively low. This low mineral production was to be expected, however, as the cells were not supplemented with β -glycerol phosphate (β -GP), which provides an inorganic phosphate that would be required for effective mineralisation. Furthermore, day 21 is still a relatively early time point for bone culture from MSCs.

4.5.3 Cell seeding optimisation.

Cell seeding onto scaffolds was assessed, to find the best conditions to allow for effective attachment and proliferation on the scaffolds. PCL is known to be a highly hydrophobic material, so without surface modification in some way, it would be unlikely for cell attachment to occur. Atmospheric plasma treatment is a common way to modify the surface of a material and is seen to dramatically increase surface wettability. By this method, it should theoretically increase cell attachment, and increase cellular spreading.

To avoid any effect of repeated resazurin exposure on cell metabolic activity, resazurin was carried out only on day 7. For this experiment, there is notably less variability, which supports the idea that the resazurin assays are having a detrimental effect on either the cell's viability, inferred from metabolic activity, or causing detachment. There was little difference in the number of cells at the end of 7 days between plasma treating only or plasma + fibronectin coating, which suggests that plasma treatment is sufficient to allow for increased cell attachment. Fibronectin-only did not support as high cell metabolic activity compared to plasma + fibronectin coating combined. As the PCL is highly hydrophobic, the fibronectin deposition is likely affected by this. Cells did attach to some extent, however, evidencing that it is still effective at encouraging cell

attachment, compared to no surface treatment where cells were seen to not attach at all.

As the aim of this work was to investigate collagen organisation, the collagen deposited in each coating condition was assessed. As discussed previously, and shown in **section 4.5.2**, the addition of fibronectin increased the deposition of collagen by the h-TERT Y201 cells. It is also shown that fibronectin plays a role in the structuring and organisation of the collagen network, with fibronectin being seen to act as a template for collagen deposition. For this work, it was investigated whether or not the addition of fibronectin coating had any effect on the structure of the subsequent collagen deposited over the scaffold fibres.

It was seen that collagen appeared to be deposited on all scaffolds, however, without plasma coating, the fibronectin-only condition did appear to show its collagen to be produced by the cells in a nodular fashion. It has been shown that although fibronectin can be adsorbed to both hydrophobic and hydrophilic surfaces, it may adsorb in different conformations on the two surfaces [30]. Furthermore, it was seen that at low concentrations, fibronectin may only be biologically active on hydrophilic surfaces, and that fibrillar formations were also only seen on hydrophilic surfaces [30]–[32]. AFM studies have also shown that proteins adsorbed on hydrophobic surfaces adopted more rigid conformations and tighter binding while looser conformations were observed on more hydrophilic surfaces [33]. Altankov et al showed that fibroblasts were able to deposit fibronectin, but were unable to subsequently organise fibronectin into a fibrillar matrix when cultured on hydrophobic polyvinyl chloride (PVC) [31]. Due to the co-dependent nature of collagen and fibronectin, this may also hold for collagen deposition when deposited onto hydrophobic surfaces. Sirius red

stain is not exclusive to fibrillar collagen, and also stains pro-collagen subunits within the cell, which may also explain a nodular appearance if pro-collagen subunits are not being assembled into collagen fibres. As this project is aiming to look at recreating the lamellae-like orientation of collagen fibres, the use of fibronectin without plasma coating was excluded for all further experiments from this point. The results gained in this work may be used for future guidance in serum-free bone tissue engineering.

4.6 Summary and conclusions

PCL fibres were electrospun into aligned and non-aligned fibres, and surface modifications of air plasma deposition and fibronectin coating were carried out, to make the scaffolds more favourable for cell attachment. In future work, it may be of interest in incorporating other bioactive materials such as hydroxyapatite into the fibres, which would further assist in osteoinduction and osteoconduction. This would likely require a new optimisation process, as the addition of hydroxyapatite would likely affect the materials' spinnability, due to factors such as increased viscosity.

These results highlight for the first time the possibility to culture the h-TERT Y201 cell line in xenofree media and optimise the conditions for its 2D culture. This data guided the conditions used for chapter 4 of this thesis and can provide direction for future projects moving to xenofree medium for bone tissue engineering. Although the use of xeno-free is beneficial for minimising variability and unknown interacting factors that can be observed through the use of FBS, future work would aim to further minimise these even further, through the use of chemically defined media. Xeno-free may still contain human-based serums, so may still contain undefined products such as growth factors,

hormones and proteins. With the use of chemically defined mediums, this variability would be almost eliminated, allowing for further reproducibility and clarity on any observed effects that may arise from an *in vitro* model.

- PCL fibre alignment is controllable through variation of voltage, where higher voltages result in increasing levels of disorganisation.
- Aligned electrospun PCL fibres had a 2-fold higher UTS when a load is applied in the longitudinal orientation, compared to that of non-aligned fibres.
- 11.5kV was used to spin fibres both aligned and non-aligned in all future experiments
- Plasma deposition greatly increases the hydrophilicity of the fibres and allows for the production of fibrillar collagen.
- Fibronectin coating supports higher collagen production of h-TERT Y201 cells seeded in 2D
- Dexamethasone has no inhibitory effects on the production of collagen in the h-TERT Y201 cell line
- Supplementation of AA2P above 250 µg/mL has an inhibitory effect on collagen deposition.

5 Investigation of Microfibres Effect on Spatial Collagen Organisation of Osteogenically Differentiated MSCs

5.1 Introduction

Cortical bone has a unique structure, formed of osteons. Osteons have a highly organised lamellar structure to their collagen, which is fundamental for its anisotropic strength. To be able to recreate this specific structural anisotropy could provide great benefit for not only the development of better-suited implants and the development of *in vitro* bone models but also for a better understanding of osteogenesis and studying the molecular pathways involved in the development of structured collagen. To date, we still do not have a strong understanding of the mechanistic pathways in which bone lamellae form.

A recent finding on the effects of aligned nanofibres on the deposition of collagen was described previously within the Reilly group. With the use of aligned polymer fibres seeded with murine-derived osteocyte cell line, MLOA-5, it appeared initially that collagen deposition was directed along the alignment of the PCL fibres[61]. However, when analysed by SHG, with an ability to image deeper into the scaffold, it was seen that there was a shifting of collagen alignment with increasing depth. The small changes in the angle of orientation relative to the long axis may be comparable to that seen within the “twisted plywood” style structure seen within the lamellae of the osteonal microstructure[189]. These findings using aligned nanofibers give light to potentially novel methods for recreating a more organised and histologically similar structure to cortical bone. However, this also leads to further questions

about whether this is reproducible across different materials and cell types. As MLOA-5's are a murine cell line and also exhibit characteristics such as rapid proliferation and mineralisation, it would be of interest to investigate whether this change of orientation may be an intrinsic behaviour of bone cells of varying stages of differentiation and species, or if this is a phenomenon unique to this specific cell type [197]. Furthermore, this phenomenon was observed in the presence of FBS, which adds an increased level of complexity, due to the unknown composition of proteins and other chemicals within the serum which may be affecting the cell behaviour. Furthermore, the addition of FBS is undesirable for uses with *in vitro* models, due to its batch-to-batch variability as discussed within the literature review (**Section 1.9.3**).

5.3 Aims and Objectives

This chapter aims to use the material developed in Chapter 4 and assess its potential for guiding collagen regeneration and recreating a construct that is more representative of the cortical bone lamellae. Two types of fibrous scaffolds were produced in chapter 3, aligned and non-aligned scaffolds, which were used as the basis of the scaffolds. It was hypothesised that the use of a highly aligned scaffold would allow for the development of a bone-like matrix with a higher degree of orientation, and hence maturity. As discussed previously, non-aligned scaffolds are regularly used as a model of bone and provide a good base for collagen and mineral deposition. However, it may be argued that the resulting construct is more representative of that woven bone due to its high levels of disorganisation in its collagen and mineral deposition.

The aims of this chapter are as follows:

1. Produce two differentially orientated polymer scaffolds and elucidate their effects on growth and matrix production on aligned and non-aligned scaffolds
2. Investigate how collagen organisation changes with depth using second harmonic generation
3. Assess the maturity of the resulting matrix on aligned and non-aligned scaffolds

5.4 Experimental Design

h-TERT Y201 cells were seeded onto either aligned or non-aligned scaffolds developed in Chapter 3. Scaffolds were either treated with plasma, or plasma + fibronectin coated before seeding with cells. The timeline of culture is outlined in **Figure 5-1**. Cells were cultured on the scaffolds in either osteogenic media (OM) or expansion media (EM) for 28 days, and assessed for their matrix production throughout. Second harmonic generation (SHG) was used to visualise collagen orientation on the scaffolds.

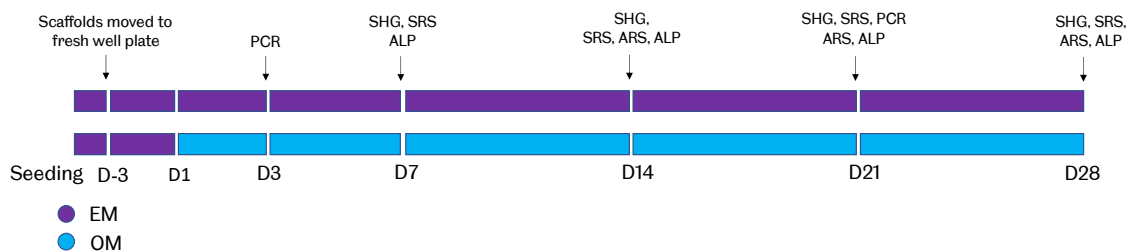


Figure 5-1: Timeline of assays carried out at each time point. Samples are either treated with expansion media (EM), formed of xenofree media supplemented with ascorbic-2-phosphate (AA2P), or osteogenic media (OM), formed of xenofree media supplemented with dexamethasone, AA2P and β -glycerolphosphate (β -GP). Quantitative Polymerase Chain Reaction (PCR), second harmonic generation (SHG), Sirius red stain (SRS), Alizarin Red stain (ARS) and alkaline phosphatase enzyme activity (ALP) were all carried out were indicated along the timeline.

5.5 Results

5.5.1 Mineral and Collagen Deposition

Scaffolds were plasma treated or plasma treated and then coated with fibronectin. This was to assess whether an exogenous fibronectin source had any effect on collagen and mineral deposition and organisation.

Sirius red stain for collagen showed that there were no significant differences in the quantity of collagen produced by h-TERT Y201 in all conditions at all time points (**Figure 5-2**). Large amounts of collagen were produced, rising steadily until day 21. Between days 21 and 28, there was no significant increase in Sirius red stain, however.

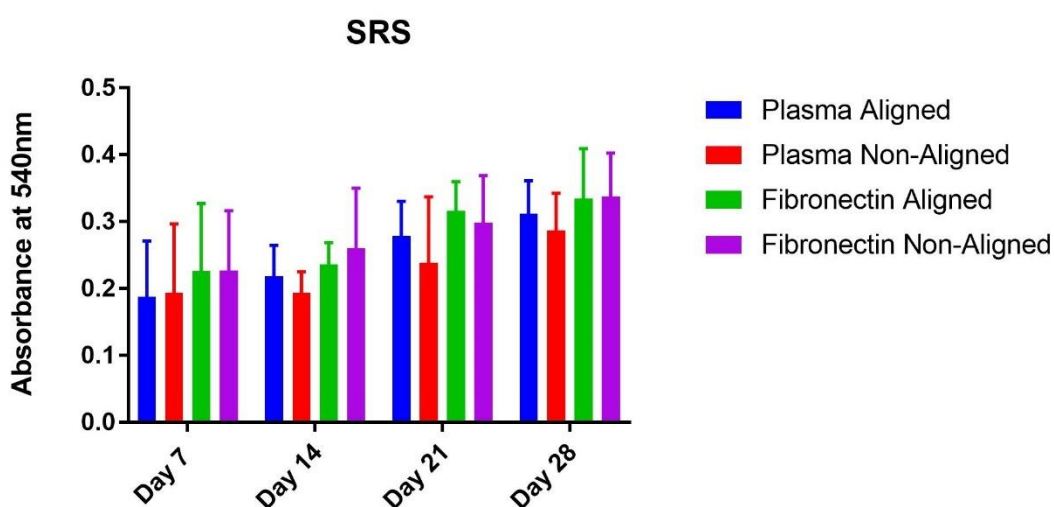


Figure 5-2 Quantification of collagen deposition using Sirius Red Stain and cell attachment of Y201 cells seeded on aligned and non-aligned fibres treated with either plasma only or plasma + fibronectin coated. Statistical analysis carried out using a two-way ANOVA and Tukey's *post-hoc* test for multiple comparisons. Results shown as mean \pm SD (n=9)

Alizarin red staining was carried out on days 21 and 28, to quantify the degree of mineralisation (**Figure 5-3**). Very little mineral was deposited on day 21, but by

day 28 there were significant increases in the amount deposited in all conditions. All conditions examined supported mineral deposition, however, plasma-treated aligned scaffolds did have significantly less mineralisation than all other conditions. dsDNA quantification was also carried out as a method to infer the number of cells present on each of the scaffolds, and it was observed that the cell number was comparable in all conditions across each time point (**Figure 5-4**).

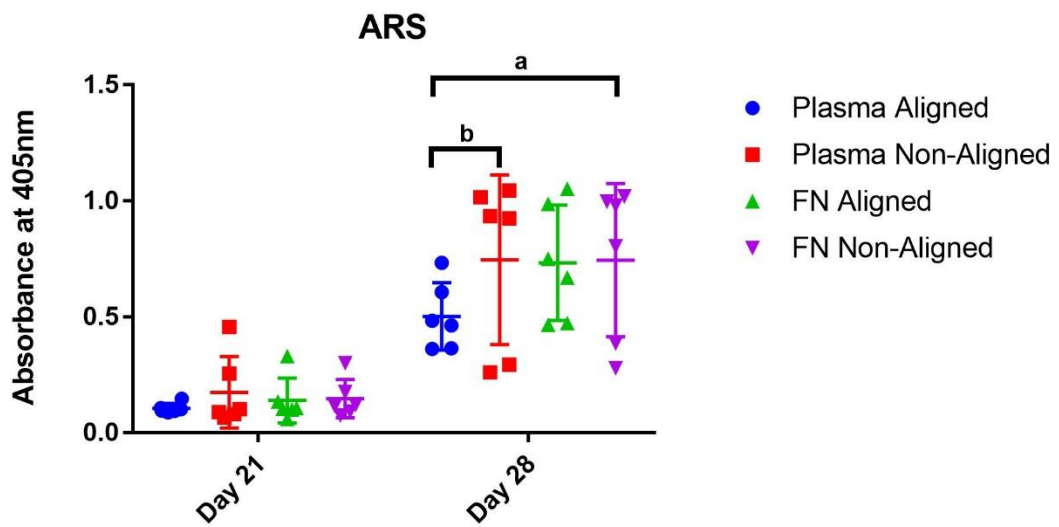


Figure 5-3: Quantification of mineral deposition using Alizarin Red Stain (ARS). Statistical analysis carried out using Kruskal-Wallis test with Dunn's multiple comparisons. Results shown as mean±SD. n=6. p values are reported as a=0.0173 b=0.0374

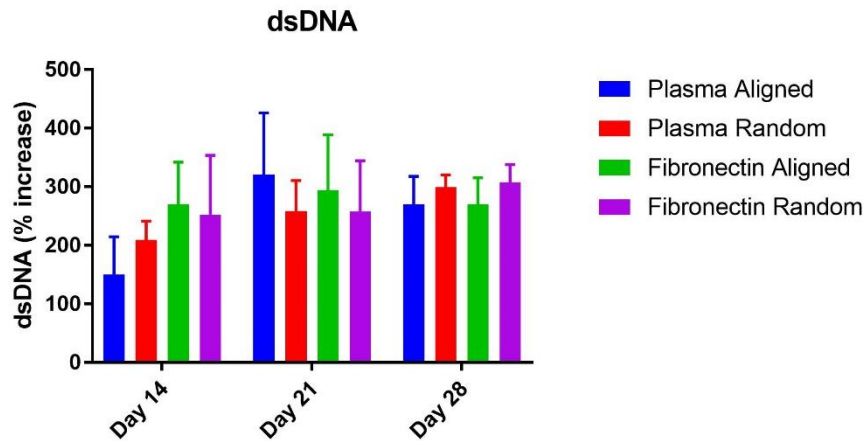


Figure 5-4: Quantification of double sided DNA content using Quant-IT dsDNA quantification. Tested using Kruskal-Wallis test with Dunn's multiple comparisons. Results shown as mean \pm SD. n=9

The mean gray value (MGV) of full-thickness z-stacks obtained via SHG was also obtained to quantitate SHG signal. The MGV is proportional to the overall intensity of the SHG signal. From the MGVs, there was seen to be significantly lower intensity on days 14 and 21 for plasma-only non-aligned scaffolds, signifying a lower SHG arising from the collagen (**Figure 5-5**). On day 7, SHG signal was significantly lower for all conditions, with almost no signal observed.

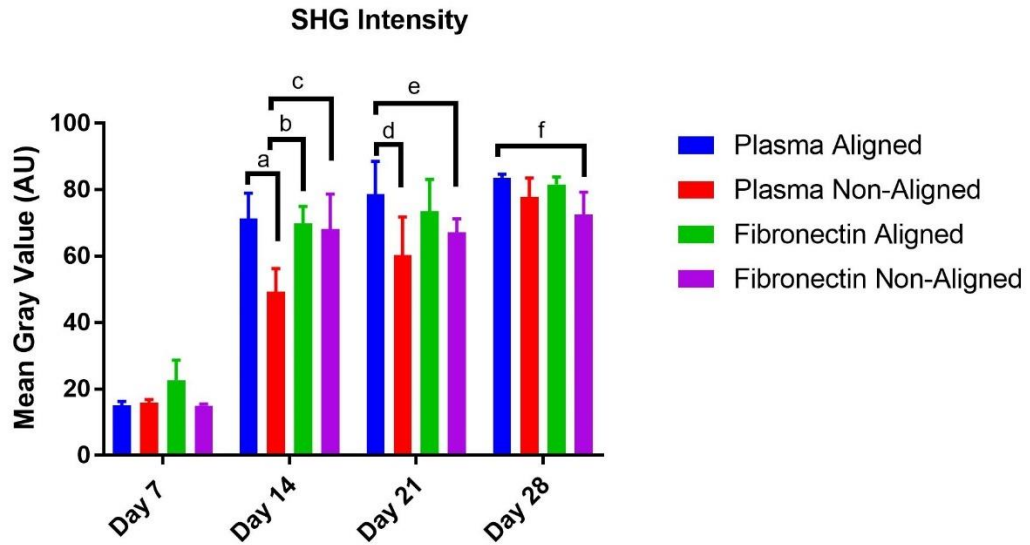


Figure 5-5: Quantification of SHG intensity using mean gray value. Results shown as mean±SD of 18 separate images across a sample size of n=9. Statistical analysis performed using two-way ANOVA with Tukey's *post-hoc* test for multiple comparisons. Significant p values shown as a=<0.0001 b=0.0001 c=0.0002 d=<0.0001 e=0.0044 f

5.5.2 Alkaline phosphatase activity

Alkaline phosphatase activity (ALP) measurements were taken, as ALP is considered to be an initial marker of osteoblast differentiation, and an increase in the level of ALP suggests active bone formation will occur. It was shown that there were no significant differences between any of the conditions in the amount of ALP produced (**Figure 5-6**). Between day 7 and day 28 there was significant increase in ALP production for all conditions other than Plasma Non-aligned, which failed to reach significance. There were no significant differences between each condition, however.

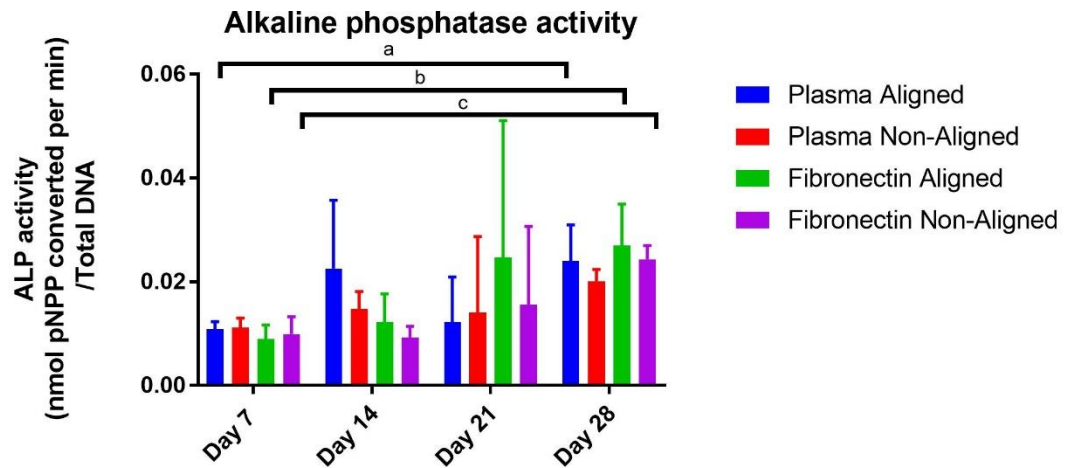


Figure 5-6: Alkaline phosphatase activity taken at days 7, 14, 21 and 28. Enzyme activity was calculated as nmol pNPP converted per minute and normalised to total DNA within the sample. Tested with two-way ANOVA and Tukey's *post-hoc* test for multiple comparisons. Results show mean \pm SD (n=9) a=0.0321 b=0.0013 c=0.0146

5.5.3 Collagen Organisation

The organisation of the collagen was imaged using second harmonic generation to obtain information about the direction of collagen fibres. On day 7, there was no fibrillar collagen observable via SHG signal, but by day 14 of culture, there was an extensive matrix of collagen beginning to form for all conditions (**Figure 5-7**). On the aligned PCL fibres, the collagen deposition appeared to be orientated in the direction of the PCL fibres (**Figure 5-7A-B**). As expected, the orientation of the collagen on the non-aligned PCL fibres had no distinct orientation on either fibronectin + plasma or plasma-only treated samples (**Figure 5-7C-D**). The overall SHG signal was also visibly lower on the plasma-treated non-aligned scaffolds.

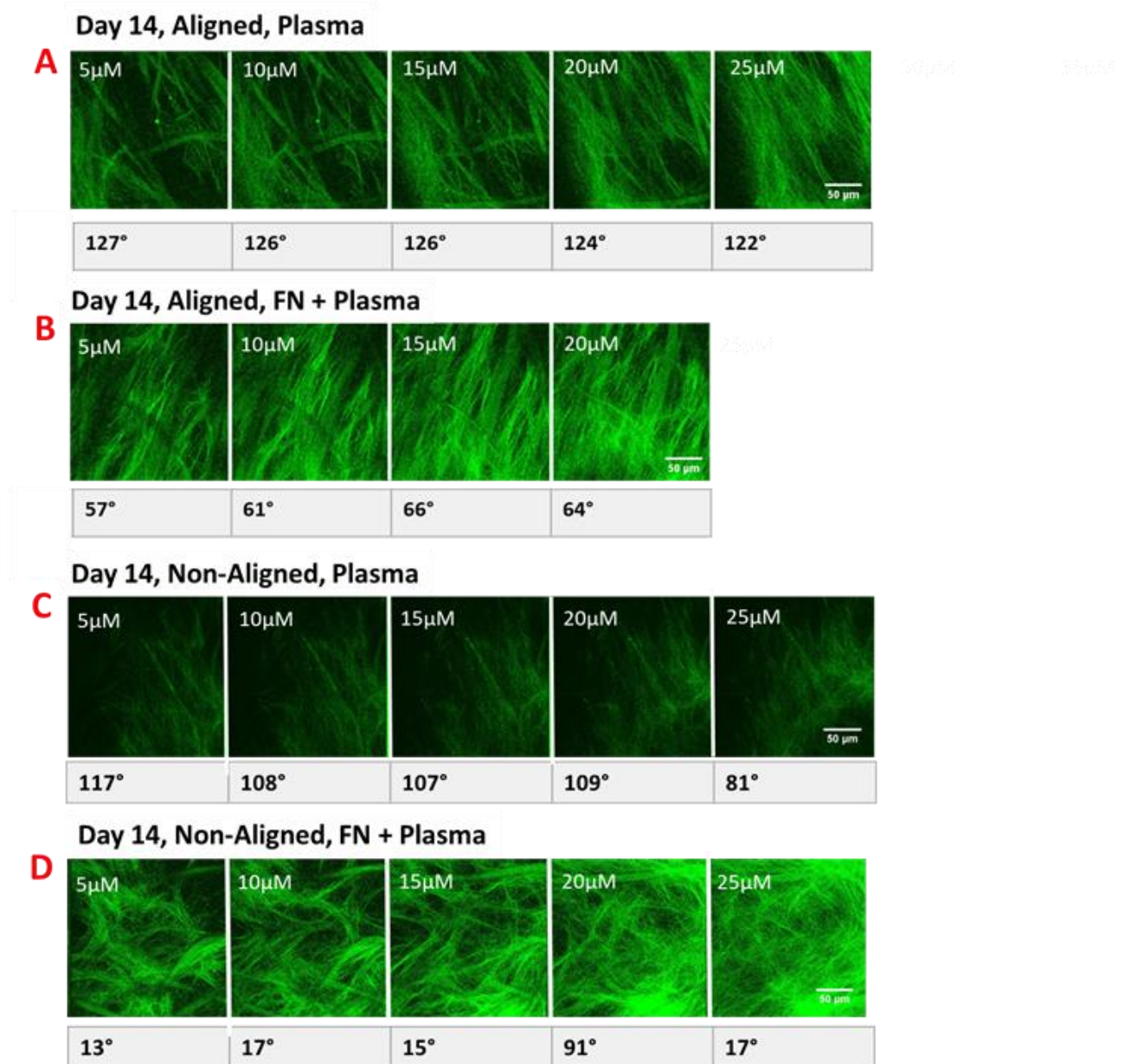


Figure 5-7: A-D: Representative SHG images of collagen deposited by Y201 cells cultured on aligned and non-aligned fibres at day 14 of culture with OM. Each image represents 5 μ m slices, with the average (mean) orientation of the fibres from the original PCL fibre axis written beneath. Measurement in top left describes distance from PCL scaffold. Scale bar represents 100 μ m.

Furthermore, the collagen appeared to only be deposited on top of the plasma-

treated non-aligned scaffolds, as opposed to within the scaffold, as is observed in other conditions. This may be explained by the potential increased fibre packing density occurring during the non-aligned fibre electrospinning process.

After 21 days of culture, collagen fibres appeared to have penetrated the depth of the scaffold for all conditions, and there was no difference in the overall intensity of the SHG signal (**Figure 5-8**). For the aligned PCL fibres, there was a noticeable difference in orientation in the collagen deposited directly above the PCL fibres (**Figure 5-8A-B**). Overall orientation in each 5 μ m slice appeared to be slightly offset from the slice below, in the anti-clockwise direction, whilst within the individual slice, alignment between collagen fibres within the same plane was mostly parallel. On non-aligned scaffolds, there was no notable trend in the orientation of collagen (**Figure 5-8C-D**). Plotted histograms of the fibre distribution in each 5 μ M image stack show a notable peak within the deeper layers deposited closer to the scaffold (**Figure 5-8E-F**). However, with increasing height from the PCL fibres, the peak is flatter. This is observed in both surface treatments examined. For the collagen deposited on the non-aligned scaffolds, there is generally a wider spread of fibre orientation distribution, resulting in less notable peaks (**Figure 5-8G-H**). The average difference in collagen direction closest to the substrate, compared to the highest detectable layer was $16.53^\circ \pm 13.22$ for fibronectin + plasma and $22.35^\circ \pm 16.95$ for plasma only.

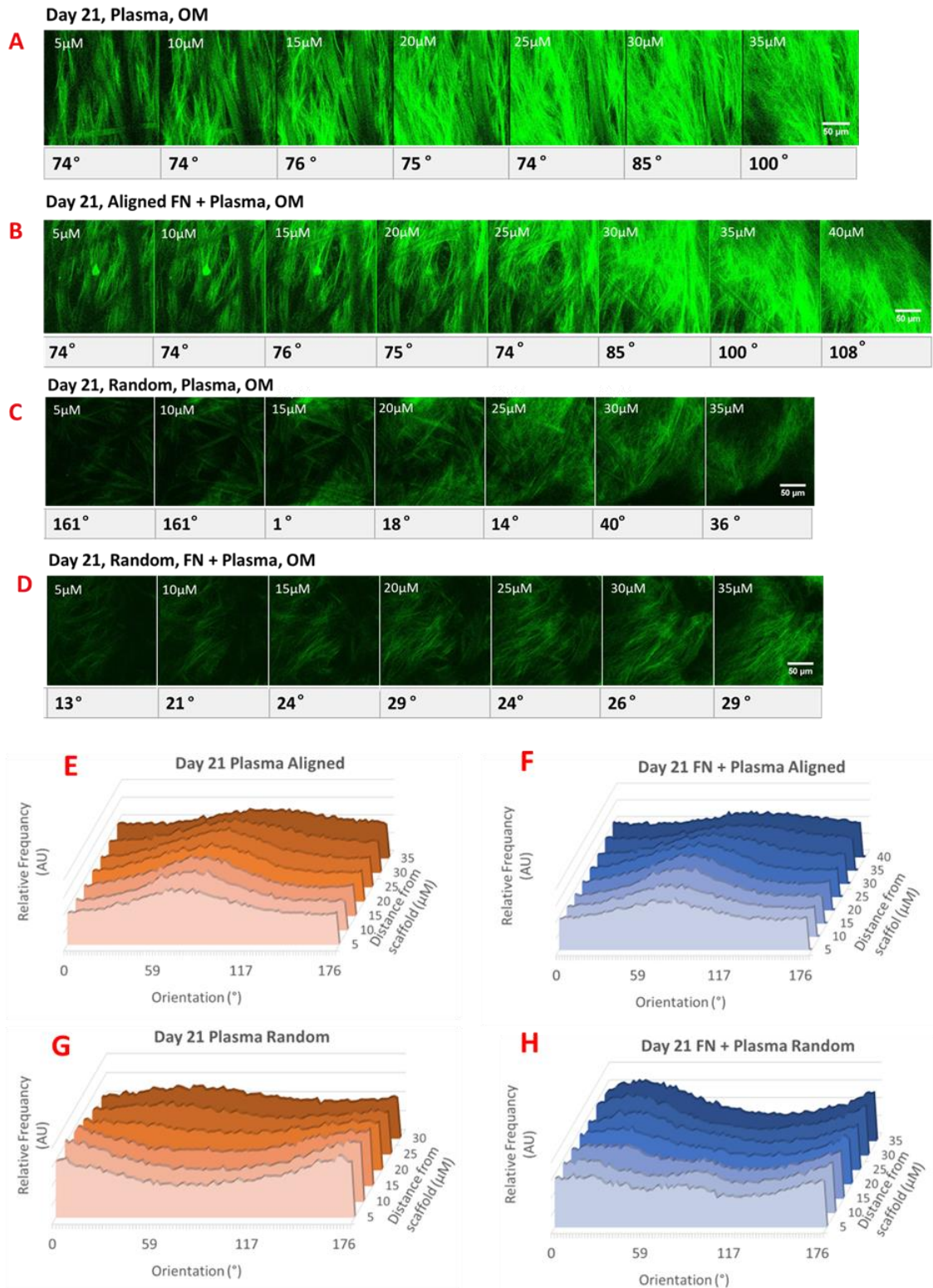


Figure 5-8: A-D: SHG images of collagen cultured on aligned and non-aligned fibres at day 21 of culture with OM. Each image represents 5 μm slices, with the average orientation of the fibres from the original PCL fibre axis written beneath. Scale bar represents $100\mu\text{m}$. **E-H:** 3D histograms highlighting changes in directionality of collagen fibres in relation to depth for each $5\mu\text{m}$ stack of SHG slices. Y-axis: Ratio of fibres in each analysed image at a particular angle from 0 to 180. Each histogram is of a single Z-stack image that is deemed representative of the general trend for each condition.

Within the histograms, the peaks remain distinct, but shift as they move further from the polymer scaffold whilst, for the non-aligned condition, there are no notable peaks (**Figure 5-10 E-H**).

By day 28, the twisting in orientation between layers became more notable in SHG images, with fibronectin scaffolds showing a significantly larger difference in orientation at $54.74^{\circ} \pm 17.19$ from the initial PCL orientation for fibronectin-coated, compared to $38^{\circ} \pm 17.6$ for Plasma only. orientation at $54.74^{\circ} \pm 17.19$ from the initial PCL orientation for fibronectin-coated, compared to $38^{\circ} \pm 17.6$ for Plasma only (**Figure 5-10**).

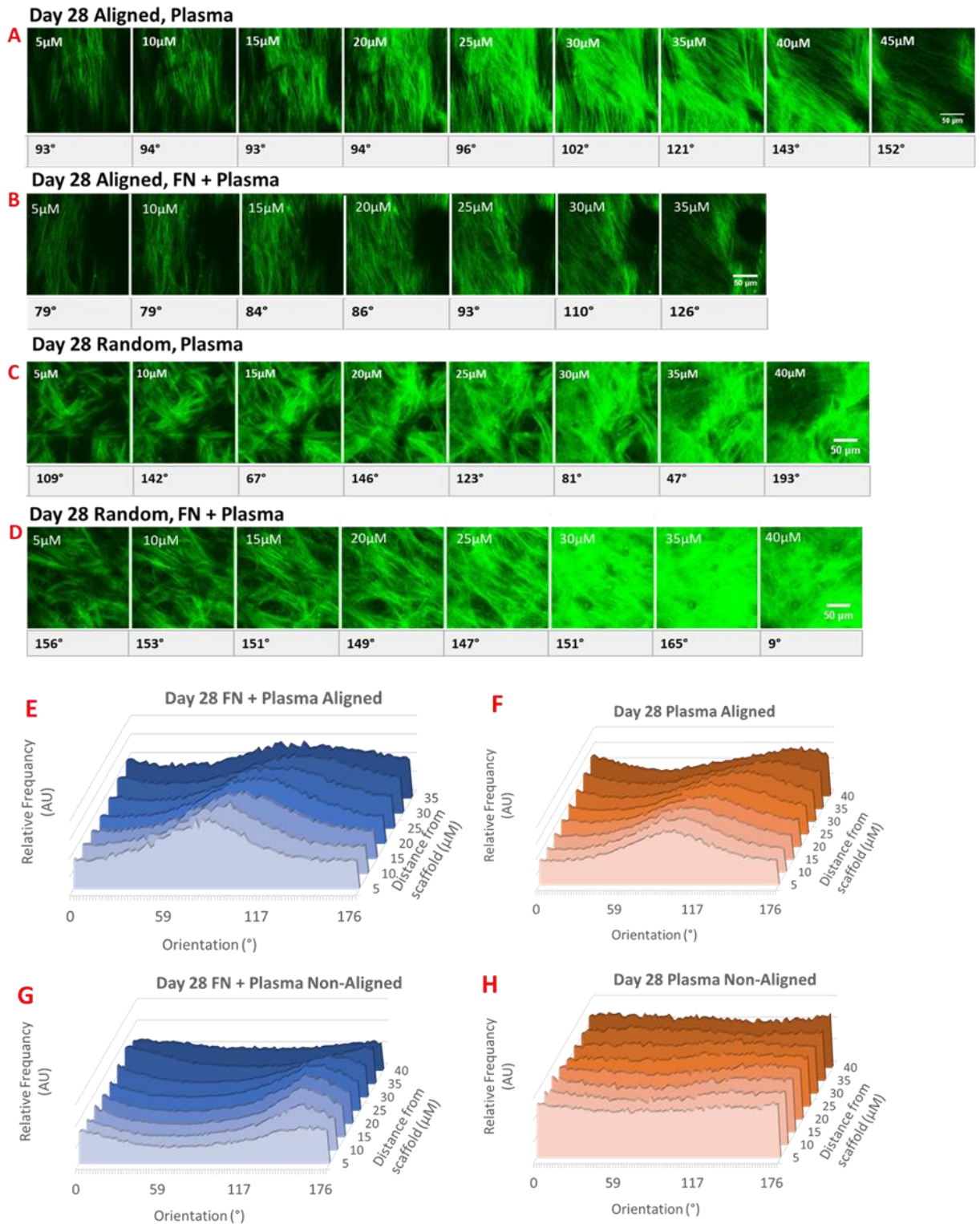


Figure 5-9: A-D SHG images of collagen cultured on aligned and non-aligned fibres taken on day 28 of culture with OM. Each image represents 5 1 μ m slices, with the average orientation of the fibres from the original PCL fibre axis written beneath. Scale bar represents 50 μ m. E-H 3D histograms highlighting changes in the directionality of collagen fibres in relation to depth for each 5 μ m stack of SHG slices. Y-axis: Ratio of fibres in each analysed image at a particular angle from 0 to 180. Each histogram is of a single Z-stack image that is deemed representative of the general trend for each condition.

When cultured in regular expansion media containing no dexamethasone or β -GP (EM), the collagen was seen to orientate in a consistent direction in the same direction as the PCL fibres of the aligned scaffolds, even after 28 days of culture (**Figure 5-13A-B**). Histograms of the distribution of collagen fibres show distinct peaks in all images within a single stack, but with no shifting of the peak between layers (**Figure 5-13C-D**). For cells cultured on the non-aligned PCL fibres, there was no noticeable orientation of the collagen fibres observed.

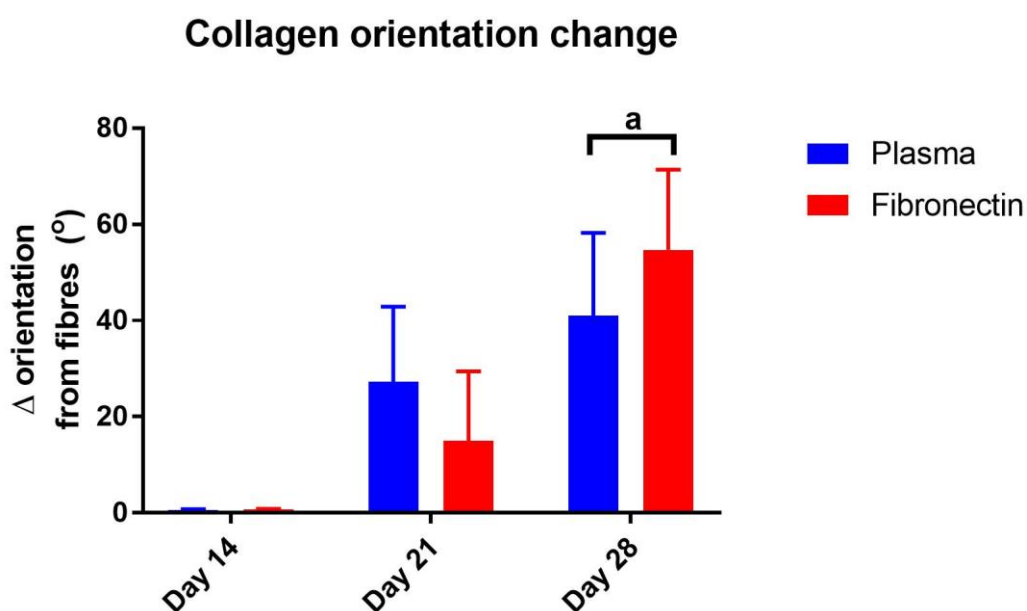


Figure 5-10: Difference in the orientation of collagen fibre alignment from the slice closest to the scaffold, compared to the top-most slice. Y201 cells were seeded on either plasma-coated or fibronectin-coated aligned fibres and measurements taken at days 14, 21, and 28. Measurements were taken across 10-16 separate images per condition, across a sample size of $n=9$. Results show mean \pm SD Tested with a two-way ANOVA with Sidak's *post-hoc* test for multiple comparisons. Significant p number is shown as $a=0.0382$

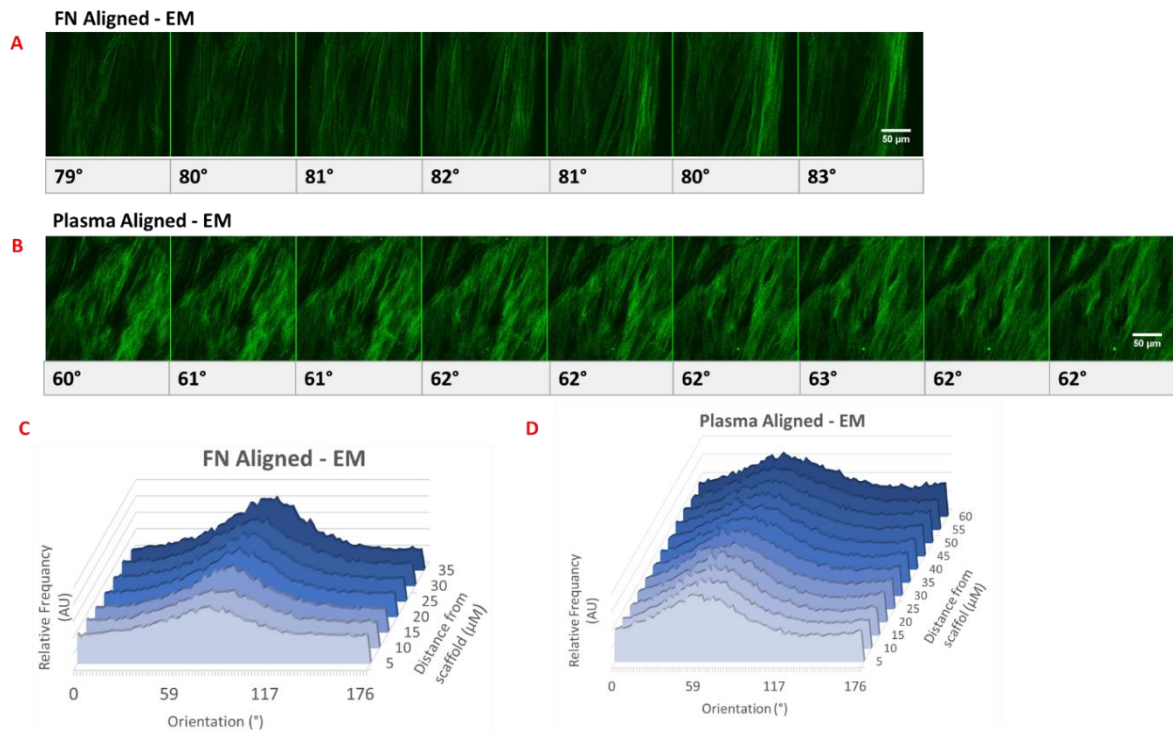


Figure 5-12: **A-B** SHG images of aligned fibres taken at day 28 of culture with EM. Each image represents 5 μm slices, with the average orientation of the fibres from the original PCL fibre axis written beneath. Scale bar represents $50\mu\text{m}$. **E-H** 3D histograms highlighting changes in directionality of collagen fibres in relation to depth for each $5\mu\text{m}$ stack of SHG slices. Y-axis: Ratio of fibres in each analysed image at a particular angle from 0 to 180. Each histogram is of a single Z-stack image that is deemed representative of the general trend for each condition.

Orientation change EM - Day 28

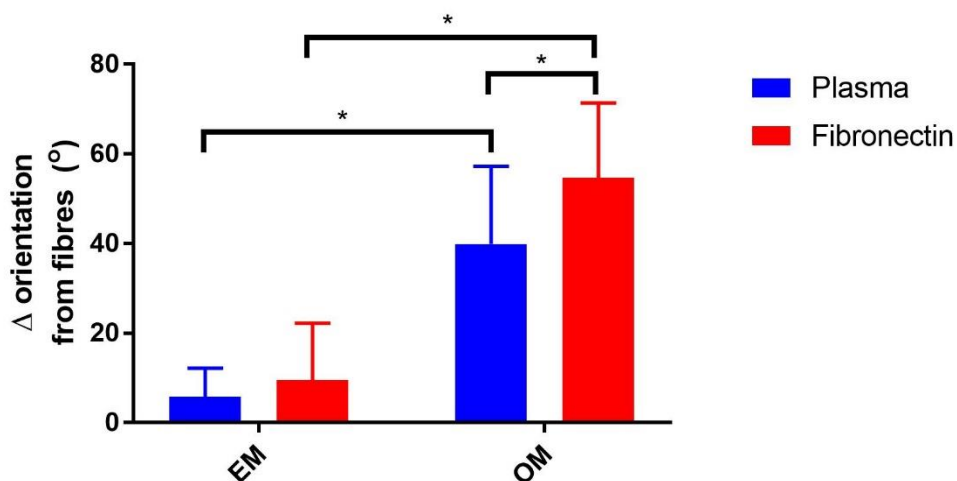


Figure 5-11: Change in orientation of fibre alignment from the PCL fibres on plasma coated or fibronectin coated aligned fibres at day 28 in either EM or OM. Measurements were taken across 16-20 separate images per condition, across a sample size of $n=9$ (OM) and $n=6$ (EM). Results show mean \pm SD. Tested with a two-way ANOVA with Sidak's *post-hoc* test for multiple comparisons. Significant p numbers indicated as $*= < 0.001$

5.5.4 Cell alignment

Cell morphology along the PCL fibres was also assessed over 28 days of culture. From this point forward fibronectin + plasma coating condition was used as the baseline surface coating, as previous work has shown that the addition of fibronectin was more favourable for mineral deposition. It was seen that after 7 days in culture, h-TERT Y201 cells cultured on the non-aligned scaffolds, appeared to adopt a stellate morphology, whilst the cells on the aligned scaffold elongated along the axis of the aligned PCL fibres (**Figure 5-13 A-B**). On day 7, although the cytoskeleton of the cells has elongated, the nucleus is still a rounded shape.

DAPI(Blue)/Nucleus staining, Phalloidin(Red)/Actin Staining

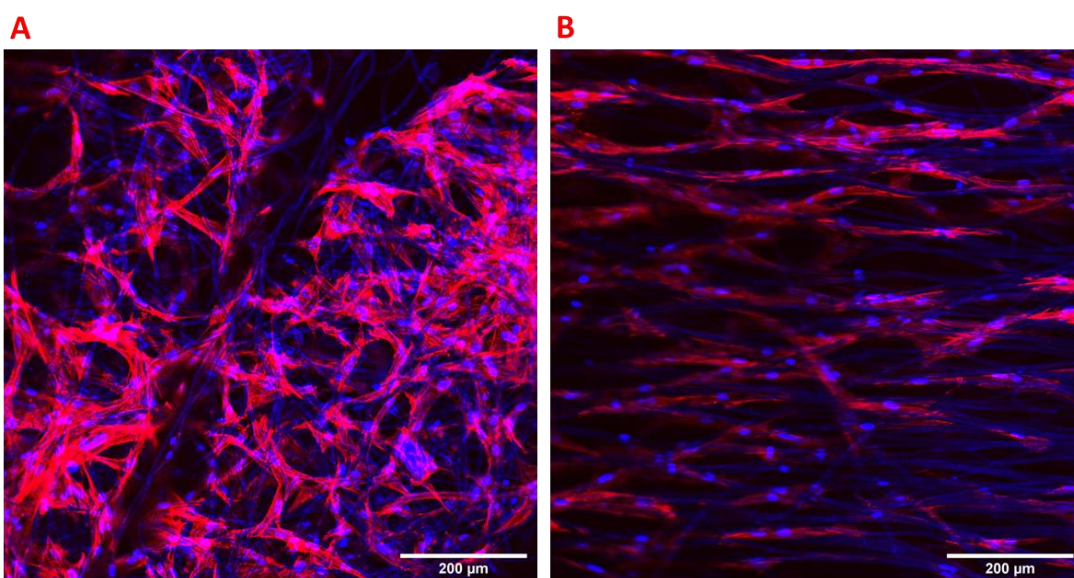


Figure 5-13: Confocal images of the cell nucleus (DAPI in blue) and cytoskeleton (phalloidin-TRITC in red) of h-TERT Y201 cells seeded on non-aligned (A) and aligned (B) scaffolds at day 7. Cells on aligned PCL fibres show a cytoskeleton that is aligned along the axis of the fibres, whilst non-aligned PCL fibres appear to have no notable organisation. Scale bar at 200 µM

The shape of the cell nucleus was also assessed over the 28 days of culture on aligned and non-aligned PCL fibres with seeded h-TERT Y201 cells cultured in either EM or OM. The nuclear morphology was analysed using ImageJ, and measurements of area and circularity were taken. It was seen that the nucleus was seen to be deformed in shape, becoming elongated throughout the culture

period (**Figure 5-15**). At day 28, cells cultured on aligned fibres in OM were seen to be significantly less elongated than in all other conditions. It was also observed in all conditions examined, the nuclear shape began to enlarge over the 28 days, with no significant differences between each condition (**Figure 5-15**)

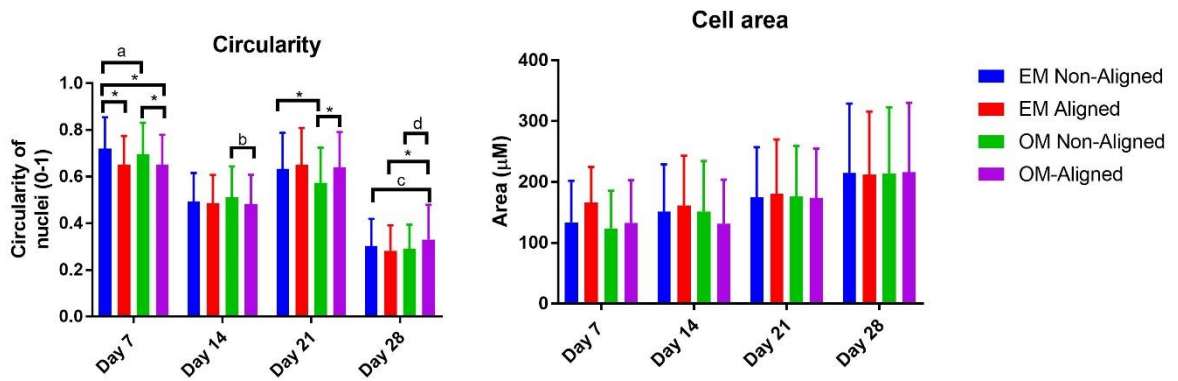


Figure 5-14: Circularity and nuclear area of h-TERT Y201 cells at days 7, 14, 21 and 28 of culture on aligned or non-aligned scaffolds in either expansion media (EM), or osteogenic media (OM). Results are shown as mean \pm SD of 500 measurements taken over 9-12 separate images per condition. Analysed using Kruskal-Wallis test with Dunn's *post-hoc* for multiple comparisons. Significant p values represented by a=0.055 b=0.0325 c=0.0419 d=0.0213 and * = $p \leq 0.0001$

5.5.5 Construct mechanical properties

Mechanical testing on the scaffolds was carried out after 28 days of culture with h-TERT Y201 cells, in either OM or EM media. A blank, acellular control was also used, which was stored in OM for 28 days at 37°C. Aligned scaffolds were tested in both the transverse and longitudinal directions with respect to the fibre alignment, with Young's Modulus, ultimate tensile strength (UTS) and toughness being calculated from the stress/strain curves generated (**Section 2.4.3**). It was observed that the toughness and UTS were increased significantly in constructs made with non-aligned PCL fibres by culturing with cells in both EM and OM (**Figure 5-16 A+D**). A significant increase in toughness was also observed in the aligned fibre-cell constructs when cultured in OM compared to EM (**Figure**

5-16 B). When cells were cultured in OM, aligned PCL fibres were seen to support a 4.4-fold increase in toughness, compared to the 3.5-fold observed for non-aligned. UTS, when measured in the longitudinal direction, showed a significant increase when cultured with cells in both OM and EM, but even more significantly so when cultured in OM (Figure 5-16 E). An increase in toughness, UTS and Young's modulus were observed in the transverse orientation when cells were cultured in OM, but none of these reached statistical significance (Figure 5-16).

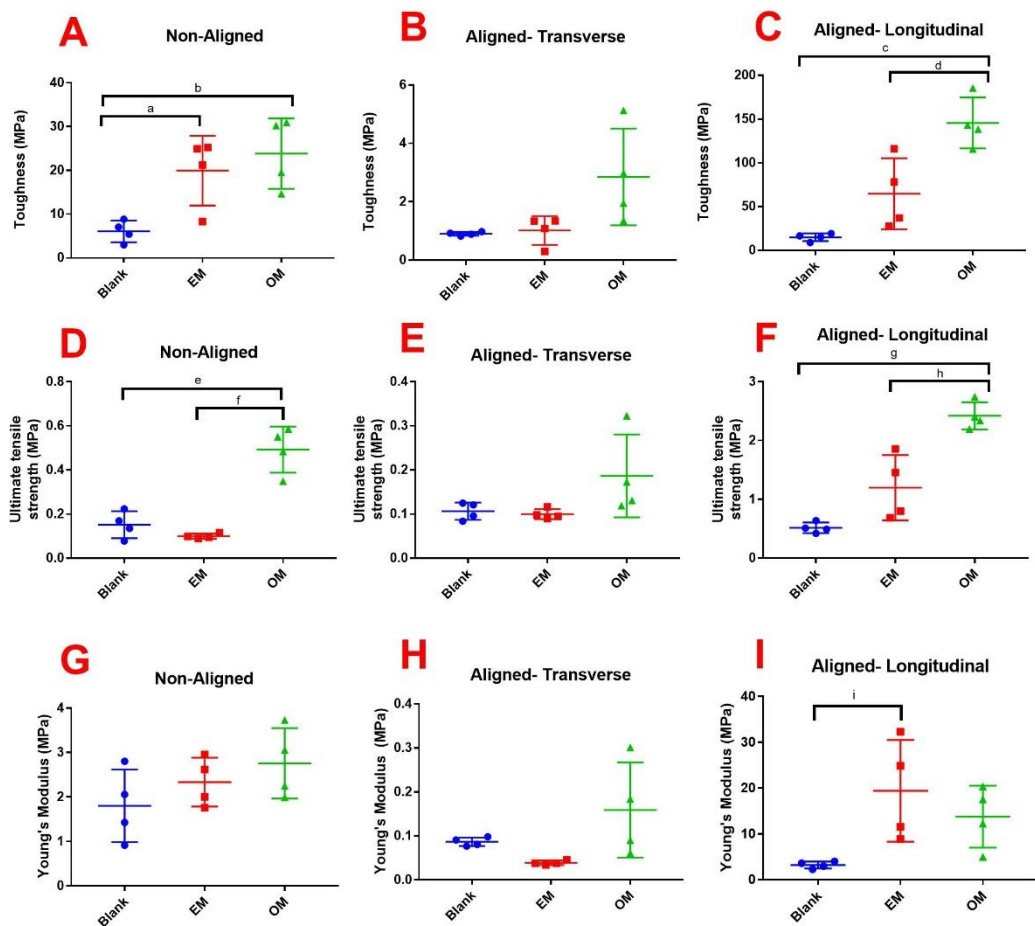


Figure 5-15: Toughness (A-C), ultimate tensile strength (UTS) (D-F) and Young's modulus (G-I) measured on aligned and non-aligned PCL fibres, cultured with h-TERT Y201 cells for 28 days in either EM or OM. Blank condition represents an acellular scaffold placed in OM for 28 days at 37°C All PCL fibres were plasma + fibronectin coated. Aligned fibres were tested in both the transverse and longitudinal orientations. Results are shown as mean \pm SD. n=4 Analysed using a one-way ANOVA with Tukey's *post-hoc* test for multiple comparisons. Significant p values are shown as a=0.041 b=0.0113 c=0.0003 d=0.0084 e=0.0002 f=<0.0001 g=<0.0001 h=0.0021

5.5.6 Gene expression on aligned and non aligned PCL fibres

qPCR was carried out on days 3 and 21, to assess the gene expression at both an early stage of differentiation and later stages. ALP(Alkaline phosphatase), SPPI (Osteopontin/secreted phosphoprotein 1), RUNX2 (Runt-related transcription factor 2) and BGLAP(Osteocalcin) were all investigated. SPPI, ALP and RUNX2, are all expressed by pre-osteoblasts from early stages of osteogenic differentiation, whilst BGLAP is generally seen at a slightly later stage secreted by the mature osteoblasts. It was observed that there was high variability in the expression of SPPI, ALP and BGLAP, making analysis of the data difficult, with the gene often being undetected. This is likely due to low total RNA, with an average of 30.83ng/ μ L \pm 13.63 being extracted from each sample.

RUNX2, SPPI and ALP expression fold-change for Y201 cells were calculated on days 3 and 21, using Y201 cells cultured in OM directly on TCP as a control. It was seen that initially that all three were downregulated in the first 3 days of culture in relation to 2D controls (**Figure 5-16A**). After 21 days, expression began to be upregulated for all genes examined, but with no significant differences between aligned and non-aligned fibres (**Figure 5-16B**).

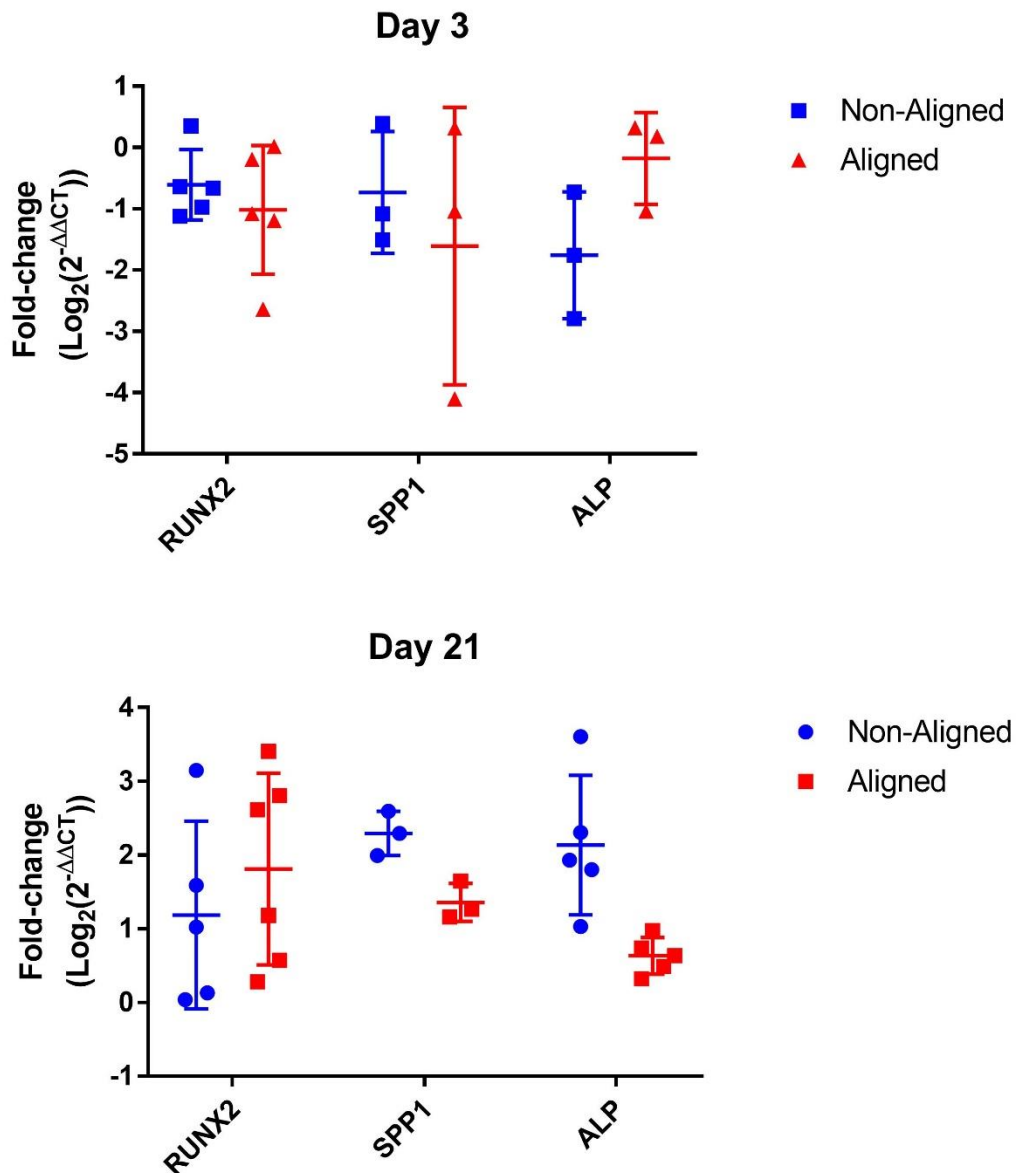


Figure 5-16: Osteogenic gene expression of Y201 cells at days 3 and 21, shown as log₂ of fold-change, compared to OM-treated 2D controls. Results shown mean±SD (n=3 (SPP1) n=3-5 (ALP) or n=5-6 (RUNX2))

The effects of the fibres themselves without the presence of dexamethasone as a differentiating factor were also investigated. It was seen that culturing even in EM conditions, both aligned and non-aligned fibres induced the increased expression of RUNX2, but with no significant difference between the two conditions (**Figure 5-18**). In OM, it is observed that there is a significant increase in RUNX2 expression compared to EM conditions (p=0.0041). It is also seen that

there is a significant increase in gene expression of cells on aligned fibres, compared to non-aligned.

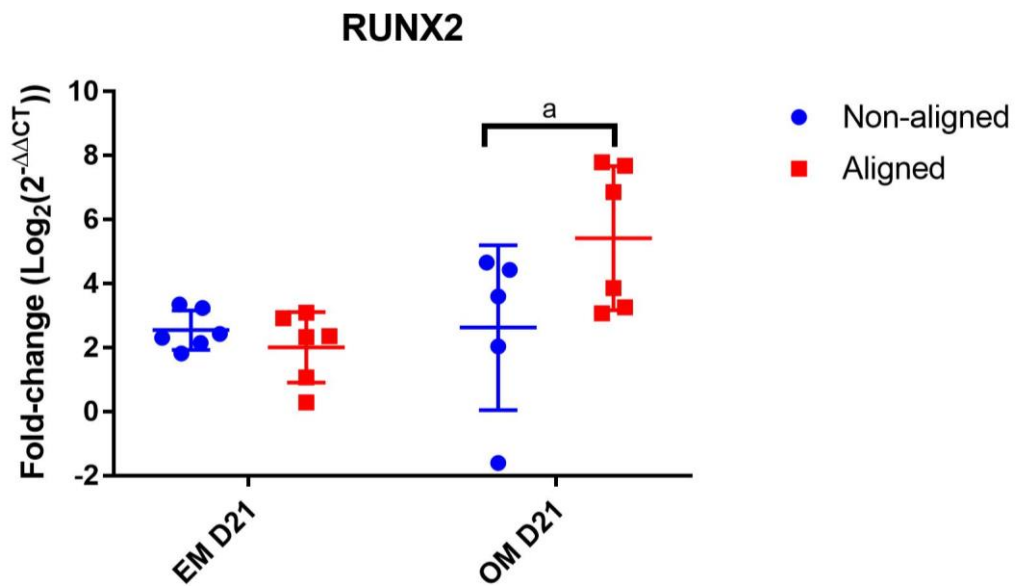


Figure 5-17: RUNX2 expression from h-TERT Y201 cells at day 21, cultured in either EM or OM. Results are shown as log₂ of fold-change, compared to EM-treated 2D controls. Results shown mean±SD (n=5-6) Statistical analysis performed using two-way ANOVA with Tukey's *post-hoc* test for multiple comparisons. Significant p values shown as a=0.0211

RhoA and YAP were also examined as genes of mechanotransduction. RhoA expression was downregulated initially when cultured to both aligned and non-aligned, whilst YAP was seen to be upregulated (**Figure 5-19**). At day 21, gene expression of RhoA is also downregulated from TCP cultured controls (**Figure 5-19**).

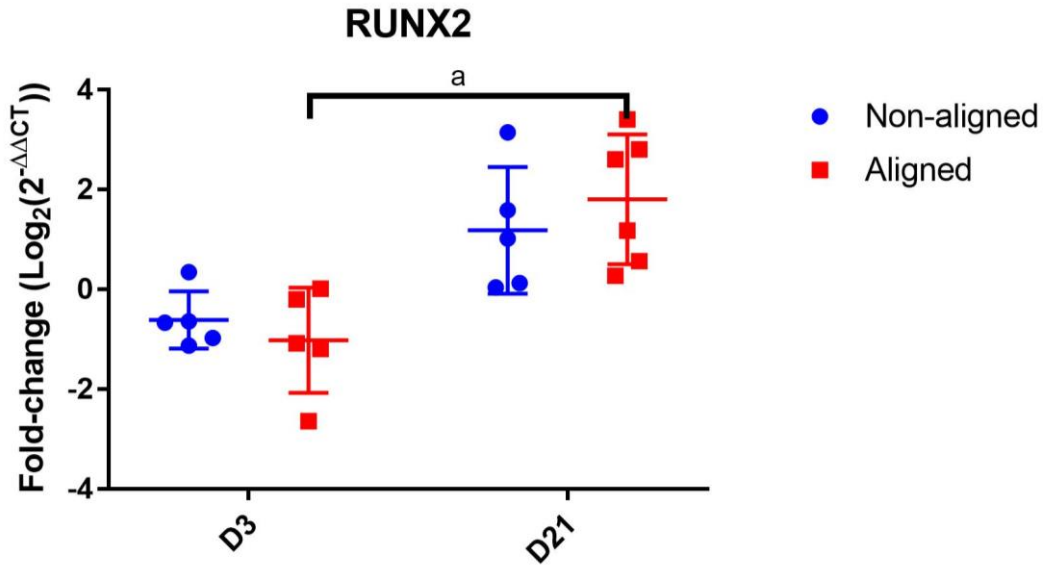


Figure 5-19: Mechanotransduction-related gene expression of Y201 cells at day 3. Shown as \log_2 of fold-change, compared to OM treated 2D controls. Results shown mean \pm SD (n=5-6). Statistical analysis performed using two-way ANOVA with Tukey's *post-hoc* test for multiple comparisons. Significant p values shown as a=0.0028.

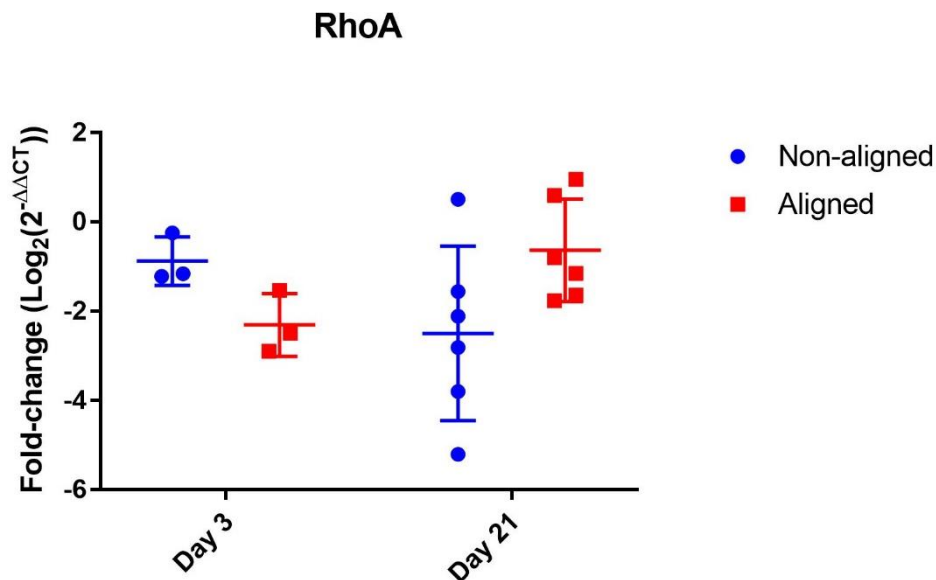


Figure 5-18: RhoA expression of h-TERT Y201 cells at days 3 and 21. Shown as \log_2 of fold-change, compared to OM treated 2D controls. Results shown mean \pm SD (n=3 (Day 3) or n=6 (Day 21)). Statistical analysis performed using two-way ANOVA with Tukey's *post-hoc* test for multiple comparisons

5.6 Collagen deposition of MG-63 cells

Collagen deposition of the osteosarcoma-derived human cell MG-63 was also assessed, to examine whether the twisting phenomenon was present in a more mature osteoblast-like cell when cultured on aligned plasma + fibronectin-coated PCL fibres. It was observed, however, that after 21 days in culture, the resulting matrix was disorganised and was not shown to have the lamellae-like organisation observed in Y201 cells (**Figure 5-21**). The collagen matrix appeared generally sparse, and the matrix quickly lost orientation 5-10 μ M from the axis of the fibres.

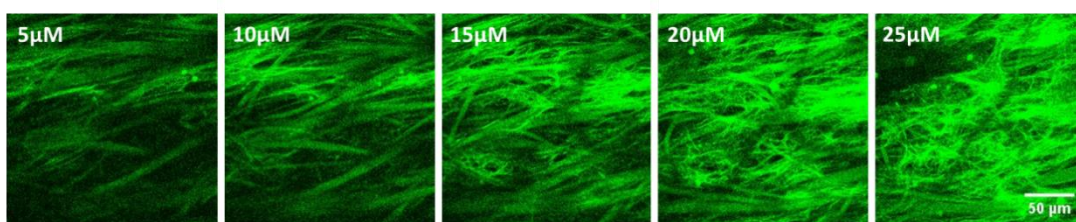


Figure 5-20: SHG images of collagen produced by MG63 cells after 21 days in culture with osteogenic supplementation. Each image represents 5 μ m slices, with the average orientation of the collagen fibres from the original PCL fibre axis written beneath. Scale bar represents 50 μ m

5.7 Discussion

5.7.1 Matrix deposition and organisation

Osteogenic differentiation on aligned and non-aligned scaffolds is widely reported, spanning across a variety of different materials. However, successful osteogenic differentiation is usually considered by the quantity of collagen or mineral produced, over the quality and organisation. For tissue-engineered constructs intended for implantation, this is often desirable, as rapidly deposited ECM allows for integration into the surrounding tissue, which can then be more gradually remodelled. However, for *in vitro* models, biomimetic replication of the mature tissues' organisation would be more desirable, to accurately represent the mechanical properties and functionality of *in vivo* bone.

This work aimed to investigate the effects of fibre alignment, more specifically on the organisation of the matrix and in particular the collagen, with the aim of producing a structure more representative of the lamellar collagen in cortical bone.

Both the aligned and non-aligned scaffolds did support the osteogenic differentiation of MSC-like Y201 cells. All conditions showed a similar upregulation of ALP activity, however, aligned fibres without fibronectin treatment showed significantly less mineralisation. Previous work on aligned and non-aligned substrates has shown differing effects of fibre alignment and osteogenesis. For example, Younesi *et al* seeded hMSCs on aligned collagen fibrous scaffolds and had a significantly lower osteocalcin expression at day 14 compared to those seeded on non-aligned fibres [253]. Similarly, Delaine-Smith *et al* also observed non-aligned fibres to better support collagen and mineral

deposition of embryonically derived human embryonic stem cell-derived mesenchymal progenitor cells (hES-MPs), but that aligned fibres better support mineral deposition and ALP activity in the murine-derived mature osteoblast cell line, MLOA-5 [61].

Remarkably, the SHG signal observed on day 7 was extremely low, compared to a relatively high stain observed via Sirius red staining. Sirius red is known to bind via its sulphonic acid groups to basic groups along the collagen molecule[254]. However, it is seen to not only stain fibrillar collagens but also other proteins containing basic amino acids, as well as non-fibrillated tropocollagen molecules[255]. Alternatively, the SHG signal allows for the visualisation of the fibrillar collagen quantity and orientation and can give a qualitative assessment of the fibrillar collagen present [62], [86]. As SHG generation requires a non-centrosymmetric molecule, signal generation is dependent on the molecule being sufficiently organised [85], [86]. Furthermore, the epi-generated SHG signal is seen to be wavelength dependant. Green *et al* modelled the theoretical wavelength dependency of two differentially sized fibrils and showed that small changes in fibril diameter may emit SHG signal at differing wavelengths[85]. The high degree of staining compared to the poor SHG signal observed may suggest that although collagen is being produced, it is not yet fibrillated into a mature, organised matrix. It may also be concluded that quantification of collagen via Sirius red staining on its own, without a more visual qualitative assessment such as SHG or immunostaining, may not be a definitive method for assessing collagen production during osteogenic differentiation.

Collagen quantity was also seen to not significantly increase between days 21 and 28, however, SHG analysis showed that the collagen twisting observed on the

aligned scaffolds further progressed in its overall pitch. This may suggest that the collagen is being physically manipulated through either cell action or a remodelling process, over being deposited directly in a lamellar-like formation [68], [69], [199].

The gradual shift in the orientation of the collagen with height was similar to what was observed in the work by Tetteh *et al*, where the collagen produced by a murine osteoblast cell line MLO-A5 was seen to organize in a lamellar-like fashion on a different polymer scaffold (polyurethane). Examinations of the lamellae fibril organisation *in vivo* have generally shown a periodicity of about 5-7 μ m, and gradual change of fibril direction, varying from 10-60° from the initial orientation of the lamellae closest to the osteon's centre [90], [256], [257]. Within the present work, although the difference in collagen orientation is comparable to that of the *in vivo* lamellae, it occurred over a much larger depth of 35-45 μ m, similar to what was also observed by Tetteh *et al*, where the twisting phenomenon was reported over distances of 36-84 μ m.

For non-aligned constructs, UTS was unchanged when cultured in EM, which may be explained by a more disorganised collagen matrix without significant mineralisation. For aligned constructs, when culturing within EM, where no lamellar-like twisting of collagen was observed, it can be seen that the UTS and toughness were also significantly less than when cultured in OM. Furthermore, it was also seen that h-TERT Y201 cells cultured on aligned constructs in OM facilitated a greater fold-increase in mechanical properties compared to non-aligned, despite both conditions having no significant differences in the quantity of mineral and collagen. It therefore may be suggested that it is the lamellar-like twisting that may be the cause of the improved mechanical properties observed

when h-TERT Y201 cells are cultured on aligned fibres. The twisted plywood phenomenon observed in load-bearing bone is theorised to be an ideal structure to cope with compressive and tensile loads of various directions, as well as an efficient barrier to crack propagation [258]–[261]. Furthermore, it is known that aligned collagen acts as a guide for mineralization, with the central axis of hydroxyapatite crystals running parallel to the orientation of the collagen[57], [65]. Alignment of hydroxyapatite crystals is seen to play a critical role in the bone matrix quality and final structural integrity of regenerated bone, providing greater mechanical strength to an overall tissue, compared to simply an increased mineral density [57], [262]. The use of aligned scaffolds and their ability to facilitate a lamellar-like twisting of collagen may therefore be suggested as a route for producing scaffolds with a superior capacity to mimic the mechanical function of lamellar bone over non-aligned scaffolds. Furthermore, although these scaffolds were suggested for use in *in vitro* models, it may be of interest to develop these further for an application within bone tissue engineering.

Lamellar-like self-assembly of collagen on aligned topographies has been previously reported to occur in other cell types, where the tissue of origin also has a lamellar collagen structure. In one study, corneal fibroblasts were observed to originally align along a topographically aligned substrate, but after 9 days of culture, showed an observable difference in the orientation of the cells growing above the original layer[263]. This was at an orientation of $53^{\circ} \pm 8$ relative to the first corneal fibroblast layer. When the authors repeated using dermal fibroblasts, this same shift was not observed, with the second layer becoming disorganised and without orientation. The same authors also presented a similar occurrence in smooth muscle cells, showing an angle difference of 38.55 ± 4.24 degrees compared to the first layer[263]. This study used mature, differentiated

cells, however. Interestingly, in the case of corneal lamellae or the annulus fibrosus, the alternating collagen pattern is observed only to form during embryonic development and without an intermediate, disorganised phase[264]. In comparison, lamellar bone is formed throughout adult life, through a gradual remodelling of the disorganised woven bone[18]. To my knowledge at the point of writing, the work presented in this thesis is the first instance of a self-assembled lamellar-like twisting of collagen produced from an originally undifferentiated cell.

The addition of fibronectin coating on the scaffold was assessed, due to its previously discussed synergistic effects on collagen organisation. It was hypothesised that without the exogenous source of fibronectin that would normally be supplied through FBS supplementation, there may be a delay in the formation of a mature and organised matrix of collagen. However, although it was shown that the addition of fibronectin coating in 2D did significantly increase the collagen deposition, there was no significant increase in the deposition of collagen observed when fibronectin was coated onto fibres. When collagen organisation was observed using the SHG technique, both fibronectin coating and plasma-only coating resulted in a lamellar-like structure of the collagen. However, with the addition of fibronectin, the collagen did appear to be twisted to a significantly greater degree than observed on plasma-coated only scaffolds. As discussed in chapter 3, there is a strong interaction observed between the deposition of collagen and fibronectin. Paten *et al* observed that fibronectin is able to accelerate the nucleation of type I collagen deposition into fibrils *in vitro*, resulting in a co-localised network of collagen and fibronectin [76]. Fibronectin is seen to interact with the $\alpha 1(I)$ chain of collagen via a gelatin-binding at amino acid residues 757–791, covering the enzymatic cleavage site and

subsequently protecting the initial collagen matrix from enzymatic degradation[265]–[267]. It has also been shown that fibronectin-templated type I collagen deposition can play a role in the enhanced migration of myofibroblasts and other cell types, resulting in more efficient remodelling of the ECM [266], [268]. Although the fibronectin-coated scaffolds would not be coated in a fibrillar form, it is shown that soluble exogenous fibronectin can be quickly fibrillated in the presence of cells and collagen[81]. Therefore, the enhanced exogenous source of fibronectin via the coating protocol may assist in the catalysation of matrix reorganisation and subsequent increase in differential orientation.

When cultured in the absence of dexamethasone (DM), collagen was seen to be deposited only in the orientation of the PCL fibres, with no observable twisting of the collagen with height. These results may suggest that the orientation is a product of the cell's osteogenic differentiation. However, qPCR analysis showed that both aligned and non-aligned fibres did seem to mildly induce osteogenic differentiation, although to a lesser extent compared with the samples cultured in DM directly on tissue culture plastic. It is well established that fibres, both aligned and non-aligned have the potential to improve matrix deposition and osteogenesis, however many of these are supplemented with dexamethasone or other differentiation-inducing factors [149], [186], [226], [269]. Some studies do explore the effects of the fibres alone, without osteogenic supplementation, and observe various markers of differentiation, indicating that osteogenesis may occur through a topographically mediated mechanism. Wang *et al.* similarly observed that RUNX2, as well as osteocalcin, was upregulated by rat MSCs on poly(3-hydroxybutyrate-co-3-hydroxy-hexanoate) fibres when cultured in non-osteogenic media, with aligned fibres showing greater upregulation than non-aligned. In osteogenic media, markers were seen to be expressed similarly [253].

Delaine-Smith *et al.* also showed that ALP activity can be increased in the embryonic MSC cell line hES-MPs without the addition of dexamethasone, whilst Badami *et al* conversely showed that the MC3TC-E1 osteoprogenitor cell line showed no increase in ALP when cultured on non-aligned fibres of varying diameters without differentiating factors[226]. However, as MC3T3-E1 cells are pre-osteoblasts, they can be further differentiated without the addition of dexamethasone and only the addition of ascorbic acid and β -GP. In the present work, RUNX2 was upregulated in Y201 cells grown on fibres in EM but was upregulated to a greater extent when cultured in OM. RUNX2 is first expressed in pre-osteoblasts. It is then upregulated in immature osteoblasts before finally being downregulated at later stages of differentiation[270], [271]. It may be theorised that topographical cues provided by the fibres may assist with earlier stages of differentiation of MSCs into pre-osteoblasts, but that further stimulation via the form of differentiating factors such as dexamethasone may be required to reach later stages of maturity.

There are several theories as to why osteogenic differentiation may occur on fibres even in the absence of differentiating factors. In the present work, the cellular morphology of the h-TERT Y201 cells can be seen to be elongated on the fibrous scaffolds, which is a well-documented phenomenon of culturing cells on aligned fibres[61], [272], [273]. It has been observed that changes that increased actin-myosin-generated tension, caused via cytoskeletal spreading, can result in increased RhoA activity [115]. McBeath *et al* showed that by increasing RhoA activity, it was possible to switch hMSC commitment to an osteogenic lineage [114]. Furthermore, with the use of nanofibrous micro-islands for single cell culture, Chang *et al* showed that there was significant upregulation of Rho-associated protein kinase (ROCK), the effector of RhoA linked to myosin II, as

well as increased ALP activity indicating osteogenesis. Furthermore, with the addition of a ROCK inhibitor, ALP activity was subsequently inhibited[274]. In the present work, however, it was seen that RhoA was downregulated on both aligned and non-aligned fibres in comparison to TCP on both day 3 and day 21. In the previously discussed studies, however, the effects on RhoA are examined at much earlier time points than day 3, usually examining a few hours after plating. RhoA is seen to reduce at higher densities, so the high confluences observed at later time points of culture on the fibres may explain the low expression of RhoA. It is also of note, that the TCP control, will have an extremely high stiffness, with cell culture plastics generally seen to have stiffnesses of around 1GPa, remarkably higher than that of PCL fibres used within this work.

When cultured in OM, both non-aligned and aligned fibres caused similar upregulation in osteogenesis-related gene expression, which may suggest that the mechanism of the collagen guidance is not due to the aligned fibres simply supporting a greater degree of osteogenic differentiation of the cells compared to non-aligned. Furthermore, when cultured in EM there is no observable collagen twisting. Therefore, it can also be assumed that the collagen orientation control is not solely related to mechanotransduction pathways induced by cellular morphology specifically on aligned fibres. It may be therefore theorised that the twisting is a combination of both mechanotransductive and osteogenesis-induced pathways.

When MG-63 cells were cultured on the aligned fibres, the orientation of the collagen did not appear to follow the orientation of the scaffolds. MG-63 is an osteosarcoma-derived cell line, and although it is frequently used as a model cell line for bone, it is known to have dysregulated functions in comparison to

healthy *in vivo* osteoblasts, as well as differential gene analysis[196], [275]. Although studies have looked at the effect of MG63 behaviour on aligned fibres, none of these have investigated collagen orientation. Wang *et al* showed that MG63 cells were able to orientate along the axis of the aligned poly(L-lactic-acid) nano-fibres, but that there was significantly less collagen produced compared to when cultured on non-aligned scaffolds or TCP controls[276]. Conversely, Tsai *et al* observed that MG-63 cells saw upregulation of osteogenesis markers RUNX2, COL1, ALP, BSP and SPP1 when cultured on aligned strontium-substituted hydroxyapatite nanofibers compared to non-aligned fibres[277]. They also observed the elongation of the cells along the axis of the aligned fibres. These results suggest that MG63 cells can sense substrate orientation and elongate along the axis, but that their capacity for orientated collagen deposition is affected, which also suggests collagen deposition orientation is not just a product of the cell's predominant orientation but is related to many other aspects of the cell's regulatory behaviours. It may be of interest to carry out a panel analysis of differential gene expression between the Y201, MG-63 and MLO-A5 cell lines, to elucidate potential pathways of interest for further study.

5.8 Summary

This chapter explored the use of fibrous scaffolds for culture and osteogenic differentiation of an MSC cell line *in vitro*. It documented for the first time a self-assembled lamellar-like structure being produced by an MSC. Furthermore, this work has been carried out in xeno-free media, in absence of FBS, minimising any variability of unknown interacting effects that may stem from FBS-derived components., increasing its translatability to be used as an *in vitro* model.

Gene analysis was carried out and showed that there was little difference in the expressed genes in cells cultured on non-aligned and aligned scaffolds, and when cultured in EM, there was still an upregulation of osteogenesis-related genes, but to a lesser extent than with OM.

- Fibronectin coating does not increase collagen quantity but may facilitate the faster reorganisation of the matrix.
- Matrix deposition on both aligned and non-aligned scaffolds is comparable in quantity, but with notable differences in organisation.
- The culture of MSC cell line Y201 on aligned fibres results in a lamellar-like twisting of collagen.
- Osteosarcoma-derived cell line MG-63 shows an inability to align its collagen.
- The resulting mechanical properties from culturing Y201 cells on aligned fibres are more greatly improved than on non-aligned.
- Expression of osteogenic markers from Y201 cells is comparable between aligned and non-aligned fibres.
- Both non-aligned and aligned fibres are able to induce osteogenic differentiation of Y201 cells
- Aligned fibrous scaffolds may be a promising material for studying the development of cortical bone and collagen dynamics.

6 Methacrylated Polycaprolactone-triol and Gelatin Methacrylate Emulsions for the Production of Stiff and Porous Bioinks for Use in 3D Cell Printing.

6.1 Introduction

Trabecular bone is inherently a porous material, organised into larger macroscale pores formed by the trabecular struts, with the cells residing in microscale pores within the struts. Therefore, to create a model of bone, it would be logical to choose a material that could recreate this multiscale porosity. With this in mind, the ideal material should have an interconnected network of micropores, into which cells can easily infiltrate. It must also be able to be formed into a material with a macroporous structure, without collapsing of the micropores. This ideally would be obtained by 3D printing, to allow constructs with more intricate geometries. Moulding and casting may also be simpler and significantly cheaper options for producing multiscale porosity, especially on a mass scale, however, those methods considerably reduce the geometrical complexity obtainable.

Emulsion templating was selected as the method of choice for the development of a trabecular bone-like material. Other fabrication methods such as porogen leaching for the development of porous scaffolds were considered. Porogen leaching involves a soluble porogen mixed with a polymer, before being

solidified and the porogens washed away with a solvent, leaving a porous construct. However, these were not chosen due to general limitations in lack of control of pore distribution, and the difficulty to produce materials with multiple scales of porosity. With the use of emulsion-templated materials, it should be possible to control pore size and 3D print into a construct with a multiscale porous structure.

Emulsion templating does, however, come with issues, with many of the components used, such as solvents, surfactants and photoinitiators, being toxic and requiring extensive post-processing. Processing steps often include solvent washes, to draw out excess solvent within the polymer, PBS washes to then remove these solvents, before ethanol washing and further PBS washing for sterility. Each one of these steps takes 1-2 days, which results in the time taken from scaffold fabrication to use for direct cell seeding to potentially over a week. This section explores an alternative method of producing an emulsion-templated porous ink, that bypasses the use of solvents and surfactants and minimises lengthy post-processing steps, as well as a potential use in live cell printing.

With minimal cytotoxic components, it may then be of interest to try and create a porous bioink that can be used to directly print live cells encapsulated within an emulsion. One common material used for bio-inks would be gelatin methacrylate (GelMA), which is widely used as a bioink due to its excellent biocompatibility and low cost. However, its poor mechanical strength makes it an unattractive option alone as a bone substitute material. Therefore, it would be beneficial to improve the overall mechanical properties of this material, through the addition of a reinforcing material with more favourable mechanical properties.

6.2 Aims and objectives.

In this section, a novel method for producing a printable, emulsion-templated bioink, with higher mechanical properties than that of pure gelMA is explored. The resulting scaffold would need to have pores large enough to allow infiltration of cells or be compatible with direct encapsulation for live cell printing. It should also be possible to process into multi-scale porous scaffolds that allow for effective media flow throughout the depths of the construct.

A further aim was to minimise the use of cytotoxic components such as organic solvents and surfactants, to reduce long post-processing steps often required with other emulsion templating protocols.

The possibility of directly encapsulating cells within a bioink for direct 3D printing would present a possibility of overcoming the size limitation of many porous scaffolds due to the poor infiltration of cells.

To this extent, the main objectives of this chapter were:

1. Develop an emulsion without the need for toxic solvents and surfactants.
The resulting emulsion must be stable at room temperature for at least a short period to enable printing and cross-linking.
2. Characterise the material's properties, including morphology and mechanical properties.
3. Examine the material's biocompatibility with seeded cells.
4. Explore the potential for encapsulation and subsequent live-cell printing.

6.3 Experimental Design

Different formulations were explored, with varying percentages of PEO, alginate and gelMA, and imaged via fluorescent and confocal imaging in order to assess the construct morphologies. Mechanical testing was also performed.

Cell culture was carried out on the scaffolds, using the osteosarcoma cell line MG-63 and murine preosteoblast cell line MC3T3-E1. Various mechanisms of scaffold seeding were explored, including post-fabrication seeding, where cells were seeded onto pre-cured scaffolds, and encapsulation, where cells were directly encapsulated before the construct is cured.

6.4 Results

Materials and methods specific to this chapter can be found in Chapter 2, section 2.8.

6.4.1 Stability

GelMA and 3PCLMA warmed to room temperature and thus in their liquid state, were able to be mixed to form an emulsion, without the addition of any surfactants. The formulation of each emulsion examined, and the outcome of its stability after incubation for 1 hour at 37°C is outlined in **Table 10**. Without the addition of alginate to the gelMA, the emulsions did not appear to be stable, beginning to separate almost immediately after mixing. After 1 hr of incubation at 37 °C, the two phases had completely separated, with gelMA visible as the aqueous phase on top, and the 3PCLMA sitting at the bottom (**Figure 6-1**). By increasing the viscosity of a material, it is possible to increase its kinetic stability[278]. Therefore it was seen that with the addition of alginate, the

emulsions became increasingly stable, with an increase of PEO also further increasing the stability. With 6 % (w/w) PEO, the resulting emulsions were extremely viscous and showed no visible phase separation after 1 hr incubation at 37 °C in all conditions other than those with no added alginate. Finally, with 5 % alginate, all conditions were shown to be stable.

Table 10: Compositions tested with varied wt/wt% of PEO and alginate. Stability was assessed after 1hr after incubation at 37°. Emulsions were considered to be stable if no visible separation was observed.

Figure Label	Sample ID	PEO (wt%)	Alginate (wt%)	Stable during mixing	Stable after 1hr @ 37°
1	P3A0	3	0	N	N
2	P4A0	4	0	N	N
3	P5A0	5	0	N	N
4	P6A0	6	0	N	N
5	P3A1	3	1	Y	N
6	P4A1	4	1	Y	N
7	P5A1	5	1	Y	N
8	P6A1	6	1	Y	Y
9	P3A3	3	3	N	N
10	P4A3	4	3	N	N
11	P5A3	5	3	N	N
12	P6A3	6	3	N	N
13	P3A5	3	5	Y	Y
14	P4A5	4	5	Y	Y
15	P5A5	5	5	Y	Y
16	P6A5	6	5	Y	Y

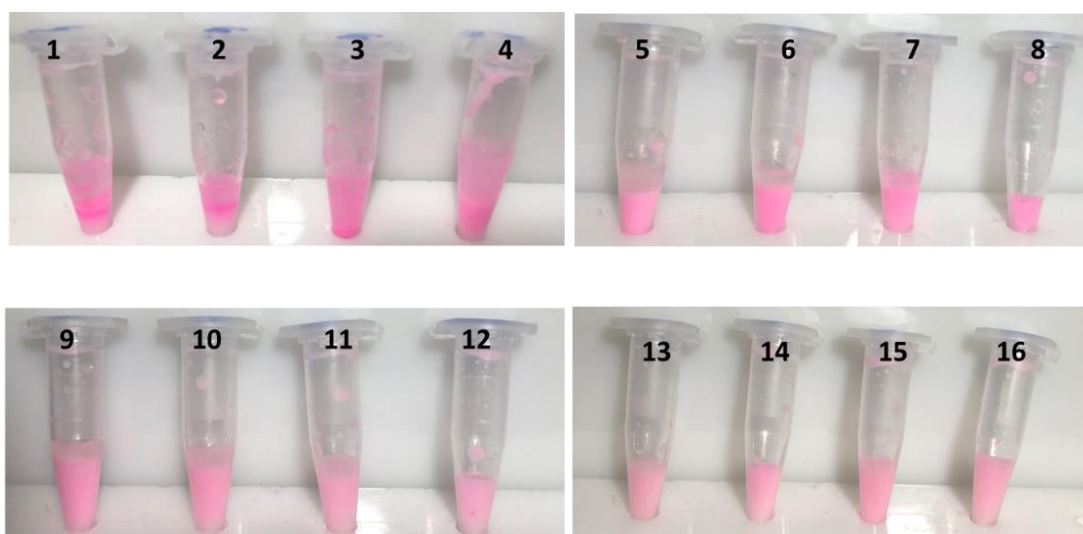


Figure 6-1: Emulsions after 1hr of incubation at 37°C with varying wt/wt% of alginate and PEO in standard 1.5 mL Eppendorf tubes . Rhodamine B was added to assist with visualisation of separation of the aqueous and oil phase. Labels correspond to samples outlined in Table 1.

6.4.2 Fluorescent imaging

Fluorescent staining through the addition of rhodamine B allowed for the observation of the porosity of the material (**Figure 6-2**). It was seen that all emulsions had a porous structure but there was no relationship between alginate and PEO concentrations and the overall morphology of the resulting emulsions.

Sample 5 % PEO with 3 % alginate (P5A3) was then used for all future work due to its stability and lower alginate percentage. Although 5 % alginate generally showed better stability, increasing the alginate concentration may reduce the overall ability of cells to spread and proliferate. This is due to the increased viscosity of the aqueous phase which is predicted to hinder the cell's ability to spread and proliferate[153].

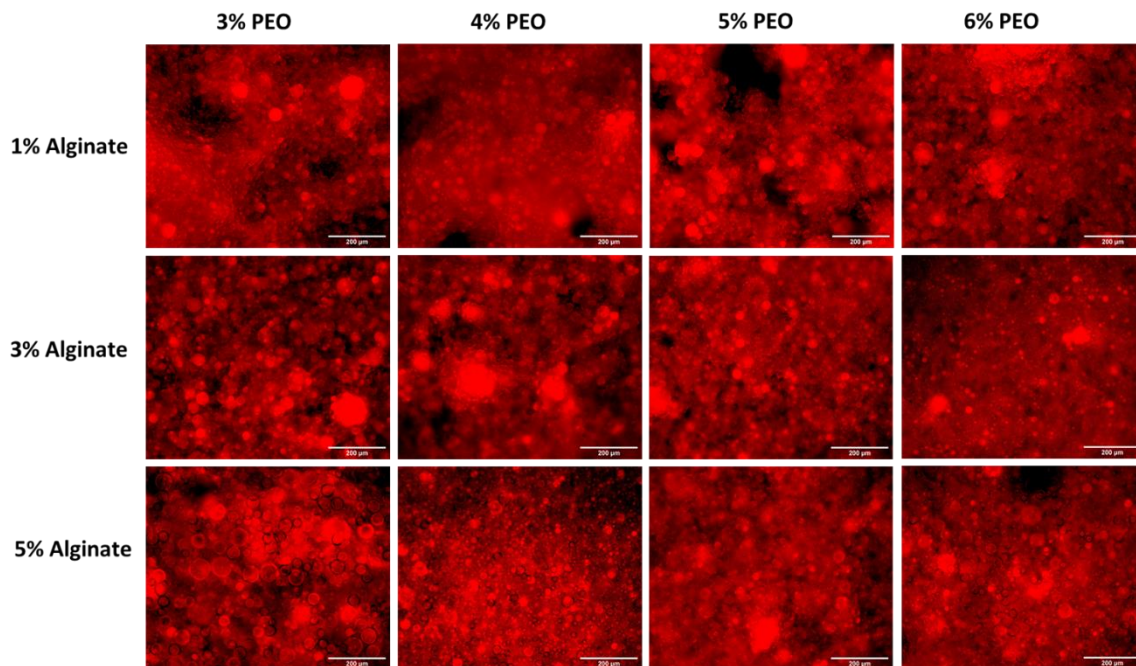


Figure 6-2: Fluorescent microscope images of 60% emulsions imaged with varying percentages of alginate and PEO. Samples labelled with Rhodamine B and imaged at $\lambda_{ex}550/\lambda_{em}573$ nm. Scale bar at 200 μ M

P5A3 was then imaged with varying aqueous phase percentages to assess its effects on the aqueous phase bead size- from this point forward described as “pores” (**Figure 6-2**). All formulations produced emulsions, with a general decrease in pore size with increasing aqueous phase percentage (**Figure 6-3**). With lower aqueous phase percentages, there was a large distribution of pore sizes compared to the higher aqueous phase percentages.

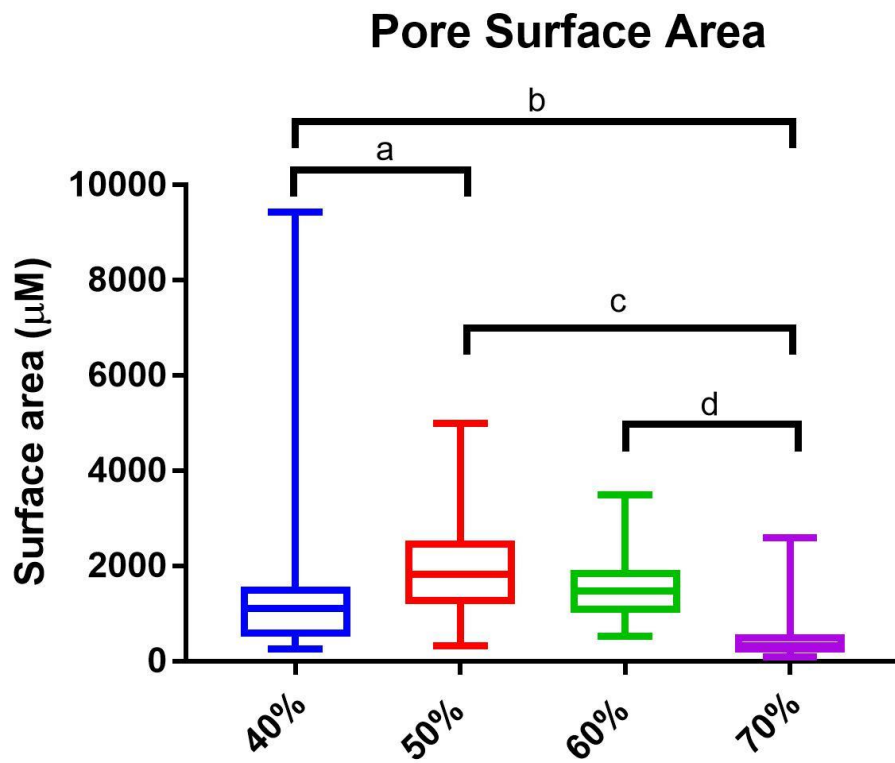


Figure 6-3: Analysis of pore size of 3PCLMA emulsions at varying degrees of the aqueous phase. Graph shows the mean \pm SD of 100 pores measured using imageJ. Statistical analysis performed using Kruskal-Wallis with Dunn's *post-hoc* test for multiple comparisons. Significant p values shown as a=0.008 b<0.0001 c<0.0001

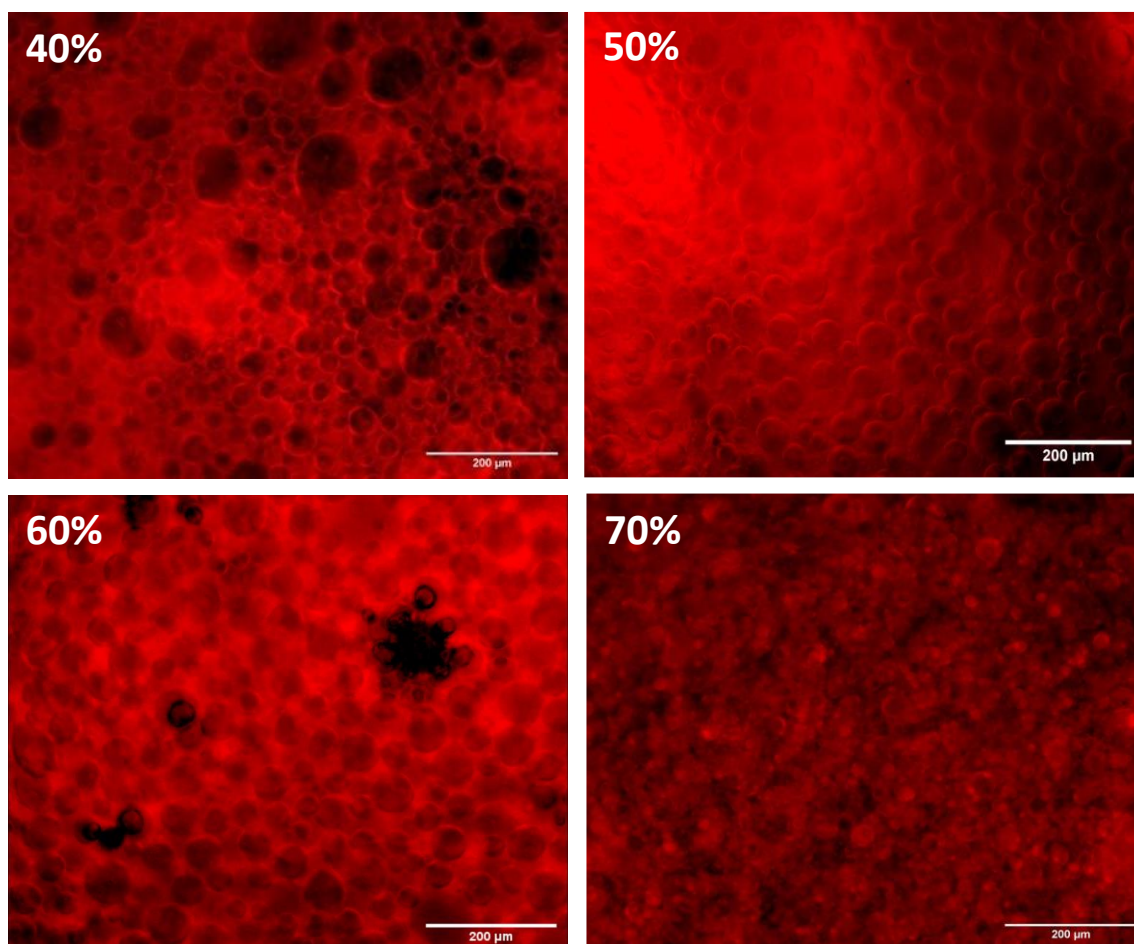
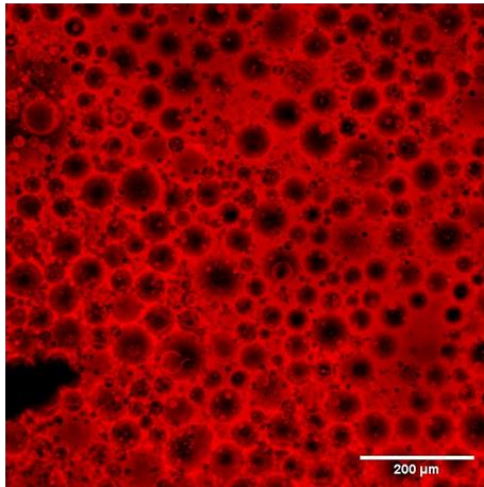


Figure 6-4: Fluorescent microscope images of P5A3 emulsions imaged with varying percentages of aqueous percentages. Samples labelled with Rhodamine B and imaged at $\lambda_{ex}550/\lambda_{em}573$ nm. Scale bar at 200μM

Samples were left for 48 hours in EM, to allow for total elution of the PEO within the scaffold. When imaged using confocal microscopy, 1 hour after curing, there are discrete pores that do not appear to be interconnected. However, after 48 hours in EM, it is observed that there is an extremely interconnected and porous network (**Figure 6-5**).

1 hour post-curing



48 Hours in EM

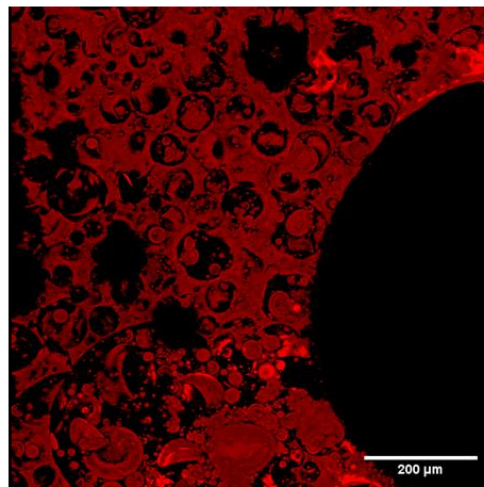


Figure 6-5: Confocal images of 60% emulsions stained with Rhodamine B (PCLMA, red) either immediately after curing (Left), and after 48 hours in expansion media (EM) (right), to allow for elution of polyethylene oxide (PEO) Scale bar at 200 μ M.

6.4.3 Mechanical testing

Mechanical testing was carried out after 48 hours in EM, in order for the remaining PEO to elute out. The stress-strain curves of the material with increasing aqueous phases show the material has a large elastic region before brittle fracture (**Figure 6-6**)

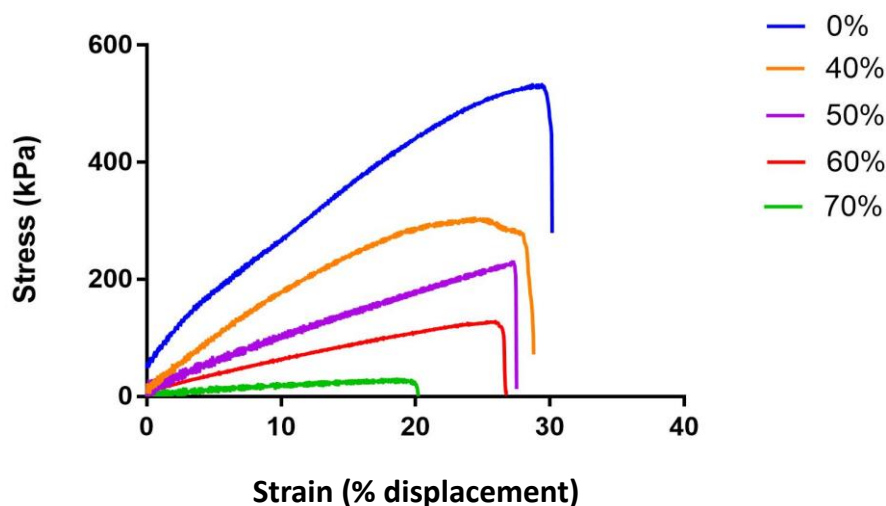


Figure 6-6: Representative tensile stress/strain curves of 3PCLMA emulsions with varying aqueous phase percentages.

Mechanical testing showed there was a linear relationship between the percentage volume of gelMA and the resulting elastic modulus (**Figure 6-6 A**).

At 70 % gelMA, the elastic modulus of the resulting emulsion was increased to 0.16 MPa, compared to 3.08 kPa in pure 5% gelMA [279]. With the addition of 40 % gelMA with respect to 3PCLMA, the elastic modulus was increased over 10-fold to 1.7 MPa, indicating that the stiffness of the emulsion was reinforced with the addition of the 3PCLMA. The ultimate tensile strength also showed a linear relationship up to 60 %, but with a larger decrease in UTS for 70 % emulsions (**Figure 6-7 B**).

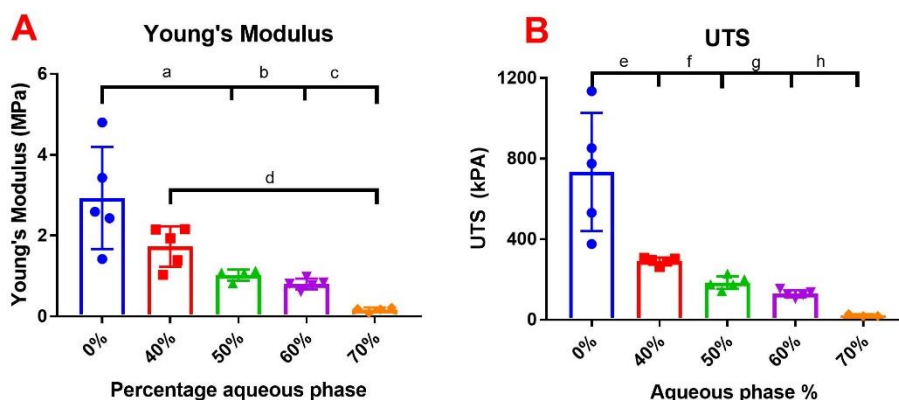


Figure 6-7: Young's modulus (A) and ultimate tensile strength (B) of 3PCLMA emulsions with varying aqueous phase percentages. Results show as mean \pm SD (n=5). Statistical analysis performed using one-way ANOVA with Tukey's *post-hoc* test for multiple comparisons. Significant p values shown as a=0.0028 b=0.0005 c=<0.0001 d=0.0153 e=0.0008 f-h=<0.0001

Autoclaving of the pure 3PCLMA was investigated, to assess whether it can be sterilised without any significant changes to its mechanical properties. It was seen however, after autoclaving at 121 °C for 20 minutes, there was a significant decrease in Young's modulus of the material (**Figure 6-6A**). There was also a decrease in UTS, but with no statistical significance ($p=0.1549$) (**Figure 6-6B**).

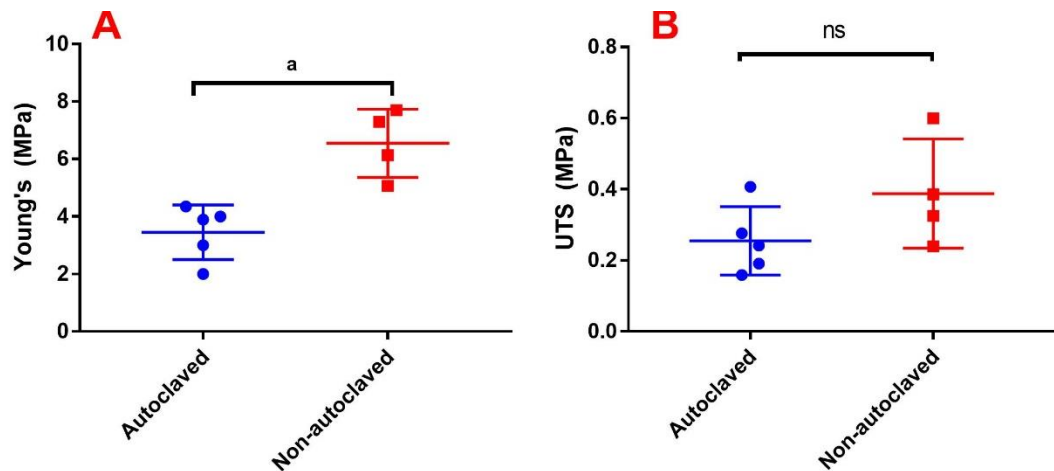


Figure 6-6: Young's modulus (A) and ultimate tensile strength (B) of pure 3PCLMA after autoclaving at 121°C for 30 minutes. Results show as mean \pm SD (n=5) Statistical analysis performed using an unpaired t-test. Significant p values shown as a=0.0033 and ns=0.1549

6.4.4 Addition of hydroxyapatite.

HAp was added to the emulsions and its effect on mechanical properties was assessed (**Figure 6-7**). At 1 % HAp, there was no significant difference in Young's modulus or UTS compared to 0 % HAp. However, with 5 % and 10 %, there was a large and significant decrease in both Young's modulus (**Figure 6-8A**) and UTS (**Figure 6-8B**)

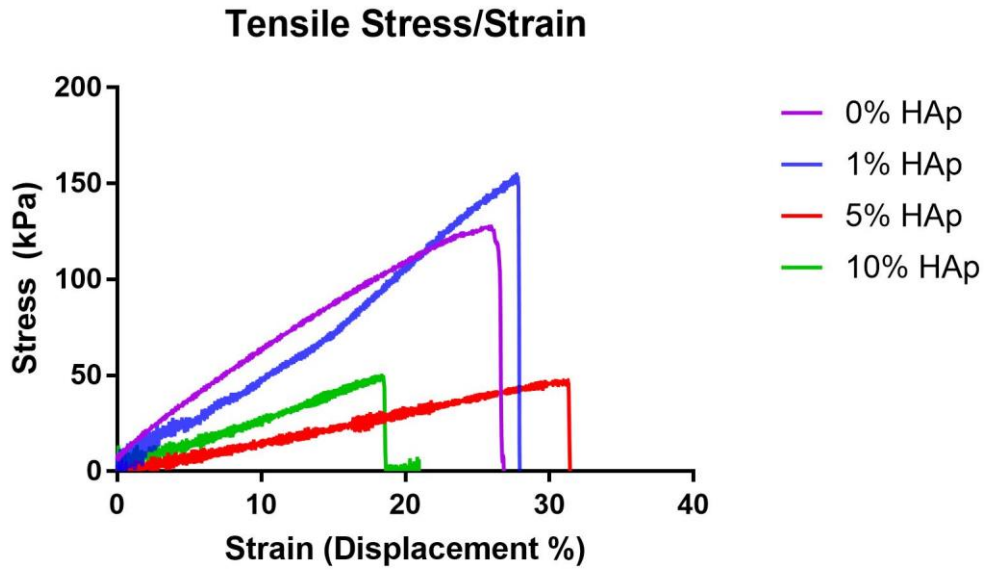


Figure 6-7: Representative tensile stress/strain curves of 60% aqueous phase 3PCLMA emulsions with varying degrees of HAp dispersed within the oil phase.

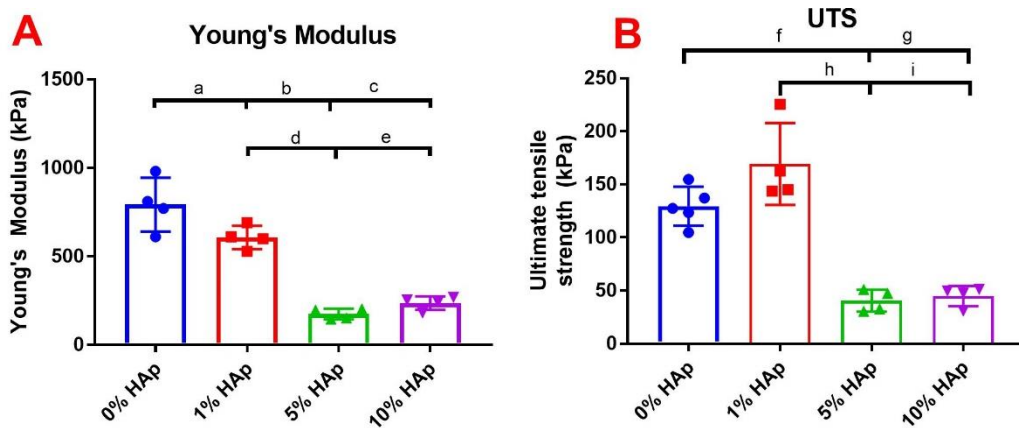


Figure 6-8: A) Young's modulus and **B)** ultimate tensile strength of 60% aqueous phase 3PCLMA emulsions with varying degrees of HAp. Results show as mean \pm SD (n=5). Statistical analysis performed using one-way ANOVA with Tukey's *post-hoc* test for multiple comparisons. Significant p values shown as a=0.047 b=<0.0001 c=<0.0001 d=<0.0001 e=0.0003 f=0.0002 g=0.0004 h=<0.0001 i=<0.0001

6.4.5 Effects of UV Exposure on cells

The effects of prolonged UV exposure directly on the MG-63 cells were assessed, to establish the maximum duration that the cells can be exposed without any

adverse effects. Cells can all be seen to maintain their elongated, fibroblast-like morphology (**Figure 6-9**)

Initial seeding of the cells showed that regardless of the exposure time, there were no significant effects of UV exposure on the cell's ability to attach to the TCP, and growth was not affected at any point in culture (**Figure 6-10 A**). The culture was then carried out for a further 14 days, and the cells were assessed for their matrix deposition, including mineral and collagen.

It was seen that after 14 days, there was no significant difference in the mineral or collagen produced by the MG63 cells at any dose tested (**Figure 6-10 A-B**).

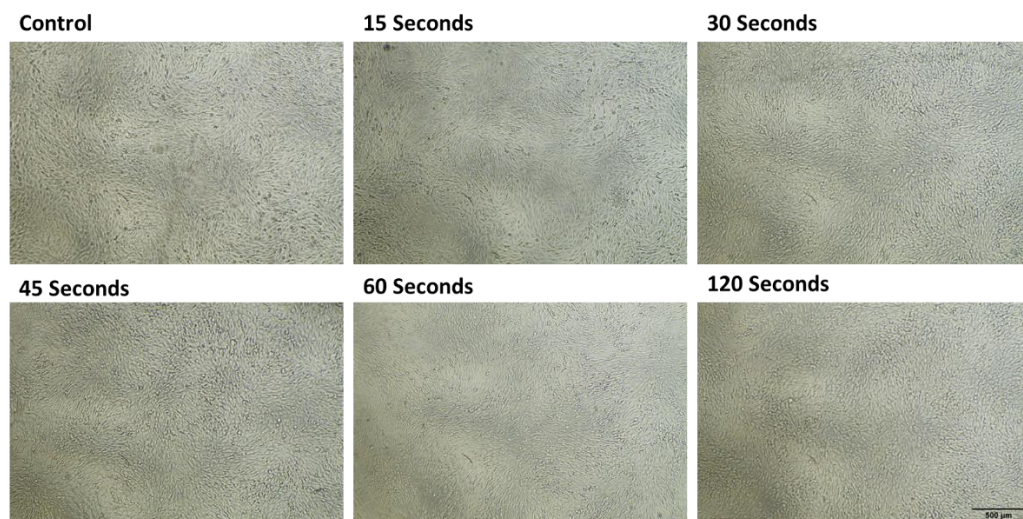


Figure 6-9: Light microscopy images of MG63 cells after 14 days of culture, with varying degrees of exposure to UV. Scale bar at 500μM.

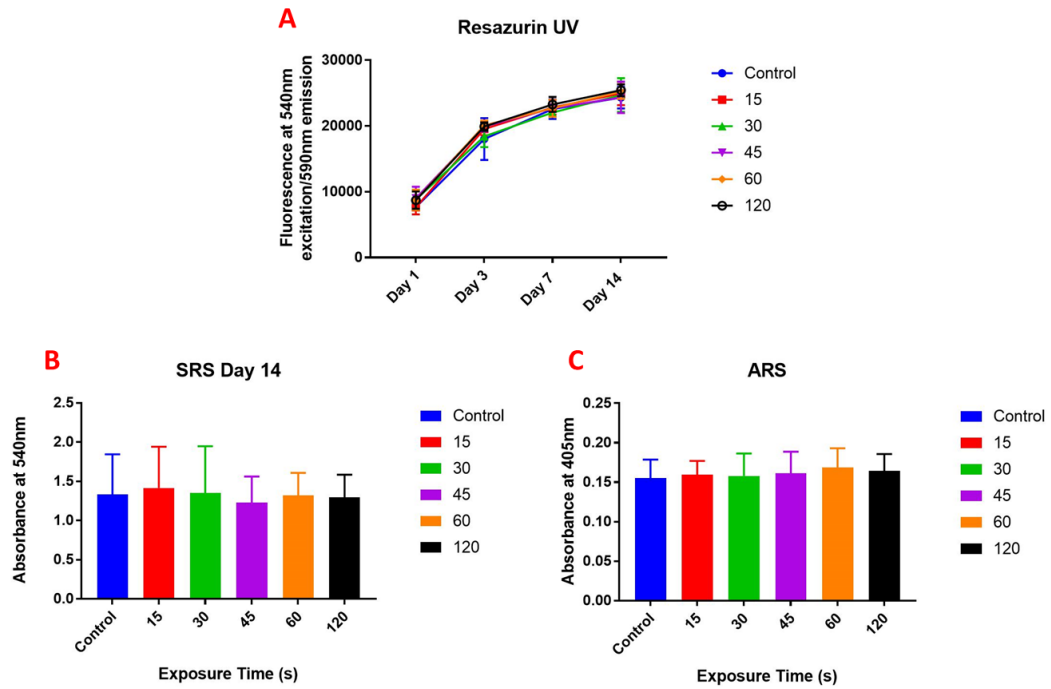


Figure 6-10: Assessment of the metabolic activity and matrix-producing potential of MG63 cells exposed to UV for varying durations. It was seen that there were no significant effects of exposure duration on either metabolic activity or matrix production. Results shown as mean \pm SD (n=9) Statistical analysis performed using one-way ANOVA with Tukey's *post-hoc* test for multiple comparisons

6.4.6 Cell toxicity- Encapsulation

Cell encapsulation was carried out, to assess its capacity to be used as an ink directly for 3D printing. The results showed that cells were not able to survive 1-day post-encapsulation in the 3PCLMA emulsions when cultured in DMEM. In pure gelMA/alginate hydrogels, there was a significant decrease in cell metabolic activity compared to cells seeded directly onto the TCP (**Figure 6-11**).

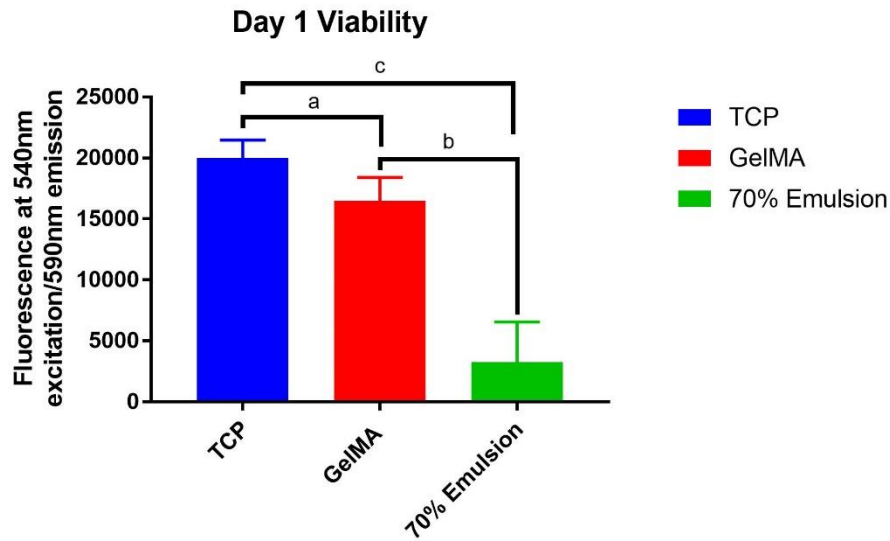


Figure 6-11: Resazurin assay for metabolic activity of cells encapsulated in GelMA/alginate, or a 3PCLMA emulsion at 70% aqueous phase 24 hours after encapsulation. Results shown as mean \pm SD (n=9). Statistical analysis performed using one-way ANOVA with Tukey's *post-hoc* test for multiple comparisons. Significant p values represented as a=0.0170 b=<0.0001 c=<0.0001

Live/Dead carried out on pure gelMA showed a large number of live cells proportionally to dead cells distributed throughout. However, on the emulsions there was a high degree of autofluorescence from the scaffold, preventing the visibility of the cells (**Figure 6-12**)

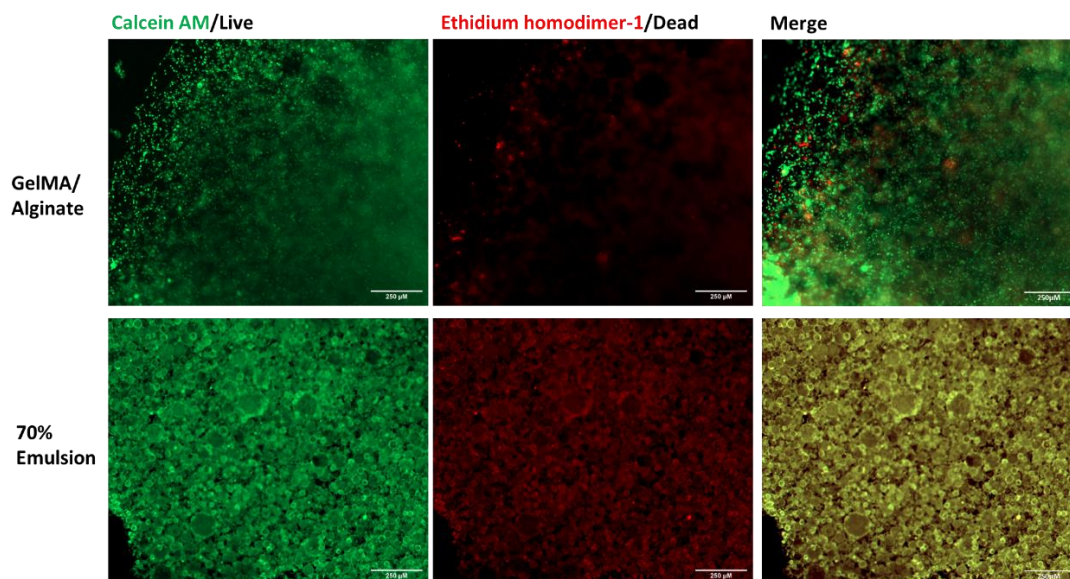


Figure 6-12: Fluorescent microscopy of 3T3 cells encapsulated in either pure GelMA/Alginate (Top) or a 3PCLMA emulsion containing 70% aqueous phase (Bottom) labelled with Calcein AM (Live cells) or ethidium homodimer-1 (dead cells). It is seen that the emulsions give off a high degree of autofluorescence, preventing the observation of live and dead cells. Scale bar at 200μM

3.1.1 Indirect toxicity testing

MG63 cells were seeded directly onto TCP, and the cured emulsions were placed on top after the cells reached 80 % confluency, to assess whether the poor survival was occurring through the encapsulation process itself, or the elution of toxic components in the scaffold into the media. After 3 days in culture, the cells were able to continue proliferating. It was seen that the addition of a washing step post-fabrication did have a significant increase in the metabolic activity of the cell by day 3 of culture, however, washing multiple times did not have any increased significance compared to a single wash.

Viability of MG63 cells

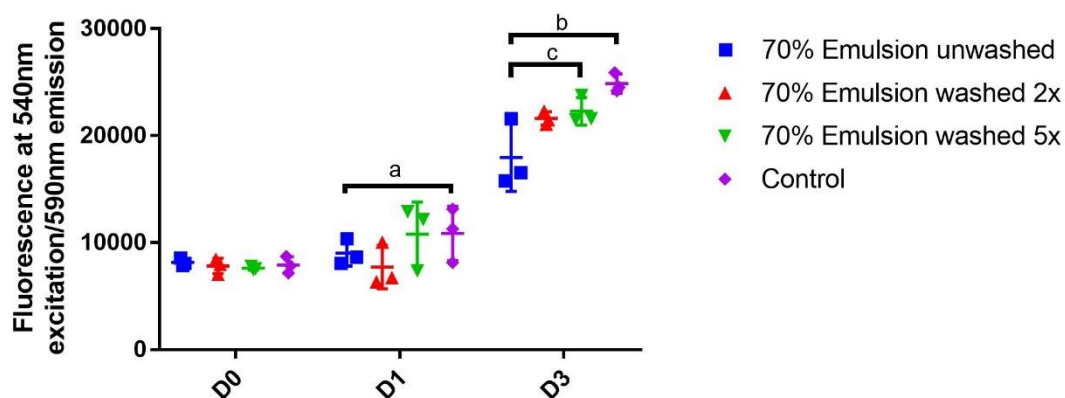


Figure 6-13: Metabolic activity of MG63 cells seeded on TCP with the addition of cured 60% emulsions directly on top. D0 represents the metabolic activity of the MG63 directly before the addition of scaffolds. Results shown as mean \pm SD (n=3). Statistical analysis performed using one-way ANOVA with Tukey's *post-hoc* test for multiple comparisons. Significant p values shown as a=0.0048 b=0.0194 c=<0.0001

6.4.7 Cellular adhesion to scaffolds

Post-fabrication and curing, MG-63 cells were seeded directly onto the scaffold. It was seen that there was some adhesion to the scaffolds, but with roughly 68.56 % \pm 4.89 of cells preferentially adhering to TCP.

Despite the lower initial attachment onto the scaffolds, the growth rate of MG63 cells between day 1 and day 7 was comparable to that of the cells seeded directly onto TCP.

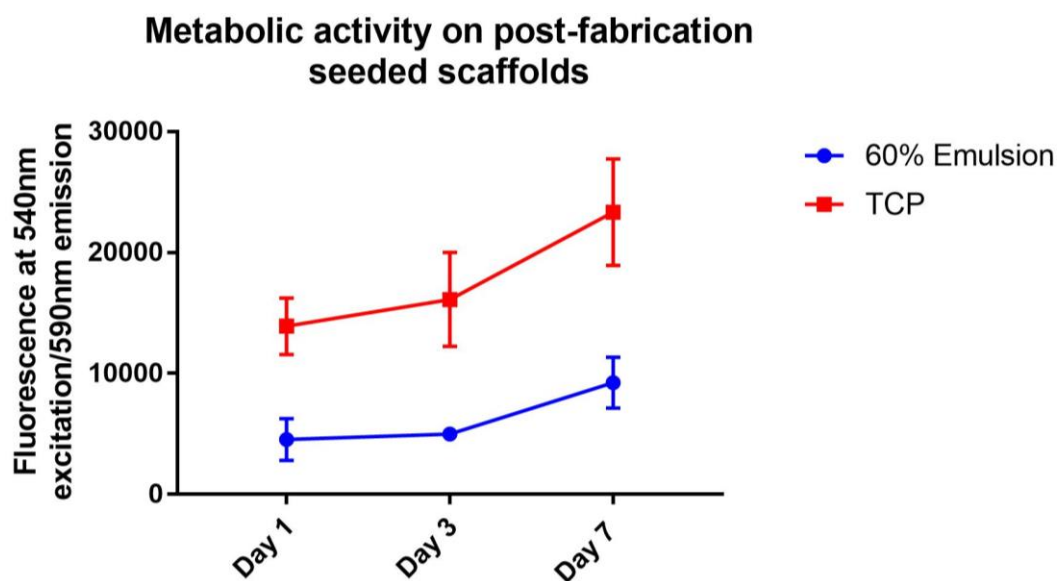


Figure 6-14: Metabolic activities of cells seeded post-fabrication on scaffolds containing a 60% aqueous phase in comparison to TCP, taken days 1, 3 and 7. Results shown as mean \pm SD (n=6)

6.5 Discussion

The final system used for the trabecular-like structure in this thesis comprised of 3PCLMA, with 5 % (w/w) PEO for the oil phase, and with 5 % (w/w) and 4 % (w/w) of gelMA and alginate respectively within the aqueous phase. The addition of 5 % (w/w) PEO into the oil phase aimed to allow for a more interconnected resulting porosity (**Figure 6-15**).

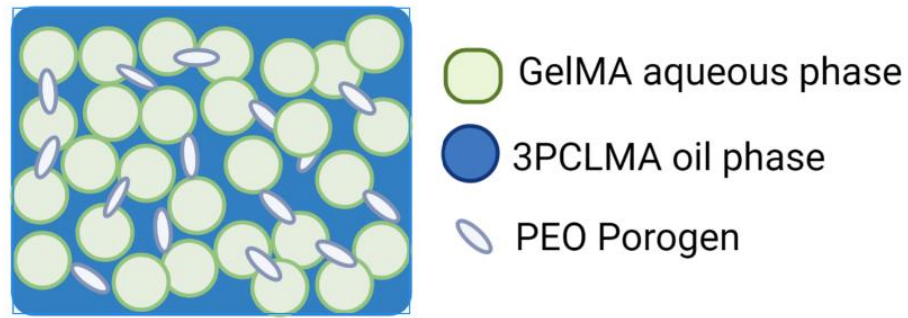


Figure 6-15: Schematic of the final system. Green represents the dispersed aqueous phase formed of GelMA and alginate, whilst the blue continuous phase is formed of 3PCLMA. PEO dispersed within the oil phase acts as a soluble porogen to form interconnects between the 3PCLMA.

Traditional HIPEs usually rely on the use of surfactants to provide the interconnected network often observed. During the polymerisation process, the contraction of the monomer pulls on the thin film surrounding the water droplets between the aqueous and oil phase, causing it to be pulled apart[153]. With the absence of solvent and surfactants, it was not expected for the resulting material to have interconnected pores. Without interconnection in the resulting material, it would be likely that the cells would be trapped within discreet capsules of gelMA and fully encapsulated by the 3PCLMA. PEO, also known at higher molecular weights as polyethylene glycol (PEG), is a water-soluble molecule, that is approved for use in humans by the FDA [280]. PEO can then be subsequently eluted off out of the 3PCLMA phase with washing steps, to leave a final material with interconnected porosity.

Compared to the long processing times required to produce traditional solvent/surfactant-based polyHIPEs, these emulsions required only pre-sterilisation of the individual components. GelMA is able to be autoclaved without adverse effects on its chemical structure, but with some minor

reduction in the achievable stiffness[281]. Alginate, however, is seen to suffer from significant changes in properties, including viscosity, molecular weight and shear strength when subjected to autoclaving[281]. In order to achieve sterility for alginate, sterile filtering through a 0.22 μM filter was necessary. However, due to the high viscosity of the alginate at the concentrations used, it was unable to pass through a 0.22 μM filter. Instead, a solution of 0.5 % (w/v) was used, then lyophilised before reconstituting at the desired percentage. By autoclaving the lyophilised gelMA and 3PCLMA, it was possible to ensure the sterility of all components of the emulsion. Although autoclaving did significantly affect Young's modulus, it was still able to polymerise and create an emulsion with comparable stability to the non-autoclaved polymer. Where higher mechanical properties are desired, alternate options for sterilisation of the material may be possible, such as UV sterilisation before the addition of a photoinitiator.

A successful emulsion was considered to have formed when mixing of the two phases resulted in an opaque, white solution with a viscous, mayonnaise-like consistency due to the refractive differences of the oil and water phases. Without the addition of alginate, the emulsions were not stable, separating into two separate phases quickly, due to the absence of a stabilising surfactant, and likely due to the lower viscosity. In a traditional emulsion system, it is necessary to add a high percentage of potentially harmful surfactants, to prevent the coalescence of the phases[147], [282]–[284]. The surfactant plays a key role in stabilising the inherently unstable system. The two immiscible phases without a surfactant would experience too high a surface tension, and immediately separate back out into the two phases. However, in this system, there is no addition of a specific surfactant, yet the emulsion remains stable. With a very viscous oil phase, as is used in this work, a notably less viscous water phase will

not be able to be mixed efficiently into the oil phase, inhibiting stable emulsion formation. With the addition of alginate, the viscosity of the aqueous phase is dramatically increased. By matching the viscosity of the two phases, it is possible to reduce the speed of coalescence, the joining of two pores to form a single pore, through a decrease in the interfacial energy, and a subsequent increase in stability[153].

Another compounding factor to the emulsion's stability may be due to the gelatin-containing aqueous phase, where it is hypothesised that gelatin may also act as a mild surfactant. As gelatin is an amphiphilic compound, it may be used as a mild emulsifier, stabilising through the Pickering mechanism[285]. Previously, gelatin has been successfully used both in combination with other common surfactants such as Span 80 and Tween 80 and on its own, to stabilise emulsions [286]–[288]. Tan *et al* recently also showed it to be effective at stabilising at very low concentrations of less than 0.5 % (wt) gelatin [287]. It may be hypothesised that small amounts of the gelatin backbone remaining in the gelMA may be present, acting as a physical barrier between the two phases and stabilising through the Pickering mechanism.

There was a general decrease in pore size with an increase in aqueous phase percentage. This was an expected result, as it is largely reported that with increasing aqueous percentage in emulsion, there is a decrease in overall pore size[289], [290]. However, within the present work, there was a large variability in the pore size within a single emulsion. This may be explained by the fact mixing was carried out manually in small batches within an Eppendorf to conserve material. There are likely discrepancies due to human error with the shear applied to each sample with manual mixing, which may explain the

variation of pore sizes, as it is commonly seen that increase mixing speed results in reduced pore size of emulsions due to the increased shear energy [289], [290].

The mechanical properties of the material were generally shown to increase linearly with increasing 3PCLMA across a range of 1.7 MPa-0.16 MPa, which suggests the material is mechanically tuneable. This may provide alternate applications across a range of stiffness requirements. For example, nerve tissue has Young's modulus of around 0.6–8 MPa, whilst cartilage production by chondrocytes is seen to benefit from stiffnesses 20-30 kPa[291]–[293]. The change in Young's modulus follows a linear relationship between the volume fraction of gelMA and the resulting stiffness. As there is no dramatic decrease in modulus or strength even when the material reaches >50% wt gelMA, this suggests that there is a strong interfacial bonding occurring between the gelMA and 3PCLMA phases, likely via chemical-crosslinking of the methacrylate groups on both GelMA and 3PCLMA.

The proposed gelMA/3PCLMA emulsions may also have potential applications for producing scaffolds with a stiffness gradient, which has been seen to be desirable for various applications, particularly within cartilage regeneration. Previous attempts have been made with the use of laminar models, with distinct layers to represent different regions of the osteochondral interface[6], [10]. Issues arise, however, at the interfaces of these models, where discontinuities in material properties result in stress concentrations or delamination of the layers [138], [294]. To effectively model the gradual changes in stiffness within cartilage tissue, it may be necessary to use a gradient scaffold which mimics the range of continuous changes that exist throughout the osteochondral interface, such as changes within its mechanical and/or biochemical properties. With the use of an

ink with tuneable mechanical properties, it should be possible to print a gradient scaffold without delamination of the layers. *Liu et al.* describe a novel 3D printing design for the simultaneous spatial control of up to 7 different bio-inks, each with a distinct capillary combined into a single point in a print head [295]. Within the same study, the use of varying hydroxyapatite concentrations within gelMA/alginate hydrogels, it was possible to create a near-continuous gradient with the combination of multiple nozzles and the ability to mix and extrude simultaneously.

Incorporation of HAp is a common method for increasing the osteoconductive properties of a material and is very widely combined with many different materials for uses in tissue-engineered bone biomaterials [186], [187], [192], [198], [296]–[300]. HAp, however, is extremely brittle and alone has very poor tensile strength. Depending on the material to which HAp is added, it may result in an increase or a decrease in the desired mechanical properties, as this is affected by the interfacial bond formed between the HAp particles and the other materials within the composite [198], [301], [302]. Within the present work, the addition of over 5% was seen to have a dramatic effect on the mechanical properties, significantly reducing the Young's and UTS, whilst 1% was seen to have no effect. A similar behaviour was observed by *Hu et al.* when nano-hydroxyapatite was combined with PCL and silica to form a Pickering HIPE [179]. It is suggested that a high proportion of HAp nanoparticles might form aggregations throughout the material, leading to a poorly distributed stress transfer, therefore decreasing the subsequent mechanical properties[302].

Although the addition of hydroxyapatite at 1% wt showed to have little effect on the overall mechanical properties compared to higher proportions, this small

percentage may not be enough to provide any significant biological relevance. Hydroxyapatite when combined within polymers for the goal of creating a more osteoinductive material is generally seen in much higher proportions than 1 %. For example, both Cestari *et al* and Hu *et al* used a 15 % wt hydroxyapatite in a PCL scaffold with the aim to produce bioactive, porous materials for bone tissue engineering, whilst hydroxyapatite-polyethylene compounds have been shown to have bioactive properties at around 20-30 % vol [179], [303], [304]. Choi *et al* investigated a range of hydroxyapatite percentages from 0-20 % wt in PCL, to electrospin aligned fibres for bone tissue scaffolds and reported no significant increase in ALP at 5 % wt hydroxyapatite[305]. As 1 % wt hydroxyapatite was unlikely to add any additional bioactive properties to the scaffold, and provided no mechanical benefits, it was not used for any future investigations.

When cells were added to the emulsion, it was seen that there was no survival from even 1-hour post-encapsulation. Therefore, it was necessary to explore the reasons for this poor outcome. The first hypothesis was that the cells were unable to survive due to damage caused by UV irradiation. To test this hypothesis, MG63 cells were exposed to UV light for increasing durations of time, before being cultured for 14 days, to assess the effects of UV on their survival, growth and osteogenic behaviours.

It was observed that even at the highest UV duration, there appeared to be minimal effects on the resulting survival and matrix deposition capacity. UV exposure is known to be highly damaging to cells, causing DNA damage, oxidative stress and protein denaturation, dependent on whether it is UVA or UVB [306], [307]. More specifically, it is known that damage is often caused through the gene product, the P53 tumour suppressor, which regulates the cell

cycle and resulting damage pushes cells down the route of apoptosis[306]. However, the cell line MG-63 used within this study is derived from an osteosarcoma, meaning that there is also a dysregulation of cell cycle mechanism. Furthermore, within this study and in the protocol for UV curing of the emulsions, the UV exposure is carried out through tissue culture plastic, and within media. Although UV was calculated through the TCP, it is not possible to submerge the UV measuring Power Puck in media. This may have decreased the theoretical dose that the cells would receive compared to if irradiation had occurred directly without any occlusions between UV source and cells. Therefore, the effective dose of UV that the cells would receive can be considered negligible, and therefore not the reason for the poor outcomes during encapsulation.

The next hypothesis was that the scaffolds may have been leaching toxic components into the media. To assess this, scaffolds were fabricated and placed on top of a confluent layer of MG63s and the effects of the scaffolds on the cells were examined. Although there was significant a difference in metabolic activity of the MG63 cell culture containing unwashed scaffolds compared to TCP controls, there was still a continuous increase in metabolic activity between day 0 (before the addition of scaffolds) and day 3, evidencing that the eluting components were not causing complete cell death that was seen during encapsulation. Therefore, it was then hypothesised that cell death was occurring at the point of encapsulation.

Methacrylated polymers are widely used across many medical applications, due to methacrylation generally being seen to be well tolerated *in vivo*. However, some *in vitro* studies have reported that methacrylates used for dental

applications, such as 2-hydroxyethyl methacrylate, glycerol-dimethacrylate and methyl-methacrylate, do show a degree of cytotoxicity[308]. Methacrylate monomers have been seen to react with cysteine-containing residues within glutathione, an antioxidant involved in various functions involved in tissue repair and regulation. Glutathione prevents cellular damage through the action of reactive oxygen species and free radicals[309]. Damage to glutathione has been seen to result in cell damage, disrupted cell cycles, reduced proliferation and differentiation capacities, as well as cell death[310]. However, the ability for methacrylates to bind to glutathione varies, with some methacrylated monomers showing little to no effects, suggesting that chemical structure and properties are able to influence cellular uptake [308]. Once polymerised, methacrylated monomers are unable to react with glutathione, however, there is often a remaining percentage of uncured monomer left after photocuring.

3PCLMA pre-polymer has been shown to be toxic to cells before curing, however, it has previously been shown that if the polymerisation occurs within 10 minutes of exposure then cells remain viable[311]. Within the present work, it is hypothesised that excess pre-polymer remains within the emulsion, causing toxicity towards the scaffolds.

Although the direct encapsulation did not appear to have favourable results, alternatively it was shown to be possible to seed onto the scaffolds post-fabrication. The use of gelMA within the scaffold would still provide the RGD-residues, which could provide benefits for adhesion and proliferation into the construct. There are currently existing methods for two-stage seeding and decellularization, including previous work in my group, to produce “conditioned” scaffolds[147]. The first step involves seeding with a usually less

clinically relevant cell with high matrix-producing capacity, allowing deposition of the matrix, before undergoing a decellularization step and reseeded with a more clinically relevant cell line, or for direct implantation. However, this is a lengthy and complicated process with a risk of immunogenic response with the addition of non-human cell lines within the scaffold. These conditioned scaffolds do show additional benefits for bone applications, however, as it is thought that the deposited mineral provides more bioactive cues for the differentiation of MSCs into an osteogenic lineage[147].

When MG63 cells were seeded directly onto the scaffolds, the growth rate was comparable to that of TCP. Generally, when seeded directly onto pure PCL constructs, extremely poor adhesion and spreading are observed, due to the high hydrophobicity of the material, as observed in Chapter 3. The proliferative capacity observed here may suggest an alternative, porous material that requires minimal post-processing or surface modification. As noted previously, traditionally fabricated HPEs involve the use of surfactants and solvents, which require lengthy processing via solvent washing, Soxhlet extraction and PBS washing, to extract them, as well as further processing steps for sterilisation, bringing the time from scaffold fabrication time to cell seeding to several days long [147], [179], [283], [284].

Furthermore, PCL HPEs would require plasma treatment to improve hydrophobicity. It is debatable whether plasma treatment can effectively fully penetrate into the pores, resulting in a construct with a variable surface coating. Furthermore, functional groups added through plasma coating may be affected by downstream sterilisation processes such as ethanol washes, ethylene oxide treatment or acetic acid washing, diminishing the added hydrophobicity. Plasma

coating may be then carried out after sterilisation, but this would no longer be considered terminally sterilised. The construct developed within this chapter contains the RGD-residues evenly throughout, due to the emulsified gelMA, whilst all materials are sterilised prior to fabrication. It is therefore possible to seed directly onto the scaffolds after curing, without any further processing required.

4.4 Summary and conclusions

This chapter developed a novel method for creating tuneable gelMA-containing emulsions in a one-pot manner. Although the current work was unable to successfully maintain and print cells within the bioink, it did demonstrate a novel, printable material that cells can be successfully cultured on without any downstream processing required post-fabrication. Mechanical properties of the material could be tuned through the increasing % (w/w) of 3PCLMA.

- GelMA/3PCLMA emulsions can be stabilised through the addition of alginate to increase the viscosity of the aqueous phase.
- Increasing the viscosity of the aqueous phase further stabilises the emulsions.
- Dramatic increases in mechanical properties compared to pure gelMA (or gelMA/Alginate) hydrogels are achievable.
- Tuneable mechanical properties are achievable by varying the ratio of GelMA to 3PCLMA.
- The proliferation and matrix-producing capacity of MG63 cells is not significantly affected by UV exposure within culture media.
- 3PCLMA in uncured form is seen to be cytotoxic, potentially due to interactions with glutathione.
- GelMA/3PCLMA may be used as a printable ink but is not compatible in its current state as a bioink.
- GelMA/3PCLMA emulsions may have potential uses in the one-pot fabrication of biocompatible scaffolds with minimal post-processing required.

7 Development of a 3D porous ink with Minimal Cytotoxic Components – Alternative Attempts

7.1 Introduction

This chapter explores alternate methods of fabricating porous scaffolds that were first attempted, before switching to the final system described in chapter 6. First attempts at producing a porous material for use in *in vitro* trabecular bone modelling also focused on minimising the need for other cytotoxic components, as well as reduced downstream processing times. The initial method investigated was the development of a non-photocurable Pickering-polyHIPE. This would bypass the need for methacrylation of PCL, and remove the need for photoinitiators, which can be seen to be cytotoxic.

As discussed in the literature review, the use of initiators, monomers or cross-linkers used to solidify the emulsions may result in a reduction in cell viability. Similarly, the polymer would have to be photocurable, which generally requires chemical modifications such as acylation or methacrylation that allow for the material to be cross-linked. As photocurable PCL is not commercially available, it would have to be synthesised in-house. An alternate method is to produce a polymer emulsion, or HIPE, that can be solidified via a freeze-drying process and therefore not require any upstream modifications to make it photocurable.

Pickering emulsions were also explored, as an alternative to surfactant-stabilised emulsions. Similar to photoinitiators, surfactants are generally seen to be cytotoxic and therefore require downstream processing to remove them from the

scaffold. In order to stabilise a Pickering emulsion, a stabilising particle is required. These particles sit at the water-oil interface, allowing for protection against coalescence and effectively stabilising the emulsion. For this chapter, the use of hydrophobically modified nano-silica was explored, due to its general biocompatibility, low toxicity, and being chemically inert.

7.2 Aims and Objectives

This chapter outlines the development of a protocol for producing polyHIPEs, directly from non-modified PCL. This would simplify the process of producing polyHIPEs, whilst bypassing the need for photoinitiators. It also aimed to remove surfactants through the use of Pickering particles, to further remove the use of toxic components.

To this extent, the objectives of this chapter stand as:

1. Produce and modify nano-silica to make it super hydrophobic.
2. Investigate diluting solvents and their effects on emulsion formation capacity and morphology.
3. Improve morphology and produce an interconnected-porous construct.

7.3 Results

7.3.1 Production of hydrophobic nano-silica

As discussed in section 1.7.2, to form Pickering HIPEs, a stabilising particle is needed. As super hydrophobic nano-silica is generally not available commercially in small quantities, it must be synthesised in-house. For this work, two protocols derived from the Stöber process are attempted, to form super hydrophobic silica nanoparticles (m-SiO₂). Method 1 and 2 were obtained and adapted from Ebrahimi *et al* and Saeid Jalali *et al* respectively [184], [185].

Method 1 was found to be highly variable in the yield achieved (**Figure 7-2**), while method 2 also produced very low yields of <0.5g per batch. The hydrophobicity of the m-SiO₂ particles was tested briefly by adding the particles to water and

shaking them vigorously for 10 seconds, before placing them back down and allowing them to settle for 1 minute. It was observed that both methods produced hydrophobic particles that would not combine with water when compared to the industrially purchased fumed SiO_2 which can be seen to sink to below the surface of the water. (**Figure 7-1**).



Figure 7-1: m-SiO₂ made via method 1. Shows profound differences between the two yields.

Due to the difficulties in producing m-SiO₂, an industrially modified nano silica was kindly donated by Wacker Chemie, which was used going forward.

7.3.2 Pickering emulsion solvent optimisation

W/O emulsions were formed, using PCL in various solvents, and with silica as the stabilising Pickering particle (**Table 11**). The choice of solvent is also known to have effects on an emulsion's stability, due to their different densities and volatilities. Therefore, a variation of solvents was explored.

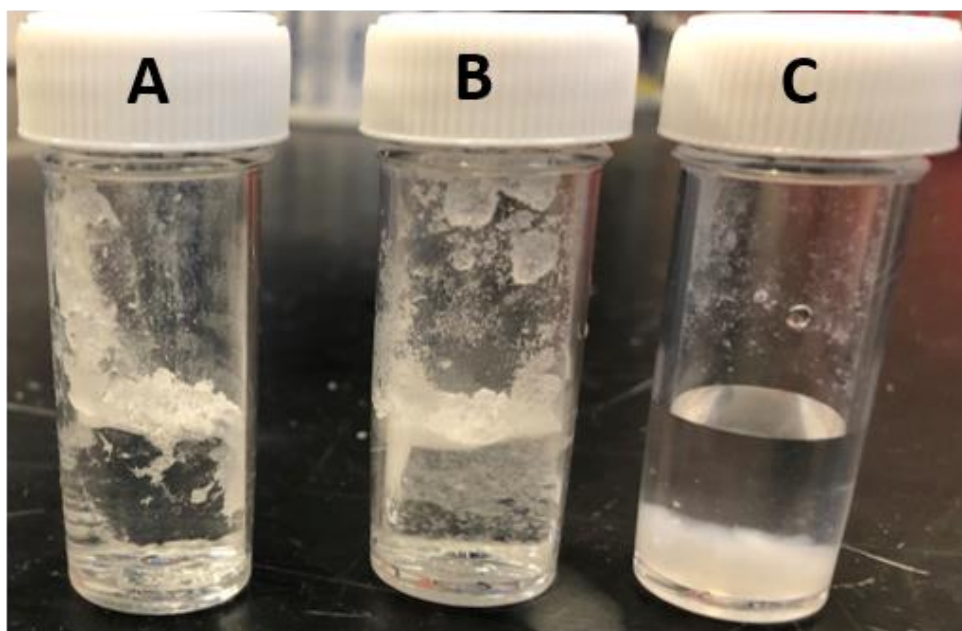


Figure 7-2: Simple test for hydrophobicity of resulting m-SiO₂ particles. Particles are combined with water and shaken for 10 seconds. **A)** m-SiO₂ made via method 1. **B)** m-SiO₂ made by method 2 **C)** Unmodified fumed SiO₂

Table 11: Formulation of emulsions, formed with varying solvents and % Wt of m-SiO₂. Maximum aqueous phase is the maximum amount of water that can be emulsified into the system before phase separation occurs. %silica is calculated relative to the solvent volume. An emulsion is considered formed once it turns an opaque white with a viscous, mayonnaise-like consistency.

Solvent	m-SiO₂ (%Wt)	Emulsion formed (Y/N)	Maximum aqueous Phase (%)
Toluene	3	Y	78
Toluene	5	Y	72
Toluene	8	N	N/A
Chloroform	3	Y	63
Chloroform	5	Y	78
Chloroform	8	N	N/A
DCM	3	N	N/A
DCM	5	N	N/A
DCM	8	N	N/A
Toluene/Chloroform (50/50)	3	Y	78
Toluene/Chloroform (70/30)	3	N	N/A

Emulsions would not readily form when using only DCM as a solvent, separating immediately into two phases. When chloroform or toluene was used as a solvent, stable W/O emulsions formed when up to 5% m-SiO₂ was added. At 8% m-SiO₂, neither chloroform nor toluene formed emulsions. Water was added until the point in which it began to form a visible bead on the surface of the emulsion.

This indicates the point at which the emulsion can no longer accept any more water and would reach its maximum aqueous phase percentage. At both 3% m-SiO₂ with toluene as a solvent and 5% m-SiO₂, with chloroform as a solvent, the maximum aqueous phase percentage achieved was 78%, above the 74% minimum phase percentage required to be defined as a HIPE.

The successful emulsions were then frozen at -80°C, before being freeze-dried for 24 hours. The freeze-drying approach appeared to result in a collapsing of the pores for the majority of the samples (**Figure 7-3**). It did result in a rough, semi-porous morphology for all samples; however, it did not produce “HIPES”, due to the visibly low internal surface areas. With the addition of chloroform, there did appear to be more distinct pores forming compared to when toluene or chloroform/toluene blends were used. However, due to the lack of surfactant, these were not interconnected (**Figure 7-3**). The surfactant Span 80 was therefore then added to investigate the effects of surfactant on Pickering emulsions.

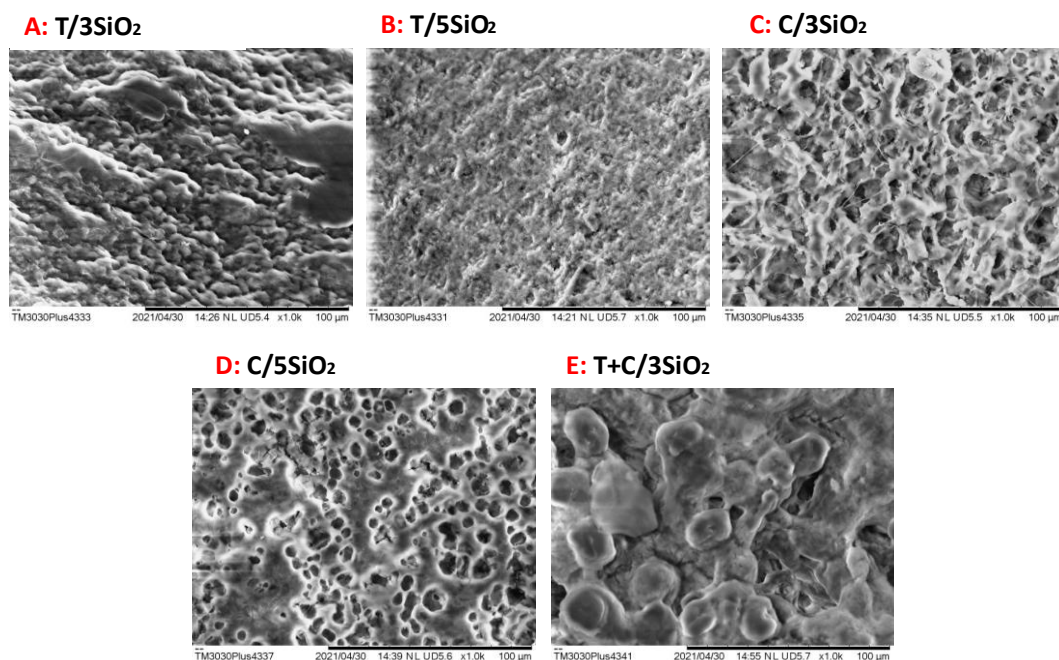


Figure 7-3: SEM images of emulsions formed with varying solvents and % Wt of m-SiO₂. Scale bar = 100μM. **A)** Toluene with 3% m-SiO₂ **B)** toluene with 5% m-SiO₂ **C)** Chloroform with 3% m-SiO₂ **D)** Chloroform with 5% m-SiO₂ **E)** Toluene and chloroform with 3% m-SiO₂

7.3.3 Effects of surfactant on morphology

Chloroform as a singular solvent was used for future studies going forward, and the effects of the surfactant, Span 80, and m-SiO₂ %wt on the material morphology were examined (**Table 12**).

It can be seen that with both 3% and 5 %wt m-SiO₂, the addition of Span 80 resulted in a more porous structure (**Figure 7-4**). These pores appeared to decrease in size with increasing %wt of Span 80. At 5% m-SiO₂, the pores do appear to be less uniform in comparison to only 3% m-SiO₂ (**Figure 7-4**). However, it was not possible to accurately define the pore sizes from the SEM images, due to the irregular morphology of the material, making pore measurement and analysis infeasible.

Table 12: Attempted emulsion set ups using Span 80 surfactant. Solvent is chloroform and used to form a 10% PCL solution (Oil phase). Maximum aqueous phase is the maximum amount of water that can be emulsified into the system before phase separation occurs. %silica is calculated relative to the solvent volume. An emulsion is considered formed once it turns an opaque white with a viscous, mayonnaise-like consistency.

Solvent	Surfactant (g)	m-SiO₂ (%Wt)	Maximum aqueous Phase (%)	Emulsion formed (Y/N)
Chloroform	0	3	78	Y
Chloroform	0.1	3	83	Y
Chloroform	0.15	3	86	Y
Chloroform	0.3	3	86	Y
Chloroform	0	5	72	Y
Chloroform	0.1	5	78	Y
Chloroform	0.15	5	86	Y
Chloroform	0.3	5	86	Y

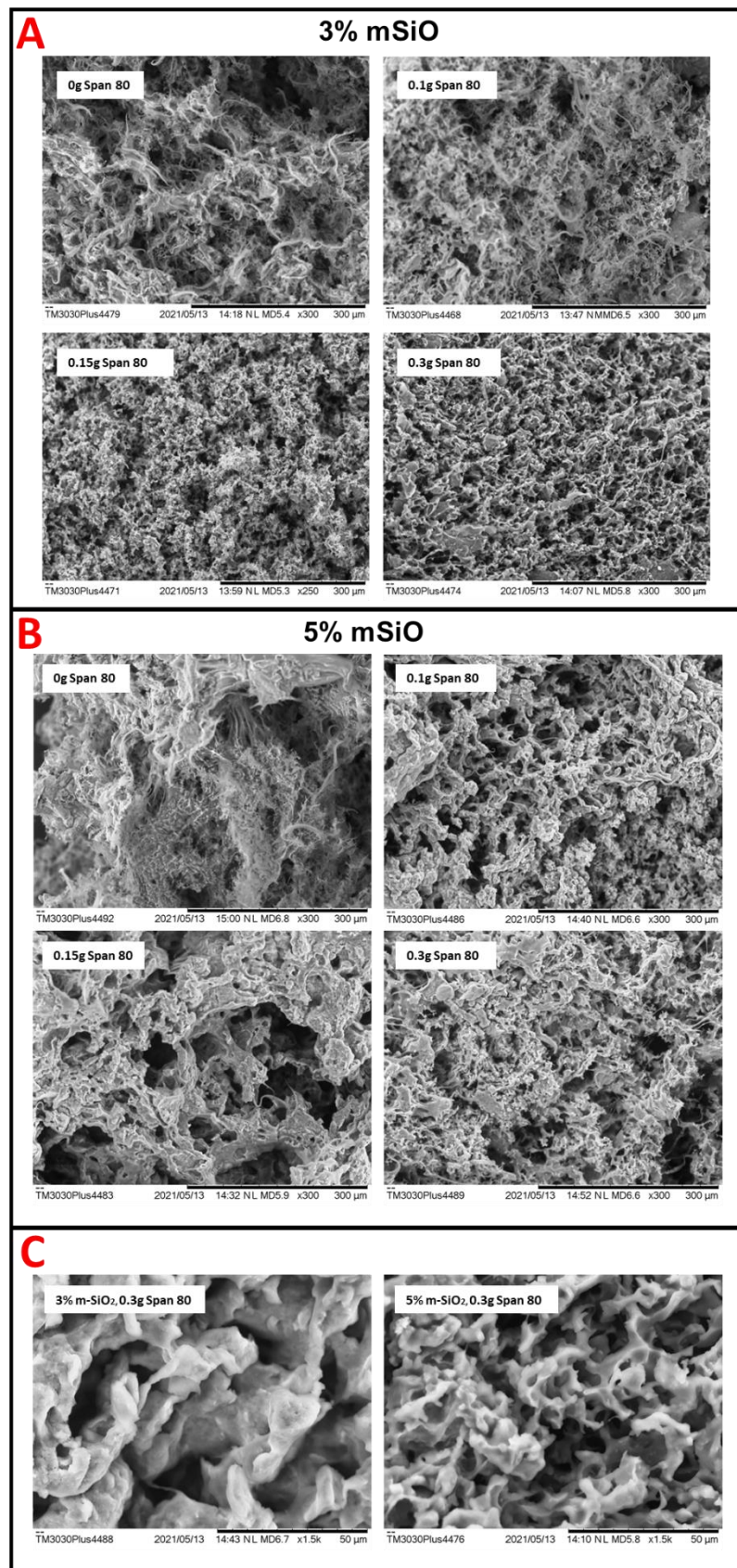


Figure 7-4: SEM images of emulsions formed with chloroform and varying % wt. of m-SiO₂ and Span 80. **A)** 3% m-SiO₂. Scale bar at 300 μm **B)** 5%SiO₂. Scale bar at 300 μm. **C)** High magnification SEM images of 3 %wt and 5 %wt m-SiO₂ emulsions with 0.3g Span 80. Scale bar at 50 μm.

7.4 Discussion

The development of a Pickering emulsion that requires no upstream chemical modifications of PCL would be beneficial within the production of polyHIPEs for large-scale production of *in vitro* chips, due to its simplicity and potential use as a “one-pot” mechanism for producing highly porous and interconnected biomaterials.

Hydrophobically modified nano-silica (m-SiO₂) is a commonly used Pickering particle. In the present work, it was attempted to be synthesised in-house but suffered from low yield and poor reproducibility between batches. The low yield of both these methods could be explained by the nucleation process, which can be affected by a multitude of factors. One of these is temperature, which needs to be carefully controlled throughout the reaction[183], [185], [312]. Due to unforeseen circumstances, the temperature in the laboratory at the time was below 12°, making temperature maintenance difficult. Higher temperatures result in the particle growth rate becoming much higher than the nucleation rate, leading to coarse particles and a greater distribution of particle size, which would be undesirable for this work [184]. As a commercially available hydrophobically modified nano-silica became available during this project, this was used throughout the present work, to ensure reproducibility.

In the production of HIPEs, diluting solvents may be needed for reducing the viscosity of the oil phase. Without dilution, the water would be unable to be incorporated into the oil phase due to its high viscosity, inhibiting efficient mixing. It was seen in the present work that the solvent also plays a role in the stability and morphology of the resulting material, with chloroform and toluene

much better supporting the incorporation of water into the emulsion. It is seen that non-polar solvents, with a lower solubility, generally are more effective in HIPE formation [284], [313], [314]. As DCM is mildly more polar than both chloroform and toluene, this may be playing a role in its inability to stabilise the emulsions.

The viscosity of the emulsion is greatly enhanced with the use of m-SiO₂. Due to this high viscosity, printing small constructs may be possible, with it able to hold its shape for enough time to be flash-frozen within liquid nitrogen. However, this would not be possible for more complex geometries. Alternatively, solvent evaporation may be an alternative, where a single layer is printed and left to be cured through solvent evaporation before the next layer is then printed on top. This method is time-consuming, however, so may not be appropriate when producing large constructs or for mass production.

Within the present work, the pores did not have any apparent interconnection. In surfactant-stabilised polyHIPEs it is thought that the surfactant may play a role in the formation of the interconnects, due to the shrinkage of the polymer upon curing, causing rupture of the thin monomer/surfactant films in between macropores and resulting in the interconnects sometimes observed in polyHIPEs[315], [316]. However, others have shown it to be possible to produce Pickering HIPEs with an interconnected structure without the addition of surfactant. It was described that an emulsion was formed using a blend of polymers PLLA and PCL and Pickering particles of hydrophobic nano silica and hydrophobic hydroxyapatite and that at high aqueous volumes above 74%, thin films of polymer were ruptured during the solvent evaporation process leaving an interconnected porous network [316]. Alternatively Hu *et al*, also similarly

fabricated a PLLA/PCL Pickering HIPE with m-SiO₂ particles as the Pickering particle, but did not observe any interconnection of the pores[179]. Pure PCL with m-SiO₂ has been previously used by Samanta *et al* to produce a stable emulsion for electrospinning[180]. However, the resulting fibres did not appear to have a porous structure. Within the present work, 80,000 kDa PCL was chosen, as it has been shown that high molar mass polymers should produce a more distinguished porous morphology[313]. However, at very high volume fractions of water required to produce a HIPE, the resulting polymer fraction will be low, significantly reducing the mechanical properties and increasing the risk of collapse upon drying[313].

Although the resulting material had a semi-porous structure, without larger micropores, this may not be applicable to bone tissue engineering. The microporosity, which would in this scenario have been formed through 3D printing of moulding, is necessary for both vascularization and new bone ingrowth. The microporosity then be necessary for proper cell attachment and nutrient diffusion. The pores in the presently described material, however, are visibly smaller than the size needed for cellular infiltration of Y201 cells, which were seen to have an average area of 852 μm^2 . Despite this, the surface roughness of the material may still have used as a biomaterial, with it known that surface roughness can assist in cell adhesion, spreading and differentiation of certain cell types [317], [318]

Various parameters such as mixing speed, polymer concentration, water volume, solvent blends, surfactant type and stabilising particles are all shown to affect pore morphology and size [283], [284], [313], [315], [319]. This work has shown it to be possible to produce a porous material without the use of any additional

photocuring agents. With a carefully planned design of experiments, it may be possible to more accurately characterise the effects of each of these on the resulting morphology to produce a Pickering HIPE with a tuneable, open-pore morphology. Due to the restrictions in geometry when 3D printing or moulding, and the requirement for both the cytotoxic solvents and surfactants, it was decided that this protocol would not be investigated further during the project.

8 Future Work

8.1 Development of a lamellar-like organisation for modelling of lamellar bone

The current proposed model used within this thesis has applications for the study of lamellar bone formation and particularly could be of use in elucidating the mechanisms behind how lamellar formation occurs. This could be achieved in a variety of ways. First, a larger scale microarray analysis to explore the differentially expressed genes known to be involved in mechanotransduction, between Y201 cells cultured on the aligned and non-aligned fibres, as well as on the MG-63, which were observed to have a poor organisation of collagen on aligned fibres. Microarray analysis allows for large-scale screening of entire panels of genes, as opposed to choosing a select few for full qPCR analysis. Any genes or pathways that are notably different between the conditions can then be chosen for further qPCR analysis and study.

Within the present work, the HIPPO-linked pathway was investigated, through the examination of RhoA and YAP. HIPPO is known to play a key role in mechanotransduction and may be activated by cell densities, and subsequently inhibits cell proliferation by the accumulation of YAP within the nucleus. Higher cell densities are seen within the woven bone, compared to the lower cell densities observed in cortical, however, in cortical bone, the cells are seen to be flat and elongated, compared to rounder/cuboidal within the woven bone. It may be suggested that this pathway may be more strongly activated by cell morphology, as opposed to simply density, as shown in studies by Wada et al

[110]. They also showed the role of F-Actin in the localisation of YAP in the nucleus, and that treatment with anti-actin drugs significantly reduced nuclear YAP. These stress fibres may then be able to trigger polarity protein expression, as well as trigger key differentiation pathways. YAP was seen to be upregulated on both aligned and non-aligned fibres in this study, however, it was not known the localisation of YAP. Further work would aim to look at this pathway in more detail, whilst also carrying out immunolabelling of YAP/TAZ, to assess the localisation of the molecules.

There is also evidence that the primary cilia, microtubule-based organelles play a pivotal role in the organisation of collagen within tendon, with a singular primary cilium per cell which is seen to align along the direction of the collagen fibres within the tendon[320]. More recently it has also been shown that the primary cilia are also required for osteoblast and osteocyte mechanotransduction, alignment, and subsequent deposition behaviour[71], [321], [322]. The primary cilia are believed to act as sensors for oscillatory fluid flow, and it has been shown that a primary cilium is required for flow-induced deposition of calcium matrix[71]. Oscillatory fluid flow was not used within this work, which may also contribute to the variability within the mineralisation seen. Primary cilia can be immunolabelled and their orientation can be observed. It would be of interest to examine these, and their orientation relative to the overall collagen, as well as the effects on mineral deposition.

The qPCR within the present study has a notably small sample size, due to difficulties extracting high quantities of mRNA. Repeats of this work, with larger scaffolds and higher cell numbers, may be one method to confirm the results observed. Within the present work, RNeasy kits were used for the isolation of

RNA. RNEasy is a more traditional method of isolation, using a column and series of washing steps to capture RNA within a membrane, before eluting it in a final step. This method is non-specific, and isolates all forms of RNA, with mRNA being only 1-5%. Alternatively, the use of DynaBeads could be explored as an alternative method of extraction. This involves the conjugation of magnetic beads to mRNA via the polyadenylated (Poly(A)) tails. Poly(A) tails are generally only seen on mRNA, making this a highly selective process. With the use of a magnet, the beads can be selectively drawn out, before being released from the remaining total RNA, resulting in purer isolation of mRNA. This ideally may allow for more efficient isolation without significantly increasing the seeding density, as increased seeding densities may affect cellular behaviour.

Further investigations on the effects of shear stress would also be of interest. Effects of shear flow were originally planned, but due to equipment failure, were unable to be completed. Shear stress was intended to be applied either parallel to the scaffold's predominant orientation, perpendicular to the scaffold's orientation, or with no preferential orientation, to assess any potential changes to the resulting collagen. Bone cells experience shear stresses via the oscillatory flow of fluid through the canalicular channel. Both substrate orientation and shear stresses are seen to play a role in the guidance of collagen orientation, and it would be interesting to see how it affects the subsequent layers when cultured on aligned fibres, once the collagen is offset to the polymer fibre alignment. It was also noted that the distance that the lamellar-like twisting occurred over was large (30-45 μ M), compared to the periodicity of the *in vivo* lamellae (5-7 μ M). It may then be of interest to examine whether this *in vitro* periodicity may be altered through the addition of further stimuli such as shear flow or compression regimes. A better understanding of how to control organised

collagen development could be an important tool for the production of more effective drugs for the treatment of various diseases of the bone.

h-TERT Y201 was used as the model cell choice throughout, due to its reproducibility, ease of culture and ability to differentiate into an osteogenic lineage. However, for future models, it would be interesting to see the difference within primary cells. Furthermore, if this effect is seen to be present within a population of primary MSCs, it would then be worth exploring the effects of different backgrounds and phenotypes, as well as the behaviour of primary MSCs taken from patients within specific bone-related diseases, for example, osteogenesis imperfecta.

8.2 Methacrylated polycaprolactone-triol and gelatin methacrylate emulsions for the production of stiff and porous bio-inks for use in 3D cell printing

This study demonstrated the potential for a non-cytotoxic scaffold that can be directly seeded post-fabrication. However, more would need to be done to characterise its capacity for facilitating osteogenesis and matrix deposition. For this, it will be necessary to carry out longer-term assessments, carrying out similar assays done in Chapter 3, such as Sirius red staining, alizarin red staining and alkaline phosphatase activity assays.

The addition of hydroxyapatite within the scaffold did dramatically reduce the mechanical properties of the material, however, it may be possible to adjust the scaffold properties in other ways to provide it with bioactive properties or further alter the mechanical properties. As it is hypothesised that the reduced

Young's modulus observed was due to hydroxyapatite aggregates, it may also be worth exploring whether methods of better distributing the nano-hydroxyapatite particles. The use of an ultrasonic probe to disperse the particles evenly may be beneficial.

The degree of 3PCLMA is also seen to be tuneable. If the toxicity of the emulsion as a bioink is caused by action of methacrylate groups on glutathione, decreasing the degree of methacrylation may be beneficial to improving the viability of any encapsulated cells. Furthermore, it was shown that the interactions between the methacrylate groups and glutathione were dependent on the chemical structure[308]. Alternate structures of PCL may be possible, including 2-arm or 4-arm, that are also liquid at room temperature at low molecular weights, so investigation of these may be of note. It would be interesting to repeat the encapsulation studies, but using the different variations as described.

An alternative method for encapsulation worth examining would be to pre-cure the cells within gelMA for a short period to form a loosely crosslinked hydrogel, and then emulsify this within the 3PCLMA. As it was seen that 3PCLMA appears to only be highly toxic in its monomeric form, pre-encapsulating within gelMA may provide a temporary barrier against these monomers, preventing direct contact. This would allow for washing with PBS to occur, to remove excess unreacted pre-polymer.

As the material has been shown to be biocompatible, printable, and requires minimal post-processing, it would be interesting to begin to explore 3D-printed architectures. Further exploration into the best methods of printing, such as extrusion, digital light processing (DLP) or stereolithography, would be of interest. One other option to further this may be to take CT scans and translate

these into printable G-codes that could be used to develop patient-specific models.

Other methods of seeding, such as dynamic seeding where cells are distributed using a flow system may be beneficial, and of interest to explore cellular infiltration into the scaffold. Longer term culture over 28 days could then be carried out, in order to assess matrix producing capacity on the material.

GelMA itself comes from a gelatin pre-cursor, in the case of this work from a cold-water fish source. As this project focused on the minimisation of xeno-derived products, it would be of interest to explore alternatives to animal-derived gelatin. It is possible to purchase recombinant humanised gelatin, produced using a recombinant yeast system. This is also seen to express specified fragments of type I α 1 human sequence collagen. To the best of my knowledge, gelMA has not been attempted to be synthesised with humanised recombinant gelatins, so it would also be necessary to explore whether methacrylation is possible, and the resulting physical and mechanical properties. If humanised gelMA is possible, not only would this eliminate any animal-derived sources and issues with immunogenicity, it may provide an environment that is more representative of the physiological ECM.

Finally, *in vivo* bone is generally seen to be formed of both cortical and trabecular bone, however as previously discussed, many *in vitro* models of bone simplify these to just an osteoid-like construct. It is known that some diseases and drugs can have differing effects on both trabecular and cortical bone. It would be of interest to combine the cortical and trabecular phases developed within this work to produce a bi-phasic model. Work should aim to investigate

integrating the two layers with good interfacial bonding, to prevent delamination.

For both constructs, it would be interesting to look for markers of terminal osteocyte differentiation. Present work looked for early markers of osteoblast differentiation, but over longer term culture, it would be interesting to explore whether full osteocyte differentiation is achieved. This may be done by examination of expression and production of osteocyte specific proteins such as SOST, DMP1 and FGF23, through either qPCR or ELISAs[323].

Once a two-phase model has been established, there is a great degree of further work that can be carried out. As previously mentioned, the application of oscillatory flow may provide a further environment that closely mimics the physiological bone. A simple rocker method was discussed previously, however more advanced flow systems, such as the Quasi Vivo® *in vitro* bioreactor, allow for the application of oscillatory flow regimes with a more controllable shear and flow rate [324]. This could allow for the mimicry of a more physiological shear than is obtainable with simple rocker regimes. Furthermore, when being used as an *in vitro* model, Quasi Vivo® is a modular system, that can be connected with other model systems in parallel. All *in vivo* systems within the network would share a singular source of media from a large reservoir, so could theoretically interact. Since media is circulatory, it is then not changed, so the effects of metabolites can also be observed.

As previously discussed, certain drugs are shown to have differential effects on cortical and trabecular bone, one of which is recombinant parathyroid hormone (PTH). In one study PTH was shown to have less substantial effects on trabecular bone mass gain than in cortical, with the addition of loading. It would be

interesting to explore whether any similar effects can be observed within our developed *in vitro* model.

Appendix

Serum-free mediums for replacement of FBS

Cells are generally cryogenically stored in a mixture of FBS:DMSO at a ratio of 10:1. FBS is used to help with cell survival and assist with their revival post-thawing, due to its high concentration of proteins and other cell nutrients, whilst DMSO prevents crystal formation. However, FBS is animal-derived which as discussed previously, comes with ethical issues as well as suffering from batch-to-batch variability. This section looks at a variety of different freezing media which may be used as an alternative.

The freezing mediums examined were commercially available, however, they had not been tested with the cell line currently used in the present work.

Methods

Y201 cells at passage 76 were frozen in either xeno-free (CryoStem™ Freezing Medium, Biological Industries), xeno-free and DMSO-free (CryoSOfree Freezing solution) or a 1:10 solution of DMSO: FBS. Cells were frozen at a density of 750,000 cells per 1ml vial before being placed in a Mr Frosty and left in a -80° C freezer for 21 days.

After 21 days, cells were thawed at 37 °C and replated into T75 flasks. At 80% confluency, they were replated at a seeding density of 1×10^5 cells per 12-well plate and cultured for 14 days in either un-supplemented EM or OM.

Table 13: Summary of freezing solutions examined

Freezing solution	Type	Acronym
CryoStem™ Freezing Medium, Biological Industries	Xeno-free Contains DMSO	XF1
CryoSOfree Freezing solution	Xeno-free DMSO Free	XF2
1:10 solution of DMSO: FBS	Contains FBS Contains DMSO	DMSO: FBS

Results and discussion

After 3 days of culture, cells thawed from DMSO:FBS and XF1 had a regular, fusiform shape in both EM and OM. Cells defrosted from XF2 showed to have a similar shape in EM, but to form rounded nodules of cells when cultured in EM. These continued to form throughout the culture. After 10 days in culture, the metabolic activity of the cells showed no significant differences.

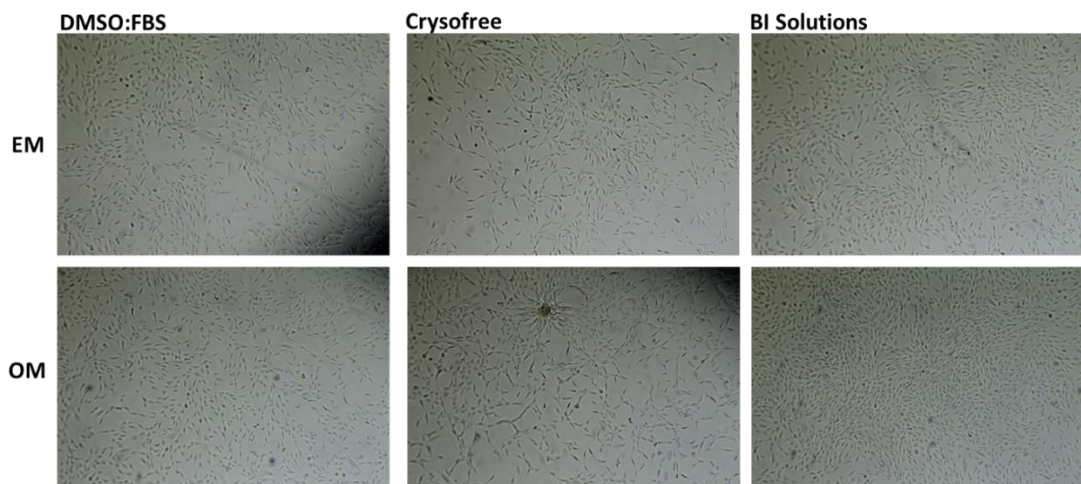


Figure 1: Light microscope images of Y201 cells

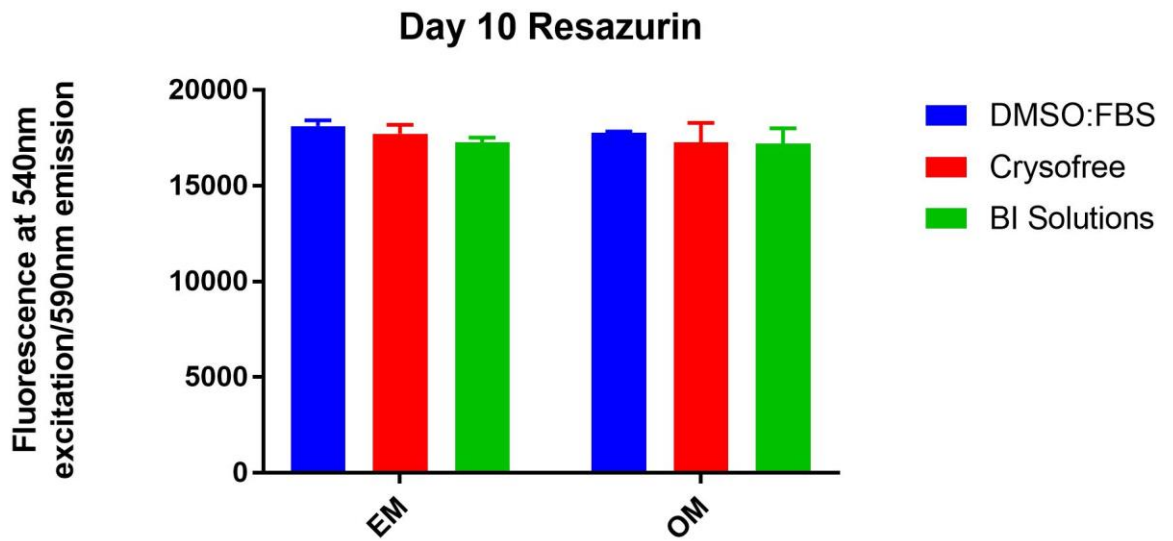


Figure 2 Day 10 metabolic activity of h-TERT Y201 cells seeded on TCP. Results are shown as mean \pm SD. n=6 Statistical analysis performed using two-way ANOVA with Tukey's *post-hoc* test for multiple comparisons. * = $p \leq 0.05$

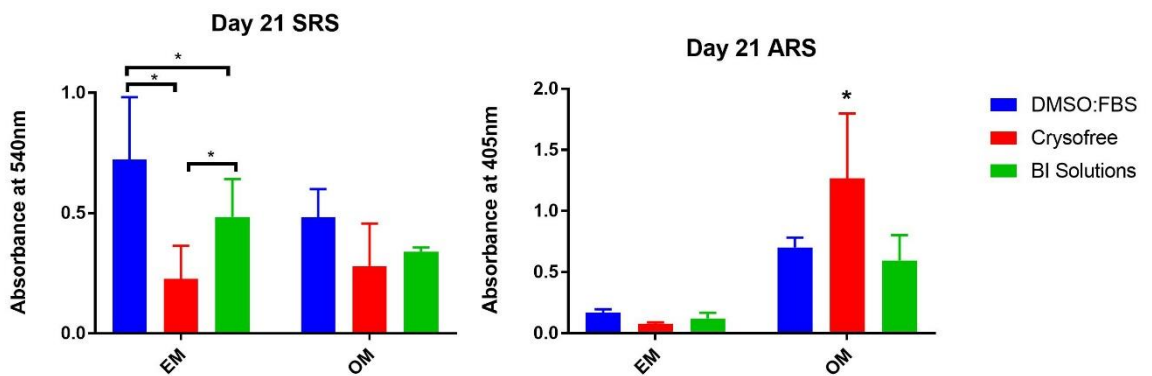


Figure 3: Day 21 collagen (SRS) and mineral (ARS) deposition of h-TERT Y201 cells cultured on TCP. Results are shown as mean \pm SD. n=6 Statistical analysis performed using two-way ANOVA with Tukey's *post-hoc* test for multiple comparisons. * = $p \leq 0.05$

After culturing in OM for 21 days, there was a significant decrease in collagen output of both XF1 and XF2, compared to DMSO: FBS. A similar pattern was also observed in OM treated cells; however this did not reach statistical significance. Crysofree also appeared to show significantly higher degrees of mineralisation than the other freezing mediums when cultured in OM.

The reduced collagen deposition observed when thawed both XF1 and XF2, and altered morphology and mineral output from XF2, suggested that cell behaviour

was altered by the xeno-free freezing mediums. Although mineral deposition and morphology was comparable with DMSO:FBS when frozen with BI Solutions, the project focused on collagen deposition, so the reduced collagen output also made it a less desirable option. From this work, it was concluded that DMSO: FBS will be used from this point forward.

References

- [1] G. Hulsart-Billström *et al.*, “A surprisingly poor correlation between in vitro and in vivo testing of biomaterials for bone regeneration: Results of a multicentre analysis,” *Eur. Cells Mater.*, vol. 31, pp. 312–322, 2016.
- [2] “The Principles of Humane Experimental Technique,” *Med. J. Aust.*, vol. 1, no. 13, pp. 500–500, Mar. 1960.
- [3] J. Y. Wong, J. B. Leach, and X. Q. Brown, “Balance of chemistry, topography, and mechanics at the cell-biomaterial interface: Issues and challenges for assessing the role of substrate mechanics on cell response,” in *Surface Science*, 2004, vol. 570, no. 1–2, pp. 119–133.
- [4] V. W. Tang, “Collagen, stiffness, and adhesion: The evolutionary basis of vertebrate mechanobiology,” *Mol. Biol. Cell*, vol. 31, no. 17, pp. 1823–1834, 2020.
- [5] X. Cai, K. C. Wang, and Z. Meng, “Mechanoregulation of YAP and TAZ in Cellular Homeostasis and Disease Progression,” *Front. Cell Dev. Biol.*, vol. 9, no. May, pp. 1–12, 2021.
- [6] W. J. Hadden *et al.*, “Stem cell migration and mechanotransduction on linear stiffness gradient hydrogels,” *Proc. Natl. Acad. Sci. U. S. A.*, vol. 114, no. 22, pp. 5647–5652, May 2017.
- [7] F. J. Alenghat and D. E. Ingber, “Mechanotransduction: all signals point to cytoskeleton, matrix, and integrins.,” *Sci. STKE*, vol. 2002, no. 119, pp. 1–5, 2002.
- [8] A. Das, S. Adhikary, A. R. Chowdhury, and A. Barui, “Leveraging Substrate Stiffness to Promote Stem Cell Asymmetric Division via Mechanotransduction-Polarity Protein Axis and Its Bayesian Regression Analysis,” *Rejuvenation Res.*, vol. 25, no. 2, pp. 59–69, Apr. 2022.
- [9] A. S. Rowlands, P. A. George, and J. J. Cooper-White, “Directing osteogenic and myogenic differentiation of MSCs: Interplay of stiffness and adhesive ligand presentation,” *Am. J. Physiol. - Cell Physiol.*, vol. 295, no. 4, pp. 1037–1044, Oct. 2008.
- [10] W. J. Hadden *et al.*, “Stem cell migration and mechanotransduction on linear stiffness gradient hydrogels,” *Proc. Natl. Acad. Sci. U. S. A.*, vol. 114, no. 22, pp. 5647–5652, May 2017.
- [11] A. J. Engler *et al.*, “Embryonic cardiomyocytes beat best on a matrix with heart-like elasticity: Scar-like rigidity inhibits beating,” *J. Cell Sci.*, vol. 121, no. 22, pp. 3794–3802, Nov. 2008.
- [12] N. TL *et al.*, “Rapid cortical bone loss in patients with chronic kidney disease,” *J. Bone Miner. Res.*, vol. 28, no. 8, pp. 1811–1820, Aug. 2013.

- [13] B. C. Roberts *et al.*, “PTH(1–34) treatment and/or mechanical loading have different osteogenic effects on the trabecular and cortical bone in the ovariectomized C57BL/6 mouse,” *Sci. Reports 2020 101*, vol. 10, no. 1, pp. 1–16, Jun. 2020.
- [14] T. Rimmelé *et al.*, “Diffusion of levofloxacin into bone and synovial tissues,” *J. Antimicrob. Chemother.*, vol. 53, no. 3, pp. 533–535, Mar. 2004.
- [15] J. P. Bilezikian, L. G. (Lawrence G. Raisz, and T. J. Martin, “Principles of bone biology,” 2008.
- [16] J. R. Dwek, “The periosteum: what is it, where is it, and what mimics it in its absence?,” *Skeletal Radiol.*, vol. 39, no. 4, p. 319, Apr. 2010.
- [17] J. R. Dwek, “The periosteum: what is it, where is it, and what mimics it in its absence?,” *Skeletal Radiol.*, vol. 39, no. 4, p. 319, Apr. 2010.
- [18] F. Shapiro and J. Y. Wu, “Woven bone overview: Structural classification based on its integral role in developmental, repair and pathological bone formation throughout vertebrate groups,” *Eur. Cells Mater.*, vol. 38, pp. 137–167, 2019.
- [19] X. Feng and J. M. McDonald, “Disorders of Bone Remodeling,” *Annu. Rev. Pathol. Mech. Dis.*, vol. 6, no. 1, pp. 121–145, Feb. 2011.
- [20] S. C. Moser and B. C. J. van der Eerden, “Osteocalcin—A Versatile Bone-Derived Hormone,” *Front. Endocrinol. (Lausanne)*, vol. 9, no. JAN, p. 794, Jan. 2019.
- [21] J. Sodek, B. Ganss, and M. D. McKee, “Osteopontin,” *Crit. Rev. Oral Biol. Med.*, vol. 11, no. 3, pp. 279–303, Jul. 2000.
- [22] S. Cremers, P. Garnerio, and M. J. Seibel, “Biochemical Markers of Bone Metabolism,” in *Principles of Bone Biology, Two-Volume Set*, vol. 2, Elsevier Inc., 2008, pp. 1857–1881.
- [23] Y. Zhu, Y. Gu, C. Jiang, and L. Chen, “Osteonectin regulates the extracellular matrix mineralization of osteoblasts through P38 signaling pathway,” *J. Cell. Physiol.*, vol. 235, no. 3, pp. 2220–2231, Mar. 2020.
- [24] D. Kanjilal and J. A. Cottrell, “Bone morphogenetic proteins (BMPs) and bone regeneration,” in *Methods in Molecular Biology*, vol. 1891, Humana Press Inc., 2019, pp. 235–245.
- [25] S. M. Ott and G. Elder, “Osteoporosis Associated with Chronic Kidney Disease,” in *Osteoporosis: Fourth Edition*, Elsevier Inc., 2013, pp. 1387–1424.
- [26] G. Marotti, “A new theory of bone lamellation,” *Calcif. Tissue Int.*, vol. 53 Suppl 1, no. 1 Supplement, Feb. 1993.
- [27] T. G. Bromage, H. M. Goldman, S. C. McFarlin, J. Warshaw, A. Boyde, and C. M. Riggs, “Circularly polarized light standards for investigations of collagen fiber orientation in bone,” *Anat. Rec. Part B New Anat.*, vol. 274B,

no. 1, pp. 157–168, Sep. 2003.

- [28] G. Marotti, M. Ferretti, and C. Palumbo, “The problem of bone lamellation: An attempt to explain different proposed models,” *J. Morphol.*, vol. 274, no. 5, pp. 543–550, 2013.
- [29] M. M. Giraud-Guille, “Twisted plywood architecture of collagen fibrils in human compact bone osteons,” *Calcif. Tissue Int.*, vol. 42, no. 3, pp. 167–180, May 1988.
- [30] S. Weiner, T. Arad, I. Sabanay, and W. Traub, “Rotated plywood structure of primary lamellar bone in the rat: Orientations of the collagen fibril arrays,” *Bone*, vol. 20, no. 6, pp. 509–514, 1997.
- [31] W. Wagermaier, H. S. Gupta, A. Gourrier, M. Burghammer, P. Roschger, and P. Fratzl, “Spiral twisting of fiber orientation inside bone lamellae,” *Biointerphases 2006 II*, vol. 1, no. 1, pp. 1–5, Mar. 2006.
- [32] N. Reznikov, R. Almany-Magal, R. Shahar, and S. Weiner, “Three-dimensional imaging of collagen fibril organization in rat circumferential lamellar bone using a dual beam electron microscope reveals ordered and disordered sub-lamellar structures,” *Bone*, vol. 52, no. 2, pp. 676–683, Feb. 2013.
- [33] N. Reznikov, R. Shahar, and S. Weiner, “Three-dimensional structure of human lamellar bone: The presence of two different materials and new insights into the hierarchical organization,” *Bone*, vol. 59, pp. 93–104, 2014.
- [34] J. G. Skedros and K. J. Hunt, “Does the degree of laminarity correlate with site-specific differences in collagen fibre orientation in primary bone? An evaluation in the turkey ulna diaphysis,” *J. Anat.*, vol. 205, no. 2, pp. 121–134, Aug. 2004.
- [35] J. K. Kalmey and C. O. Lovejoy, “Collagen fiber orientation in the femoral necks of apes and humans: do their histological structures reflect differences in locomotor loading?,” *Bone*, vol. 31, no. 2, pp. 327–332, 2002.
- [36] W. T. Tung *et al.*, “Coaxial electrospinning of PEEU/gelatin to fiber meshes with enhanced mesenchymal stem cell attachment and proliferation1,” *Clin. Hemorheol. Microcirc.*, pp. 1–15, 2019.
- [37] Y. Z. Cai, L. L. Wang, H. X. Cai, Y. Y. Qi, X. H. Zou, and H. W. Ouyang, “Electrospun nanofibrous matrix improves the regeneration of dense cortical bone,” *J. Biomed. Mater. Res. Part A*, vol. 95A, no. 1, pp. 49–57, Oct. 2010.
- [38] N. Reznikov, H. Chase, V. Brumfeld, R. Shahar, and S. Weiner, “The 3D structure of the collagen fibril network in human trabecular bone: Relation to trabecular organization,” *Bone*, vol. 71, pp. 189–195, 2015.
- [39] N. Reznikov, M. Bilton, L. Lari, M. M. Stevens, and R. Kröger, “Fractal-like hierarchical organization of bone begins at the nanoscale,” *Science*, vol. 360, no. 6388, May 2018.

- [40] M. A. Rubin and I. Jasiuk, "The TEM characterization of the lamellar structure of osteoporotic human trabecular bone," *Micron*, vol. 36, no. 7–8, pp. 653–664, Oct. 2005.
- [41] B. Clarke, "Normal Bone Anatomy and Physiology," *Clin. J. Am. Soc. Nephrol.*, vol. 3, no. Suppl 3, p. S131, 2008.
- [42] J. W. Smith, "Collagen fibre patterns in mammalian bone," *J. Anat.*, vol. 94, no. Pt 3, p. 329, Jul. 1960.
- [43] J. A. Siddiqui and N. C. Partridge, "Physiological bone remodeling: Systemic regulation and growth factor involvement," *Physiology*, vol. 31, no. 3, pp. 233–245, 2016.
- [44] I. Nakamura, N. Takahashi, E. Jimi, N. Udagawa, and T. Suda, "Regulation of osteoclast function," *New pub Oxford Univ. Press*, vol. 22, no. 2, pp. 167–177, Apr. 2014.
- [45] M. Zaidi, O. A. Adebajo, B. S. Moonga, L. Sun, and C. L. H. Huang, "Emerging Insights into the Role of Calcium Ions in Osteoclast Regulation," *J. Bone Miner. Res.*, vol. 14, no. 5, pp. 669–674, May 1999.
- [46] K. H. Park-Min, "Mechanisms involved in normal and pathological osteoclastogenesis," *Cell. Mol. Life Sci.*, vol. 75, no. 14, pp. 2519–2528, Jul. 2018.
- [47] J. Yovos, "Osteoclastogenesis-Current knowledge and future perspectives."
- [48] L. T. Duong, P. Lakkakorpi, I. Nakamura, and G. A. Rodan, "Integrins and signaling in osteoclast function," *Matrix Biol.*, vol. 19, no. 2, pp. 97–105, May 2000.
- [49] P. J. Kostenuik, "Osteoprotegerin and RANKL regulate bone resorption, density, geometry and strength," *Curr. Opin. Pharmacol.*, vol. 5, no. 6, pp. 618–625, Dec. 2005.
- [50] S. Tanaka, K. Nakamura, N. Takahashi, and T. Suda, "Role of RANKL in physiological and pathological bone resorption and therapeutics targeting the RANKL–RANK signaling system," *Immunol. Rev.*, vol. 208, no. 1, pp. 30–49, Dec. 2005.
- [51] L. J. Raggatt and N. C. Partridge, "Cellular and molecular mechanisms of bone remodeling," *J. Biol. Chem.*, vol. 285, no. 33, pp. 25103–25108, Aug. 2010.
- [52] B. R. Williams, R. A. Gelman, D. C. Poppe, and K. Piez, "Collagen fibril formation. Optimal in vitro conditions and preliminary kinetic results.," *J. Biol. Chem.*, vol. 253, no. 18, pp. 6578–6585, Sep. 1978.
- [53] S. M. Siadat, A. A. Silverman, C. A. DiMarzio, and J. W. Ruberti, "Measuring Collagen Fibril Diameter with Differential Interference Contrast Microscopy," *J. Struct. Biol.*, vol. 213, no. 1, p. 107697, Mar. 2021.

- [54] D. J. Prockop and A. Fertala, "Inhibition of the self-assembly of collagen I into fibrils with synthetic peptides: Demonstration that assembly is driven by specific binding sites on the monomers," *J. Biol. Chem.*, vol. 273, no. 25, pp. 15598–15604, 1998.
- [55] M. D. Shoulders and R. T. Raines, "Collagen structure and stability," *Annu. Rev. Biochem.*, vol. 78, pp. 929–958, 2009.
- [56] S. Weiner and W. Traub, "Organization of hydroxyapatite crystals within collagen fibrils," 1986.
- [57] T. Ishimoto, T. Nakano, Y. Umakoshi, M. Yamamoto, and Y. Tabata, "Degree of biological apatite c-axis orientation rather than bone mineral density controls mechanical function in bone regenerated using recombinant bone morphogenetic protein-2," *J. Bone Miner. Res.*, vol. 28, no. 5, pp. 1170–1179, May 2013.
- [58] T. Nakano, K. Kaibara, T. Ishimoto, Y. Tabata, and Y. Umakoshi, "Biological apatite (BAP) crystallographic orientation and texture as a new index for assessing the microstructure and function of bone regenerated by tissue engineering," *Bone*, vol. 51, no. 4, pp. 741–747, Oct. 2012.
- [59] S. Lee, F. Nagata, K. Kato, and T. Nakano, "Bone apatite anisotropic structure control: Via designing fibrous scaffolds," *RSC Adv.*, vol. 10, no. 23, pp. 13500–13506, Apr. 2020.
- [60] S. J. Jones, A. Boyde, and J. B. Pawley, "Osteoblasts and Collagen Orientation."
- [61] R. M. Delaine-Smith, A. J. Hann, N. H. Green, and G. C. Reilly, "Electrospun Fiber Alignment Guides Osteogenesis and Matrix Organization Differentially in Two Different Osteogenic Cell Types," *Front. Bioeng. Biotechnol.*, vol. 9, p. 564, Oct. 2021.
- [62] R. M. Delaine-Smith, N. H. Green, S. J. Matcher, S. MacNeil, and G. C. Reilly, "Monitoring Fibrous Scaffold Guidance of Three-Dimensional Collagen Organisation Using Minimally-Invasive Second Harmonic Generation," *PLoS One*, vol. 9, no. 2, p. e89761, Feb. 2014.
- [63] X. Fu and H. Wang, "Spatial arrangement of polycaprolactone/collagen nanofiber scaffolds regulates the wound healing related behaviors of human adipose stromal cells," *Tissue Eng. - Part A*, vol. 18, no. 5–6, pp. 631–642, Mar. 2012.
- [64] R. M. Delaine-Smith, "Mechanical and physical guidance of osteogenic differentiation and matrix production," Feb. 2013.
- [65] A. Matsugaki, Y. Isobe, T. Saku, and T. Nakano, "Quantitative regulation of bone-mimetic, oriented collagen/apatite matrix structure depends on the degree of osteoblast alignment on oriented collagen substrates," *J. Biomed. Mater. Res. - Part A*, vol. 103, no. 2, pp. 489–499, 2015.
- [66] D. M. Darvish, "Collagen fibril formation in vitro: From origin to

- opportunities,” *Mater. Today Bio*, vol. 15, Jun. 2022.
- [67] F. Gobeaux, E. Belamie, G. Mosser, P. Davidson, P. Panine, and M. M. Giraud-Guille, “Cooperative ordering of collagen triple helices in the dense state,” *Langmuir*, vol. 23, no. 11, pp. 6411–6417, May 2007.
- [68] Y. Lu *et al.*, “Live Imaging of Type I Collagen Assembly Dynamics in Osteoblasts Stably Expressing GFP and mCherry-Tagged Collagen Constructs,” *J. Bone Miner. Res.*, vol. 33, no. 6, pp. 1166–1182, Jun. 2018.
- [69] L. A. Shiflett, L. A. M. Tiede-Lewis, Y. Xie, Y. Lu, E. C. Ray, and S. L. Dallas, “Collagen Dynamics During the Process of Osteocyte Embedding and Mineralization,” *Front. Cell Dev. Biol.*, vol. 7, Sep. 2019.
- [70] S. Kapur, D. J. Baylink, and K. H. W. Lau, “Fluid flow shear stress stimulates human osteoblast proliferation and differentiation through multiple interacting and competing signal transduction pathways,” *Bone*, vol. 32, no. 3, pp. 241–251, 2003.
- [71] R. M. Delaine-Smith, A. Sittichokechaiwut, and G. C. Reilly, “Primary cilia respond to fluid shear stress and mediate flow-induced calcium deposition in osteoblasts,” *FASEB J.*, vol. 28, no. 1, pp. 430–439, Jan. 2014.
- [72] N. Saeidi, E. A. Sander, R. Zareian, and J. W. Ruberti, “Production of highly aligned collagen lamellae by combining shear force and thin film confinement,” *Acta Biomater.*, vol. 7, no. 6, pp. 2437–2447, Jun. 2011.
- [73] N. Saeidi, E. A. Sander, R. Zareian, and J. W. Ruberti, “Production of highly aligned collagen lamellae by combining shear force and thin film confinement,” *Acta Biomater.*, vol. 7, no. 6, pp. 2437–2447, 2011.
- [74] R. M. Delaine-Smith, S. MacNeil, and G. C. Reilly, “Matrix production and collagen structure are enhanced in two types of osteogenic progenitor cells by a simple fluid shear stress stimulus,” *Eur. Cells Mater.*, vol. 24, no. 0, pp. 162–174, 2012.
- [75] D. A. O’loughlin, “Using nanotopography and macromolecular crowding to influence in vitro collagen deposition in a corneal stroma model.”
- [76] J. A. Paten *et al.*, “Molecular Interactions between Collagen and Fibronectin: A Reciprocal Relationship that Regulates De Novo Fibrillogenesis,” 2019.
- [77] C. A. Sevilla, D. Dalecki, and D. C. Hocking, “Regional Fibronectin and Collagen Fibril Co-Assembly Directs Cell Proliferation and Microtissue Morphology,” *PLoS One*, vol. 8, no. 10, pp. 1–17, 2013.
- [78] P. RA, “Fibronectin: a brief overview of its structure, function, and physiology,” *Rev. Infect. Dis.*, vol. 9 Suppl 4, 1987.
- [79] C. Klecker and L. S. Nair, “Matrix Chemistry Controlling Stem Cell Behavior,” *Biol. Eng. Stem Cell Niches*, pp. 195–213, Apr. 2017.

- [80] G. B. Fields, H. E. Van Wart, and H. Birkedal-Hansen, "Sequence specificity of human skin fibroblast collagenase. Evidence for the role of collagen structure in determining the collagenase cleavage site.," *J. Biol. Chem.*, vol. 262, no. 13, pp. 6221–6226, 1987.
- [81] J. A. Paten *et al.*, "Molecular Interactions between Collagen and Fibronectin: A Reciprocal Relationship that Regulates De Novo Fibrillogenesis," *Chem*, vol. 5, no. 8, pp. 2126–2145, 2019.
- [82] M. W. Conklin *et al.*, "Aligned Collagen Is a Prognostic Signature for Survival in Human Breast Carcinoma," *Am. J. Pathol.*, vol. 178, no. 3, pp. 1221–1232, Mar. 2011.
- [83] W. R. Zipfel, R. M. Williams, R. Christie, A. Y. Nikitin, B. T. Hyman, and W. W. Webb, "Live tissue intrinsic emission microscopy using multiphoton-excited native fluorescence and second harmonic generation," *Proc. Natl. Acad. Sci.*, vol. 100, no. 12, pp. 7075–7080, Jun. 2003.
- [84] P. P. Provenzano, K. W. Eliceiri, J. M. Campbell, D. R. Inman, J. G. White, and P. J. Keely, "Collagen reorganization at the tumor-stromal interface facilitates local invasion," *BMC Med.*, vol. 4, pp. 1–15, 2006.
- [85] N. H. Green, R. M. Delaine-Smith, H. J. Askew, R. Byers, G. C. Reilly, and S. J. Matcher, "A new mode of contrast in biological second harmonic generation microscopy," *Sci. Rep.*, vol. 7, no. 1, pp. 1–10, Dec. 2017.
- [86] X. Chen, O. Nadiarynkh, S. Plotnikov, and P. J. Campagnola, "Second harmonic generation microscopy for quantitative analysis of collagen fibrillar structure," *Nat. Protoc.* 2012 74, vol. 7, no. 4, pp. 654–669, Mar. 2012.
- [87] S. Weiner and H. D. Wagner, "THE MATERIAL BONE: Structure-Mechanical Function Relations," *Annu. Rev. Mater. Sci.*, vol. 28, no. 1, pp. 271–298, Aug. 1998.
- [88] E. F. Morgan, G. U. Unnikrisnan, and A. I. Hussein, "Bone Mechanical Properties in Healthy and Diseased States," *Annu. Rev. Biomed. Eng.*, vol. 20, pp. 119–143, 2018.
- [89] E. Dall'Ara, P. Grabowski, P. Zioupos, and M. Viceconti, "Estimation of local anisotropy of plexiform bone: Comparison between depth sensing micro-indentation and Reference Point Indentation," *J. Biomech.*, vol. 48, no. 15, pp. 4073–4080, Nov. 2015.
- [90] H. S. Gupta, U. Stachewicz, W. Wagermaier, P. Roschger, H. D. Wagner, and P. Fratzl, "Mechanical modulation at the lamellar level in osteonal bone," *J. Mater. Res.*, vol. 21, no. 8, pp. 1913–1921, 2006.
- [91] E. Dall'Ara, C. Öhman, M. Baleani, and M. Viceconti, "The effect of tissue condition and applied load on Vickers hardness of human trabecular bone," *J. Biomech.*, vol. 40, no. 14, pp. 3267–3270, 2007.
- [92] B. Clarke, "Normal Bone Anatomy and Physiology," *Clin. J. Am. Soc. Nephrol.*, vol. 3, no. Supplement 3, pp. S131–S139, Nov. 2008.

- [93] H. Beaupied, E. Lespessailles, and C. L. Benhamou, "Evaluation of macrostructural bone biomechanics," *Jt. Bone Spine*, vol. 74, no. 3, pp. 233–239, 2007.
- [94] J. Klein-Nulend and A. D. Bakker, "Osteocytes: Mechanosensors of bone and orchestrators of mechanical adaptation," *Clinical Reviews in Bone and Mineral Metabolism*, vol. 5, no. 4. Springer, pp. 195–209, 13-Dec-2007.
- [95] B. Li and R. M. Aspden, "Mechanical and material properties of the subchondral bone plate from the femoral head of patients with osteoarthritis or osteoporosis."
- [96] P. Braidotti, E. Bemporad, T. D'Alessio, S. A. Sciuto, and L. Stagni, "Tensile experiments and SEM fractography on bovine subchondral bone," *J. Biomech.*, vol. 33, no. 9, pp. 1153–1157, 2000.
- [97] C. E. Misch, Z. Qu, and M. W. Bidez, "Mechanical properties of trabecular bone in the human mandible: implications for dental implant treatment planning and surgical placement," *J. Oral Maxillofac. Surg.*, vol. 57, no. 6, pp. 700–706, 1999.
- [98] J. Y. Rho, R. B. Ashman, and C. H. Turner, "Young's modulus of trabecular and cortical bone material: Ultrasonic and microtensile measurements," *J. Biomech.*, vol. 26, no. 2, pp. 111–119, Feb. 1993.
- [99] J. Krasnoff and P. Painter, "The Physiological Consequences of Bed Rest and Inactivity," *Adv. Ren. Replace. Ther.*, vol. 6, no. 2, pp. 124–132, Apr. 1999.
- [100] S. Weinbaum, S. C. Cowin, and Y. Zeng, "A model for the excitation of osteocytes by mechanical loading-induced bone fluid shear stresses," *J. Biomech.*, vol. 27, no. 3, pp. 339–360, 1994.
- [101] X. Li *et al.*, "Stimulation of piezo1 by mechanical signals promotes bone anabolism," *Elife*, vol. 8, pp. 1–22, 2019.
- [102] B. T. MacDonald, K. Tamai, and X. He, "Wnt/ β -Catenin Signaling: Components, Mechanisms, and Diseases," *Developmental Cell*, vol. 17, no. 1. NIH Public Access, pp. 9–26, 21-Jul-2009.
- [103] Y. Kobayashi, K. Maeda, and N. Takahashi, "Roles of Wnt signaling in bone formation and resorption," *Jpn. Dent. Sci. Rev.*, vol. 44, no. 1, pp. 76–82, 2008.
- [104] N. T. Yasuhiro Kobayashi, Kazuhiro Maeda, "New advances in osteocyte mechanotransduction," *Physiol. Behav.*, vol. 176, no. 3, pp. 139–148, 2017.
- [105] E. G. Canty *et al.*, "Actin Filaments Are Required for Fibripositor-mediated Collagen Fibril Alignment in Tendon," *J. Biol. Chem.*, vol. 281, no. 50, pp. 38592–38598, Dec. 2006.
- [106] S. Dupont *et al.*, "Role of YAP/TAZ in mechanotransduction," *Nat. 2011 4747350*, vol. 474, no. 7350, pp. 179–183, Jun. 2011.

- [107] R. McBeath, D. M. Pirone, C. M. Nelson, K. Bhadriraju, and C. S. Chen, "Cell Shape, Cytoskeletal Tension, and RhoA Regulate Stem Cell Lineage Commitment," *Dev. Cell*, vol. 6, no. 4, pp. 483–495, Apr. 2004.
- [108] A. Kim, N. Lakshman, and W. M. Petroll, "Quantitative assessment of local collagen matrix remodeling in 3-D Culture: The role of Rho kinase," *Exp. Cell Res.*, vol. 312, no. 18, pp. 3683–3692, Nov. 2006.
- [109] H. Kovar, L. Bierbaumer, and B. Radic-sarikas, "cells The YAP / TAZ Pathway in Osteogenesis and Bone," *Cells*, vol. 9, no. 972, pp. 1–34, 2020.
- [110] K. I. Wada, K. Itoga, T. Okano, S. Yonemura, and H. Sasaki, "Hippo pathway regulation by cell morphology and stress fibers," *Development*, vol. 138, no. 18, pp. 3907–3914, Sep. 2011.
- [111] G. Kumar, M. S. Waters, T. M. Farooque, M. F. Young, and C. G. Simon, "Freeform fabricated scaffolds with roughened struts that enhance both stem cell proliferation and differentiation by controlling cell shape," *Biomaterials*, vol. 33, no. 16, pp. 4022–4030, Jun. 2012.
- [112] P. Viswanathan *et al.*, "3D surface topology guides stem cell adhesion and differentiation," *Biomaterials*, vol. 52, no. 1, pp. 140–147, Jun. 2015.
- [113] M. J. Dalby *et al.*, "The control of human mesenchymal cell differentiation using nanoscale symmetry and disorder," *Nat. Mater.*, vol. 6, no. 12, pp. 997–1003, Sep. 2007.
- [114] R. McBeath, D. M. Pirone, C. M. Nelson, K. Bhadriraju, and C. S. Chen, "Cell shape, cytoskeletal tension, and RhoA regulate stem cell lineage commitment," *Dev. Cell*, vol. 6, no. 4, pp. 483–495, Apr. 2004.
- [115] K. Bhadriraju, M. Yang, S. Alom Ruiz, D. Pirone, J. Tan, and C. S. Chen, "Activation of ROCK by RhoA is regulated by cell adhesion, shape, and cytoskeletal tension," *Exp. Cell Res.*, vol. 313, no. 16, pp. 3616–3623, Oct. 2007.
- [116] S. Donell, "Subchondral bone remodelling in osteoarthritis," *EFORT Open Rev.*, vol. 4, no. 6, pp. 221–229, Jun. 2019.
- [117] A. M. Bendele, "Animal models of osteoarthritis," 2001.
- [118] J.-P. Pelletier, M.-P. Faure, J. A. Dibattista, S. Wilhelm, D. Visco, and J. Martel-Pelletier, "Coordinate Synthesis of Stromelysin, Interleukin-1, and Oncogene Proteins in Experimental Osteoarthritis," 1993.
- [119] G. Liu *et al.*, "Selection and investigation of a primate model of spontaneous degenerative knee osteoarthritis, the cynomolgus monkey (*Macaca fascicularis*)," *Med. Sci. Monit.*, vol. 24, pp. 4516–4527, Jul. 2018.
- [120] P. Singh, K. B. Marcu, M. B. Goldring, and M. Otero, "Phenotypic instability of chondrocytes in osteoarthritis: on a path to hypertrophy," *Annals of the New York Academy of Sciences*, vol. 1442, no. 1. Blackwell Publishing Inc., pp. 17–34, 01-Apr-2019.

- [121] K. Lampropoulou-Adamidou *et al.*, “Useful animal models for the research of osteoarthritis,” *European Journal of Orthopaedic Surgery and Traumatology*, vol. 24, no. 3. Springer-Verlag France, pp. 263–271, 13-Mar-2014.
- [122] G. A. Van Norman, “Limitations of Animal Studies for Predicting Toxicity in Clinical Trials: Is it Time to Rethink Our Current Approach?,” *JACC Basic to Transl. Sci.*, vol. 4, no. 7, pp. 845–854, Nov. 2019.
- [123] J. Etich *et al.*, “Osteogenesis imperfecta—pathophysiology and therapeutic options,” *Mol. Cell. Pediatr.*, vol. 7, no. 1, 2020.
- [124] F. S. Van Dijk, G. Pals, R. R. Van Rijn, P. G. J. Nikkels, and J. M. Cobben, “Classification of Osteogenesis Imperfecta revisited,” *Eur. J. Med. Genet.*, vol. 53, no. 1, pp. 1–5, Jan. 2010.
- [125] F. S. Van Dijk and D. O. Silience, “Osteogenesis imperfecta: Clinical diagnosis, nomenclature and severity assessment,” *Am. J. Med. Genet. Part A*, vol. 164, no. 6, pp. 1470–1481, Jun. 2014.
- [126] P. H. Byers, G. A. Wallis, and M. C. Willing, “Osteogenesis imperfecta: translation of mutation to phenotype,” *J. Med. Genet.*, vol. 28, no. 7, p. 433, 1991.
- [127] J. C. Marini *et al.*, “Osteogenesis imperfecta,” *Nat. Rev. Dis. Prim.*, vol. 3, pp. 1–19, 2017.
- [128] R. C. Pollitt *et al.*, “Phenotypic variability in patients with osteogenesis imperfecta caused by BMP1 mutations,” *Am. J. Med. Genet. Part A*, vol. 170, no. 12, pp. 3150–3156, 2016.
- [129] P. V. Asharani *et al.*, “Attenuated BMP1 Function Compromises Osteogenesis, Leading to Bone Fragility in Humans and Zebrafish,” *Am. J. Hum. Genet.*, vol. 90, no. 4, p. 661, Apr. 2012.
- [130] E. G. Canty and K. E. Kadler, “Procollagen trafficking, processing and fibrillogenesis,” *J. Cell Sci.*, vol. 118, no. 7, pp. 1341–1353, Apr. 2005.
- [131] Z. Ashkavand, H. Malekinejad, and B. S. Vishwanath, “The pathophysiology of osteoarthritis The pathophysiology of osteoarthritis,” *JOPR J. Pharm. Res.*, vol. 7, no. 1, pp. 132–138, 2013.
- [132] S. M. Botter, G. J. V. M. van Osch, S. Clockaerts, J. H. Waarsing, H. Weinans, and J. P. T. M. van Leeuwen, “Osteoarthritis induction leads to early and temporal subchondral plate porosity in the tibial plateau of mice: An in vivo microfocal computed tomography study,” *Arthritis Rheum.*, vol. 63, no. 9, pp. 2690–2699, Sep. 2011.
- [133] P. J. Watson, T. A. Carpenter, L. D. Hall, and J. A. Tyler, “Cartilage swelling and loss in a spontaneous model of osteoarthritis visualized by magnetic resonance imaging,” in *Osteoarthritis and Cartilage*, 1996, vol. 4, no. 3, pp. 197–207.

- [134] M. D. Grynblas, B. Alpert, I. Katz, I. Lieberman, and K. P. H. Pritzker, "Subchondral bone in osteoarthritis," *Calcif. Tissue Int.*, vol. 49, no. 1, pp. 20–26, Jan. 1991.
- [135] C. Buckland-Wright, "Subchondral bone changes in hand and knee osteoarthritis detected by radiography," *Osteoarthr. Cartil.*, vol. 12, no. SUPPL., pp. 10–19, Jan. 2004.
- [136] C. S. Carlson, R. F. Loeser, C. B. Purser, J. F. Gardin, and C. P. Jerome, "Osteoarthritis in cynomolgus macaques III: Effects of age, gender, and subchondral bone thickness on the severity of disease," *J. Bone Miner. Res.*, vol. 11, no. 9, pp. 1209–1217, Dec. 2009.
- [137] F. Chicatun, E. Rezabeigi, N. Muja, M. T. Kaartinen, M. D. McKee, and S. N. Nazhat, "A bilayered dense collagen/chitosan hydrogel to model the osteochondral interface," *Emergent Mater.*, vol. 2, no. 2, pp. 245–262, Jun. 2019.
- [138] B. A. Harley, A. K. Lynn, Z. Wissner-Gross, W. Bonfield, I. V. Yannas, and L. J. Gibson, "Design of a multiphase osteochondral scaffold III: Fabrication of layered scaffolds with continuous interfaces," *J. Biomed. Mater. Res. Part A*, vol. 9999A, no. 3, p. NA-NA, Mar. 2009.
- [139] A. C. Lawson and J. T. Czernuszka, "Collagen-calcium phosphate composites," <http://dx.doi.org/10.1243/0954411981534187>, vol. 212, no. 6, pp. 413–425, Jun. 1998.
- [140] C. Du, F. Z. Cui, W. Zhang, Q. L. Feng, X. D. Zhu, and K. De Groot, "Formation of calcium phosphate/collagen composites through mineralization of collagen matrix," 2000.
- [141] D. A. Wahl and J. T. Czernuszka, "Collagen-hydroxyapatite composites for hard tissue repair," *Eur. Cells Mater.*, vol. 11, pp. 43–56, 2006.
- [142] J. A. Inzana *et al.*, "3D printing of composite calcium phosphate and collagen scaffolds for bone regeneration," *Biomaterials*, vol. 35, no. 13, pp. 4026–4034, 2014.
- [143] J. Kozłowska and A. Sionkowska, "Effects of different crosslinking methods on the properties of collagen-calcium phosphate composite materials," *Int. J. Biol. Macromol.*, vol. 74, pp. 397–403, 2015.
- [144] B. Bhaskar, R. Owen, H. Bahmaee, Z. Wally, P. Sreenivasa Rao, and G. C. Reilly, "Composite porous scaffold of PEG/PLA support improved bone matrix deposition in vitro compared to PLA-only scaffolds," *J. Biomed. Mater. Res. - Part A*, vol. 106, no. 5, pp. 1334–1340, 2018.
- [145] B. A. Dikici, S. Dikici, G. C. Reilly, S. Macneil, and F. Claeysens, "materials A Novel Bilayer Polycaprolactone Membrane for Guided Bone Regeneration: Combining Electrospinning and Emulsion Templating," 2019.
- [146] F. Sharifi, S. Irani, M. Zandi, M. Soleimani, and S. M. Atyabi, "Comparative

of fibroblast and osteoblast cells adhesion on surface modified nanofibrous substrates based on polycaprolactone,” *Prog. Biomater.*, vol. 5, no. 3–4, pp. 213–222, Dec. 2016.

- [147] B. Aldemir Dikici, G. C. Reilly, and F. Claeysens, “Boosting the Osteogenic and Angiogenic Performance of Multiscale Porous Polycaprolactone Scaffolds by in Vitro Generated Extracellular Matrix Decoration,” *ACS Appl. Mater. Interfaces*, vol. 12, no. 11, pp. 12510–12524, Mar. 2020.
- [148] X. Yang, X. Chen, and H. Wang, “Acceleration of osteogenic differentiation of preosteoblastic cells by chitosan containing nanofibrous scaffolds,” *Biomacromolecules*, vol. 10, no. 10, pp. 2772–2778, Oct. 2009.
- [149] T. Yao, H. Chen, M. B. Baker, and L. Moroni, “Effects of Fiber Alignment and Coculture with Endothelial Cells on Osteogenic Differentiation of Mesenchymal Stromal Cells,” *Tissue Eng. - Part C Methods*, vol. 26, no. 1, pp. 11–22, Jan. 2020.
- [150] K. Ren, Y. Wang, T. Sun, W. Yue, and H. Zhang, “Electrospun PCL/gelatin composite nanofiber structures for effective guided bone regeneration membranes,” *Mater. Sci. Eng. C*, vol. 78, pp. 324–332, Sep. 2017.
- [151] Q. Yao *et al.*, “Three dimensional electrospun PCL/PLA blend nanofibrous scaffolds with significantly improved stem cells osteogenic differentiation and cranial bone formation,” *Biomaterials*, vol. 115, pp. 115–127, Jan. 2017.
- [152] L. Elomaa, S. Teixeira, R. Hakala, H. Korhonen, D. W. Grijpma, and J. V. Seppälä, “Preparation of poly(ϵ -caprolactone)-based tissue engineering scaffolds by stereolithography,” *Acta Biomater.*, vol. 7, no. 11, pp. 3850–3856, 2011.
- [153] B. Aldemir Dikici, C. Sherborne, G. C. Reilly, and F. Claeysens, “Emulsion templated scaffolds manufactured from photocurable polycaprolactone,” *Polymer (Guildf.)*, vol. 175, pp. 243–254, Jun. 2019.
- [154] L. Elomaa, E. Keshi, I. M. Sauer, and M. Weinhart, “Development of GelMA/PCL and dECM/PCL resins for 3D printing of acellular in vitro tissue scaffolds by stereolithography,” *Mater. Sci. Eng. C*, vol. 112, p. 110958, Jul. 2020.
- [155] R. Diez-Ahedo *et al.*, “UV-Casting on Methacrylated PCL for the Production of a Peripheral Nerve Implant Containing an Array of Porous Aligned Microchannels,” *Polym. 2020, Vol. 12, Page 971*, vol. 12, no. 4, p. 971, Apr. 2020.
- [156] J. Field, J. W. Haycock, F. M. Boissonade, and F. Claeysens, “Tissue Engineering — Synthesis , Characterisation and Use in Stereolithography,” 2021.
- [157] J. Field, J. W. Haycock, F. M. Boissonade, and F. Claeysens, “A Tuneable, Photocurable, Poly(Caprolactone)-Based Resin for Tissue Engineering— Synthesis, Characterisation and Use in Stereolithography,” *Mol. 2021, Vol. 26, Page 1199*, vol. 26, no. 5, p. 1199, Feb. 2021.

- [158] L. Xu *et al.*, “Bioprinting small diameter blood vessel constructs with an endothelial and smooth muscle cell bilayer in a single step,” *Biofabrication*, vol. 12, no. 4, p. 045012, Jul. 2020.
- [159] S. R. Ur Rehman, R. Augustine, A. A. Zahid, R. Ahmed, M. Tariq, and A. Hasan, “Reduced Graphene Oxide Incorporated GelMA Hydrogel Promotes Angiogenesis For Wound Healing Applications,” *Int. J. Nanomedicine*, vol. 14, p. 9603, 2019.
- [160] A. Hasan, A. Paul, A. Memic, and A. Khademhosseini, “A multilayered microfluidic blood vessel-like structure,” *Biomed. Microdevices*, vol. 17, no. 5, pp. 1–13, Oct. 2015.
- [161] M. Vigata, C. D. O’connell, S. Cometta, D. W. Hutmacher, C. Meinert, and N. Bock, “Gelatin Methacryloyl Hydrogels for the Localized Delivery of Cefazolin,” *Polym. 2021, Vol. 13, Page 3960*, vol. 13, no. 22, p. 3960, Nov. 2021.
- [162] J. Wang *et al.*, “Microfluidic Preparation of Gelatin Methacryloyl Microgels as Local Drug Delivery Vehicles for Hearing Loss Therapy,” *ACS Appl. Mater. Interfaces*, vol. 14, no. 41, pp. 46212–46223, Oct. 2022.
- [163] H. J. Yoon *et al.*, “Cold Water Fish Gelatin Methacryloyl Hydrogel for Tissue Engineering Application,” *PLoS One*, vol. 11, no. 10, p. e0163902, Oct. 2016.
- [164] J. W. Nichol, S. T. Koshy, H. Bae, C. M. Hwang, S. Yamanlar, and A. Khademhosseini, “Cell-laden microengineered gelatin methacrylate hydrogels,” *Biomaterials*, vol. 31, no. 21, pp. 5536–5544, Jul. 2010.
- [165] S. A. Goldstein, “The mechanical properties of trabecular bone: Dependence on anatomic location and function,” *J. Biomech.*, vol. 20, no. 11–12, pp. 1055–1061, Jan. 1987.
- [166] G. L. Ying *et al.*, “Aqueous Two-Phase Emulsion Bioink-Enabled 3D Bioprinting of Porous Hydrogels,” *Adv. Mater.*, vol. 30, no. 50, Dec. 2018.
- [167] Y. Wang *et al.*, “Development of a photo-crosslinking, biodegradable GelMA/PEGDA hydrogel for guided bone regeneration materials,” *Materials (Basel)*, vol. 11, no. 8, pp. 6–8, 2018.
- [168] D. N. Heo *et al.*, “Enhanced bone regeneration with a gold nanoparticle–hydrogel complex,” *J. Mater. Chem. B*, vol. 2, no. 11, pp. 1584–1593, Feb. 2014.
- [169] J. R. Xavier *et al.*, “Bioactive nanoengineered hydrogels for bone tissue engineering: A growth-factor-free approach,” *ACS Nano*, vol. 9, no. 3, pp. 3109–3118, Mar. 2015.
- [170] F. You, X. Wu, and X. Chen, “3D printing of porous alginate/gelatin hydrogel scaffolds and their mechanical property characterization,” *Int. J. Polym. Mater. Polym. Biomater.*, vol. 66, no. 6, pp. 299–306, Apr. 2017.
- [171] R. Seyedmahmoud *et al.*, “Three-dimensional bioprinting of functional skeletal muscle tissue using gelatin methacryloyl-alginate bioinks,”

Micromachines, vol. 10, no. 10, 2019.

- [172] A. A. Aldana, F. Valente, R. Dilley, and B. Doyle, “Development of 3D bioprinted GelMA-alginate hydrogels with tunable mechanical properties,” *Bioprinting*, vol. 21, no. June 2020, p. e00105, 2021.
- [173] Z. Wu, S. Xie, Y. Kang, X. Shan, Q. Li, and Z. Cai, “Biocompatibility evaluation of a 3D-bioprinted alginate-GelMA-bacteria nanocellulose (BNC) scaffold laden with oriented-growth RSC96 cells,” *Mater. Sci. Eng. C*, vol. 129, no. May, p. 112393, 2021.
- [174] J. A. McKenzie, E. C. Bixby, and M. J. Silva, “Differential gene expression from microarray analysis distinguishes woven and lamellar bone formation in the rat ulna following mechanical loading,” *PLoS One*, vol. 6, no. 12, 2011.
- [175] M. Whitely *et al.*, “Porous PolyHIPE microspheres for protein delivery from an injectable bone graft,” *Acta Biomater.*, vol. 93, pp. 169–179, 2019.
- [176] Y. Cao *et al.*, “The influence of architecture on degradation and tissue ingrowth into three-dimensional poly(lactic-co-glycolic acid) scaffolds in vitro and in vivo,” *Biomaterials*, vol. 27, no. 14, pp. 2854–2864, 2006.
- [177] H. Bahmaee *et al.*, “Design and Evaluation of an Osteogenesis-on-a-Chip Microfluidic Device Incorporating 3D Cell Culture,” *Front. Bioeng. Biotechnol.*, vol. 8, p. 1042, Sep. 2020.
- [178] T. E. Paterson *et al.*, “Porous microspheres support mesenchymal progenitor cell ingrowth and stimulate angiogenesis,” *APL Bioeng.*, vol. 2, no. 2, 2018.
- [179] Y. Hu *et al.*, “Facile preparation of bioactive nanoparticle/poly(ϵ -caprolactone) hierarchical porous scaffolds via 3D printing of high internal phase Pickering emulsions,” *J. Colloid Interface Sci.*, vol. 545, pp. 104–115, Jun. 2019.
- [180] A. Samanta, S. Takkar, R. Kulshreshtha, B. Nandan, and R. K. Srivastava, “Facile Fabrication of Composite Electrospun Nanofibrous Matrices of Poly(ϵ -caprolactone)–Silica Based Pickering Emulsion,” 2017.
- [181] Y. Yang *et al.*, “An overview of pickering emulsions: Solid-particle materials, classification, morphology, and applications,” *Front. Pharmacol.*, vol. 8, no. MAY, pp. 1–20, 2017.
- [182] C. Li, Y. Li, P. Sun, and C. Yang, “Pickering emulsions stabilized by native starch granules,” *Colloids Surfaces A Physicochem. Eng. Asp.*, vol. 431, pp. 142–149, 2013.
- [183] W. Stöber, A. Fink, and E. Bohn, “Controlled growth of monodisperse silica spheres in the micron size range,” *J. Colloid Interface Sci.*, vol. 26, no. 1, pp. 62–69, Jan. 1968.
- [184] F. Ebrahimi, R. Farazi, E. Z. Karimi, and H. Beygi, “Dichlorodimethylsilane

- mediated one-step synthesis of hydrophilic and hydrophobic silica nanoparticles,” *Adv. Powder Technol.*, vol. 28, no. 3, pp. 932–937, 2017.
- [185] S. R. Saeid Jalali, S. Sobat, and G. Farzi, “Surface modification of silica nanoparticle using dichlorodimethylsilane for preparation of self-cleaning coating based on polyurethane and polydimethylsiloxane,” *Mater. Res. Express*, vol. 5, no. 9, p. 95311, Sep. 2018.
- [186] J. Xie *et al.*, “Osteogenic differentiation and bone regeneration of iPSC-MSCs supported by a biomimetic nanofibrous scaffold,” *Acta Biomater.*, vol. 29, pp. 365–379, Jan. 2016.
- [187] W. Shao *et al.*, “Coaxial electrospun aligned tussah silk fibroin nanostructured fiber scaffolds embedded with hydroxyapatite-tussah silk fibroin nanoparticles for bone tissue engineering,” *Mater. Sci. Eng. C*, vol. 58, pp. 342–351, Jan. 2016.
- [188] M. A. Woodruff and D. W. Hutmacher, “The return of a forgotten polymer - Polycaprolactone in the 21st century,” *Prog. Polym. Sci.*, vol. 35, no. 10, pp. 1217–1256, 2010.
- [189] G. A. J. Tetteh and G. C. Reilly, “Polyurethane-based Sca olds for Bone Tissue Engineering,” The University of Sheffield, 2016.
- [190] V. Karageorgiou and D. Kaplan, “Porosity of 3D biomaterial scaffolds and osteogenesis,” *Biomaterials*, vol. 26, no. 27. Elsevier BV, pp. 5474–5491, 01-Sep-2005.
- [191] S. A. Irvine and S. S. Venkatraman, “Bioprinting and differentiation of stem cells,” *Molecules*, vol. 21, no. 9. MDPI AG, 08-Sep-2016.
- [192] S. C. Cox, J. A. Thornby, G. J. Gibbons, M. A. Williams, and K. K. Mallick, “3D printing of porous hydroxyapatite scaffolds intended for use in bone tissue engineering applications,” *Mater. Sci. Eng. C*, vol. 47, pp. 237–247, Feb. 2015.
- [193] T. Billiet, E. Gevaert, T. De Schryver, M. Cornelissen, and P. Dubruel, “The 3D printing of gelatin methacrylamide cell-laden tissue-engineered constructs with high cell viability,” *Biomaterials*, vol. 35, no. 1, pp. 49–62, 2014.
- [194] B. Webb and B. J. Doyle, “Parameter optimization for 3D bioprinting of hydrogels,” *Bioprinting*, vol. 8, pp. 8–12, Dec. 2017.
- [195] A. I. Van Den Bulcke, B. Bogdanov, N. De Rooze, E. H. Schacht, M. Cornelissen, and H. Berghmans, “Structural and rheological properties of methacrylamide modified gelatin hydrogels,” *Biomacromolecules*, vol. 1, no. 1, pp. 31–38, 2000.
- [196] C. Pautke *et al.*, “Characterization of osteosarcoma cell lines MG-63, Saos-2 and U-2 OS in comparison to human osteoblasts,” *Anticancer Res.*, vol. 24, no. 6, pp. 3743–3748, 2004.

- [197] Y. Kato, A. Boskey, L. Spevak, M. Dallas, M. Hori, and L. F. Bonewald, "Establishment of an osteoid preosteocyte-like cell MLO-A5 that spontaneously mineralizes in culture," *J. Bone Miner. Res.*, vol. 16, no. 9, pp. 1622–1633, Sep. 2001.
- [198] G. Tetteh, A. S. Khan, R. M. Delaine-Smith, G. C. Reilly, and I. U. Rehman, "Electrospun polyurethane/hydroxyapatite bioactive Scaffolds for bone tissue engineering: The role of solvent and hydroxyapatite particles," *J. Mech. Behav. Biomed. Mater.*, vol. 39, pp. 95–110, Nov. 2014.
- [199] S. L. Dallas *et al.*, "Time lapse imaging techniques for comparison of mineralization dynamics in primary murine osteoblasts and the late osteoblast/early osteocyte-like cell line MLO-A5," in *Cells Tissues Organs*, 2008, vol. 189, no. 1–4, pp. 6–11.
- [200] S. Takamizawa, Y. Maehata, K. Imai, H. Senoo, S. Sato, and R. I. Hata, "Effects of ascorbic acid and ascorbic acid 2-phosphate, a long-acting vitamin C derivative, on the proliferation and differentiation of human osteoblast-like cells," *Cell Biol. Int.*, vol. 28, no. 4, pp. 255–265, 2004.
- [201] B. Wang, Q. Cai, S. Zhang, X. Yang, and X. Deng, "The effect of poly (L-lactic acid) nanofiber orientation on osteogenic responses of human osteoblast-like MG63 cells," *J. Mech. Behav. Biomed. Mater.*, vol. 4, no. 4, pp. 600–609, May 2011.
- [202] K. C. Russell, D. G. Phinney, M. R. Lacey, B. L. Barrilleaux, K. E. Meyertholen, and K. C. O'Connor, "In vitro high-capacity assay to quantify the clonal heterogeneity in trilineage potential of mesenchymal stem cells reveals a complex hierarchy of lineage commitment," *Stem Cells*, vol. 28, no. 4, pp. 788–798, Apr. 2010.
- [203] S. James *et al.*, "Multiparameter Analysis of Human Bone Marrow Stromal Cells Identifies Distinct Immunomodulatory and Differentiation-Competent Subtypes," *Stem Cell Reports*, vol. 4, no. 6, pp. 1004–1015, Jun. 2015.
- [204] D. A. Hoey, S. Tormey, S. Ramcharan, F. J. O'Brien, and C. R. Jacobs, "Primary cilia-mediated mechanotransduction in human mesenchymal stem cells," *Stem Cells*, vol. 30, no. 11, pp. 2561–2570, Nov. 2012.
- [205] B. Bhaskar, R. Owen, H. Bahmaee, P. S. Rao, and G. C. Reilly, "Design and Assessment of a Dynamic Perfusion Bioreactor for Large Bone Tissue Engineering Scaffolds," *Appl. Biochem. Biotechnol.*, vol. 185, no. 2, pp. 555–563, Jun. 2018.
- [206] C. Wittkowske, G. C. Reilly, D. Lacroix, and C. M. Perrault, "In Vitro Bone Cell Models: Impact of Fluid Shear Stress on Bone Formation," *Front. Bioeng. Biotechnol.*, vol. 4, no. NOV, Nov. 2016.
- [207] X. Zhou, D. Liu, L. You, and L. Wang, "Quantifying fluid shear stress in a rocking culture dish," *J. Biomech.*, vol. 43, no. 8, pp. 1598–1602, 2010.
- [208] R. M. Delaine-Smith, S. MacNeil, and G. C. Reilly, "Matrix production and

collagen structure are enhanced in two types of osteogenic progenitor cells by a simple fluid shear stress stimulus," *Eur. Cells Mater.*, vol. 24, no. July, pp. 162–174, 2012.

- [209] S. Puwanun, R. M. Delaine-Smith, H. E. Colley, J. M. Yates, S. MacNeil, and G. C. Reilly, "A simple rocker-induced mechanical stimulus upregulates mineralization by human osteoprogenitor cells in fibrous scaffolds," *J. Tissue Eng. Regen. Med.*, vol. 12, no. 2, pp. 370–381, 2018.
- [210] K. T. Lim *et al.*, "Enhanced osteogenesis of human alveolar bone-derived mesenchymal stem cells for tooth tissue engineering using fluid shear stress in a rocking culture method," *Tissue Eng. - Part C Methods*, vol. 19, no. 2, pp. 128–145, Feb. 2013.
- [211] X. Zhou, D. Liu, L. You, and L. Wang, "Quantifying fluid shear stress in a rocking culture dish," *J. Biomech.*, vol. 43, no. 8, pp. 1598–1602, May 2010.
- [212] J. van der Valk *et al.*, "Fetal Bovine Serum (FBS): Past - Present - Future," *ALTEX*, vol. 35, no. 1, pp. 99–118, 2018.
- [213] C. E. A. Jochems, J. B. F. Van der Valk, F. R. Stafleu, and V. Baumans, "The use of fetal bovine serum: Ethical or scientific problem?," *ATLA Altern. to Lab. Anim.*, vol. 30, no. 2, pp. 219–227, 2002.
- [214] S. Schubert, W. Brehm, A. Hillmann, and J. Burk, "Serum-free human MSC medium supports consistency in human but not in equine adipose-derived multipotent mesenchymal stromal cell culture," *Cytom. Part A*, vol. 93, no. 1, pp. 60–72, Jan. 2018.
- [215] W. G. Whitford, M. Lundgren, and A. Fairbank, "Cell Culture Media in Bioprocessing," in *Biopharmaceutical Processing: Development, Design, and Implementation of Manufacturing Processes*, Elsevier, 2018, pp. 147–162.
- [216] J. Schindelin *et al.*, "Fiji - an Open platform for biological image analysis," *Nat. Methods*, vol. 9, no. 7, 2009.
- [217] T. Peng *et al.*, "Evasion of the Mucosal Innate Immune System by Herpes Simplex Virus Type 2," *J. Virol.*, vol. 83, no. 23, pp. 12559–12568, Dec. 2009.
- [218] M. Z. Xu *et al.*, "Yes-Associated Protein Is an Independent Prognostic Marker in Hepatocellular Carcinoma," *Cancer*, vol. 115, no. 19, p. 4576, Oct. 2009.
- [219] K. Görür *et al.*, "RhoA, ROCK-1, and ROCK-2 Gene Expression and Polymorphisms in Cholesteatoma Patients," *J. Int. Adv. Otol.*, vol. 17, no. 6, pp. 530–535, Nov. 2021.
- [220] F. Verisqa, J. R. Cha, L. Nguyen, H. W. Kim, and J. C. Knowles, "Digital Light Processing 3D Printing of Gyroid Scaffold with Isosorbide-Based Photopolymer for Bone Tissue Engineering," *Biomol. 2022, Vol. 12, Page 1692*, vol. 12, no. 11, p. 1692, Nov. 2022.

- [221] S. Onizuka *et al.*, “ZBTB16 as a Downstream Target Gene of Osterix Regulates Osteoblastogenesis of Human Multipotent Mesenchymal Stromal Cells,” *J. Cell. Biochem.*, vol. 117, no. 10, p. 2423, Oct. 2016.
- [222] R. T. Pace and K. J. L. Burg, “Toxic effects of resazurin on cell cultures,” *Cytotechnology*, vol. 67, no. 1, p. 13, Jan. 2015.
- [223] V. Kishore, W. Bullock, X. Sun, W. S. Van Dyke, and O. Akkus, “Tenogenic differentiation of human MSCs induced by the topography of electrochemically aligned collagen threads,” *Biomaterials*, vol. 33, no. 7, pp. 2137–2144, Mar. 2012.
- [224] J. S. Park *et al.*, “The effect of matrix stiffness on the differentiation of mesenchymal stem cells in response to TGF- β ,” *Biomaterials*, vol. 32, no. 16, pp. 3921–3930, Jun. 2011.
- [225] K. Chatterjee *et al.*, “The effect of 3D hydrogel scaffold modulus on osteoblast differentiation and mineralization revealed by combinatorial screening,” *Biomaterials*, vol. 31, no. 19, pp. 5051–5062, Jul. 2010.
- [226] A. S. Badami, M. R. Kreke, M. S. Thompson, J. S. Riffle, and A. S. Goldstein, “Effect of fiber diameter on spreading, proliferation, and differentiation of osteoblastic cells on electrospun poly(lactic acid) substrates,” *Biomaterials*, vol. 27, no. 4, pp. 596–606, Feb. 2006.
- [227] G. Le Saux *et al.*, “Cell-Cell Adhesion-Driven Contact Guidance and Its Effect on Human Mesenchymal Stem Cell Differentiation,” *ACS Appl. Mater. Interfaces*, vol. 12, no. 20, pp. 22399–22409, 2020.
- [228] D. H. Reneker, I. Chun, J. M. Deitzwl, J. D. Kleinmeyer, D. Harris, and N. C. Beckettan, “Effect of Humidity on the Microstructures of Electrospun Polystyrene Nanofibers,” *Microsc Microanal*, vol. 7, no. 2, pp. 261–272, 2019.
- [229] W. Li, B. Zhu, Z. Strakova, and R. Wang, “Biochemical and Biophysical Research Communications Two-way regulation between cells and aligned collagen fibrils : Local 3D matrix formation and accelerated neural differentiation of human decidua parietalis placental stem cells,” *Biochem. Biophys. Res. Commun.*, vol. 450, no. 4, pp. 1377–1382, 2014.
- [230] J. B. Lee *et al.*, “Highly porous electrospun nanofibers enhanced by ultrasonication for improved cellular infiltration,” *Tissue Eng. - Part A*, vol. 17, no. 21–22, pp. 2695–2702, Nov. 2011.
- [231] A. Celebioglu and T. Uyar, “Electrospun porous cellulose acetate fibers from volatile solvent mixture,” *Mater. Lett.*, vol. 65, no. 14, pp. 2291–2294, Jul. 2011.
- [232] J. Xia, Y. Yuan, H. Wu, Y. Huang, and D. A. Weitz, “Decoupling the effects of nanopore size and surface roughness on the attachment, spreading and differentiation of bone marrow-derived stem cells,” *Biomaterials*, vol. 248, p. 120014, Jul. 2020.
- [233] S. Oh *et al.*, “Stem cell fate dictated solely by altered nanotube dimension,”

Proc. Natl. Acad. Sci. U. S. A., vol. 106, no. 7, pp. 2130–2135, Feb. 2009.

- [234] R. Ghobeira, M. Asadian, C. Vercruyse, H. Declercq, N. De Geyter, and R. Morent, “Wide-ranging diameter scale of random and highly aligned PCL fibers electrospun using controlled working parameters,” *Polymer (Guildf)*, vol. 157, pp. 19–31, Nov. 2018.
- [235] Y. M. Kolambkar, M. Bajin, A. Wojtowicz, D. W. Hutmacher, A. J. García, and R. E. Guldberg, “Nanofiber orientation and surface functionalization modulate human mesenchymal stem cell behavior in vitro,” *Tissue Eng. - Part A*, vol. 20, no. 1–2, pp. 398–409, Jan. 2014.
- [236] H. A. Lynch, W. Johannessen, J. P. Wu, A. Jawa, and D. M. Elliott, “Effect of Fiber Orientation and Strain Rate on the Nonlinear Uniaxial Tensile Material Properties of Tendon,” *J. Biomech. Eng.*, vol. 125, no. 5, pp. 726–731, 2003.
- [237] “StemMACS™ MSC Expansion Media Kit XF, human | Stem cell culture media | Cell culture media | MACS Cell Culture and Stimulation | Products | Miltenyi Biotec | Great Britain.” [Online]. Available: <https://www.miltenyibiotec.com/GB-en/products/stemmaacs-msc-expansion-media-kit-xf-human.html#gref>. [Accessed: 13-Jan-2023].
- [238] “Mesenchymal Stem Cell Growth Medium XF - PromoCell.” [Online]. Available: https://promocell.com/product/mesenchymal-stem-cell-growth-medium-xf/#tab-data_figures. [Accessed: 13-Jan-2023].
- [239] C. Knight *et al.*, “Epidermal growth factor can signal via β -catenin to control proliferation of mesenchymal stem cells independently of canonical Wnt signalling,” *Cell. Signal.*, vol. 53, pp. 256–268, Jan. 2019.
- [240] R. A. Rocha, J. M. Fox, P. G. Genever, and Y. Hancock, “Biomolecular phenotyping and heterogeneity assessment of mesenchymal stromal cells using label-free Raman spectroscopy,” *Sci. Reports 2021 III*, vol. 11, no. 1, pp. 1–16, Feb. 2021.
- [241] F. Saleh, A. Carstairs, S. L. Etheridge, and P. Genever, “Real-Time Analysis of Endogenous Wnt Signalling in 3D Mesenchymal Stromal Cells,” *Stem Cells Int.*, vol. 2016, 2016.
- [242] E. F. Smeets, E. J. U. von Asmuth, C. J. van der Linden, J. F. M. Leeuwenberg, and W. A. Buurman, “A Comparison of Substrates for Human Umbilical Vein Endothelial Cell Culture,” <http://dx.doi.org/10.3109/10520299209110072>, vol. 67, no. 4, pp. 241–250, 2009.
- [243] C. Somaiah *et al.*, “Collagen Promotes Higher Adhesion, Survival and Proliferation of Mesenchymal Stem Cells,” *PLoS One*, vol. 10, no. 12, p. e0145068, Dec. 2015.
- [244] A. B. Bello, D. Kim, D. Kim, H. Park, and S. H. Lee, “Engineering and functionalization of gelatin biomaterials: From cell culture to medical applications,” *Tissue Eng. - Part B Rev.*, vol. 26, no. 2, pp. 164–180, Apr.

2020.

- [245] S. I. Kurata and R. I. Hata, “Epidermal growth factor inhibits transcription of type I collagen genes and production of type I collagen in cultured human skin fibroblasts in the presence and absence of L-ascorbic acid 2-phosphate, a long-acting vitamin C derivative,” *J. Biol. Chem.*, vol. 266, no. 15, pp. 9997–10003, May 1991.
- [246] S. I. Kurata, H. Senoo, and R. I. Hata, “Transcriptional activation of type I collagen genes by ascorbic acid 2-phosphate in human skin fibroblasts and Its failure in cells from a patient with $\alpha 2(I)$ -chain-defective Ehlers-Danlos syndrome,” *Exp. Cell Res.*, vol. 206, no. 1, pp. 63–71, 1993.
- [247] M. H. Wu, J. P. G. Urban, F. C. Zhan, Z. Cui, and X. Xu, “Effect of extracellular pH on matrix synthesis by chondrocytes in 3D agarose gel,” *Biotechnol. Prog.*, vol. 23, no. 2, pp. 430–434, Mar. 2007.
- [248] N. Anderson, R. R. Fergus, and C. Nm, “Vitamin C: A Concentration-Function Approach Yields Pharmacology and Therapeutic Discoveries,” *Adv. Nutr.*, vol. 2, no. Xii, pp. 78–88, 2001.
- [249] E. G. Hayman and E. Ruoslahti, “Distribution of fetal bovine serum fibronectin and endogenous rat cell fibronectin in extracellular matrix,” *J. Cell Biol.*, vol. 83, no. 1, pp. 255–259, 1979.
- [250] C. A. Sevilla, D. Dalecki, and D. C. Hocking, “Regional Fibronectin and Collagen Fibril Co-Assembly Directs Cell Proliferation and Microtissue Morphology,” *PLoS One*, vol. 8, no. 10, p. 77316, 2013.
- [251] Z. Hamidouche *et al.*, “FHL2 mediates dexamethasone-induced mesenchymal cell differentiation into osteoblasts by activating Wnt/ β -catenin signaling-dependent Runx2 expression,” *FASEB J.*, vol. 22, no. 11, pp. 3813–3822, Nov. 2008.
- [252] J. N. Beresford, J. H. Bennett, C. Devlin, P. S. Leboyt, and M. E. Owen, “Evidence for an inverse relationship between the differentiation of adipocytic and osteogenic cells in rat marrow stromal cell cultures,” *J. Cell Sci.*, vol. 102, pp. 341–351, 1992.
- [253] Y. Wang *et al.*, “The differential effects of aligned electrospun PHBHHx fibers on adipogenic and osteogenic potential of MSCs through the regulation of PPAR γ signaling,” *Biomaterials*, vol. 33, no. 2, pp. 485–493, Jan. 2012.
- [254] L. Feldskov Nielsen, D. Moe, S. Kirkeby, and C. Garbarsch, “Sirius Red and Acid Fuchsin Staining Mechanisms,” *Biotech. Histochem.*, vol. 73, no. 2, pp. 71–77, 1998.
- [255] M. J. Post *et al.*, “Scientific, sustainability and regulatory challenges of cultured meat,” *Nat. Food 2020 17*, vol. 1, no. 7, pp. 403–415, Jul. 2020.
- [256] W. Wagermaier, H. S. Gupta, A. Gourrier, M. Burghammer, P. Roschger, and P. Fratzl, “Spiral twisting of fiber orientation inside bone lamellae,”

Biointerphases, vol. 1, no. 1, pp. 1–5, 2006.

- [257] M. Granke *et al.*, “Microfibril Orientation Dominates the Microelastic Properties of Human Bone Tissue at the Lamellar Length Scale,” *PLoS One*, vol. 8, no. 3, pp. 1–11, 2013.
- [258] P. Fratzl, H. S. Gupta, F. D. Fischer, and O. Kolednik, “Hindered crack propagation in materials with periodically varying young’s modulus - Lessons from biological materials,” *Adv. Mater.*, vol. 19, no. 18, pp. 2657–2661, 2007.
- [259] O. Kolednik, J. Predan, F. D. Fischer, and P. Fratzl, “Improvements of strength and fracture resistance by spatial material property variations,” *Acta Mater.*, vol. 68, pp. 279–294, 2014.
- [260] F. D. Fischer, O. Kolednik, J. Predan, H. Razi, and P. Fratzl, “Crack driving force in twisted plywood structures,” *Acta Biomater.*, vol. 55, pp. 349–359, 2017.
- [261] Z. Song, Y. Ni, and S. Cai, “Fracture modes and hybrid toughening mechanisms in oscillated/twisted plywood structure,” *Acta Biomater.*, vol. 91, pp. 284–293, 2019.
- [262] A. Matsugaki, G. Aramoto, T. Ninomiya, H. Sawada, S. Hata, and T. Nakano, “Abnormal arrangement of a collagen/apatite extracellular matrix orthogonal to osteoblast alignment is constructed by a nanoscale periodic surface structure,” *Biomaterials*, vol. 37, pp. 134–143, Jan. 2015.
- [263] M. D. Guillemette *et al.*, “Surface topography induces 3D self-orientation of cells and extracellular matrix resulting in improved tissue function,” *Integr. Biol.*, vol. 1, no. 2, pp. 196–204, 2009.
- [264] S. Ghazanfari, A. Khademhosseini, and T. H. Smit, “Mechanisms of lamellar collagen formation in connective tissues,” *Biomaterials*, vol. 97, pp. 74–84, 2016.
- [265] O. Menzel and W. Borth, “Influence of Plasma Fibronectin on Collagen Cleavage by Collagenase,” *Collagen Rel. Res.*, vol. 3, pp. 217–230, 1983.
- [266] F. Shi, J. Harman, K. Fujiwara, and J. Sottile, “Collagen I matrix turnover is regulated by fibronectin polymerization,” *Am. J. Physiol. - Cell Physiol.*, vol. 298, no. 5, p. C1265, May 2010.
- [267] H. K. Kleinman, E. B. Mcgoodwin, and R. J. Klebe, “Localisation of the Cell Attachment Region In Types I and II Collagens,” *Biochem. Biophys. Res. Commun.*, vol. 72, no. 2, 1976.
- [268] J. Sottile, F. Shi, I. Rublyevska, H. Y. Chiang, J. Lust, and J. Chandler, “Fibronectin-dependent collagen I deposition modulates the cell response to fibronectin,” *Am. J. Physiol. Cell Physiol.*, vol. 293, no. 6, Dec. 2007.
- [269] A. Tahmasebi *et al.*, “Micro-RNA-incorporated electrospun nanofibers improve osteogenic differentiation of human-induced pluripotent stem

- cells,” *J. Biomed. Mater. Res. - Part A*, vol. 108, no. 2, pp. 377–386, Feb. 2020.
- [270] M. Bruderer, R. G. Richards, M. Alini, and M. J. Stoddart, “Role and regulation of runx2 in osteogenesis,” *Eur. Cells Mater.*, vol. 28, pp. 269–286, 2014.
- [271] T. Komori, “Regulation of osteoblast differentiation by Runx2,” *Adv. Exp. Med. Biol.*, vol. 658, pp. 43–49, 2010.
- [272] X. Li *et al.*, “Effects of aligned and random fibers with different diameter on cell behaviors,” *Colloids Surf. B. Biointerfaces*, vol. 171, pp. 461–467, Nov. 2018.
- [273] T. L. Jenkins and D. Little, “Synthetic scaffolds for musculoskeletal tissue engineering: cellular responses to fiber parameters,” *NPJ Regen. Med.*, vol. 4, no. 1, Dec. 2019.
- [274] B. Chang, C. Ma, and X. Liu, “Nanofibers Regulate Single Bone Marrow Stem Cell Osteogenesis via FAK/RhoA/YAP1 Pathway,” 2018.
- [275] G. Bilbe, E. Roberts, M. Birch, and D. B. Evans, “PCR phenotyping of cytokines, growth factors and their receptors and bone matrix proteins in human osteoblast-like cell lines,” *Bone*, vol. 19, no. 5 SUPPL., pp. 437–445, 1996.
- [276] B. Wang, Q. Cai, S. Zhang, X. Yang, and X. Deng, “The effect of poly (L-lactic acid) nanofiber orientation on osteogenic responses of human osteoblast-like MG63 cells,” *J. Mech. Behav. Biomed. Mater.*, vol. 4, no. 4, pp. 600–609, 2011.
- [277] S. W. Tsai, Y. W. Hsu, W. L. Pan, A. Vadivelmurugan, P. A. Hwang, and F. Y. Hsu, “Influence of the Components and Orientation of Hydroxyapatite Fibrous Substrates on Osteoblast Behavior,” *J. Funct. Biomater.*, vol. 13, no. 4, 2022.
- [278] R. Butler, I. Hopkinson, and A. I. Cooper, “Synthesis of Porous Emulsion-Templated Polymers Using High Internal Phase CO₂-in-Water Emulsions,” *J. Am. Chem. Soc.*, vol. 125, no. 47, pp. 14473–14481, 2003.
- [279] Y. Wu *et al.*, “The influence of the stiffness of GelMA substrate on the outgrowth of PC12 cells,” *Biosci. Rep.*, vol. 39, no. 1, Jan. 2019.
- [280] S. N. S. Alconcel, A. S. Baas, and H. D. Maynard, “FDA-approved poly(ethylene glycol)–protein conjugate drugs,” *Polym. Chem.*, vol. 2, no. 7, pp. 1442–1448, Jun. 2011.
- [281] P. Chansoria, L. K. Narayanan, M. Wood, C. Alvarado, A. Lin, and R. A. Shirwaiker, “Effects of Autoclaving, EtOH, and UV Sterilization on the Chemical, Mechanical, Printability, and Biocompatibility Characteristics of Alginate,” *ACS Biomater. Sci. Eng.*, vol. 6, no. 9, pp. 5191–5201, Sep. 2020.
- [282] B. Aldemir Dikici, “Development of emulsion templated matrices and their use in tissue engineering applications,” no. June, 2020.

- [283] N. A. Sears, P. S. Dhavalikar, and E. M. Cosgriff-Hernandez, "Emulsion Inks for 3D Printing of High Porosity Materials," *Macromol. Rapid Commun.*, vol. 37, no. 16, pp. 1369–1374, Aug. 2016.
- [284] B. Aldemir Dikici, C. Sherborne, G. C. Reilly, and F. Claeysens, "Emulsion templated scaffolds manufactured from photocurable polycaprolactone," *Polymer (Guildf.)*, vol. 175, pp. 243–254, Jun. 2019.
- [285] L. H. Lin and K. M. Chen, "Preparation and surface activity of gelatin derivative surfactants," *Colloids Surfaces A Physicochem. Eng. Asp.*, vol. 272, no. 1–2, pp. 8–14, 2006.
- [286] J. O'Sullivan, B. Murray, C. Flynn, and I. Norton, "The effect of ultrasound treatment on the structural, physical and emulsifying properties of animal and vegetable proteins," *Food Hydrocoll.*, vol. 53, pp. 141–154, 2016.
- [287] T. Zhang, M. Ding, N. Tao, X. Wang, and J. Zhong, "Effects of surfactant type and preparation pH on the droplets and emulsion forms of fish oil-loaded gelatin/surfactant-stabilized emulsions," *Lwt*, vol. 117, no. September 2019, p. 108654, 2020.
- [288] H. Tan, G. Sun, W. Lin, C. Mu, and T. Ngai, "Gelatin particle-stabilized high internal phase emulsions as nutraceutical containers," *ACS Appl. Mater. Interfaces*, vol. 6, no. 16, pp. 13977–13984, Aug. 2014.
- [289] M. Su, R. Liska, G. Unter, R. Uller, J. Ri Kotek, and P. Krajnc, "Microcellular Open Porous Monoliths for Cell Growth by Thiol-Ene Polymerization of Low-Toxicity Monomers in High Internal Phase Emulsions a."
- [290] R. S. Moglia, J. L. Holm, N. A. Sears, C. J. Wilson, D. M. Harrison, and E. Cosgriff-Hernandez, "Injectable PolyHIPEs as High Porosity Bone Grafts," *Biomacromolecules*, vol. 12, no. 10, p. 3621, Oct. 2011.
- [291] E. Liu, D. Zhu, E. Gonzalez Diaz, X. Tong, and F. Yang, "Gradient Hydrogels for Optimizing Niche Cues to Enhance Cell-Based Cartilage Regeneration," *Tissue Eng. Part A*, vol. 27, no. 13–14, pp. 929–939, Jul. 2021.
- [292] B. Bachmann *et al.*, "Stiffness Matters: Fine-Tuned Hydrogel Elasticity Alters Chondrogenic Redifferentiation," *Front. Bioeng. Biotechnol.*, vol. 8, p. 373, Apr. 2020.
- [293] L. Zilic, S. P. Wilshaw, and J. W. Haycock, "Decellularisation and histological characterisation of porcine peripheral nerves," *Biotechnol. Bioeng.*, vol. 113, no. 9, pp. 2041–2053, Sep. 2016.
- [294] P. J. Yang and J. S. Temenoff, "Engineering orthopedic tissue interfaces," *Tissue Engineering - Part B: Reviews*, vol. 15, no. 2, pp. 127–141, 01-Jun-2009.
- [295] W. Liu *et al.*, "Rapid Continuous Multimaterial Extrusion Bioprinting," *Adv. Mater.*, vol. 29, no. 3, p. 1604630, Jan. 2017.
- [296] H. Yoshikawa and A. Myoui, "Bone tissue engineering with porous hydroxyapatite ceramics," *Journal of Artificial Organs*, vol. 8, no. 3, pp.

131–136, Sep-2005.

- [297] F. Peng, X. Yu, and M. Wei, “In vitro cell performance on hydroxyapatite particles/poly(L-lactic acid) nanofibrous scaffolds with an excellent particle along nanofiber orientation,” *Acta Biomater.*, vol. 7, no. 6, pp. 2585–2592, Jun. 2011.
- [298] S. C. Cox, J. A. Thornby, G. J. Gibbons, M. A. Williams, and K. K. Mallick, “3D printing of porous hydroxyapatite scaffolds intended for use in bone tissue engineering applications,” *Mater. Sci. Eng. C*, vol. 47, pp. 237–247, Feb. 2015.
- [299] G. Presbítero-Espinosa *et al.*, “Characterization of Sodium Alginate Hydrogels Reinforced with Nanoparticles of Hydroxyapatite for Biomedical Applications,” *Polymers (Basel)*, vol. 13, no. 17, Sep. 2021.
- [300] M. Shbeh *et al.*, “Incorporation of HA into porous titanium to form Ti-HA biocomposite foams,” *J. Mech. Behav. Biomed. Mater.*, vol. 96, pp. 193–203, Aug. 2019.
- [301] Q. Liu, J. R. De Wijn, D. Bakker, and C. A. Van Blitterswijk, “Surface modification of hydroxyapatite to introduce interfacial bonding with Polyactive® 70/30 in a biodegradable composite,” *J. Mater. Sci. Mater. Med.*, vol. 7, no. 9, pp. 551–557, 1996.
- [302] P. Cheang and K. A. Khor, “Effect of particulate morphology on the tensile behaviour of polymer–hydroxyapatite composites,” *Mater. Sci. Eng. A*, vol. 345, no. 1–2, pp. 47–54, Mar. 2003.
- [303] C. Ohtsuki, “Ceramic–polymer composites,” *Bioceram. their Clin. Appl.*, pp. 501–517, Jan. 2008.
- [304] F. Cestari, M. Petretta, Y. Yang, A. Motta, B. Grigolo, and V. M. Sglavo, “3D printing of PCL/nano-hydroxyapatite scaffolds derived from biogenic sources for bone tissue engineering,” *Sustain. Mater. Technol.*, vol. 29, no. May, p. e00318, 2021.
- [305] W. Y. Choi, H. E. Kim, and Y. H. Koh, “Production, mechanical properties and in vitro biocompatibility of highly aligned porous poly(ϵ -caprolactone) (PCL)/hydroxyapatite (HA) scaffolds,” *J. Porous Mater.*, vol. 20, no. 4, pp. 701–708, 2013.
- [306] M. Gentile, L. Latonen, and M. Laiho, “Cell cycle arrest and apoptosis provoked by UV radiation-induced DNA damage are transcriptionally highly divergent responses,” *Nucleic Acids Res.*, vol. 31, no. 16, p. 4779, Aug. 2003.
- [307] T. P. Heffernan *et al.*, “An ATR- and Chk1-Dependent S Checkpoint Inhibits Replicon Initiation following UVC-Induced DNA Damage,” *Mol. Cell. Biol.*, vol. 22, no. 24, p. 8552, Dec. 2002.
- [308] V. Ansteinsson, H. B. Kopperud, E. Morisbak, and J. T. Samuelsen, “Cell toxicity of methacrylate monomers-The role of glutathione adduct

- formation,” *J. Biomed. Mater. Res. - Part A*, vol. 101, no. 12, pp. 3504–3510, 2013.
- [309] U. Blaschke, K. Eismann, A. Böhme, A. Paschke, and G. Schüürmann, “Structural alerts for the excess toxicity of acrylates, methacrylates, and propiolates derived from their short-term and long-term bacterial toxicity,” *Chem. Res. Toxicol.*, vol. 25, no. 1, pp. 170–180, 2012.
- [310] N. Ballatori, S. M. Krance, S. Notenboom, S. Shi, K. Tieu, and C. L. Hammond, “Glutathione dysregulation and the etiology and progression of human diseases,” *Biol. Chem.*, vol. 390, no. 3, p. 191, Mar. 2009.
- [311] J. A. Werkmeister *et al.*, “Biodegradable and injectable cure-on-demand polyurethane scaffolds for regeneration of articular cartilage,” *Acta Biomater.*, vol. 6, no. 9, pp. 3471–3481, 2010.
- [312] S. L. Greasley *et al.*, “Controlling particle size in the Stöber process and incorporation of calcium,” *J. Colloid Interface Sci.*, vol. 469, pp. 213–223, May 2016.
- [313] W. Busby, N. R. Cameron, and C. A. B. Jahoda, “Emulsion-derived foams (PolyHIPEs) containing poly(ϵ -caprolactone) as matrixes for tissue engineering,” *Biomacromolecules*, vol. 2, no. 1, pp. 154–164, 2001.
- [314] S. Changotade *et al.*, “Preliminary in Vitro Assessment of Stem Cell Compatibility with Cross-Linked Poly(ϵ -caprolactone urethane) Scaffolds Designed through High Internal Phase Emulsions,” *Stem Cells Int.*, vol. 2015, 2015.
- [315] J. L. Robinson, R. S. Moglia, M. C. Stuebben, M. A. P. Mcenery, and E. Cosgriff-Hernandez, “Achieving Interconnected Pore Architecture in Injectable PolyHIPEs for Bone Tissue Engineering,” *Tissue Eng. Part A*, vol. 20, no. 5–6, p. 1103, Mar. 2014.
- [316] T. Yang, Y. Hu, C. Wang, and B. P. Binks, “Fabrication of Hierarchical Macroporous Biocompatible Scaffolds by Combining Pickering High Internal Phase Emulsion Templates with Three-Dimensional Printing,” *ACS Appl. Mater. Interfaces*, vol. 9, no. 27, pp. 22950–22958, Jul. 2017.
- [317] T. W. Chung, D. Z. Liu, S. Y. Wang, and S. S. Wang, “Enhancement of the growth of human endothelial cells by surface roughness at nanometer scale,” *Biomaterials*, vol. 24, no. 25, pp. 4655–4661, 2003.
- [318] X. Hu, S. H. Park, E. S. Gil, X. X. Xia, A. S. Weiss, and D. L. Kaplan, “The influence of elasticity and surface roughness on myogenic and osteogenic-differentiation of cells on silk-elastin biomaterials,” *Biomaterials*, vol. 32, no. 34, pp. 8979–8989, Dec. 2011.
- [319] S. Zou, Y. Yang, H. Liu, and C. Wang, “Synergistic stabilization and tunable structures of Pickering high internal phase emulsions by nanoparticles and surfactants,” *Colloids Surfaces A Physicochem. Eng. Asp.*, vol. 436, pp. 1–9, Sep. 2013.

- [320] E. Donnelly, M.-G. Ascenzi, and C. Farnum, "Primary cilia are highly oriented with respect to collagen direction and long axis of extensor tendon," *J. Orthop. Res.*, vol. 28, no. 1, p. n/a-n/a, Jan. 2009.
- [321] S. Temiyasathit *et al.*, "Mechanosensing by the Primary Cilium: Deletion of Kif3A Reduces Bone Formation Due to Loading," *PLoS One*, vol. 7, no. 3, p. e33368, Mar. 2012.
- [322] L. Boyle, "Lithium Enhances Osteogenic Responses to Fluid Shear Stress," no. September, 2019.
- [323] S. Goring, N. Scully, D. Mason, and B. Evans, "Retinoic acid and IGF-1 stimulate the differentiation of human primary osteoblasts to osteocytes in 3D collagen gels," *Endocr. Abstr.*, pp. 1–1, Mar. 2013.
- [324] Kirkstall, "Quasi Vivo® | The Many Benefits of the Organ-on-a-chip Technology | Kirkstall Ltd." [Online]. Available: <https://kirkstall.com/why-quasi-vivo/>. [Accessed: 29-Mar-2023].
- [325] E. A. Zimmermann, B. Busse, and R. O. Ritchie, "The fracture mechanics of human bone: influence of disease and treatment," *Bonekey Rep.*, vol. 4, p. 743, Sep. 2015.